# Boron-based nanomaterials under extreme conditions

Rémi Grosjean

# Université Pierre et Marie Curie

Ecole doctorale 397, Chimie et Physico-Chimie des Matériaux

*Laboratoire Chimie de la Matière Condensée de Paris*

*Institut de Minéralogie, de Physique des Matériaux et de Cosmochimie*


# Nanomatériaux à base de bore sous conditions extrêmes

## *Boron-based nanomaterials under extreme conditions*


Par Rémi Grosjean


Thèse de doctorat en Science des Matériaux

Dirigée par David Portehault, Yann Le Godec, Corinne Chanéac

Présentée et soutenue publiquement le 17 Octobre 2016

Devant un jury composé de :

| | | |
|---|---|---|
| M. Bernard Samuel | Directeur de recherche, CNRS | Rapporteur |
| M. Machon Denis | Maître de conférences, Université Lyon 1 | Rapporteur |
| Mme. Laurencin Danielle | Chargée de recherche, CNRS | Examinatrice |
| M. Petit Christophe | Professeur, Université Paris 6 | Examinateur |
| M. Portehault David | Chargé de recherche CNRS | Co-directeur de thèse |
| M. Le Godec Yann | Chargé de recherche CNRS | Co-directeur de thèse |
| Mme. Chanéac Corinne | Professeur, Université Paris 6 | Directrice de thèse |

.

Ω
Δ >
) ¬ π
^ ´, )- ˇ•
∞ x (.) <> ∞
¿´ ∫ ◊ ~ ∂
≈ √ ]]

Alain Damasio, *La Horde du Contrevent*

# Remerciements

Bien qu'un seul nom figure sur la couverture du manuscrit, ce travail fut rendu possible par de nombreuses personnes.

Tout d'abord Clément, puis Florence qui m'ont accueilli au LCMCP, en stage puis en thèse, ainsi que Guillaume Fiquet, à l'IMPMC.

Je pense aussi à Patrick et Gervaise qui m'ont montré comment éteindre efficacement le TEM : en faisant entrer de l'air ; à Mohamed pour son aide avec les diffractos. Je remercie Isabelle pour les séances de MEB et la formation EDX. Je remercie bien sûr Cristina et Christel pour la RMN du noyau quadripolaire, j'aurais aimé avoir le temps de devenir utilisateur de niveau I.

Je pense à Tahar et Geeth, au LMV, qui m'ont permis de concilier expériences haute pression et visite de Clermont-Ferrand.

Je remercie Jean-Paul et Nicolas sur Psyché, qui nous ont confié la ligne, que nous avons consciencieusement noyée un soir d'ennui. Je remercie aussi Mohamed sur ID27, pour son guide de dépannage d'un fast-shutter par téléphone à toute heure du jour et de la nuit.

Pour leur patience devant les grilles de microscopie sans échantillon ou avec échantillon et pollution, je remercie Dario et Patricia.

Parce qu'il a toujours accepté avec plaisir mes paquets de vingt capillaires ou mes échantillons « urgents, parce que cette fois, c'est bon, on a la bonne phase », un grand merci à Ludovic.

Merci à Oleksandr pour son aide et les longues nuits passées dans les synchrotrons de France à contempler d'incompréhensibles signaux de diffraction.

Un grand merci aussi à Hélène et Corinne PdB qui ont toujours patiemment répondu à mes petites questions et qui ont rendu la vie au LCMCP plus facile, même quand un fournisseur veut envoyer ses avocats…

Pour toutes ses casquettes, merci au directeur de l'ED, ChrisBee. Merci pour avoir gravé dans ma mémoire les valeurs des spins nucléaires des isotropes du bore.

Pour m'avoir rappelé que les vannes volent (parfois seulement) en rase-motte et qu'il existe plusieurs échelles de température, merci Olivier.

Je remercie Sophie Cas' qui m'a fait entrer au labo et à l'école de la manipe robuste !

Aussi, merci à Sophie Car' pour son aide et ses conseils, au long des 3 ans et pour les démontages successifs et remontages réussis de Baggy.

Le LCMCP c'est aussi les éphémères, coupables de l'ambiance de travail (et pas que) au labo, dont la liste est longue…

Merci à François, pour les anecdotes, à Hugo, à Johanna, à Benj (préjent), à Anne, à Xavier C, à Sam, à Xavier F, à Stan, à Manue, à Morgane, à Sarah, à Jérôme, à

Clément, à Lionel, à Claiiire, et tous les autres. Notamment, je pense à Virgile, «si ce n'est pas un ami, au moins un collègue ».

Parce que la rédaction se fait seul mais accompagné, merci aux compagnons de galère qui ont su rendre avant moi sans en faire trop. Je pense évidemment à Cez & Tidu-Tidu. Merci pour les échanges (à la raquette), le soutien technique Microsoft Office et tout le reste.

Pour le partage du C4-5, des fours, de la boîte à gants et de moult histoires et anecdotes, merci Tsou-Hsi Camille.

M. Gouge et Dr Gouget, Maître Artisan en sels fondus, inventeur du bore amorphe, auteur de l'ouvrage « Le 5ème élément expliqué aux personnes âgées », dompteur de vagues du Pacifique et chantre du Saint-Hilaire, mille mercis.

Simon pour m'avoir fait découvrir les températures supérieures à celles rencontrées en hiver à Dantzig en 1709 et à celle du sang de cheval. Et pour m'avoir appris dans quelle unité on les compte. Et pour avoir pris la relève.

Mille mercis à ma famille : mes parents, mes frères, tonton (alors, cette thèse ?), mes grands-parents, ainsi qu'à Jacky, Véro, Baptiste et tous les Mei-Alenda-Carnemolla-Marchi, tous plus patients les uns que les autres et prêts à entendre parler de bore et d'enclumes, encore. Et je ne remercierai pas Sophie M.

Au 3 rue Thouin, à Budapest, à Lisbonne, à Bruxelles, en Dordogne, rue Erasme, 10 mètres sous la mer ou 30 cm sous la neige, les culs d'ours ont brillé par leur présence, leur soutien, leurs chansons parfois discutables, leur mauvaise foi. Merci Jaul, Erwan, Eska, Aco, Jérem (préjent), Baddouf, Julie$^2$, Belette, Matis, Samsam, Flobert, JiRossugue. Et courage aux docteurs à venir.

Et… place aux chefs !

Corinne, merci encore, pour l'accompagnement de la fin de la licence jusqu'à la fin de la thèse, pour ces réunions qui auront fait avancer le schmilblick (il est orange).

Il est d'usage de les nommer « encadrants ». A la fin de cette thèse, le terme ne me paraît pas adapté. David et Yann ont été deux véritables mentors : deux guides attentifs, sages. Yann qui m'a fait découvrir l'univers du GPa, le plaisir de l'usinage, les lignes de lumière, où nous avons noyé une ligne ou accumulé de nombreux diffractogrammes de la patafix. Merci pour ces soirées et week-ends passés sur la corrections du manuscrit. David, merci pour la science que j'ai apprise, la pas-science aussi (notamment la canalisation de mes innovations graphiques…), la patience, je promets de ne plus venir taper à la porte du bureau 10 fois par jour…

*Last, but not least,* je remercie « éventuellement » Nina, indéfectible soutien, phare dans la tempête aux multiples facettes, tour à tour correctrice féroce et infatigable, inquisitrice des abus de langage et anglicismes, et bien plus. Bruce Wayne a Alfred Pennyworth, j'ai Nina, qui vaut bien plus d'un penny !

# Table of contents

# Abbreviation list:

The abbreviations used in this manuscript are defined here in the following.

(HR)TEM: (High Resolution) Transmission Electron Microscopy
ABNNC: Aggregated Boron Nitride NanoComposite
ADNR: Aggregated Diamond Nanorods
CVD: Chemical Vapour Deposition
DAC: Diamond-Anvil Cell
DFT: Density Functional Theory
EDS: Energy Dispersive Spectroscopy
EELS: Electron Energy Loss Spectroscopy
EXAFS: Extended X-Ray Absorption Fine Structure
FFT: Fast Fourier Transform
HPE: Hall-Petch Effect
HPHT: High Pressure High Temperature
HPT: High Pressure Torsion
ICP-OES: Inductively Coupled Plasma Optical Emission Spectroscopy
ID: Internal Diameter
IMPMC: Institut de Minéralogie, de Physique des Matériaux et de Cosmochimie
IR: Infra-Red
LCMCP: Laboratoire de Chimie de la Matière Condensée de Paris
MAP: Multi-Anvil Press
MAS: Magic Angle Spinning
nano-$B_{am}$: SMS-derived nanostructured amorphous boron
NMR: Nuclear Magnetic Resonance
NPD: Nano-Polycrystalline Diamond
OD: Outer diameter
PDF: Pair Distribution Function
POS: Partial Occupation of Sites
SAED: Selected Area Electron Diffraction
SEM: Scanning Electron Microscopy
SMS: Synthesis in Molten-Salts
SPD: Severe Plastic Deformation
STEM-HAADF: Scanning Transmission Electron Microscopy -High Angle Annular Dark Field
STM: Scanning Tunneling Microscopy
XPS:X-Ray Photoelectron Spectroscopy
XRD: X-Ray Diffraction

# Introduction

Boron-based materials span a wide range of properties. This is illustrated by the widely spread use of boron oxide in the glass industry, as glass manufacturing and fibre glass insulation represent around 75 % of boron use.[1] Due to its strong reactivity with oxygen, boron is naturally covalently bound to oxygen. In addition to boron oxide, numerous metal and alkaline borates are used for applications from fertilisers (sodium and calcium borates) to single-crystal optical components. Boron nitrides *h*-BN and *c*-BN, isostructural to graphite and diamond, are also widely used materials: *h*-BN finds applications as solid lubricant up to 900 °C, as ceramics or cosmetic products, while *c*-BN is used as abrasive in cutting tools for ferrous alloys in which diamond is soluble at high temperature. Boron carbides such as $B_4C$ are also used for their mechanical properties, in abrasive, wear resistant coatings or armour plating. $B_4C$ is exploited in nuclear plants because of the large neutron capture cross-section of boron.

Boron also makes alloys with a large variety of metals, the so-called metal borides. These materials are used for their refractory properties, such as $HfB_2$, implemented as space-shuttle thermal shield for atmosphere re-entry. Metal borides also exhibit interesting mechanical ($TiB_2$), thermoelectric ($HfB_2$), thermo-ionic emission ($LaB_6$) or superconducting properties ($MgB_2$).[2] The various properties of metal borides stem from their numerous structures and stoichiometries, even for the same metal. Indeed, both boron and metal atoms usually have a formal null oxidation number, which emancipates metal borides from rules governing the structures of ionic compounds. For instance, Y-B alloys have various stoichiometries going from $YB_2$ to $YB_{66}$. In metal borides, structural complexity is directly linked to the increase in the boron content in the alloy: $YB_2$ consists in yttrium atoms intercalated between honeycomb boron layers, while $YB_{66}$ has a complex face-centred cubic structure (**a** = 2.34 nm, 1584 atoms per unit cell) based on the $B_{12}$ icosahedral building block.[2]

The $B_{12}$ icosahedron is the common structural unit of boron-rich borides (B/M > 12) and of all known boron allotropes. The elemental forms of boron remain challenging to both experimenters and theoreticians. Indeed, boron is the only stable element which ground state is still subject to debate, notably due to the difficulties encountered when calculating the relative energies of the modifications in competition.[3] Two new allotropes of boron have been discovered as recently as 2013.[4] In 2014 and 2016, new elemental forms of boron were reported: full-boron fullerene and two instances of 2-D boron base nanomaterials: borophene.[5–7] In 2009, the structure of an elemental modification of boron discovered in 1965 was solved.[8,9] It is the only known elemental modification to exhibit actual charge separation, a striking result.[8,9] In addition, crystallisation of boron is made difficult by the extreme sensibility of boron to the presence of foreign atoms. Indeed, numerous boron-rich borides ($PuB_{100}$), carbides ($B_{50}C_2$) or nitrides ($B_{50}N_2$) have structures differing from that of undoped-boron.[3] Because of the strength of the boron-boron covalent bonds and the complexity of the structures, the syntheses of most known boron phases are done under high pressure and temperature (HPHT) and the P,T phase diagram of boron is not set yet.[4,8,10–12] Boron allotropes share common properties: they exhibit

strong chemical inertness, notably *vs.* oxidation, and very high hardness.[8,10,13] The crystalline forms of boron are qualified of superhard materials, defined as solids exhibiting a Vicker's hardness superior to 40 GPa.[14] As indication and to put boron allotropes in perspective, the Vickers' hardness of several materials is indicated in Figure 1.

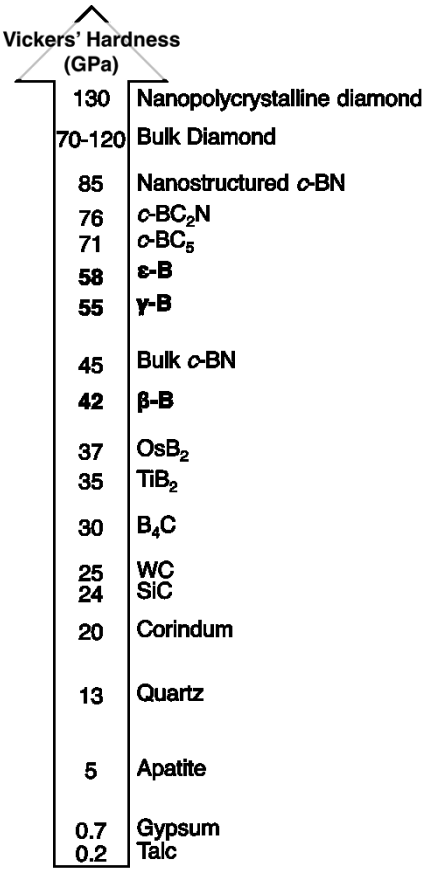


**Figure 1. Vickers' hardness order of magnitude.**

Hardness, as many inorganic materials' properties, can be tuned according to the materials' microstructure. Indeed, when the typical dimension matches the order of magnitude of physical phenomena, the resulting properties are modified. For instance, nanomaterials have specific properties in fields such as magnetism, optics or electronics. Moreover, nanostructuration of materials results in very high surface-to-volume ratio, hence enhanced reactivity, a particularly interesting feature for surface-based phenomena, such as catalysis or ion-insertion.

Compared to metal oxides, transition and noble metals, synthetic pathways towards nanostructured metal borides and boron phases remain poorly, if any, developed. Indeed, the covalent boron framework usually precludes crystallization below 400 °C, where instable and pyrophoric amorphous nanostructured borides are obtained.[2] Consequently, the synthesis of nanostructured metal borides must be done at sufficient temperature to allow crystallisation but low enough to impede grain growth, namely in the 400-1000 °C range.[2] Recently, a general route toward nanostructured metal borides has been developed: synthesis in molten salts (SMS).[15] This solution-based method relies on the reaction between molecule-scale

precursors of boron and metal and exploits the stability of molten inorganic salts in the temperature range considered. Recent works have evidenced the versatility of this route, in terms of size and stoichiometry controls.[2,15,16] Synthesis in molten salts is the only known synthetic route that reaches sub-10 nm crystalline metal borides. A specific aspect of SMS-derived materials is their nanocomposite nature: the particles are embedded in a three-dimensional matrix, mainly composed of amorphous elemental boron. Unlike previous works[17,16,18], which focused on the particles' properties and investigation of the underlying mechanism of SMS, the present PhD work aims at crystallising the amorphous matrix, while conserving (i) the borides particles and (ii) the nanocomposite nature of the material, using high pressure/high temperature (HPHT) processes.

Most recent developments of SMS have yielded a unique boron precursor: nanostructured amorphous boron (patented).[18] This material exhibits a unique reactivity that has been investigated as additive in propellants used in spatial propulsion.[19] In addition to its intrinsic properties, nanostructured amorphous boron represents a unique source of elemental boron for further synthesis and transformations. Along this PhD work, it has been used as starting material for boron crystallisation. As before-mentioned, high pressure and temperature are needed to achieve boron crystallisation.

Consequently, beyond the specific boron-based materials studied, this PhD work consists in the development of a synthetic methodology at the frontier between (i) liquid phase synthesis, (ii) nanosciences and (iii) synthesis in extreme pressure and temperature conditions.

High pressures are considered herein as exceeding 1 GPa. They are generated in the vast community of high pressure research using specific devices. Because the targeted field of this PhD work is materials synthesis, the devices chosen to explore high pressure conditions meet the requirement of high sample volume production with the compromise of high throughput experiments. Hence, two devices have been used: the Paris-Edinburgh press and the Kawai-type multi-anvil press. The pressures encountered with high pressure devices are described in Figure 2 and compared to those met in nature.

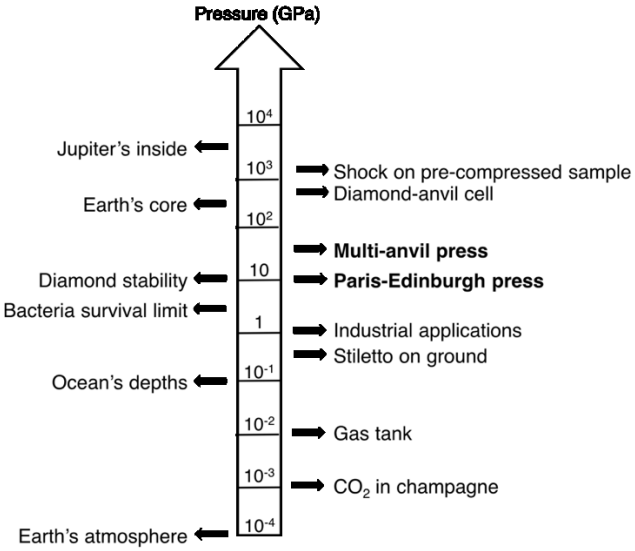


**Figure 2. Pressure orders of magnitude.**

A brief overview of the two set-ups used in this work is given below in order to provide the reader with key understanding of the experiments conducted in this work. A more detailed description is given in the appendices.

The Paris-Edinburgh and the multi-anvil press are hydraulic presses.[20] An oil pressure in the hundreds of bars range is applied to a first compression stage. The maximum pressure is reached between tungsten carbide anvils by successive surface reduction.

In the Paris-Edinburgh press, the sample is compressed between two tungsten carbide conical anvils (Figure 3), which design matches the shape of the gasket. The gasket contains the sample and the elements allowing heating. It also ensures that the pressure between the anvil is hydrostatic. The gasket is either made of pyrophyllite, for experiments dedicated to *ex situ* characterisation, or of amorphous boron and epoxy resin for *in situ* experiments monitored by X-ray diffraction. The sample is inserted inside a *h*-BN capsule (Figure 3). Heating is ensured by a resistive graphite heater. The temperature control is performed either using a thermocouple or based on power-supply output power *vs.* measured temperature calibration. In this press, it is possible to reach about 15 GPa and *ca.* 2000 °C. The reduced size and weight (*ca.* 50 kg for the instance in Figure 3) of this press allow easy installation on synchrotron or neutron beamlines.

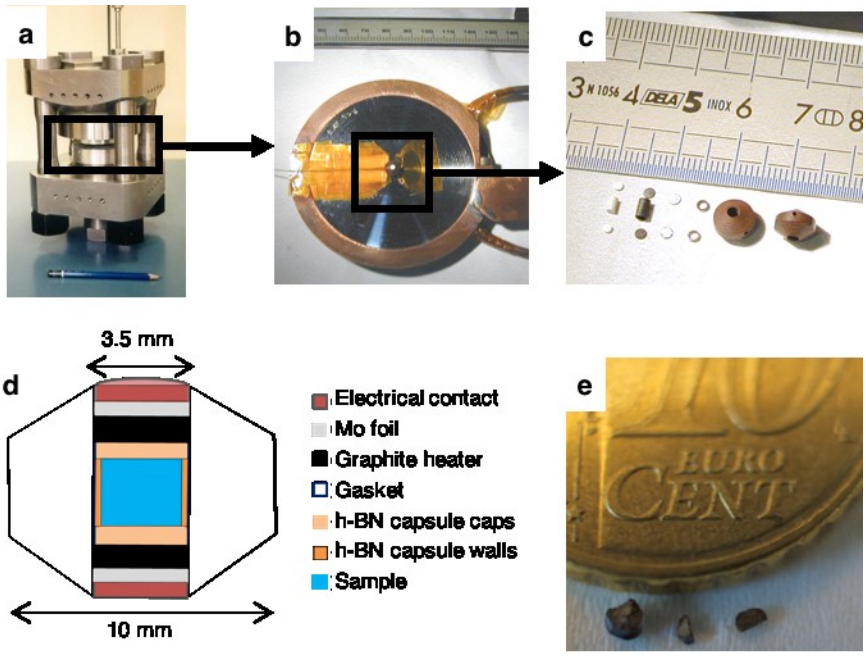


**Figure 3. (a) Paris-Edinburgh press, pencil for scale. (b) Tungsten carbide anvil. (c) High pressure assembly and gasket. (d) 3.5 mm assembly scheme. (e) Recovered sample after experiment at 5 GPa, 10 cents coin for scale.**

Multi-anvil apparatuses are much larger devices (Figure 4), in which the hydraulic pressure is transmitted to six steel outer anvils (Figure 4) then eight tungsten carbide cubic anvils. The tungsten carbide cubes are truncated on their vertexes, to form an octahedral cavity. The pressure chamber is usually a $Cr_2O_3$-doped MgO octahedron, used as pressure-transmitting medium. By varying the vertexes truncation and the octahedron dimensions, various pressures can be attained (Table 1). Heating is also resistive and is either controlled directly with a thermocouple or based on previous power-supply calibration. A whole experimental set-up in a multi anvil press is schematised in Figure 5.

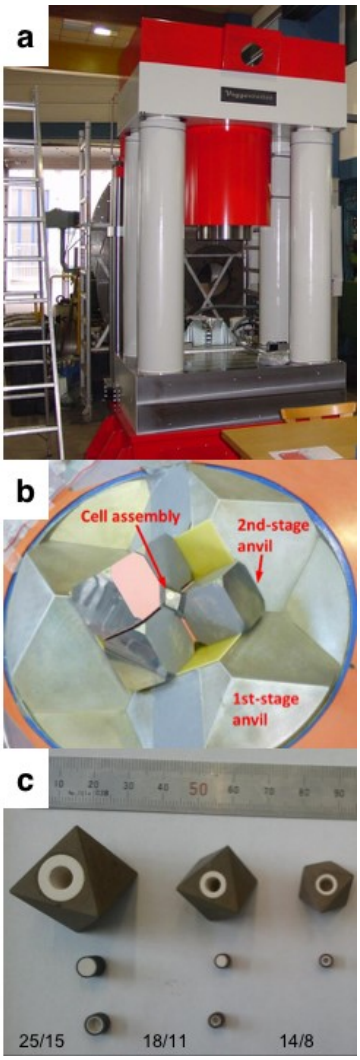


**Figure 4. (a) 1500-ton hydraulic press at Laboratoire Magma et Volcans, Clermont-Ferrand. (b) Kawai-type multi-anvil system. (c) Various sizes octahedra.**[21]

**Table 1. Sample size according to the octahedron dimension. OEL is the octahedron edge length, TEL the anvil truncation edge length.**[21]

| OEL/TEL (mm) | Capsule Volume ($mm^3$) | Maximum pressure (GPa) |
|---|---|---|
| 25/15 | 2.4 | 8 |
| 18/11 | 1.8 | 11 |
| 14/8 | 0.67 | 15 |

Note that all the elements composing the high pressure assemblies (either for the Paris-Edinburgh or the multi-anvil press) are single-use and are either extruded along compression or cut to allow sample recovery.

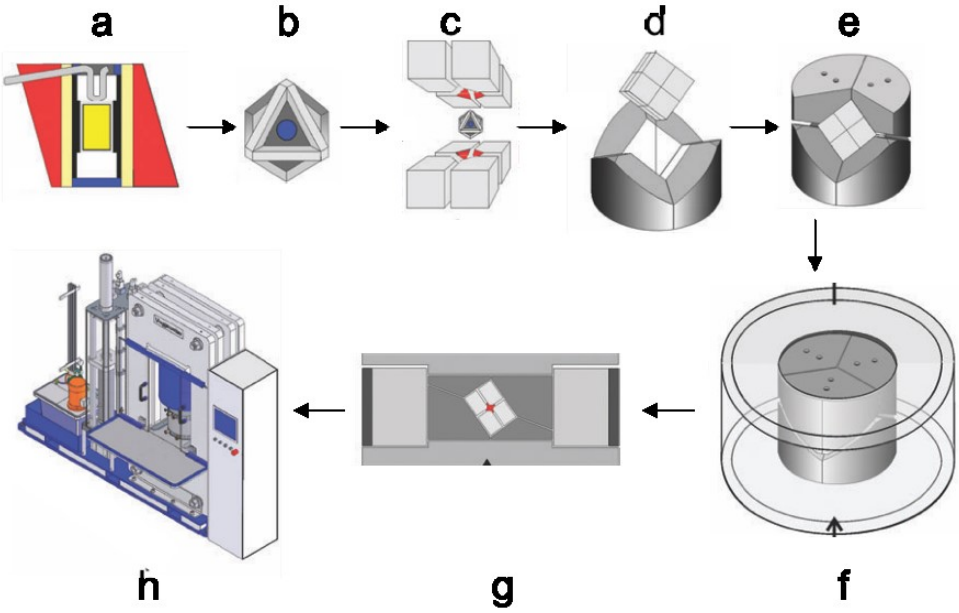


**Figure 5. Schematic preparation of a high-pressure experiment in a multi-anvil apparatus. (a) Cross-section of the pressure-cell octahedron (yellow rectangle: sample). (b) Ready-to-go octahedron. (c) Secondary anvils, consisting of eight truncated tungsten carbide cubes. (d) Three inferior wedges, incorporating the eight cubes. (e) Superior wedges. (f) Containment ring. (g) Complete high pressure module with primary anvils (top and bottom plates). (h) Uniaxial press.**[22]

As described above, the experimental volume available in such devices is in the order of magnitude of the cubic millimetre. Consequently, they belong to the class of large-volume press, in opposition to the diamond-anvil cell (Figure 6), for which the sample size is a few hundred microns. Note that no experiment was conducted in diamond-anvil cells during this work, but it is the case for several studies presented in the bibliography.

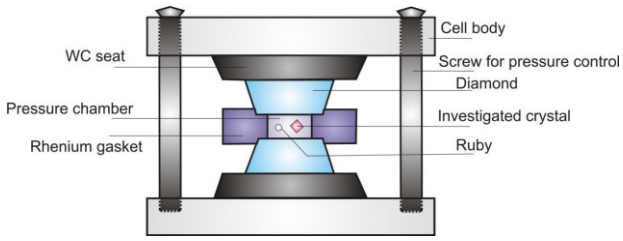


**Figure 6. Scheme of diamond-anvil cell (scale is not respected): the pressure chamber is 20 to 200 µm, total cell size is *ca.* 5 cm.**[21]

The present manuscript aims at presenting the different steps performed within this PhD work to reach the goals mentioned above. To do so, the thesis is divided into five chapters, as follows.

**Chapter I** presents the bibliographic aspects of the project around three axes. First, the development of nano-materials using HPHT techniques is discussed, either for light element-based hard materials or oxides. Then, the different elemental forms of boron and their relative stability are discussed. Finally, the focus shifts to metal borides, their structure and the synthetic pathways reaching nanostructured metal borides.

**Chapter II** describes the synthesis of nanostructured materials using the synthesis in molten salts, by focusing on the advances reached in the course of this PhD work. Two types of materials have been synthesised: (i) nanostructured crystalline metal borides ($HfB_2$ and $CaB_6$) obtained in a nanocomposite system as they are embedded in a nanostructured amorphous matrix, and (ii) nanostructured amorphous boron.

**Chapter III** describes the results of HPHT treatments of the two nanocomposites, in the case of partial oxidation of the precursor's matrix. This study shows the possibility to crystallise the matrix (into metal borates), while conserving the nanostructure of the system. The new nanocomposites boride/borates obtained also represent the first nanostructured instances of the two metal borates crystallised.

The focus of **Chapter IV** is HPHT treatments of the nanocomposite systems. In this case, the synthesis of the precursors has been optimised to limit matrix oxidation. The crystallisation of the matrix into non-oxidised phase is evidenced, notably in the light of *in situ* X-ray diffraction experiments on synchrotron beamlines. We demonstrate the successful synthesis of the first β-B/metal borides nanocomposites.

Eventually, **Chapter V** focuses on similar HPHT conditions but also higher pressures up to 10 GPa applied to nanostructured amorphous boron. The crystallisation of new nanostructured crystalline phases is established. Synthesis conditions are explored to establish the first speciation diagram originating from the transformation of nanostructured boron.

## References


(1) Huppertz, H.; Keszler, D. A. In *Encyclopedia of Inorganic and Bioinorganic Chemistry*; Wiley, **2014**; pp 1–12.
(2) Carenco, S.; Portehault, D.; Boissière, C.; Mézailles, N.; Sanchez, C. *Chem. Rev.* **2013**, *113* (10), 7981–8065.
(3) Albert, B.; Hillebrecht, H. *Angew. Chem. Int. Ed.* **2009**, *48* (46), 8640–8668.
(4) Parakhonskiya, G.; Dubrovinskaia, N.; Bykova, E.; Wirth, R.; Dubrovinsky, L. *High Press. Res* **2013**, *33* (3), 673–683.
(5) Zhai, H.-J.; Zhao, Y.-F.; Li, W.-L.; Chen, Q.; Bai, H.; Hu, H.-S.; Piazza, Z. a; Tian, W.-J.; Lu, H.-G.; Wu, Y.-B.; Mu, Y.-W.; Wei, G.-F.; Liu, Z.-P.; Li, J.; Li, S.-D.; Wang, L.-S. *Nat. Chem.* **2014**, *6* (8), 727–731.
(6) Mannix, A. J.; Zhou, X.-F.; Kiraly, B.; Wood, J. D.; Alducin, D.; Myers, B. D.; Liu, X.; Fisher, B. L.; Santiago, U.; Guest, J. R.; Yacaman, M. J.; Ponce, A.; Oganov, A. R.; Hersam, M. C.; Guisinger, N. P. *Science* **2015**, *350* (6267), 1513–1516.
(7) Feng, B.; Zhang, J.; Zhong, Q.; Li, W.; Li, S.; Li, H.; Cheng, P.; Meng, S.; Chen, L.; Wu, K. *Nat. Chem.* **2016**, *8*, 563–568.
(8) Oganov, A. R.; Chen, J.; Gatti, C.; Ma, Y.; Ma, Y.; Glass, C. W.; Liu, Z.; Yu, T.; Kurakevych, O. O.; Solozhenko, V. L. *Nature* **2009**, *457* (7231), 863–867.
(9) Wentorf, R. H. *Science* **1965**, *147* (3653), 49–50.
(10) Oganov, A. R. *Boron Rich Solids*; Orlovskaya, N., Lugovy, M., Eds.; NATO Science for Peace and Security Series B: Physics and Biophysics; Springer Netherlands: Dordrecht, **2011**.
(11) Kurakevych, O. O.; Solozhenko, V. L. *J. Superhard Mater.* **2013**, *35* (1), 60–63.
(12) Ekimov, E. A.; Zibrov, I. P.; Zoteev, A. V. *Inorg. Mater.* **2011**, *47* (11), 1194–1198.
(13) Oganov, A. R.; Solozhenko, V. L. *J. Superhard Mater.* **2009**, *31* (5), 285–291.
(14) Wentorf, R. H.; DeVries, R. C.; Bundy, F. P. *Science* **1980**, *208* (4446).
(15) Portehault, D.; Devi, S.; Beaunier, P.; Gervais, C.; Giordano, C.; Sanchez, C.; Antonietti, M. *Angew. Chem. Int. Ed.* **2011**, *50* (14), 3262–3265.
(16) Gouget, G.; Beaunier, P.; Portehault, D.; Sanchez, C. *Faraday Discuss.* **2016**.
(17) Gouget, G. Approche moléculaire vers des nanomatériaux inorganiques composés de bore : nouvelles nanostructures fonctionnelles, 2016.
(18) Portehault, D.; Gouget, G.; Gervais-Stary, C.; Sanchez, C. Matériau nanostructuré de bore amorphe, **2016**, 15/55878
(19) Gouget, G.; Portehault, D.; Sanchez, C.; Beauchet, R.; Batonneau, Y.; Kappenstein, C. Mélange Energétique contenant du bore amorphe nanostructuré, **2016**, Patent Pending
(20) Godec, Y. Le; Dove, M. T.; Redfern, S. A. T.; Tucker, M. G.; Marshall, W. G.; Syfosse, G.; Besson, J.-M. *High Press. Res.* **2001**, *21* (5), 263–280.
(21) Parakhonskiy, G. Synthesis and investigation of boron phases at high pressures and temperatures, **2012**.
(22) Huppertz, H. *Chem. Commun.* **2011**, *47* (1), 131–140.

# Chapter I: Bibliography

The first chapter focuses on bibliographic aspects. More specifically, it is divided into three distinct parts, shedding light on the project's different angles.

First, works dealing with the combination of nanostructured materials and high pressure treatment are discussed in an overview of the existing literature. Then, the interest shifts toward boron, its allotropes, their relative stability and their preparation conditions. Eventually alloys of metals and boron (metal borides) are briefly presented, considering their structure, properties and synthetic pathways toward nanostructured materials.

## I-1- Nanomaterials & high pressure

First of all, both nanomaterials and what we consider as "high pressure" should be defined. The commonly accepted definition, in agreement with IUPAC standards,[1] of a nanomaterial is a material for which one dimension at least is inferior to 100 nm. Consequently, 100 nm will be a cut-off size in the literature review. One should note that this size is not arbitrary. Indeed, nanomaterials properties arise from their high surface-to-volume ratio (*S/V*). The latter is a decreasing function of the particle size, as plotted in Figure I-1. It is clear here that under 100 nm the *S/V* ratio strongly increases, entering a *S/V* ratio domain where properties specific of nanomaterials emerge, such as catalysis or quantum confinement effects. Thus, it seems reasonable to restrain the study to sub-100 nm particles.

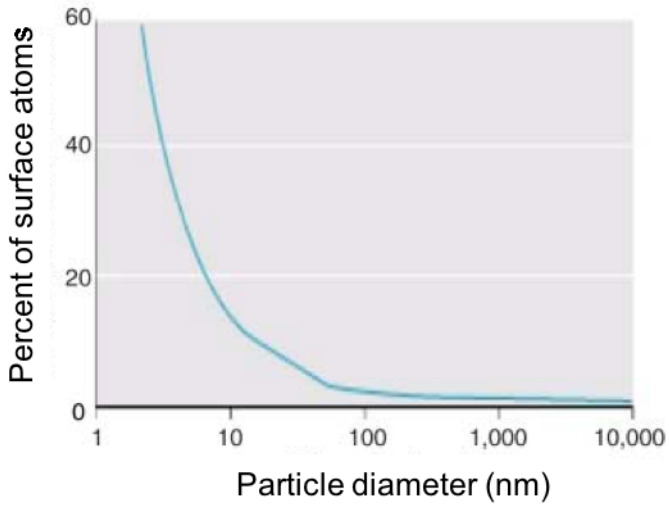


**Figure I-1. Fraction of surface atoms plotted *versus* the diameter of a spherical particle.**[2]

Concerning the pressure range, it is chosen to focus on studies conducted over 1 GPa. Two arguments justify this choice. Indeed, from atmospheric pressure ($10^{-4}$ GPa) to 0.8-0.9 GPa, the devices used differ thoroughly from those used above 1 GPa. Steel pressurised vessels generally do not operate over 1 GPa and over 500 °C. To go above 1 GPa until *ca.* 10 GPa, devices specifically designed for high pressure generation are used. Among them, one can cite the toroidal press, the Belt press, the piston-cylinder press, the multi-anvil press and the Paris-Edinburgh press.

Temperature can exceed 2200 °C in such devices. It is also interesting to note that above 1 GPa, pressure strongly reduces diffusion processes. Indeed, in first approximation, considering the following equation for self-diffusivity in a cubic crystal, with $\boldsymbol{D}$ the diffusion coefficient (Eq. I-1), where $\boldsymbol{D_0}$ includes materials dependent parameters ($\boldsymbol{D_0 = f a^2 \nu_0}$, where $\boldsymbol{f}$ is a correlation factor characterising self-diffusivity, $\boldsymbol{a}$ the cell parameter and $\boldsymbol{\nu_0}$ the attempt frequency) the diffusion coefficient $\boldsymbol{D}$ is the following (Eq. I-2).[3,4] $\boldsymbol{D_0^*}$ also comprises the entropy term. Assuming $P_1$ is room pressure and $P_2$ is 1 GPa (Eq. I-3), the ratio between the corresponding diffusion coefficient is at least $10^4$ (Eq. I-4), making diffusion process extremely slow above 1 GPa in the absence of heating.

$$\boldsymbol{D = D_0 e^{\left(-\frac{\triangle G}{k_B T}\right)}} \qquad \textbf{Eq. I-1}$$

$$\boldsymbol{D = D_0^* e^{\frac{-(\triangle E + \mathrm{P} \triangle V)}{k_B T}}} \qquad \textbf{Eq. I-2}$$

$$\boldsymbol{P_2 = 10^4 P_1} \qquad \textbf{Eq. I-3}$$

$$\boldsymbol{\frac{D_2}{D_1} = e^{\left(\frac{P_1 \triangle V}{k_B T}\right)^{-10^4}}} \qquad \textbf{Eq. I-4}$$

Consequently, to reach similar diffusion coefficients, reactions and phase transformations occurring under high pressure call for higher temperature than their ambient pressure counterparts. The problem of diffusion limitation is of specific interest when dealing with nanomaterials. Indeed, being intrinsically metastable objects, sintering nano-objects (to increase the crystallinity, for instance) usually leads to grain growth and loss of nanostructure. Therefore, high pressure studies on nanomaterials can help maintaining the nanostructure and the benefits of thermal treatment. Moreover, nanostructuration of high pressure/high temperature (HPHT) phases also leads to properties improvement. Both aspects are discussed below.

### I-1-1- Nanostructured high-pressure phases

In material sciences, the textbook case of HPHT phases is diamond. Both natural and commonly synthesised diamonds are made under pressure above 5 GPa and over 900 °C. These diamonds are usually obtained as single crystals.[5] Diamond is commonly described has the hardest known material. However, these mechanical properties are anisotropic and the Knoop hardness ($H_k$) varies from 60 to 120 GPa depending on the crystallographic plane investigated and the direction of measurement.[6] Polycrystalline diamonds have been grown either by Chemical Vapor Deposition (CVD) or with the help of a binder. CVD-grown polycrystalline diamonds have poor intergrain adhesion and their Knoop hardness does not exceed 100 GPa. Using a binder such as cobalt[7] allows the formation of sintered polycrystalline diamond but at the price of hardness ($H_k$ < 70 GPa) and thermal stability (T < 700 °C).

The interest of getting binderless nanostructured polycrystalline samples of superhard materials lies *a priori* on several effects:

- Decrease of the influence of anisotropy on mechanical properties[5,8]
- Increase in thermal stability
- Possibility to benefit from the Hall-Petch effect (HPE) (binders fill the inter-grains gap)
- Increase of hardness by reduction of crystallite sizes, in agreement with the HPE[9,10]

In relation with the latter point, it has been observed experimentally that grain boundaries limit dislocations in polycrystalline materials. This is mainly described using the concept of dislocation pile-up. Grain boundaries are barriers to dislocation motion, notably because of the crystallographic mismatch between adjacent grains. Therefore, upon stress application, dislocations concentrate in a grain until dislocation sources are activated in the neighbouring grain. Hence, reducing the grain size has a double effect. First, the number of grain boundaries per volume unit increases. Secondly, for each grain, the number of dislocations that can pile-up is reduced. Consequently, the amount of stress needed to propagate dislocations is increased compared to coarse-grained materials. At the macroscale, it means that the hardness is increased.

The relationship between the yield stress $\sigma$ and the grain size $\boldsymbol{d}$ is described by the Hall-Petch equation (Eq. I-5). Both $\boldsymbol{k}$ and $\boldsymbol{\sigma_0}$ are both material-dependent parameters, namely the strengthening coefficient and the friction stress in the absence of grain boundaries, respectively. They characterise the lattice's resistance to dislocation.

$$\boldsymbol{\sigma = \sigma_0 + \frac{k}{d^2}} \qquad \textbf{Eq. I-5}$$

However, this is not valid for all grain sizes.[11] As plotted in Figure I-2, when grains are smaller than a critical value $\boldsymbol{d^*}$ (corresponding to the golden arrow, typically around 10 to 20 nm), the hardness reduces, causing an inverse HPE. Above $\boldsymbol{d^*}$, as the grain size is reduced, less and less dislocations can pile-up in a grain, increasing the overall hardness. When the grain size is small enough, grains can accommodate only one dislocation, meaning the maximum of strengthening is reached. If the grain size is further decreased, below $\boldsymbol{d^*}$, other mechanisms are to be taken into account. If they are not entirely elucidated yet, recent studies suggest that Coble creep and other diffusional phenomena may come in play.[11]

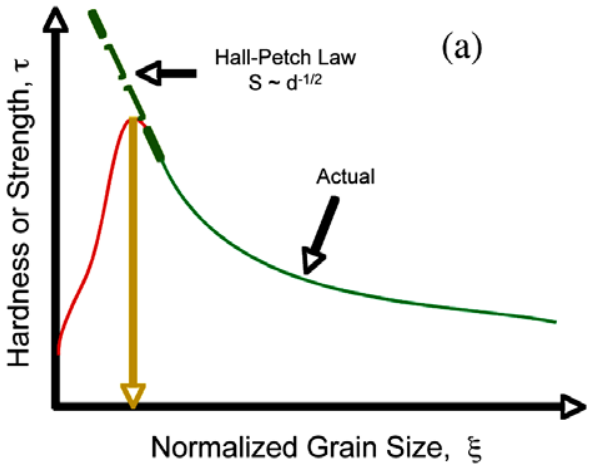


**Figure I-2. Materials' hardness as a function of grain size.**[11]

The critical grain size ***d**** would then correspond to a switch between creep and dislocation pile-up-based mechanisms as dominant fracture propagation mechanisms. Based on Masumara and co-workers studies, Pande and Cooper[11] proposed to generalise the yield stress applied to a polycrystalline material according to the following equation (Eq. I-6).

$$\boldsymbol{\sigma = \sigma_0 + \frac{k}{d^2} + k_1 + \frac{B_0}{d} + Bd^3} \qquad \textbf{Eq. I-6}$$

The last three terms describe the diffusion-based dislocation transport. $B_0$ and $k_1$ are constants and $B$ a strain and temperature dependent parameter. For large grain size, the first two terms are dominant, according to the HPE. For small sizes, the last three terms become dominant, leading to the inverse HPE. According to equation I-3, the critical value can be defined as the ***d*** value for which the first two terms are equal to the last three terms (Eq. I-7).

$$\boldsymbol{\sigma_0 + \frac{k}{d^{*2}} = k_1 + \frac{B_0}{d^*} + Bd^{*3}} \qquad \textbf{Eq. I-7}$$

To conclude, it is possible to increase hardness by diminishing grain size, particularly when reaching the nanoscale, but not under 10-20 nm. This is particularly interesting in the case of bulk hard or superhard materials as it can yield improved properties and performances. The exploitation of the HPE has been successfully applied to superhard materials, first of which diamond, reaching nanopolycrystalline diamond (NPD), as described by Irifune and co-workers and discussed below.[5]

### I-1-1-a- Nanostructured diamond

The first report of NPD dates back to 1992, by Hodeau and co-workers.[12] It was obtained by compressing $C_{60}$ at room temperature, over 20 GPa, under non-hydrostatic pressures. However, due to small sample volumes (related to the use of diamond-anvil cells) and cell explosion upon decompression, the authors could hardly investigate the properties. Still, they were able to identify the crystalline phase obtained as cubic diamond, with a grain size comprised between 2 and 100 nm.

In 2003, Irifune *et al.* prepared binderless NPD by direct conversion from graphite, under high pressure and high temperature (at 12-25 GPa and in the 2300-2500 °C temperature range). Very high hardness values and high thermal stability were claimed and more synthetic details were given in a further study.[13] Materials were prepared in a multi-anvil apparatus, allowing larger sample volumes than diamond-anvil cells.

The results obtained according to the synthesis conditions are summarised in (Figure I-3).[13] X-Ray diffraction (XRD) measurements showed that only cubic diamond is obtained over 2000 °C (Figure I-3).Transmission electron microscopy (TEM) observations show that the cubic diamond samples consist of 10-20 nm crystals, randomly oriented, as evidenced by electron diffraction in the 2003 study.[5] Along with these crystals, the samples also exhibit elongated crystals up to 200 nm long, consistent with rapid crystallisation of diamond or with the lamellar structure of initial graphite. Knoop hardness measurements were performed on the synthesised samples. At 18 GPa, 2500 °C for 1 min, transparent pure cubic diamond is obtained with $H_K$ = 100-110 GPa. At 15 GPa, 2400 °C for 1 min, yielding also transparent pure cubic diamond, $H_K$ = 130-140 GPa. At 12 GPa, 2000 °C for 5 min, opaque dark grey pure cubic diamond is reached with $H_K$ = 65-95 GPa. Consequently, it is possible to prepare NPD that possesses hardness at least equal to the one of single crystal diamond ($H_K$ = 120 GPa maximum, in the appropriate crystallographic direction) and even higher.

However, one must keep in mind that standardised hardness tests (such as Vickers or Knoop) are based on the penetration depth of a diamond tip with a specific geometry (as diamond is usually harder than the material to test). Therefore, hardness values that exceed 120 GPa are to be taken with care.[14]

NPD prepared from graphite also has interesting stability properties compared to polycrystalline diamond with binders. The latter are stable only up to 600-700 °C under argon atmosphere, however NPD can be stable up to 1200 °C (under argon flow, single crystal diamond may be stable up to 1700 °C.).[13]

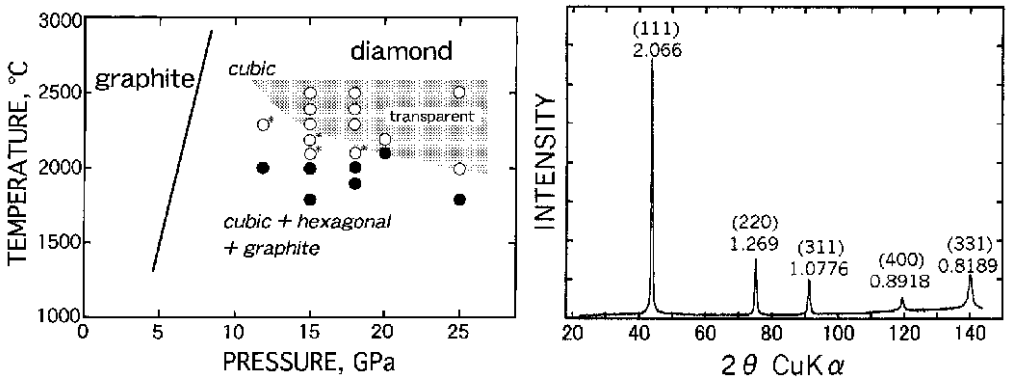


**Figure I-3. Left: Synthesis conditions of NPD and outcome. White dots correspond to cubic diamond, black dots to a mixture of cubic diamond, hexagonal diamond and compressed graphite. Asterisks indicate a grey and opaque product. Right: Powder XRD pattern of a sample synthesised at 15 GPa and 2400 °C.**[13]

The crystallisation of NPD from $C_{60}$ has also been successfully obtained by Dubrovinskaia *et al.*, at 20 GPa and 2000 °C for 1h, using a multi-anvil apparatus and hydrostatic pressures,[15] independently of the cooling rate (Figure I-4). TEM and HRTEM pictures show a particle size in the 5-12 nm range and confirm, along with electron diffraction, the cubic diamond structure. In some experiments, the authors report the presence of a small amount of 6H-diamond (based on XRD), which was not observed with TEM. The HRTEM pictures of the NPD obtained from $C_{60}$ suggest that the structure is ideal and shows no stacking faults nor defects. The Raman spectra of diamond materials are shown in Figure I-4. The diamonds synthesised from natural diamond powder and graphite have spectra dominated by the sharp peak at *ca.* 1330 $cm^{-1}$. The bands at 500, 1100 and 1420 $cm^{-1}$ are attributed to a rupture of selection rules due to small crystallite size. It is clear from Raman spectroscopy that NPD's properties are influenced by the precursor used. However, the authors insist that they have no complete explanation for the features of the NPD Raman spectra.

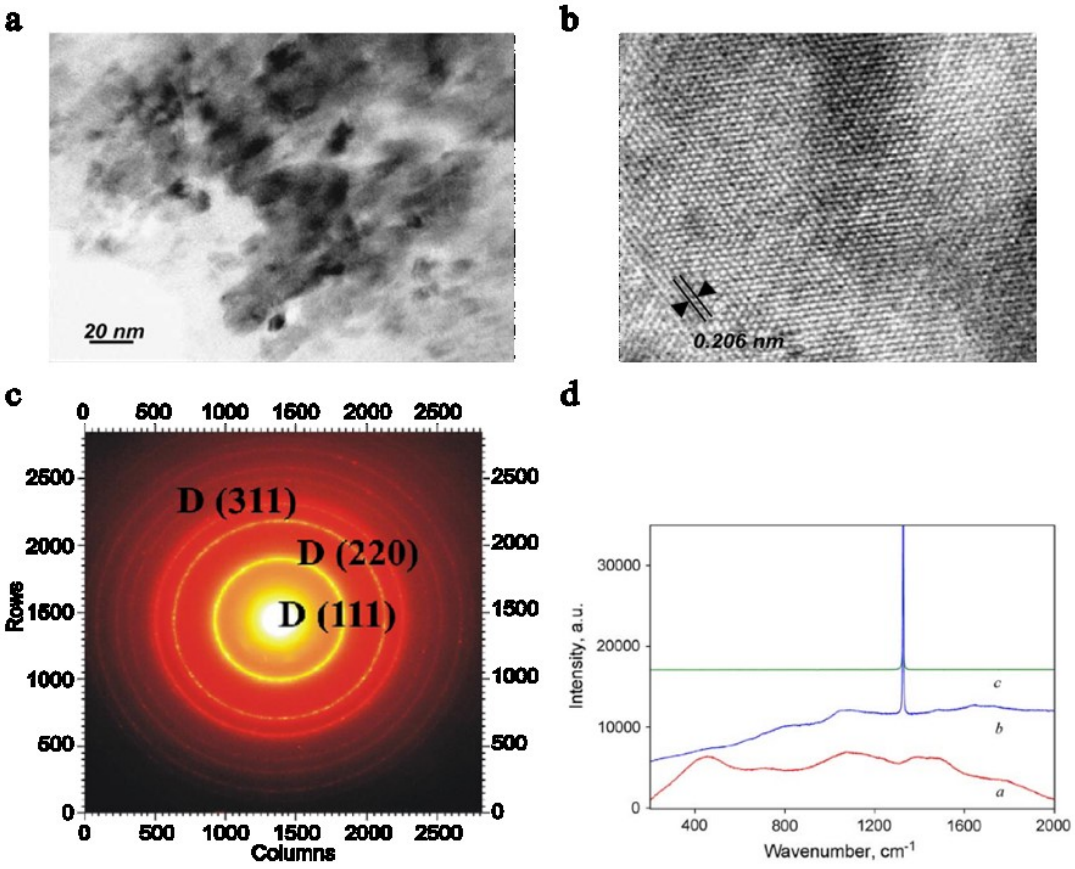


**Figure I-4. Characterisations of NPD synthesised from $C_{60}$ at 20 GPa and 2000 °C. (a) and (b): (HR)TEM pictures of NPD synthesized from $C_{60}$, evidencing 5-12 nm particles of cubic diamond with ideal structure. (c) Electron diffraction pattern, evidencing the cubic diamond phase. (d) Raman spectra of different diamond materials, synthesised at 20 GPa and 2200 K. Red line: synthesis from $C_{60}$. Blue line: synthesis from graphite. Green line: synthesis from natural diamond.**[15]

The mechanical properties of the NPD obtained from $C_{60}$ were tested with a standard Vickers-type diamond indenter. Even for important loads (4.9 N) and using a scanning electron microscope (SEM), the indenter left no visible mark on the sample, suggesting a hardness at least comparable to that of bulk diamond.

The thermal stability under inert atmosphere was also tested. Natural diamond and NPD (from $C_{60}$) were heated at 1900 K under an atmosphere composed of Ar+2% $H_2$. For natural diamond, graphitisation started at 1100 K and became rapid at 1500 K. However, NPD synthesised from $C_{60}$ did not graphitise at 1800 K and started at 1900 K, exhibiting superior thermal stability compared to natural diamond.

The authors also obtained aggregated diamond nanorods (ADNR) by treating $C_{60}$ at 20 GPa and 2200 °C.[16] After 1 h, the reaction medium was slowly cooled (*ca.* 10 °C/min). The XRD pattern and the Raman spectra are similar to that obtained for NPD. HRTEM shows (Figure I-5) that diamond is obtained as rods, which length can be superior to 1 μm and width is inferior to 20 nm. As evidenced by TEM, the rods are randomly oriented (Figure I-5). Both electron and X-Ray diffraction were

used to measure the lattice parameter, which is 3.5617(3) Å, making nanorods 0.2 to 0.4 % denser than bulk diamond (3.528(1) $g.cm^{-3}$ vs. 3.515-3.519 $g.cm^{-3}$ for bulk diamonds). The equation of state was determined, particularly the isothermal bulk modulus, which exceeds that of known materials (491 GPa, about 10 % more than that of natural diamond). Consequently, ADNR represent the densest and least compressible form of carbon. The mechanical properties were tested elsewhere.[17] The Young's modulus (1070 GPa) is comparable to that of natural diamond (*ca.* 1130 GPa). The Knoop hardness measurements give 57 to 104 GPa for natural diamond, depending on the indentation plane, but at least 105 GPa for ADNR, independently of the direction investigated. The wear coefficient, useful in order to consider applications as machining tool for instance, equals 2.14 to 5.49 for natural diamond and 10 for ADNR. The fracture toughness is also greatly increased (3.4-5.0 $MPa.m^2$ for natural diamond, 11.1 $MPa.m^2$ for ADNR). The efficiency of ADNR as grinding tool was tested, particularly with ferrous steel. Indeed, diamond tends to form iron carbide and cannot be used to grind ferrous alloys. When grinding stainless steel with either ADNR or natural diamond (Figure I-5), the authors showed that no etching could be seen on ANDR sample, suggesting higher stability toward reaction with ferrous alloys, making ADNR a very promising product for machining and cutting tools.

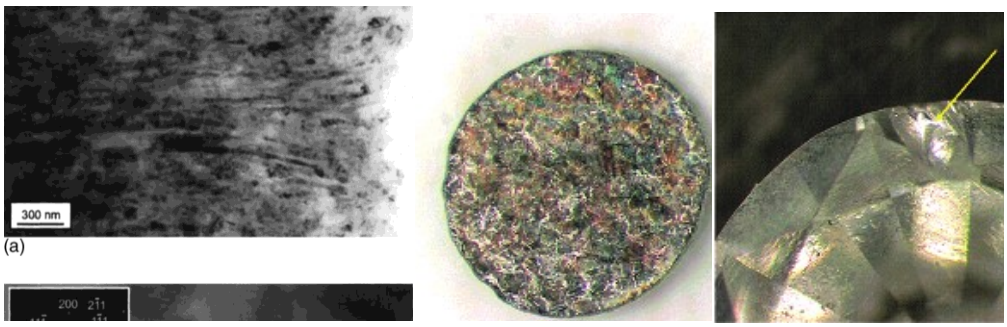


**Figure I-5. Left: TEM image of ANDR, showing randomly oriented crystals. Middle: ADNR bulk sample after grinding test on stainless steel. Right: Natural diamond sample after grinding test on stainless steel, the yellow arrow highlights the etching spot.**

Both synthesis conditions of nanopolycrystalline diamond from different carbon forms and the resulting mechanical properties have been summed up by Irifune and co-workers (see Table I-1).[18,19]

**Table I-1.NPD synthesis conditions, particle size and materials' hardness.**

| Starting Material | Synthesis Conditions | Outcome (XRD) | Particle size (TEM, nm) | Knoop Hardness (Gpa) |
|---|---|---|---|---|
| Graphite | 15 GPa, 2400 °C, 78 s | *c*-Dia | 10-30 (lamellar) | 128-138 |
| Graphite | 28 GPa, 2500 °C, 10 s | *c*-Dia 98% + *h*-Dia | 10-30 (lamellar) | 120-140 |
| Graphite | 21 GPa, 2300 °C, 10 min | *c*-Dia | 10-30 (lamellar) | 113-139 |
| Amorphous-C | 18 GPa, 2000 °C, 20 min | *c*-Dia | 10-200 | 97-119 |
| Amorphous-C | 21 GPa, 1800 °C, 10 min | *c*-Dia | 5-10 | 70-74 |

| | | | | |
|---|---|---|---|---|
| Glassy-C | 21 GPa, 2250 °C, 6 min | *c*-Dia | 50-200 | 95-112 |
| Glassy-C | 18 GPa, 2000 °C, 20 min | *c*-Dia | 5-10 | 66-86 |
| $C_{60}$ | 18 GPa, 1800 °C, 30 min | *c*-Dia | 5-10 | 70-85 |
| $C_{60}$ | 18 GPa, 2000 °C, 35 min | *c*-Dia | 20-100 | 93-104 |
| | Ref: Natural diamond | | | 110–135 (001) |

*c*-Dia: cubic diamond
*h*-Dia: hexagonal diamond

NPD was also prepared from graphite by Xu *et al.*, who studied the influence of graphite ball-milling before HPHT.[20] They compared NPD obtained either from crystalline graphite or ball-milled and/or heated under vacuum after milling. Ball-milling is used to reduce the crystallite size of the precursor. Reducing the initial grain size tends to reduce, at the same pressure, the thermal energy needed to crystallise diamond. As suggested by Guillou and co-workers, NPD nucleation and growth does not require graphitisation of disordered carbons. However, the particle size was only calculated by applying Scherrer's formula to the XRD patterns and no TEM observations were provided to confirm the particle size of NPD synthesised from ball-milled/vacuum heated graphite.[21] As emphasised by Guillou *et al.*, the rapid formation of diamond results in twinning and high residual strains after recovery, which contribute significantly to broadening of the XRD peaks. Consequently, in the absence of TEM pictures, it is difficult to assess the influence of the pre-HPHT treatment of graphite on the NPD grain size. The mechanical properties were tested under a Vickers' indenter which broke under a 20 N load without indenting the material.

As discussed above, the properties of NPD make them a potentially very useful material for applications involving cutting or machining. From a different angle, diamond's hardness is also used for static pressure generation devices, namely diamond anvil cells. NPD were successfully used as anvils.[22] For large culet sizes (*i.e.* the dimension of the flat bottom part of a gemstone, here corresponding to the pressure generating surface), NPD anvils can generate 1.5 to 2 times the pressure generated by single crystal diamond anvils.[23] Concerning laser-heating, it is possible to generate up to 5000 K at 100 GPa.[22] The increase in heating efficiency compared to single crystal diamond is linked to the lower thermal conductivity of NPD, paving the way toward performance increase in diamond anvil cells. In addition, NPD-based anvils are especially useful for EXAFS *in situ* studies: unlike single-crystals diamond anvils, NPD anvils do not exhibit Bragg reflections that otherwise superimpose the spectrum (Figure I-6).[24]

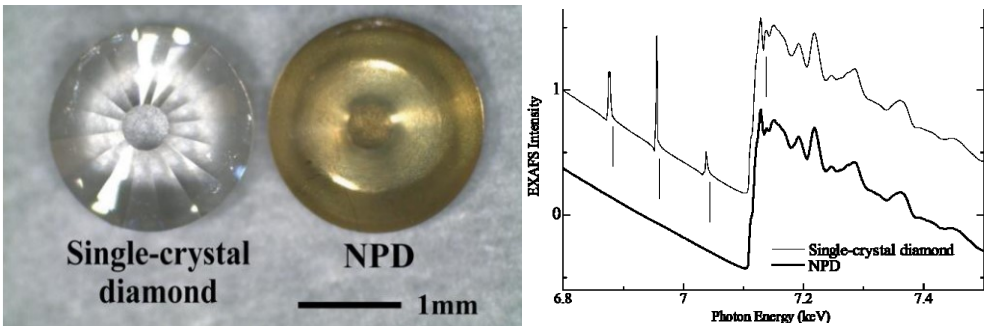


**Figure I-6. Left: diamond anvils. Right: comparison of EXAFS spectra according to the anvil type.**[24]

On a more general point of view, superhard materials are often based on light elements, such as boron, carbon or nitrogen. Indeed, they make usually strong, short and directional covalent bonds responsible for high hardness, such as $B_{13}N_2$ or $B_6O$.[25] For some of these materials, nanostructured occurrences were prepared using HPHT techniques. They are detailed in the following part.

I-1-1-b- Other nanostructured superhard materials: B-C-N system

• Cubic boron nitride

Among intrinsically superhard materials, besides diamond, cubic boron nitride is usually cited. Indeed, it is isoelectronic to carbon and the most common phase, hexagonal boron nitride (*h*-BN), has a graphitic structure. As for carbon, a denser phase is stabilised at high pressure: cubic boron nitride (*c*-BN), discovered in 1957, which exhibits high hardness ($H_V$ = 45 GPa).[26] Even if it is much less hard than diamond, *c*-BN exhibits higher thermal and chemical stability. This makes c-BN a more suitable material for cutting ferrous alloys, for which single crystal diamond is not suited.

Recently, Dubrovinskaia and co-workers reported the synthesis of aggregated boron nitride nanocomposites (ABNNC).[27] The temperature/pressure diagram in Figure I-7 sums up the results they obtained according to the synthesis conditions.[27] The XRD patterns obtained for P = 18 GPa evidence the different phases obtained and their mixture, as a function of the synthesis temperature. *w*-BN, wurtzititic boron nitride, is also obtained. It is another high pressure superhard phase of boron nitride, but with a lower thermal stability. Its structure is similar to that of hexagonal diamond.

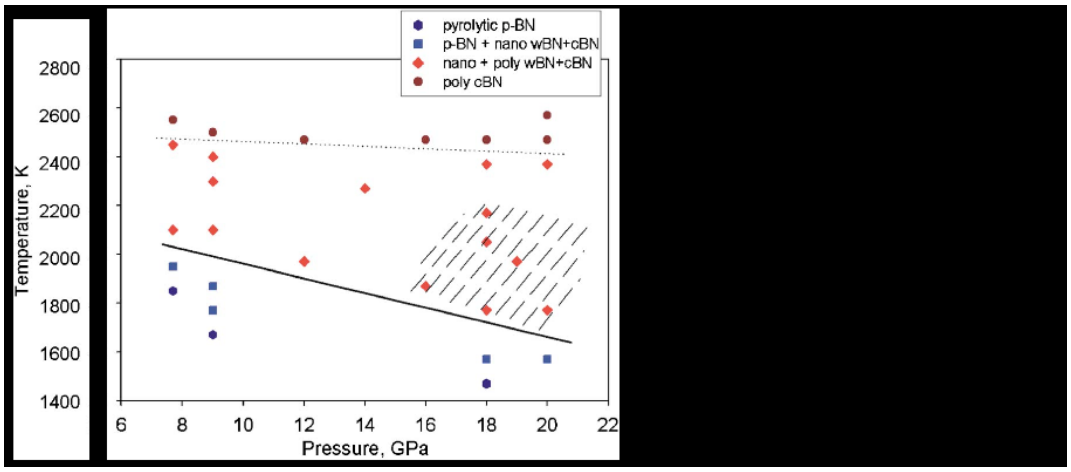


**Figure I-7. Left: P,T diagram of commercial pyrolytic BN HPHT transformations. The region under the solid line is where the starting material is present in the final product. Above the dashed line, only *c*-BN is obtained, as a polycrystalline bulk. The shaded region corresponds to the samples with the smallest grain size, around 14 nm, and highest hardness. Right: Powder XRD patterns for samples prepared at 18 GPa.**[27]

At 18 GPa and 1870 K, TEM and electron diffraction (Figure I-8) show a good agreement with the XRD data: both *c*-BN and *w*-BN are obtained, as 14-20 nm nanoparticles.

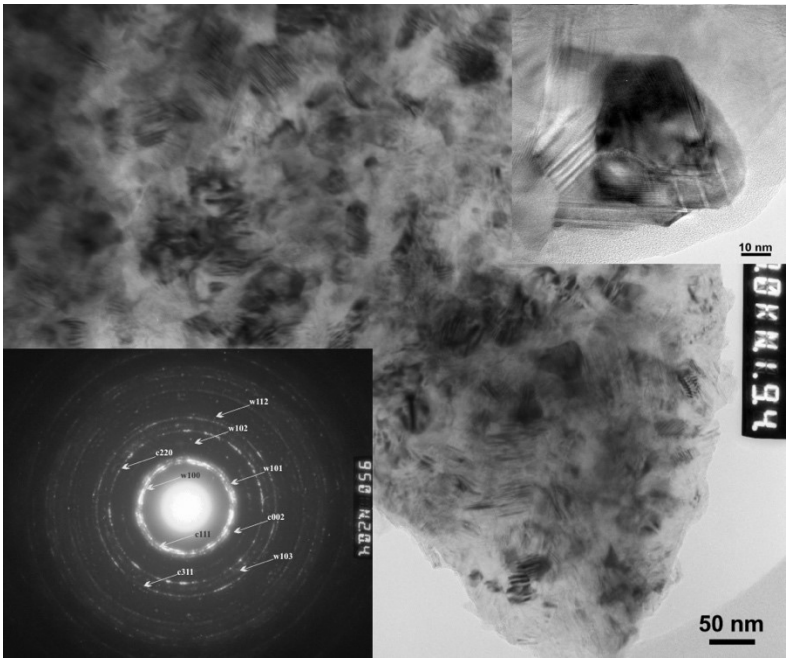


**Figure I-8 TEM picture of the sample synthesised at 18 GPa and 1870 K. The mixture of *c*- and *w*-BN is obtained as 14 nm nanoparticles. The particles consist in blocks with 2-layered *w*-BN and 3-layered *c*-BN structures, as evidenced by the TEM picture (upper right corner). The corresponding SAED pattern is shown in the lower left corner.**

For aggregated *w*-BN/*c*-BN nanocomposites, the hardness value reaches a maximum of $H_v$ = 85 GPa for a 14 nm crystallite size. Below this critical size, the inverse Hall-Petch effect applies. However, the samples with grain size below 12 nm were synthesised at 1800 K, the authors suppose than the final material may contain

residual amounts of pyrolytic (*p*-BN) that they hold responsible for the hardness decrease.

For applications in machining tools, thermal stability is important, as high-speed machining of hard materials tends to release heat. Yet, *w*-BN is a metastable phase that undergoes reverse transformation to *h*-BN at moderate temperatures,[28] thus yielding significant hardness decrease at high temperature for the *w*-BN/*c*-BN nanocomposites. Further enhancement of boron nitride properties as superhard material through nanostructuration should then avoid the presence of *w*-BN in the final material. The precursor, *p*-BN, consists in graphitic BN planes, ordered in the two dimensions of these planes. The planes are randomly oriented in respect to each other: *p*-BN exhibits no three-dimensional ordering. However, commercial *p*-BN samples do have a certain degree of ordering in the third dimension: the structure is not entirely turbostratic; some domains have *h*-BN structure. This is precisely in such domains that the crystallisation of *w*-BN is favoured, while that of *c*-BN occurs in more disordered domains.[28,29]

To avoid the presence of *w*-BN, Le Godec and co-workers used high purity *p*-BN without any three dimensional ordering, synthesised by CVD.[28] Syntheses at 12 GPa show that *w*-BN still appears at 1000 K, *c*-BN becoming the sole crystalline phase only above 2000 K. The hypothesis here is that at low pressures, temperature-induced ordering of the initial *p*-BN cannot be avoided, which calls for higher synthesis pressures. At 20 GPa, in the 1770-2570 K range, pure nanostructured *c*-BN is recovered. *In situ* X-Ray Diffraction experiments show that in this case, *w*-BN is not formed, all along the synthetic path. The pattern obtained at 1770 K (Figure I-9) shows weak "*w*-BN-type" reflections, attributed to stacking faults in the cubic lattice, that disappear upon further heating and diffusion increase. As for NPD, the Raman spectrum of sub-100 nm boron nitride particles differs from that of bigger particles and is dominated by broad vibration bands, probably due to scattering at grain boundaries. The TEM picture and corresponding selected area electron diffraction pattern (SAED) of the sample obtained at 1770 K (Figure I-9) confirm the formation of pure *c*-BN nanoparticles of diameter in the 10-40 nm range. The mechanical properties have been investigated: Vickers' hardness increases when the grain size is reduced, in good agreement with the Hall-Petch equation (Figure I-9). The maximum $H_v$ is reached for the synthesis at 1770 K and equals 85 GPa, which is around the double of that of conventional c-BN. The thermal stability tests (Figure I-9) show that the onset temperature of oxidation in air (around 1460 K) is superior to that of microcrystalline *c*-BN and NPD. All these results make nanostructured *c*-BN a very good candidate for use as a superabrasive, for carbide-forming metals or alloys –for which diamond fails–, and more generally for applications involving high-speed processing of hard materials.

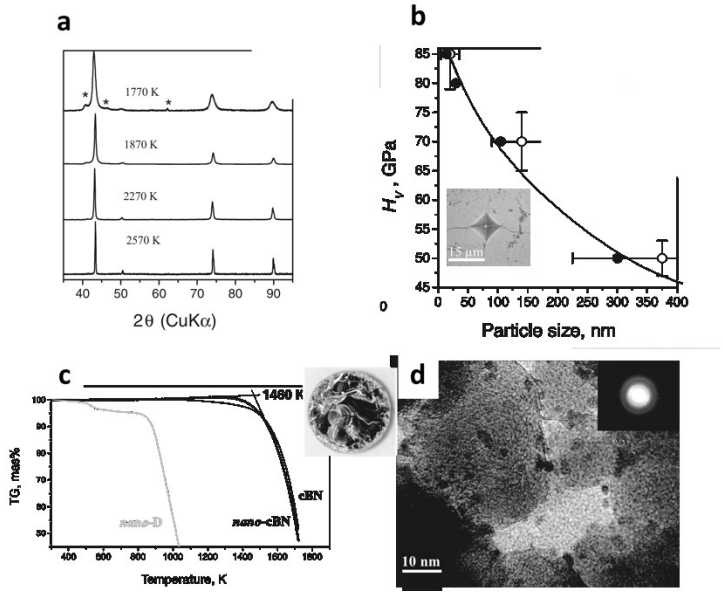


**Figure I-9 (a) XRD patterns of samples synthesised at 20 GPa and different maximal temperature reached. All peaks correspond to *c*-BN, except at 1770 K, where the weak peaks (indicated by stars) match *w*-BN but are claimed to correspond to stacking faults in the cubic lattice. (b) $H_v$ test: black dots correspond to the size calculated from XRD, white dots to values measured by TEM, the black line is the plot of the Hall-Petch equation. (c): Thermogravimetric analysis in air for nano *c*-BN, compared to NPD and bulk BN. Inset: optical microscope picture of nano *c*-BN bulk. (d): HRTEM of nano *c*-BN. Inset: SAED pattern, showing 3 circles matching the (111), (220) and (311) reflections of *c*-BN.**[28]

In agreement with the Hall-Petch effect, the increase in hardness of boron nitride by reducing the grain size is related to the increase in grain boundaries density. However, it has been showed experimentally that twin boundaries can have a hardening effect similar to that of grain boundaries. Following this observation, Tian and co-workers have used a specific *c*-BN precursor: onion like boron nitride (*o*-BN).[30] It can be described as 30 to 150 nm concentric spherical *h*-BN shells, with important puckering and stacking faults. The XRD pattern shows reflections corresponding to the (002) plane of *h*-BN, evidencing some degree of order in the third dimension, hence a non-purely turbostratic structure. The HPHT conditions used were 15 GPa and the temperature set between 1000 and 1870 °C. The corresponding XRD patterns (along with that of the precursor *o*-BN) are show in Figure I-10. The authors obtain a mixture of *c*- and i-BN between 1200 °C and 1600 °C, and pure *c*-BN above 1600 °C. The authors show that the size of the initial *o*-BN particles is retained at 1600 °C. According to TEM, the *c*-BN particles consist in twinned *c*-BN particles. The twin thickness is predominantly below 10 nm, with an average at 3.8 nm (according to the size distribution histogram). The $H_V$ reaches 196 GPa at weak loads and 108 GPa for the asymptotic value (see Figure I-10). However, as emphasised by Dubrovinsky and Dubrovinskaia,[31] the scanning electron microscopy (SEM) picture of the indentation in the asymptotic zone shows several inconsistencies that shed doubts about the reported $H_V$ values. As already discussed, the structure of *w*-BN can be seen as stacking faults in the *c*-BN structure. Therefore,

HRTEM and TEM pictures from Tian *et al.*[30] are also consistent with the formation of aggregated boron nitride nanocomposite (ABNNC).

The nature of the precursor, exhibiting a degree of three-dimensional ordering (see XRD pattern in Figure I-10) also claims for the presence of *w*-BN. However, the proportion of *w*-BN seems smaller than in ABNNC, according to the intensities of *w*-BN reflections in the XRD patterns (Figure I-7 and Figure I-10 for comparison). Though, above 1600 °C, the presented XRD patterns show high peak sharpness, inconsistent with the reported average twin size of 3.8 nm. The thermal stability toward oxidation in air of reported nanotwinned *c*-BN is extended to *ca.* 1294 °C, to compare with the 1187 °C of nano *c*-BN. However, if reported nanotwinned *c*-BN did contain *w*-BN the phase stability would be reduced, due to the reverse transformation into *h*-BN.

Considering the set of data available, nanotwinned *c*-BN is likely to be considered as a material close to ABNNC.

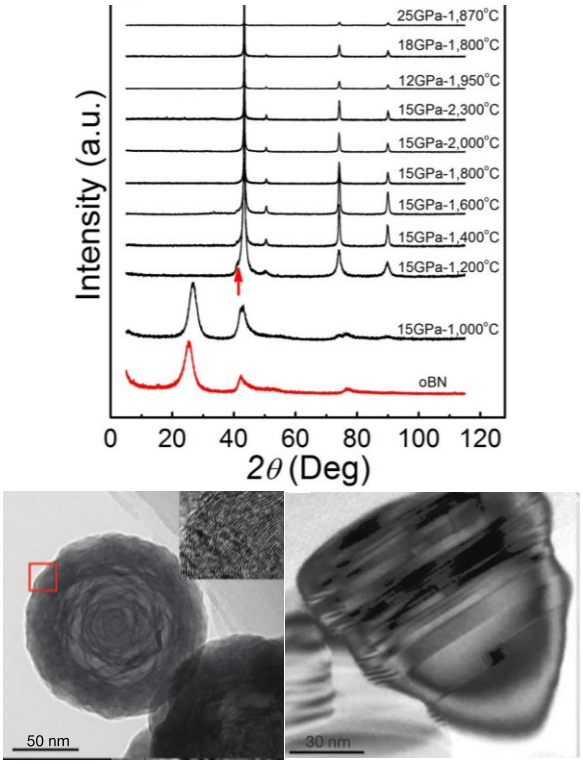


**Figure I-10. Top: XRD patterns of initial o-BN and along the HPHT experiments, showing crystallisation of *c*-BN along with small amounts of *w*-BN. Bottom left: TEM picture of initial *o*-BN. Inset: HRTEM of red square area. Bottom right: TEM picture of nano-twinned *c*-BN grain.**[30]

• Diamond-like $BC_x$, $BC_xN$

The solubility of boron in diamond under high pressure has been studied by Mezouar and co-workers.[32] Indeed, doping carbon with boron can yield interesting modified properties, such as superconductivity ($T_c$ = 5 K).[32] However, the solubility of boron into diamond is limited to amounts around 2 at%. Using turbostratic graphite substituted with boron (*t*-$BC_x$) as starting material with a controlled boron content up

to 50 at%, the authors reached under HPHT phase segregation into boron carbide and boron-doped diamond (with about 1.8 at% of boron) or a mixture of diamond, boron carbide and boron, depending on the HPHT transformation parameters and the boron content of the starting material. For low carbon content (x between 1 and 4), above 20 GPa and between 2000 and 2500 K, a mixture of boron carbides ($B_4C$ or $B_{50}C_2$) and cubic boron carbide phases (Figure I-11) is obtained. The amount of cubic boron carbides formed increases with the temperature and with the carbon content of the precursor.

After compression at 24 GPa and heating at 2200 K in a diamond-anvil cell, the XRD pattern of $BC_5$ (Figure I-11) shows the formation of a *c*-$BC_5$ phase, which is the only crystalline phase contained in the sample. The presence of amorphous component has been ruled out by TEM and Raman spectroscopy. Therefore, the totality of the precursor has been transformed into *c*-$BC_5$, conserving the initial composition $BC_5$ (the composition has been confirmed by EELS). Such stoichiometry means that boron-containing diamond has been obtained, with a boron content as high as 16 at%.

Concerning the nanostructure, the authors report from TEM that *c*-$BC_5$ is obtained as aggregates of 10-15 nm grains (though the TEM pictures are not presented in the original article). The material has been successfully obtained and quenched as a bulk using a large-volume press in the same pressure and temperature conditions. Bulk samples showed a hardness of $H_v$ = 71 GPa, which places the material among the hardest known materials. The fracture toughness is also very high at about 9.5 $MPa.m^{0.5}$ (4.5 $MPa.m^{0.5}$ for diamond). The material is stable up to 1890 K, then transforms into graphite and amorphous boron or boron carbide. All these results make nanostructured *c*-$BC_5$ a very good candidate for applications as superabrasive.

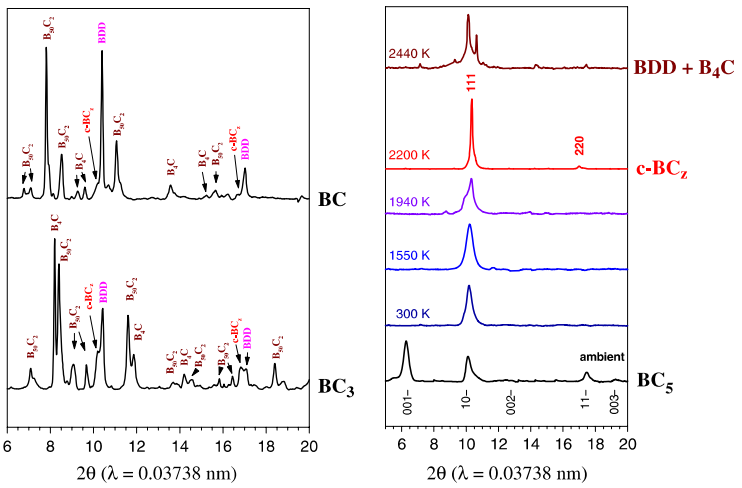


**Figure I-11. Left: XRD patterns obtained after transformation of different $BC_x$ precursors: a mixture of boron carbides $B_4C$ and $B_{50}C_2$, boron-doped diamond and *c*-$BC_x$ is obtained. Right*: In situ* XRD patterns along compression and heating of *t*-$BC_5$: compression leads to loss of (00l) reflections. The pattern is not further modified until phase transition occurs at 1940 K. The cubic phase is synthesised at 2200 K. Further heating above 2440 K leads to phase segregation into boron-doped diamond and boron carbide.**[32]

Another nanostructured boron carbide has also been reported by Zinin *et al.* who synthesised $BC_3$ by laser-heating in a diamond anvil cell (DAC) from turbostratic-like $BC_3$ (*t*-$BC_3$), containing a small amount of $B_4C$ (Figure I-12).[33] At 44 GPa, a phase transition occurs at 1980 K reaching *c*-$BC_3$. The chemical purity and stoichiometry of *c*-$BC_3$ are confirmed by EELS. However, *c*-$BC_3$ synthesis was only conducted in DAC, thus not reaching quantities allowing investigation of the mechanical properties.

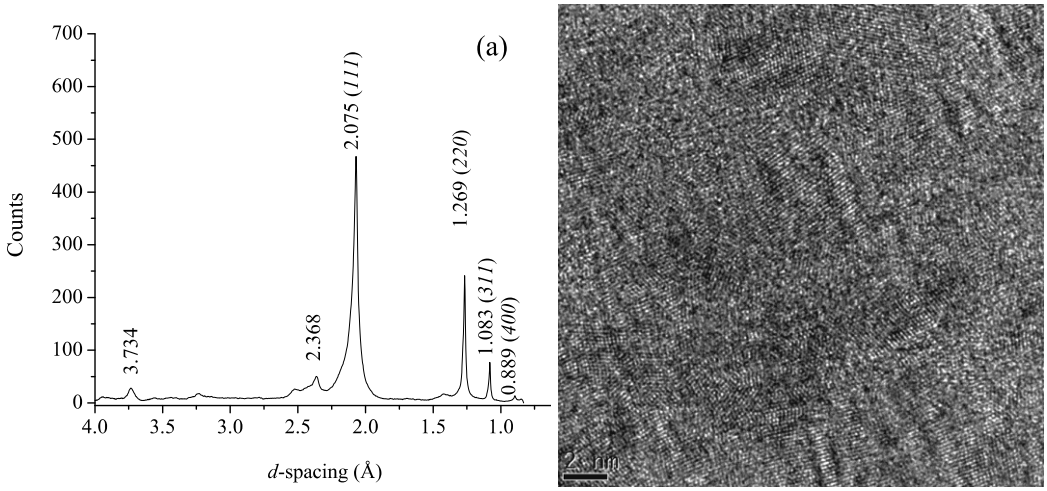


**Figure I-12. Left: XRD pattern of *c*-$BC_3$. Right: HRTEM picture of *c*-$BC_3$, evidencing its nanostructure as 3-5 nm particles.**[33]

Rubie *et al.* successfully synthesised a superhard material within the B-C-N composition triangle.[34] Indeed, at 28.5 GPa, turbostratic graphitic $BC_2N$ transformed into a cubic phase above 2200 K. EELS studies conducted on that material confirmed the composition, very close to $BC_2N$.[35,36] The synthesis was successfully reproduced in a multi-anvil press, allowing hardness investigation: $H_v$ = 76 GPa,

placing the material in the range of the hardest known materials. The thermal stability has not been tested.

The synthesis of *c*-$BC_2N$ was also performed by Zhao and co-workers at 20 GPa and 2200 K.[36] Here also, the composition has been confirmed by EELS. HRTEM (Figure I-13) shows that the cubic phase is obtained as 4-7 nm particles, embedded in an amorphous matrix (estimated to less than 5 % of the volume). The latter has been identified as amorphous diamond-like carbon. The SAED pattern confirmed the cubic structure of the crystalline phase (Figure I-13). The hardness is about $H_v$ = 62 GPa, comparable to that obtained by Rubie *et al.*[34] Though the fracture toughness has not been investigated, no extensive cracks were seen at the corners of the indentation, calling for high fracture toughness. The authors hypothesised here the influence of the amorphous matrix, strongly increasing the difficulty for microcracks propagation.[36]

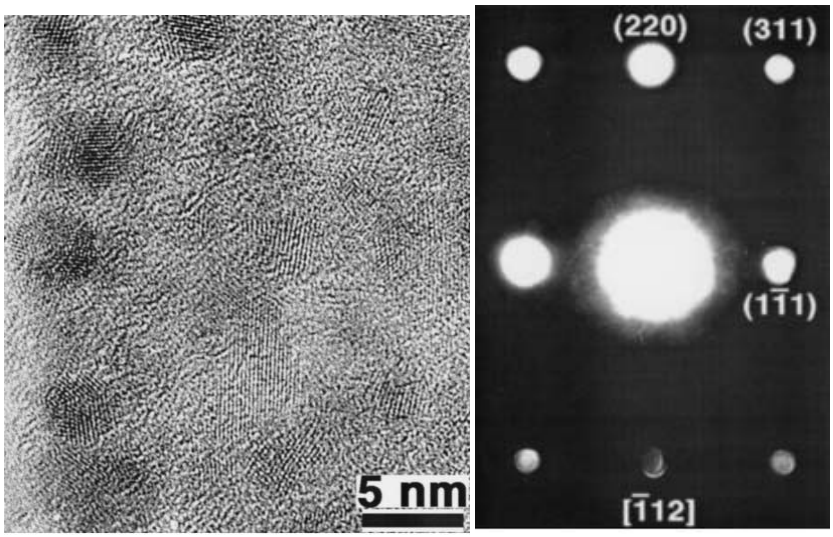


**Figure I-13. Left: HRTEM micrograph of *c*-$BC_2N$ obtained in a multi anvil press at 20 GPa and 2200 K, evidencing average 5 nm particles embedded in an amorphous matrix. Right: SAED pattern of the crystalline phase, confirming the cubic structure of $BC_2N$.**[36]

All the phases described in this part are typical from HPHT conditions, dense and superhard. The examples presented here all show the critical importance of the precursor. Indeed, either initial nanostructuration or low degree of three-dimensional ordering allows control of grain size or phase purity. Nanostructuring intrinsically superhard phases can lead to a strong increase in the mechanical properties, including hardness and fracture toughness. In the case of diamond, the thermal stability is increased, lowering the main drawback of diamond as superabrasive material.

This first part dealt with nanostructured HPHT phases. The next two parts focus on room pressure nanostructured inorganic materials (mainly oxides) under high pressure.

## I-1-2- Nanostructured materials under high-pressure

### I-1-2-a- Oxides and related materials

• Titanium dioxide

$TiO_2$ is a widely studied and used material. Nanostructured $TiO_2$ has numerous technological applications, such as photocatalysis, optoelectronic devices, chemical sensors, dielectric materials or dye-sensitised solar cells. Titania possesses eleven known phases, five of which are high pressure forms. However, only few studies got interested in the high pressure behaviour of nanostructured $TiO_2$.

For instance, Olsen and co-workers studied nanostructured rutile under high pressure.[37] In this study, rutile was used as 10 nm particles (confirmed by XRD and TEM measurements) and compressed in a DAC, up to 47 GPa, at room temperature. The evolution of the material was followed by *in situ* XRD. It shows (Figure I-14) that the baddeleyite phase starts to crystallise around 20 GPa, until the phase transition is completed at about 30 GPa. Upon further compression, the XRD pattern is not modified further than pressure-induced cell shrinking. The baddeleyite phase is conserved along decompression, until 4 GPa, where the α-$PbO_2$-type phase crystallises. It is the sole crystalline phase present under 2 GPa.

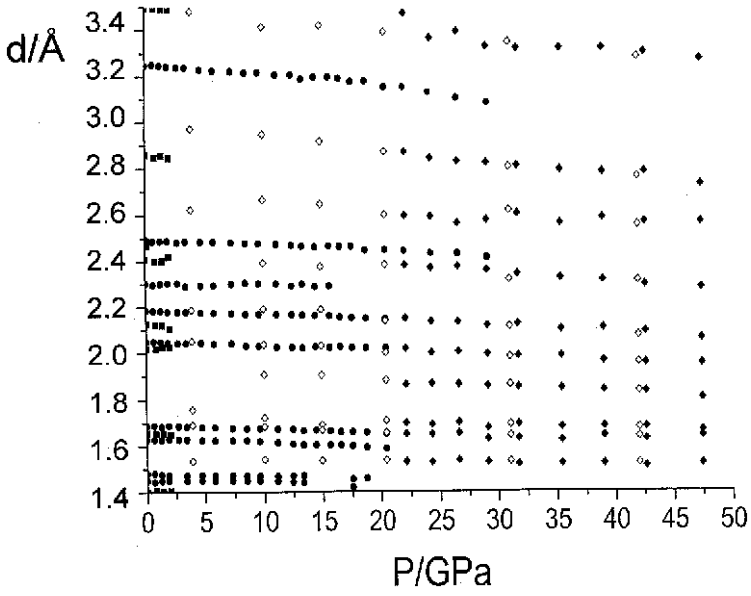


**Figure I-14. Bragg peaks of $TiO_2$ phases, plotted as d-spacings. Circles denote rutile, diamons the baddeleyite-type phase and squares the α-$PbO_2$-type phase. Hollow symbols correspond to decompression of the baddeleyite-type phase.**[37]

The phases crystallised are consistent with those obtained when using bulk rutile as precursor. Yet the transition pressures are higher (resp. lower) for nanostructured rutile during compression (resp. decompression), evidencing the influence of nanostructure on the phase diagram (results are summarised in Table I-2). However, neither the original article nor the data set provided indicate the final particle size.

**Table I-2. Phase transition pressures compared for bulk and nanostructured rutile $TiO_2$. Pressures are indicated in GPa.**[37]

| | Bulk $TiO_2$ | Nanostructured $TiO_2$ |
|---|---|---|
| Rutile to Baddeleyite starts | 12 | 20 |
| Rutile to Baddeleyite ends | 20 | 30 |
| Baddeleyite to α-$PbO_2$ starts | 7 | 4 |
| Baddeleyite to α-$PbO_2$ ends | Room Pressure | 2 |

More recently, phase transitions of nanostructured $TiO_2$ were studied under high pressure and high temperature coupled with *in situ* XRD by Daemen and co-workers.[38] Starting from either nanocrystalline (particle size around 4-8 nm) or microcrystalline anatase (particle size around 40-50 µm), the authors compressed the two samples together (*i.e.* separated in the same pressure assembly). Compression at room pressure leads to columbite-type $TiO_2$ crystallisation, only for microcrystalline $TiO_2$, which is continued upon heating treatment (Figure I-15). Nanostructured $TiO_2$ starts to transform into the columbite phase from 470 K. Upon further heating, the phase transition is completed for both materials (up to 1270 K, XRD not shown). However, as evidenced by the XRD peak width (as the two samples were compressed together, it allows easy comparison of particle size), the particle size of the crystallised columbite-$TiO_2$ is very similar, whatever the precursor used. Thus the initial nanostructure does not appear to influence more than the phase stability boundary. Yet, the two columbite-type samples were transformed into rutile at 2 GPa. *In situ* XRD yields similar final results but the onset temperature of the columbite to rutile phase transition is higher for columbite crystallised from microstructured anatase, without clear explanation so far.

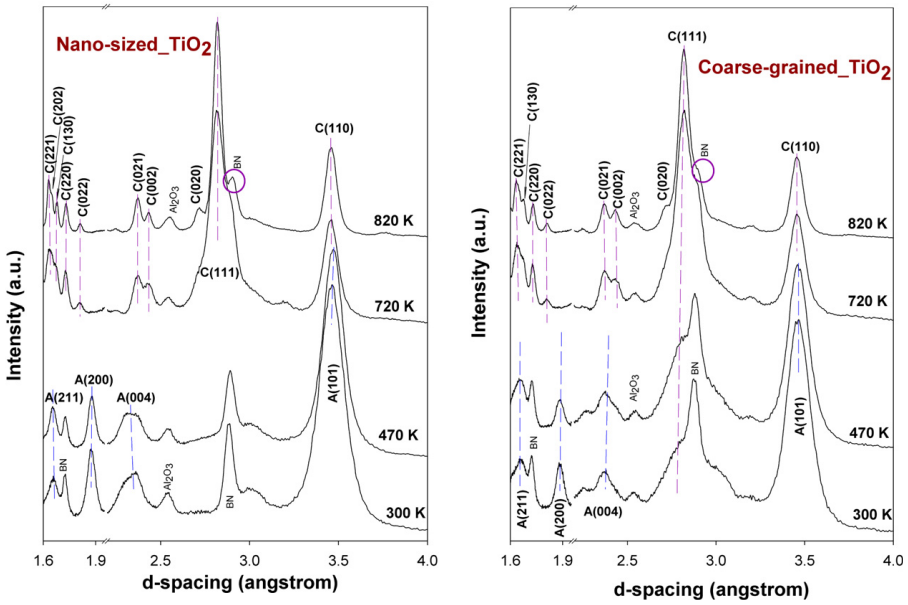


**Figure I-15. *In situ* XRD obtained along thermal treatment, at 8 GPa.**[38]

Though, phase transitions do not necessarily yield crystalline state. Indeed, as shown by Machon and co-workers, 6 nm $TiO_2$ anatase particles exhibit amorphisation

under high pressure treatment in DAC, up to 26.7 GPa.[39] Upon compression, Raman spectroscopy evidences amorphisation of the particles between 19.4 and 22.1 GPa, toward a high density amorphous phase (HDA1) (Figure I-16). Upon decompression, a transition toward a low density amorphous phase (LDA) is observed at 5.5 GPa. Starting from 6 nm particles with this low density amorphous structure, the authors evidenced a transition toward a second high density amorphous (HDA2) between 16.7 and 27.5 GPa (Figure I-16). Above 27.5 GPa, HDA2 is transformed into HDA1 (Figure I-16). Note that the reverse phase transitions (HDA1 into HDA2 into LDA) are observed upon decompression (not shown).

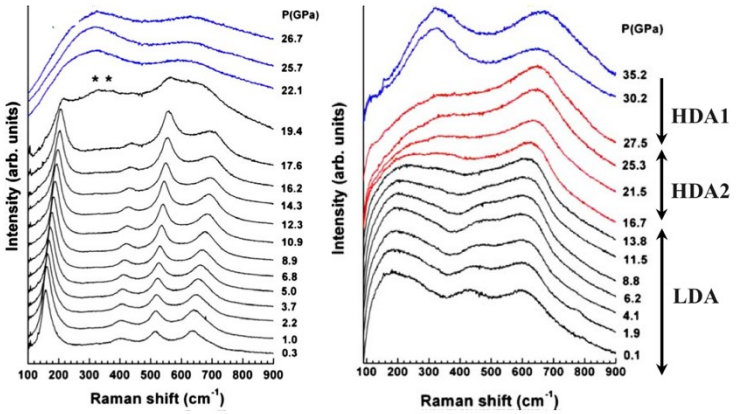


**Figure I-16. Raman spectra of nanostructured anatase (left) or amorphous $TiO_2$ (right) along compression in DAC.**[39]

Therefore, the initial structure of the nanoparticles has a clear influence on pressure-induced amorphisation processes. Yet, Machon *et al.* also demonstrated that the surface state of nano-objects can have a strong influence on transformations involved under high pressure.[40] Indeed, the authors compared the pressure-induced transformations of anatase $TiO_2$ particles either bare or citrate-coated. Bare particles exhibit a pressure-induced phase transition into the baddeleyite phase above 19.1 GPa (evidenced by *in situ* XRD and Raman spectroscopy). However, the citrate coated particles exhibit pressure-induced amorphisation, which onset pressure is lowered for higher functionalisation rates. The results are summarised in Figure I-17 and show that nanomaterials transformation under high pressure are genuinely multi-parameters dependent, even at room temperature.

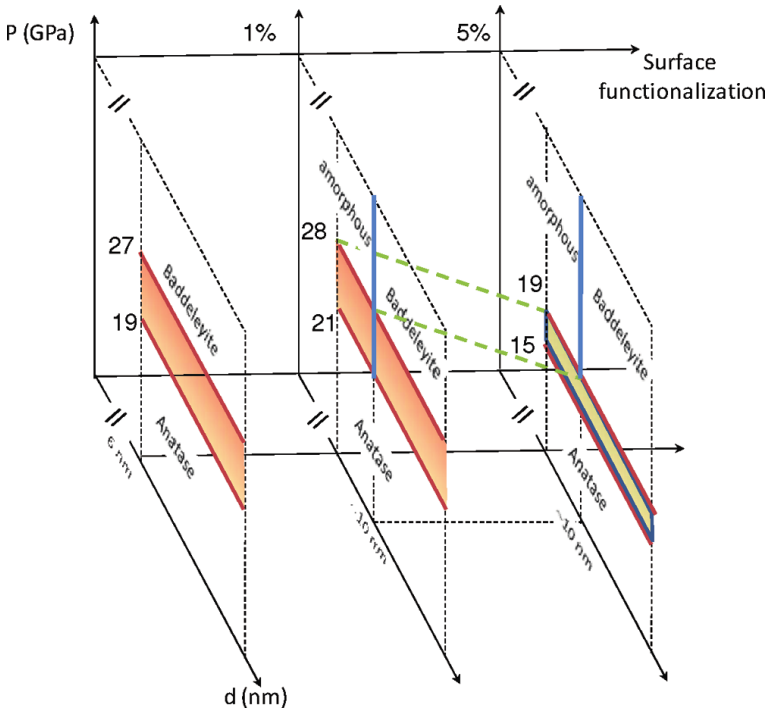


**Figure I-17. Phase diagram of $TiO_2$ nanoparticles, as a function of particle size, pressure and surface functionalisation.**[40]

Nanostructured anatase was also studied using Raman spectroscopy under high pressure by Swamy *et al.,* at room temperature.[41] This study aimed at producing a semi-quantitative phase diagram for anatase metastability, without interest in the materials' microstructure after phase transition.

Nanostructured anatase has also been studied around 2.5 GPa by Lin and co-workers.[42] In this particular case, anatase was mixed with ionic liquids and iodine (to mimic a dye-sensitised solar cell) and high pressure used as a mean to study the interactions strength between $TiO_2$ and the ionic liquid, thanks to *in situ* IR spectroscopy. However, this study did not aim at producing nanomaterials nor it involved high temperature treatments.

• Cerium dioxide

Ceria is also a widely used and studied oxide (for instance as catalyst or in solid oxide fuel cells). Nanostructured cerium oxide has been studied under high pressure, in a way similar to titanium dioxide. Indeed, these studies focus mainly on high pressure transformation at room temperature.

In 2001, Zha *et al.* studied 9-15 nm $CeO_2$ particles under high pressure, using *in situ* XRD in a DAC.[43] They evidenced a phase transition from the cubic fluorite structure toward the α-$PbCl_2$-type structure at 22.3 GPa (bulk $CeO_2$ transforms at

31 GPa), fully completed around 39 GPa. This high pressure phase is not stable and is transformed into cubic fluorite and a hexagonal phase upon decompression. The microstructure after decompression has not been studied. Several other studies conducted on nanostructured $CeO_2$ with different size or morphology (*ca.* 150 nm octahedra, *ca.* 5 nm cubes or 30-40 nm particles) tend to show that the transition pressure variation is not directly influenced by a single parameter such as the particle size: it is rather a competition between the ratio of volume collapse upon compression, surface energy and internal energy.[44–46]

• Other oxides

Few studies were conducted on other oxides. For instance, Gonzalez and co-workers studied the high pressure sintering of nanostructured $\gamma$-$Al_2O_3$ under HPHT.[47] The initial particle size is 20 nm. However, as shown in Table I-3, the treatments induced loss of the nanostructure.

**Table I-3. Mean grain size of recovered α-$Al_2O_3$ according to the sintering conditions.**[47]

| P (GPa) | T (°C) | Sintering Time (h) | $Al_2O_3$ phase | Grain size (nm) |
|---|---|---|---|---|
| 2.5 | 1300 | 5 | α | >1000 |
| 3 | 1050 | 2 | α | 223 |
| 4 | 1050 | 2 | α | 192 |
| 5 | 1050 | 2 | α | 189 |
| 5 | 1050 | 1 | α | 144 |

Recently, Yamaguchi *et al.* studied sol-gel derived yttria-doped zirconia as proton conducting material, by using room temperature compression at 4 GPa.[48] In this case, high pressure is used to remove the macroscopic pores. The 10 nm particles obtained include interfacial layers of water between the grains, responsible for conduction at high temperature in humidified atmospheres. However, the authors used combined high pressure and high temperature treatment (1000 °C), resulting in loss of nanostructure (as illustrated by the XRD peaks' width, not shown).

Yttria was used by Karak *et al.* as a nanostructured dispersion in Fe-Cr-Al-Ti alloys with various compositions (in all cases, iron weight content is superior to 70 and the weight percentage of yttria fixed at 1 %).[49] The pure metals (50 to 100 µm particle size) were first mixed with yttria in the desired proportions. The mixture is subjected to mechanical alloying by ball-milling, in order to reach particle sizes below 40 nm (Figure I-18). The resulting powder was sintered at various temperatures from 600 to 1000 °C for 3 min under a uniaxial pressure of 8 GPa. Upon HPHT treatment, BCC-Fe(Cr) was obtained as major constituent, with intermetallics ($Fe_{11}TiY$ and $Al_{9.22}Cr_{2.78}Y$), mixed oxides ($Y_2Ti_2O_7$ and $Y_2TiO_5$) and unreacted yttria. TEM evidenced that $Y_2Ti_2O_7$, $Y_2TiO_5$ and unreacted $Y_2O_3$ were obtained as 10 to 20 nm particles, embedded in a BCC-Fe(Cr) matrix. However, the authors showed that in the case of high pressure sintering, the mechanical properties (hardness, Young's

modulus compressive strength and fracture toughness) are slightly lower than the alloys sintered using either hot isostatic pressing or pulse plasma sintering.

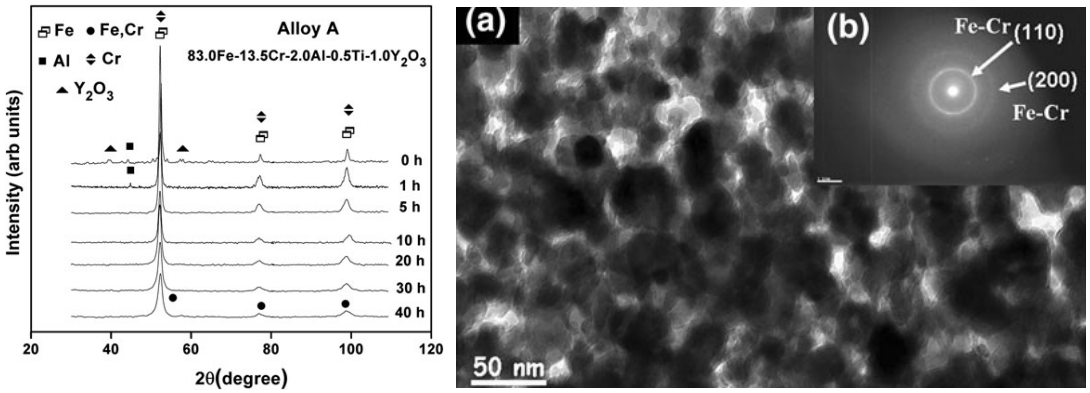


**Figure I-18. Left: XRD patterns (Co $K_\alpha$ wavelength) of one of the ferritic alloys including yttria nanoparticles, according to the ball-milling duration.**[49]

Note that the surface state dependence of pressure-induced transformations in nanostructured yttria was also evidenced by Piot and co-workers.[50] Indeed, 7-10 nm particles exposed to air before compression exhibit pressure-induced amorphisation at 18 GPa. However, the same particles kept under inter atmosphere undergo phase transition into a monoclinic structure between 20 and 25 GPa. The difference in high pressure behaviour is attributed to carbonation of the particles' surface in air.[50]

The dispersion of nanostructured oxide in metal alloys has also been successfully performed by Bera and co-workers.[51,52] In these studies, several alloys (namely Cu-Cr-Ag, Cu-Cr at various weight ratios) have been mechanically alloyed, prior to addition of nanostructured $Al_2O_3$ (at several weight ratios) and sintering at 8 GPa and 600-800 °C (for 1 min). The alloys exhibited significant grain growth while the dispersed alumina retained a grain size below 50 nm. The final composites possessed both increased hardness and wear resistance compared to their alumina-free counterparts, while maintaining the electrical conductivity. Such materials are interesting for the development of wear-resistant electrical contacts.

High pressure sintering of nanostructured $MgAl_2O_4$ spinel has been studied by Xu and co-workers.[53–55] In the 3-5 GPa pressure range and 540-700 °C temperature range, starting from $MgAl_2O_4$ 20 nm particle size, they obtained still nanostructured $MgAl_2O_4$, with a grain size in the 57-76 nm range.[55] Upon optimisation of the synthesis parameters, transparent nano-ceramics were reached (*ca*. 80 % transmitted light) at 4 GPa and 600 °C (Figure I-19). This study is a rare example of nanostructured material obtained after a HPHT treatment, working with a phase that can be synthesised at room pressure, unlike diamond or *c*-BN for instance.

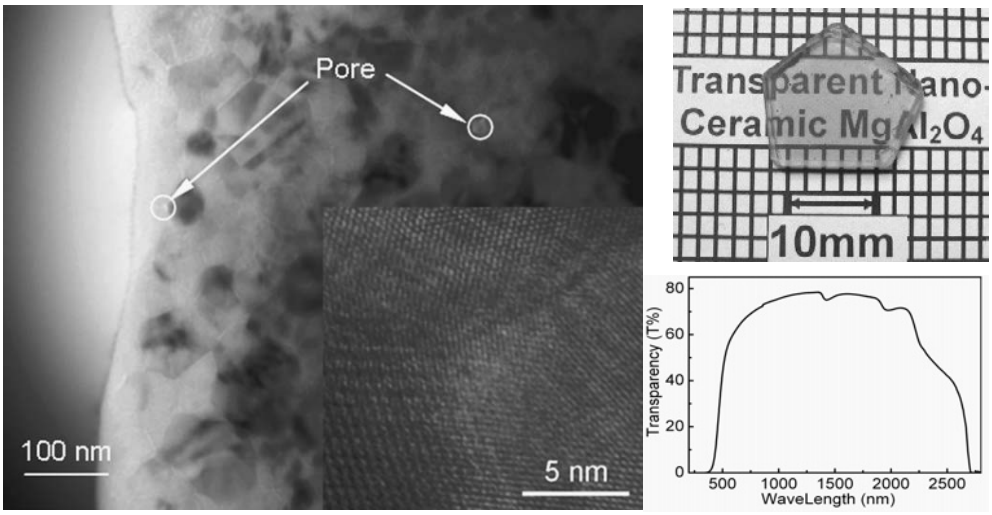


**Figure I-19. Left: TEM micrograph of $MgAl_2O_4$ nanoparticles, synthesised at 3.7 GPa and 620 °C. Inset: HRTEM of grain boundary. Right: picture and transmission spectrum of the sample synthesised at 4 GPa and 600 °C.**[55]

Some studies were also conducted on the high pressure electrical behaviour of perovskites, such as $Sr_2FeMoO_6$ or $La_{0.9}Mn_{0.8}Fe_{0.2}O_{\Delta}$, $MgTiO_3$−geikielite or $La_{0.66}Ca_{0.33}MnO_3/Se_2FeMoO_6$ nanocomposites.[56–59] However, all the experiments and measurements were done at room temperature.

Yet, still at room temperature, a recent result from Santoro and co-workers illustrated the possibility to synthesise new unique nanocomposite systems by the means of high pressure synthesis.[60] In this study, the authors used supercritical ethylene, confined in the pores of a silicalite zeolite (single crystal or polycrystalline) and loaded in a DAC. The confinement was evidenced by Raman spectroscopy, as shown in Figure I-20. Upon compression, ethylene was polymerised by the mean or UV irradiation for several hours. The resulting structure was unique (Figure I-20) and comprised the polyethylene chains inside the zeolite structure, strained so that their conformation adapted to the silicalite pores' structure. The resulting pure (as the synthesis is catalyst-free) unique organic/inorganic nanocomposite has interesting mechanical properties, as it is only 28 % softer than α-quartz but twice as stiff as pure silicalite.

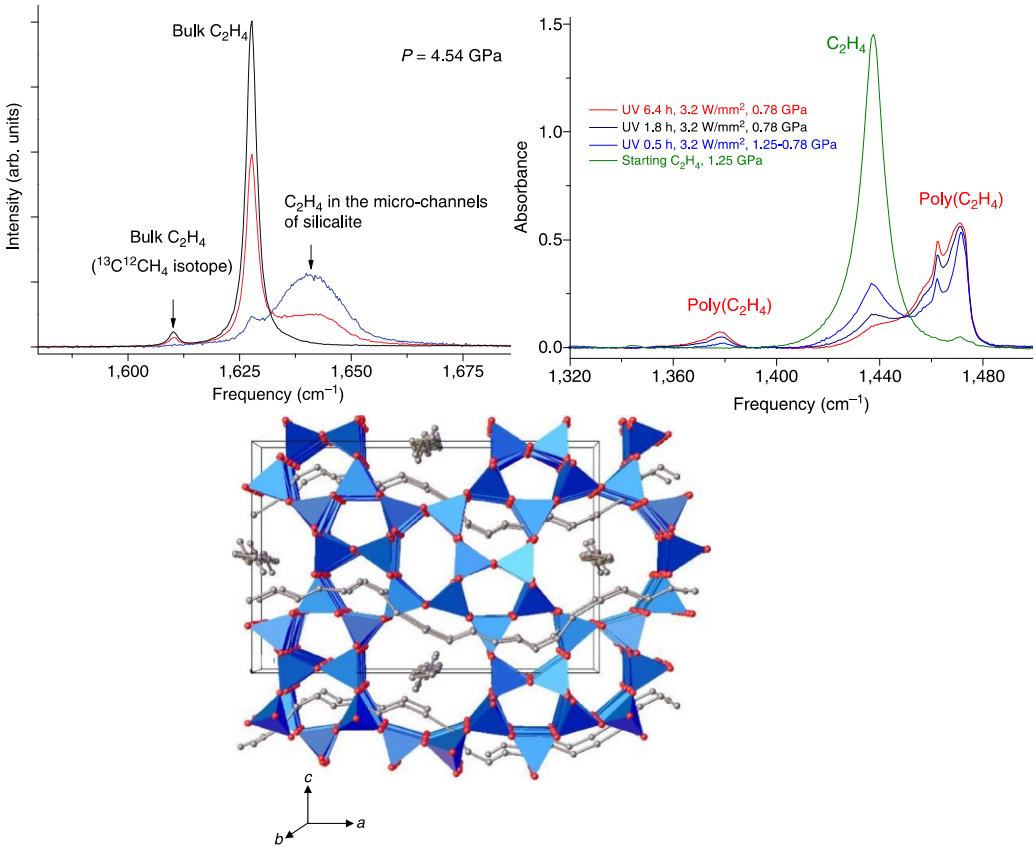


**Figure I-20. Top left: Raman spectra of the ethylene C = C stretching at 4.54 GPa. The black line corresponds to bulk $C_2H_4$ (40 µm), the red line to bulk $C_2H_4$ (40 µm thickness) at the top of a silicalite crystal, the blue line to $C_2H_4$ at the top of a silicalite crystal bridging the two anvils. The broad peak at 1641 $cm^{-1}$ is associated to the C = C stretching confined in the silicalite's channels. Top right: Raman spectra showing the polymerisation of polyethylene along UV irradiation. Bottom: structure of polyethylene-silicalite nanocomposite, exhibiting strained polyethylene in the silicalite's pores.**[60]

Apart from oxides, some other nanostructured non-carbon based materials have been studied under high pressure and temperature, which are the focus of the next part.

### I-1-2-b- Other materials

High pressure sintering of a Si-N-C powder (prepared by pyrolysis of a polysilazane) has been performed by Gao and co-workers.[61] The authors mixed the Si-N-C powder with yttria (8 wt%) by high energy ball-milling, prior to high pressure sintering. At 2 GPa and 1600 °C, a $Si_3N_4$, SiC and $SiN_2O$ nanocomposite was obtained (the grain size is about 50 nm) according to XRD and TEM measurements. However, no yttrium containing phase was mentioned and the role of initial yttria remains unclear. The mechanical properties of the nanocomposite have not been investigated so far.

A titanium-based nanocomposite has been obtained by Zheng and co-workers, based again on the high pressure high temperature sintering of a ball-milling derived precursor.[62] The authors started from a ball-milled mixture of elemental Ti

and *h*-BN. The $TiB_2$/TiN mixture along with unreacted Ti and BN was then sintered at 5 GPa and at room temperature or in the 1100-1300 °C range. Below 1300 °C, the final product still contained unreacted Ti. After sintering 1300 °C, the material was only composed of crystalline $TiB_2$ and TiN. The composite had a Vickers' hardness of 8.8 GPa, much lower than the two components (25-35 GPa for bulk $TiB_2$, 25 GPa for bulk TiN).[62]

Recently, X. Xu and co-workers produced nanostructured SiC using HPHT techniques.[63] Starting from nano-SiC (60 nm particles), the authors reacted the particles with HF and $HNO_3$, before annealing. Upon thermal treatment, a SiC@C core-shell material was obtained (see Figure I-21). The composite was mixed with silicon powder (particle size < 80 nm) and the mixture sintered at 5 GPa and 1500 °C for 1 min. For a 7 SiC@C to 1 Si molar ratio, a pure SiC crystalline phase was obtained. The ceramic was nanostructured, as attested by SEM and particle size distribution data (Figure I-21). However, the micro-hardness was measured at 32.3 GPa which was not significantly higher than for bulk SiC ceramics.[63]

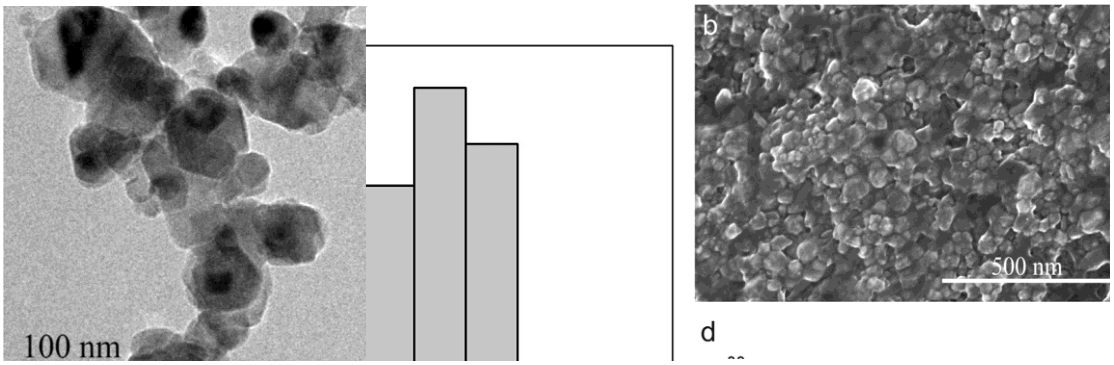


**Figure I-21. Left: HRTEM picture of SiC@C composite, showing the outer carbon shell (as poorly crystallised graphitic carbon). Middle: SEM picture of HPHT-sintered SiC, exhibiting sub-100 nm particles. Right: particle size distribution of HPHT-sintered SiC.**[63]

The study of nanostructured materials under high pressure shows the influence of nanostructuration on phase transition thermodynamic parameters. It also shows the possibility to obtain unique nanostructured composite materials. In the latter case, high pressure is used to either limit diffusion or to allow catalyst-free polymerisation. However, in a few cases, high pressure has been used as the mean toward grain size reduction, for instance by applying severe plastic deformation under pressure.

• Top-down approach: high pressure as grain size reducer

In metallurgy, severe plastic deformation (SPD) is used to strengthen metals or alloys.[64] SPD techniques allow grain size reduction by introducing extensive strains within materials. Among these techniques, High-Pressure Torsion (HPT), for instance, consists in compression of the sample in the GPa range and rotation of one of the anvils to introduce plastic torsional strains, while maintaining the sample's original shape (Figure I-22). SPD can reach nanomaterials, for instance 2024 Al alloy, obtained as 50-60 nm particles after HPT treatment, with a strong increase in

the mechanical properties.[65] However, SPD is usually performed at room temperature or below, and mostly reaches > 100 nm grain size.[65]

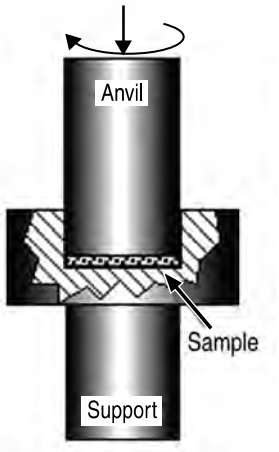


**Figure I-22. Principle of HPT: the sample is compressed between a fixed support and an anvil, which rotation once the sample is compressed introduces strains.**[64]

Also at room temperature, an original route toward grain size reduction has been mentioned by Gonzales *et al.*, and Endo and co-workers.[66,67] As first order phase transitions are accompanied with strong unit cell volume change, such phase transitions in bulk materials are accompanied with crystallite fragmentation (at defects or fractures). Therefore, in the case of pressure-induced phase transitions, applying pressure cycles (*i.e.* go over and below the phase transition pressure, thus corresponding to a phase transition cycle), the crystallite phase is reduced at each pressure cycle. This method has been applied to several materials, including CdSe, CdTe and $Cd_{0.5}Mn_{0.5}Te$, reaching sub-50 nm particles.[66,68,69]

The studies combining nanostructure and high pressure show that HPHT approach is mainly limited to light elements based materials aiming at producing new or improved functional materials for high performance cutting tools or abrasive. Other nanostructured materials such as oxides or metals have been studied under high pressure but mainly kept a room temperature (except for $MgAl_2O_4$ transparent ceramics).[54]

## I-2- Boron: elemental forms and properties of the fifth element

### I-2-1- Allotropes of boron

As argued by Oganov and Solozhenko, “boron is arguably the most complex element in the periodic table”.[70]

The discovery of boron dates back to the experiments of Thénard and Gay-Lussac in 1808, by reduction of boric acid with potassium.[70] However, it is estimated that the products obtained by Gay-Lussac, Thénard and Davy (by electrolysis, in 1808) had less than 50 % of boron. Reduction of boric acid with magnesium was conducted by Moissan later on (1897) and reached purer amorphous boron by reducing $B_2O_3$ with magnesium (mixed with $MgB_2$).[70,71] Pure boron was obtained in 1909 by Weintraub, more than a century after the discovery of the element. Boron is extremely sensitive to impurities, as boron-rich compounds exhibits structures different from that of doped boron allotropes, even with small amounts of impurities: among these, one can cite $PuB_{100}$ or $YB_{66}$ (which has more than 1500 atoms in its unit cell, 2.34 nm long, see Figure I-23). Concerning pure boron, the literature reports no less than 16 modifications subject to discussion (in 2009).[71–75]

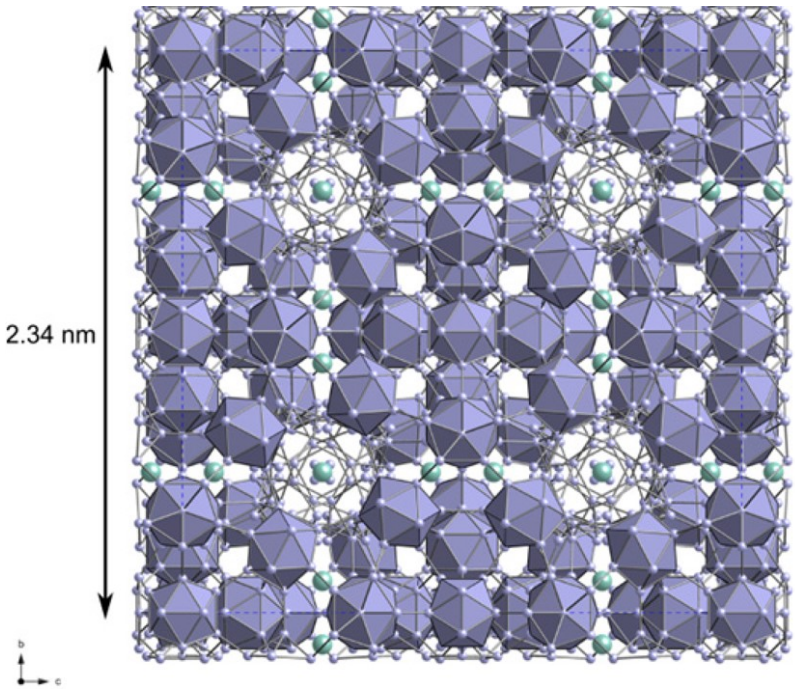


**Figure I-23. $YB_{66}$ structure, a paragon of structural complexity.**[76]

Amorphous boron is usually described as disordered $B_{12}$ icosahedra, a structural building block present in most of the known boron-rich structures. The first structure of a boron allotrope was reported in 1943, by Hoard and co-workers, a tetragonal phase (named *t*-I or $B_{52}$, referring to the number of atoms in the unit cell, also known α-tetragonal boron, referred to as α-T from now on), prepared by boron tribomide reduction with hydrogen, at T > 1200 K on a tantalum wire.[77] However, further experiments failed to obtain *t*-I boron with this technique. Two boron-rich compounds are isostructural to “$B_{52}$”: $B_{50}C_2$ and $B_{50}N_2$, which can be obtained by

pyrolysis of a $BBr_3/CH_4$ (or $N_2$)/$H_2$ mixture. These results raised doubt about the existence of α-T as a boron allotrope until recently, as it will be discussed later. The structure of α-T is shown in Figure I-27. The first structure commonly recognised as an actual boron allotrope has been discovered in the late 1950's, when Sands and Hoard reported the structure of rhombohedral boron (obtained by crystallisation of amorphous boron from melt), nowadays known as β-boron (β-$B_{106}$, though the exact number of atoms in the unit cell is subject to debate), referred as β-B from now on, which is the most common form of boron.[78] The structure of β-B is shown in Figure I-24. It exhibits $B_{12}$ icosahedra and units formed of two groups of three fused icosahedra, $B_{28}$ units, connected by a single boron atom in the centre of the unit cell (Figure I-24). β-B is a semi-conductor, with 1.6 eV band gap determined experimentally.[71] It also exhibits high hardness ($H_v$ = 42 GPa).[72] Soon afterwards, the structure of α-boron (rhombohedral α-$B_{12}$, referred to as α-B from now on) was discovered by Newkirk and co-workers, also by pyrolysis of boron halogenide on a metallic or boron nitride subtrate.[79] α-boron can also be synthesised from a platinum melt, as shown by Horn in 1959.[80] However, single crystals of α-B were not reproducibly obtained for more than 40 years, before Parakhonsky *et al.* crystallised α-B from a boron–platinum melt at high pressure (*ca.* 10-11 GPa, 1200-1600 °C) in 2011 and micron-size single crystals were obtained.[81] However, in this case, α-B is not the only boron phase crystallised (along with β-B and a high pressure phase).[81]

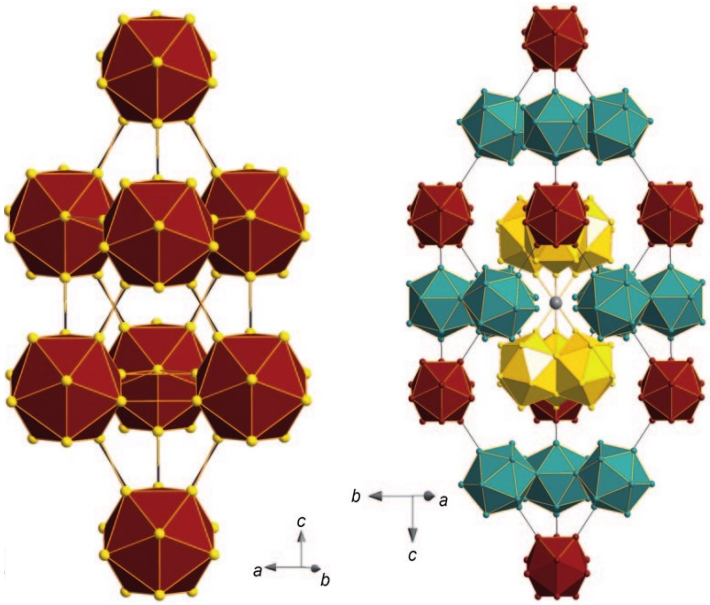


**Figure I-24. Left: α-B structure, rhombohedral setting, based on $B_{12}$ icosahedra. Right: β-B structure, with isolated icosahedra in red and green, $B_{28}$ units in yellow, connected by an isolated boron atom (metal grey).**[71]

α-B is a direct band gap semiconductor (the band gap is 2.0 eV,[80] or 2.4 eV,[82]) and has a Vickers' hardness of about 42 GPa.[70] It is also thermally and chemically highly inert and has a density of about 2.46 $g.cm^{-3}$. Another boron phase was discovered in 1960, T-192 ($B_{192}$, tetragonal), also reported as β-tetragonal boron (referred to as β-T from now on, Figure I-25).[83] The crystals were obtained by reduction of $BBr_3$ with hydrogen on tantalum and rhenium wires at 1470–1520 K. The

density is 2.36 g.cm$^{-3}$. Ma *et al.* showed that above 10 GPa and 2280 K, pure β-B is fully transformed into β-T, confirming its existence as a boron allotrope.[84]

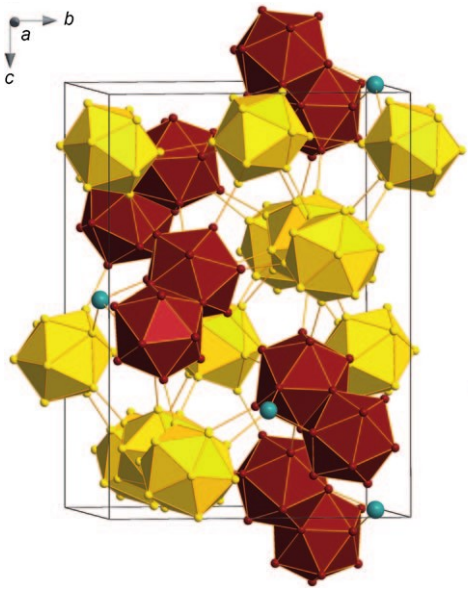


**Figure I-25. Structure of β-T, based on $B_{12}$ units.**[71]

In 1965, Wentorf published an article entitled “Boron: another form”, in which he reported a new form of boron, obtained at high pressure and temperature (P > 10 GPa and T in the 1500-2000 °C range) from β or amorphous boron.[85] However, the structure was not solved at the time. The synthesis was not reproduced before 2007 (from β-B, P = 12-20 GPa, T = 1800-2000 K) by Kurakevych *et al.*,[73] who were able to solve the structure with *ab initio* USPEX simulations. The phase could be quenched to ambient conditions and crystallises with an orthorhombic cell. The structure (Figure I-26), also $B_{12}$-based, displays an arrangement of icosahedra similar to that of α-B, with $B_2$ dumbbells filling the octahedral gaps. The unit cell contains 28 atoms. Both purity and structure were confirmed by Zarachneya *et al.*[86] who succeeded in obtaining micron-sized crystals, though probably mixed with PtB, due to reaction with the platinum capsule containing the sample. Both teams agreed on the phase being an allotrope of boron and the phase originally synthesised by Wentorf, now called γ-$B_{28}$ (referred to as γ-B from now on). The very high hardness of γ-B has been measured by both teams, $H_v$ = *ca.* 50 GPa for Kurakevych and co-workers,[72] 58 GPa for Zarechneya *et al.*,[86] anyway placing γ-B among the hardest known materials (though computation of hardness of boron allotropes pleads for a value around 50 GPa).[74,75]

However, the most striking property of γ-B lies in its binding mode. Indeed, charge density analysis and electronic structure indicate a partially ionic bonding between the dumbbells and the icosahedra. The authors therefore describe γ-B as boron boride $(B_2)^{\delta+}(B_{12})^{\delta-}$, the value of δ equals 0.52. The bonding is reported as “polar covalent”. The density of γ-B (2.544 g.cm$^{-3}$ ) is the highest among boron allotropes.[72]

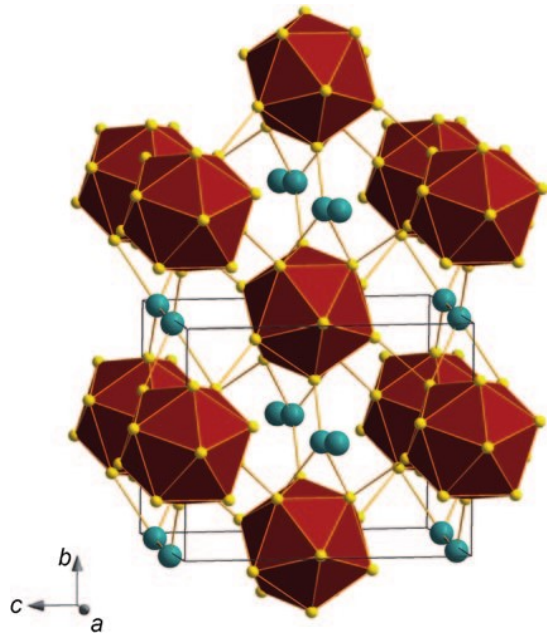


**Figure I-26. Structure of γ-B, described as a NaCl-type arrangement of $B_{12}$ icosahedra and $B_2$ dumbbells.**[71]

Recently, new experiments evidenced the existence of α-T as a boron allotrope. In 2011, Ekimov *et al.* performed the pyrolysis of highly pure diborane $B_{10}H_{14}$ in titanium or tantalum capsules, at 8-9 GPa and 1100-1600 °C.[87] The outcome has a diffraction pattern matching that of $B_{52}$ and X-Ray elemental analyses showed a carbon content inferior to 0.3 at% and a metal content inferior to 0.1 at%. The results obtained (notably the cell parameters, **a** = 9.05 Å, **c** = 5.14 Å) are independent of the nature of the capsule, therefore ruling out the presence of metal in the structure. The cell volume is about 10 % superior to that of isostructural $B_{50}N_2$ and $B_{50}C_2$ crystallised at room pressure. The authors attribute the cell volume increase to the replacement of carbon or nitrogen atoms by boron, exhibiting a higher atomic radius (in the original paper by Hoard *et al.*, the reported cell parameters were **a** = 8.743 Å and **c** = 5.03 Å).[87] At lower pressure (namely 3 GPa), pyrolysis of diborane reached β-B.

In 2013, Parakhonsky *et al.* performed HPHT transformations starting from β-B.[88] Above 9 GPa, the authors reported the synthesis of micron-size crystals (along with other synthesis products not mentioned in the article). The XRD pattern (not shown in the article) is consistent with the α-T structure. Though purity is claimed in the light of EELS analysis (notably the absence of carbon or nitrogen), the data are not shown in the article, nor the authors mentioned the reactivity with the metals used as sample-containing capsules (namely gold or platinum).[88] The refined cell parameter are **a** = 8.708 Å and **c** = 5.075 Å, hence with a smaller **a** distance than that reported by Hoard *et al.*[89] In the light of a recent article by Hammouda and co-workers (Figure I-27),[90] the length of the **a** parameter in $B_{50}C_x$ is clearly decreased when the carbon content is increased, which calls for a higher carbon content in the sample synthesised by Parakhonsky *et al.*[88] than in Ekimov's[87] sample.[90] In their 2012 study, Hammouda *et al.* also obtained a tetragonal structure matching α-T

when crystallising amorphous boron at room pressure under argon atmosphere, with $B_6(O/C/N)_x$. Starting from high purity well-crystallised β-B, α-T was observed as intermediate phase during the β-B to γ-B transformation at 11 GPa and 1400 K. In this study, *h*-BN was used as sample environment (reported inert toward boron at this temperature), eluding issues concerning reactivity with noble metal capsules. The existence of $B_{52}$ as an allotrope of boron (named δ-$B_{52}$ by Parakhonsky and co-workers, referred to as δ-B from now on) seems confirmed by the latter study but the synthesis conditions call for use of high purity starting material (also confirmed by Qin et *al.* in 2012).[90,91]

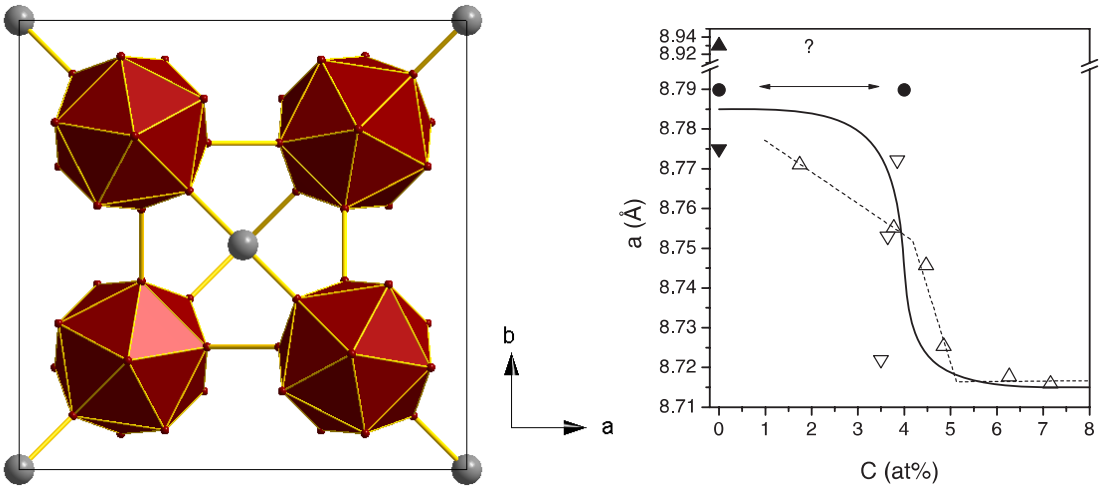


**Figure I-27. Left: Structure of α-T (isostructural to $B_{50}C_2$ and $B_{50}N_2$). As shown recently, it is an actual boron allotrope, named δ-B. Right: value of parameter a in $B_{50}C_x$, according to the carbon content. Plain triangles correspond to high pressure crystallisation, other symbols to room pressure crystallisation.**[88,90]

In their 2013 study, Parakhonsky *et al*. also reported a new boron phase, trigonal ε-B.[88] Starting from β-B and using platinum or gold capsules, this phase was obtained at 8.5-9 GPa and between 1600 and 1800 °C, along with known boron phase. This phase (structure shown in Figure I-28) is isostructural to boron carbide $B_{13}C_2$, in which the B-B-B units are C-B-C units. The EELS spectrum shown in Figure I-28 compares the signal of ε-B to $B_{13}C_2$ and boron allotropes and confirms the absence of carbon in this new phase. Unfortunately, the stoichiometries and cell parameters (notably **a** to **c** ratio) reported do not enable establishing a clear relation between foreign atom content and cell parameters as done in the case of δ-B/$B_{52}$. At 11 GPa and 2300 K in a DAC, ε-B fully transform into γ-B, hence also calling for the high purity of ε-B. Concerning properties, ε-B is the hardest reported boron allotrope with $H_v$ = 55-60 GPa.[88] ε-B has not been reported again so far.

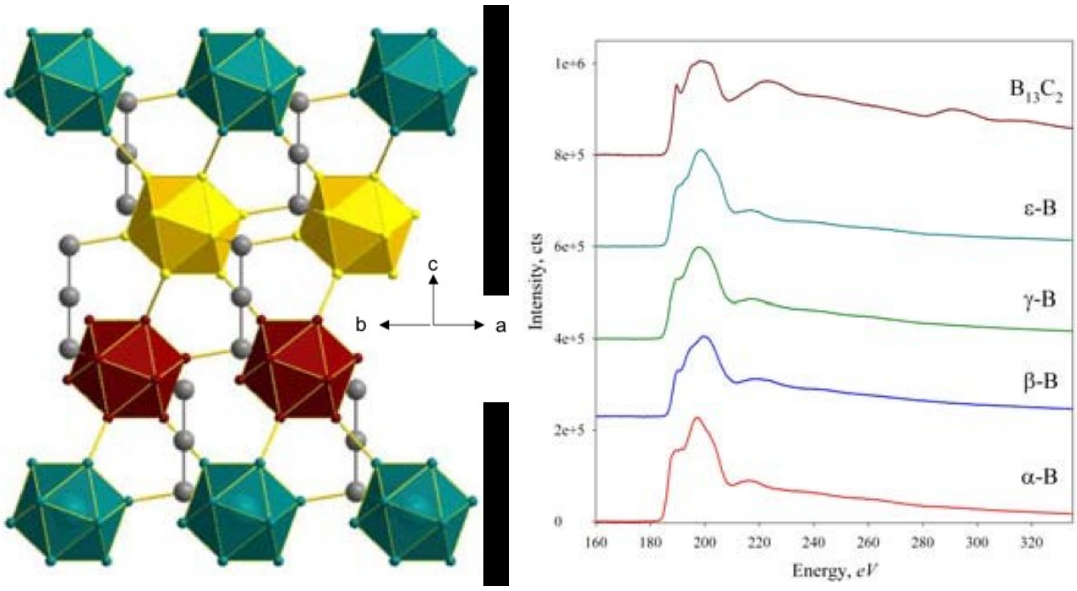


**Figure I-28. Left: Structure of ε-B (isostructural to $B_{13}C_2$). Right: EELS spectra of boron allotropes and $B_{13}C_2$.[88]**

Also in 2013, Kurakevych and Solozhenko reported the synthesis of a boron phase related to δ-B, at 20 GPa/2500 K and starting from β-B.[92] This phase is obtained as a composite with γ-B. The tetragonal structure of this new phase belongs to the $B_{52}$ family but cell parameters are significantly different (**a** = 8.294 Å, **c** = 5.864 Å), with a **a/c** ratio equals to √2. The **a/c** ratio for different $B_{52}$ phases is shown in Figure I-29. The density of this new (2.528 g.cm$^{-3}$) phase is second only to γ-B among boron allotropes. The authors underline that other key features responsible for hardness (such as coordination number or bonding type) should lead to mechanical properties close to that of γ-B. This phase has been named pc-$B_{52}$, "pc" standing for pseudo-cubic, due to the **a/c** ratio (referred to as pc-B from now on).

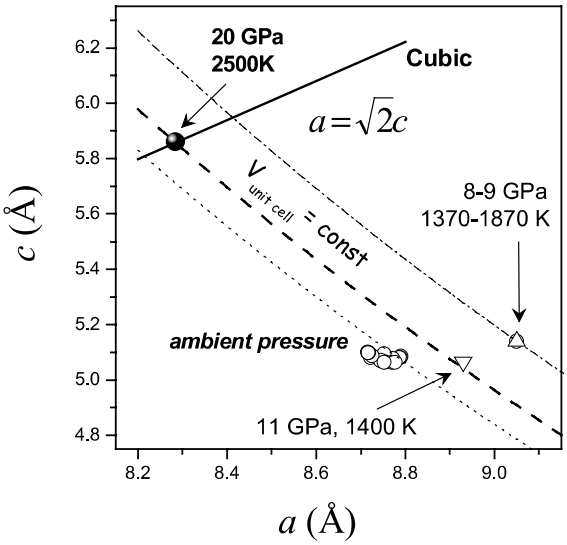


**Figure I-29. Reported cell-parameters for $B_{52}$-type phases: hollow circles corresponds to $B_{50}C_2$ structures crystallised at room pressure. ▽ corresponds to crystallisation of δ-B from $B_{10}H_{14}$ at HPHT by Ekimov,[87] △ to crystallisation of δ-B at HPHT, by Parakhonsky,[88]• to pc-B.[92]**

In the early 2000's, Eremets *et al.* compressed β-B up to 250 GPa in a DAC at room temperature.[93] Metallisation of boron occurred from 160 GPa and the authors reported pressure-induced superconductivity in boron. The critical temperature was 11.2 K at 250 GPa. However, the structure of this metallic phase remains unknown, though further experiments point toward β-B amorphisation around 100 GPa.[94] Theoretical studies predict a α-Ga type structure (Figure I-30) phase above 100 GPa that should be superconductor. This structure is the first reported yet theoretical boron structure which does not contain $B_{12}$ icosahedra.[74]

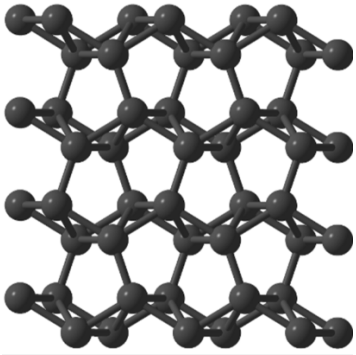

**Figure I-30. α-Ga type structure, predicted by simulations.**[74]

Theoretical studies also suggest that numerous non-icosahedral structures are possible for nano-objects, based on $B_7$ hexagonal pyramids (Figure I-31).[95] These predictions were recently confirmed by two independent studies reporting the synthesis of a new form of boron: two-dimensional sheets of boron, named borophene, grown by chemical vapour deposition on Ag(111) substrates.[96,97] Structural studies by Scanning Tunneling Microscopy (STM) confirmed the presence of $B_7$ building blocks. The overall structure is shown in Figure I-31.

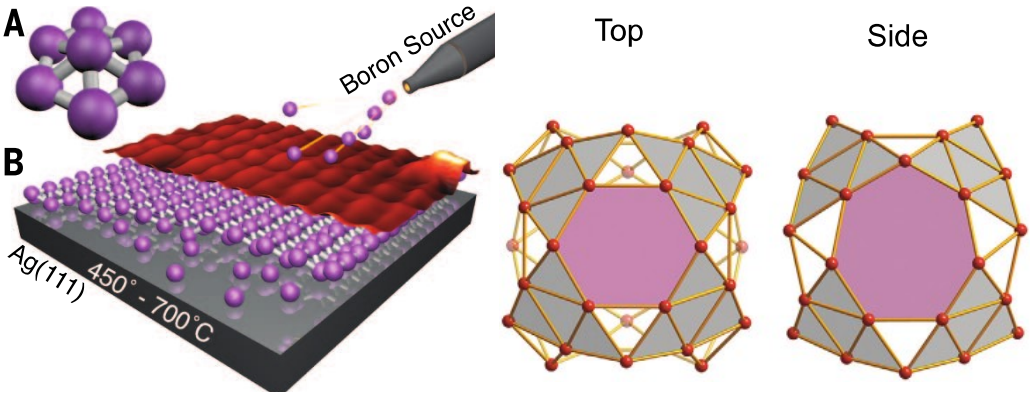


**Figure I-31. Left: Borophene (A): $B_7$ cluster. (B) Schematic description of borophene synthesis, by CVD of boron onto a Ag(111) substrate. Right: structure of the $B_{40}^-$ all-boron fullerene.**[96,98]

A last elemental boron form has been reported by Zhai *et al.* in 2014:[98] an all-boron fullerene, $B_{40}^-$, obtained by laser vaporisation of a $^{10}$B-enriched boron target, separated by time-of-flight mass spectrometer and characterised by Photo-Electron Spectroscopy. The structure proposed by the authors by comparing the theoretical spectrum to experimental data is shown in Figure I-31.

Synthetic pathways leading to nanostructured boron materials are mainly based on vapour deposition techniques (from boron halogenides or diborane).[99–103] Other techniques involve laser ablation of boron[104–106] or thermal decomposition of boranes.[107] Only one solution-based method has been reported by Pickering *et al.*,[108] consisting in boron tribromide reduction by sodium naphtalenide, reaching sub-20 nm amorphous boron. In this limited number of occurrences of nanostructured boron, it is obtained as amorphous, α,[107] β[99,100,109] or β-T[104,105] boron and as nanowires (30-100 nm), nanoribbons or isotropic particles (an instance of TEM picture is shown in Figure I-32). However, only three of the reported pathways reach oxygen-free boron, based on EELS analysis.[103,104,107]

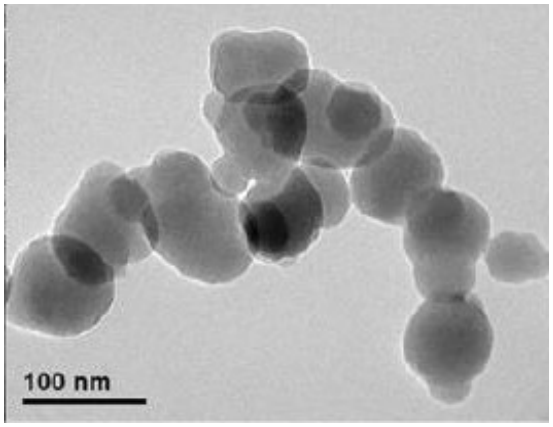


**Figure I-32. Amorphous boron nanoparticles synthesised by decaborane pyrolysis at 700-900 °C.**[107]

The latest results leading to new elemental forms of boron showed the possibility to obtain non-icosahedral local structures, bringing the number of known forms to ten: 8 allotropes (α, β, γ, δ, ε, pc, β-T and α-Ga) and two nanostructured materials (borophene and all-boron fullerene). This is interesting when it comes to crystallisation. Indeed, all known crystalline structures are mainly based on $B_{12}$ building blocks. But all known allotropes have been obtained either from amorphous boron (synthesised at high temperature) or high purity β-B (crystallised from molten boron and purified by zone melting, $T_M$ = 2349 K at RP). Yet, commercial amorphous boron, if reactive, rises concerns about its purity and crystalline boron forms are known for chemical inertness. Consequently, boron crystallisation studies would gain from a reactive, pure and non-icosahedral precursor.

### I-2-2- Stability of boron phases and phase diagram

Along with controversies concerning the existence of several boron allotropes, the nature of the most stable phase has been subject to long debates. At room pressure, liquid boron crystallises into β-B, making this allotrope the stable phase at high temperature.[71] Furthermore, at room pressure, no phase transition of β-B into other allotropes has been reported. Therefore, early reports made β-B the thermodynamically stable phase at all temperatures below the melting point at ambient pressure.[71,110] However, first computational studies established that α-$B_{12}$

has a lower energy than β-B, but these calculations were made without taking into account the macroscopic amounts of defects present in β-B, which exhibits partial occupation of numerous crystallographic sites (POS), as established by Slack *et al.*[110,111] Five sites are reported to exhibit POS, for instance the $B_{13}$ position in the $B_{28}$ triply fused iscosahedra (Figure I-33).

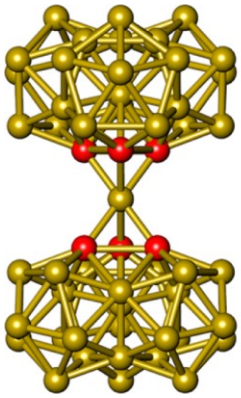

**Figure I-33. Instance of partially occupied site in β-B: $B_{13}$ site (red) in the B28 triply fused icosahedra, which full occupancy is not energetically favoured.**[110]

A recent work by Parakhonsky *et al.* on the P, T phase diagram of boron established that α-B is stable at high pressures and low temperature. The authors also extrapolated the α/β boundary to ambient conditions, making α-B the stable allotrope at room pressure and temperature.[112]

Except this study, a consensus has been found making β-B the most stable phase at ambient conditions, and likely down to 0 K, though it is, unlike α-B partially disordered (DFT indicates that β-B is the most stable allotrope when partial occupation of sites is taken into account).[110,112,113]

The phase diagram has been widely studied but is not set, notably due to the high kinetic barriers between the multiple metastable allotropes. The P, T phase diagram proposed by Oganov *et al.* up to 150 GPa in 2009, based on experiments and *ab initio* studies is shown in Figure I-34. In their 2013 review, Ogitsu and co-workers summed up the propositions for the P, T phase diagram, based on Oganov's and Parakhonsky's studies (Figure I-34), showing the uncertainties remaining as to the exact position of the phase boundaries.[110] The recent works which introduced δ and ε-B led to a slight revision of the P, T phase diagram (Figure I-34), though Parakhonsky and co-workers do not report the stability domain of β-T. Note also that δ and ε-B have never been obtained as the sole crystalline phase but rather mixed with other allotropes.[88] The P, T region of stability of the last discovered allotrope pc-$B_{52}$ has not been established, though the synthesis conditions (20 GPa, 2500 K) are in the stability domain of β-T.

However, not all the studies on boron P, T phase diagram are conducted in the same experimental conditions: for instance, it is not clear in Quin *et al.* 2012 paper which experiments have been conducted either in MgO, *h*-BN, $Al_2O_3$, Au or Pt capsules, when Oganov and co-workers' studies are conducted in h-BN and Parakhonsky *et al.*'s mostly in Au or Pt.[73,88,91] The use of noble metal capsules and

short dwell times may lead to synthesis of kinetically favoured phases (for instance Parakhonsky *et al.* report δ-B up to 16 GPa, which is not the case for any other study).

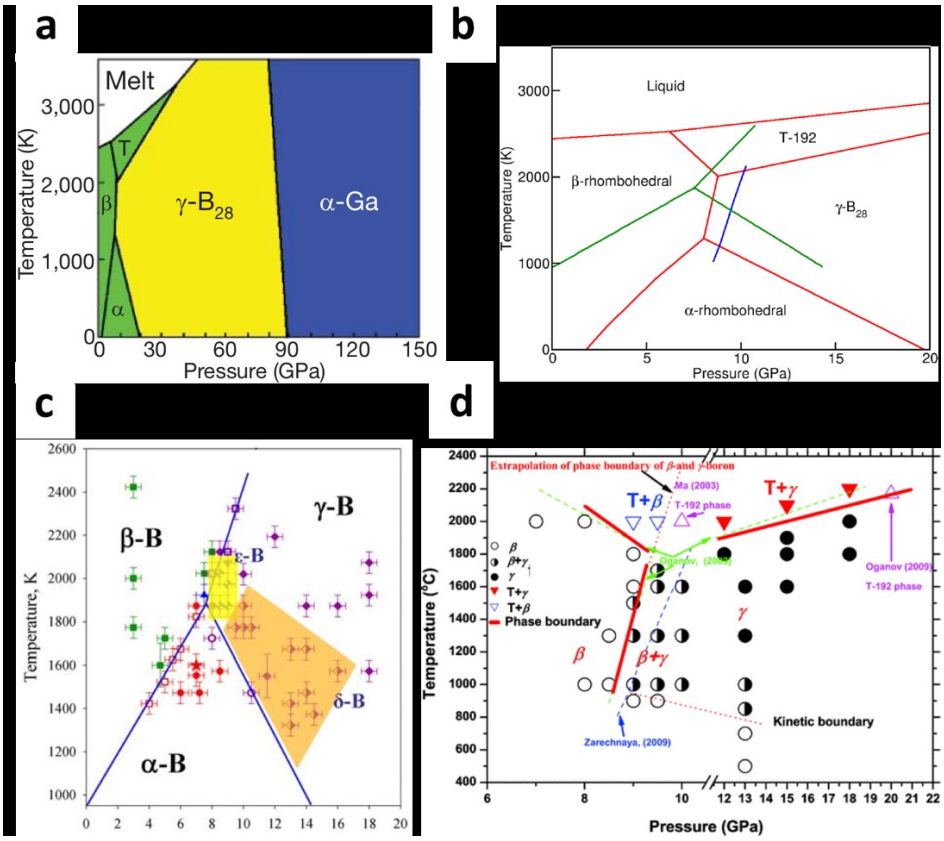


**Figure I-34. P, T phase diagrams of boron proposed in the literature. (a) Phase diagram established by Oganov *et al.* from experimental and ab-initio studies, up to 150 GPa. (b) Summary of different phase diagrams proposed (a the date of submission in 2012) by Ogitsu *et al*. The red lines correspond to Oganov's diagram, the green and blue lines to Parakhonsky's work. (c) updated phase diagram from Parakhonsky *et al.*, introducing the estimated stability domain of δ and ε-B but not showing T-$B_{192}$. (d) phase diagram summarised by Quin *et al*.**[73,88,91,110,112]

Overall, results of studies on boron are strongly precursor-dependent (either nature and purity) and strongly influenced by the synthesis conditions, either P, T, time parameters or sample environment.

Concerning precursors, it is interesting to note that either amorphous boron or β-B are synthesised at high temperature and exhibit $B_{12}$ icosahedra before the transformation (which is also the case for diborane, used by Ekimov as δ-B precursor).[73,87,88,90,91,114,115] In this context, the use of non-icosahedral reactive precursors is of interest, as it opens the ways toward new metastable forms of boron, as evidenced by recent studies yielding borophene or all-boron fullerene.[96–98]

## I-3- Boron-metal alloys: structure, properties and synthesis

### I-3-1- Properties and structures

In addition to its elemental forms, metal-boron alloys can be produced with many metals, named metal borides ($MB_x$). Metal borides are usually good refractory

materials with high melting temperature (for instance, $HfB_2$ ceramics are used as spacecraft thermal shields). In addition to their refractory behaviour, metal borides span a wide range of properties: hardness, thermo-ionic emission ($LaB_6$ is used as hot cathode in TEM), thermoelectricity or superconductivity ($MgB_2$ exhibits $T_c$ = 39 K, an extremely high value for a classical superconductor). The properties of borides with stronger metal content (or boron-poor borides) are also interesting as illustrated by “neodymium magnets”: $Nd_2Fe_{14}B$ magnets are strong permanent magnets used for numerous applications going from hard drives actuators or magnetic resonance imaging head to toys.

In most metal borides, both boron and metal(s) exhibit a zero oxidation state. Consequently, the borides’ stoichiometry is not limited by either coordination number or rules governing the crystal structure of ionic compounds. For a same metal, numerous stoichiometries may be obtained, for instance $YB_2$ to $YB_{66}$ in the case of yttrium borides. For metal-rich borides, such as $Ni_xB_y$, the boron sub-lattice consists in isolated boron atom for $Ni_3B$ (Figure I-35). When the boron content is increased to $Ni_2B$, boron forms short linear chains. Further increase (toward $Ni_4B_3$ or NiB) leads to B atoms organised as corrugated chains with short B-B distances. Boron-poor borides are generally poorly stable toward air or moisture.

For boron-rich borides, notably yttrium borides, the boron sub-lattice consists in honeycomb graphitic layers in $YB_2$ and increases in complexity and density with the boron content, reaching $B_6$ octahedra in $YB_6$, cuboctahedra in $YB_{12}$ and $B_{12}$ icosahedra for boron content beyond $YB_{12}$ (Figure I-35), arranged in a complex 3-D network in richer borides (see for instance $YB_{66}$, Figure I-23). Boron atoms are covalently bounded, with a B-B distance shortening as the boron content increases.

The structure of metal borides implies some requirements concerning their synthesis conditions their synthesis conditions, as it will be discussed in the next part.

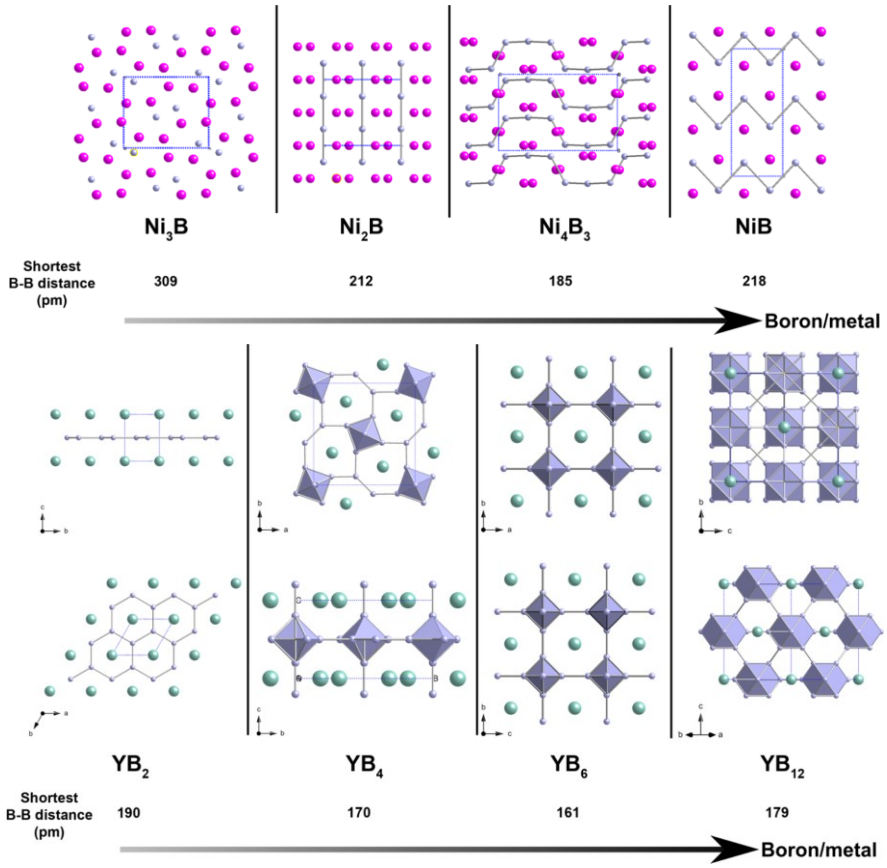


**Figure I-35. Top: structures of metal-rich borides: the boron atoms are isolated in $Ni_3B$. Increase of the boron content ($Ni_2B$) leads to boron clusters and corrugated chains ($Ni_4B_3$ and NiB). Bottom: structures of boron-rich borides. Boron atoms form honeycomb layers in $YB_2$. In richer borides ($YB_4$, $YB_6$), boron atoms form octahedra. In $YB_{12}$, boron atoms form cuboctahedra. In $YB_{25}$ (not shown) and richer borides ($YB_{50}$, $YB_{66}$), boron atoms form the $B_{12}$ structural building block**[76]

## I-3-2- Synthesis and nanostructures

Establishment of the covalent boron atoms network calls for high synthesis temperatures. Typical synthesis of MB's involves a solid state reaction between the elemental constituents but requires high temperatures to overcome the chemical inertness of elemental boron. Elemental boron can also be used in excess for borothermal reduction: boron is used to reduce a metal oxide while providing boron atoms. Such solid-state reactions are highly exothermic and are considered as self-propagating high temperature synthesis (T>1000 °C) and therefore impedes the isolation of metastable nanostructured materials. Besides the inevitable grain growth, such methods raise issues concerning the crucible's reactivity and other foreign atoms content, particularly oxygen, nitrogen or carbon.

As already mentioned, nanostructuration has a strong influence on material properties. To investigate such effects, nanostructured borides have been developed. The synthetic pathways toward these materials have been extensively reviewed recently and are plotted in Figure I-36.[76] The majority of these methods reach particles in the 30-100 nm size range. Developments have been made toward the synthesis of nanostructured $MgB_2$, notably by reacting magnesium vapour with

elemental boron. In specific cases, borothermal reduction reaches nanostructured objects, starting from already nanostructured oxides (for $NbB_2$ or $CeB_6$).

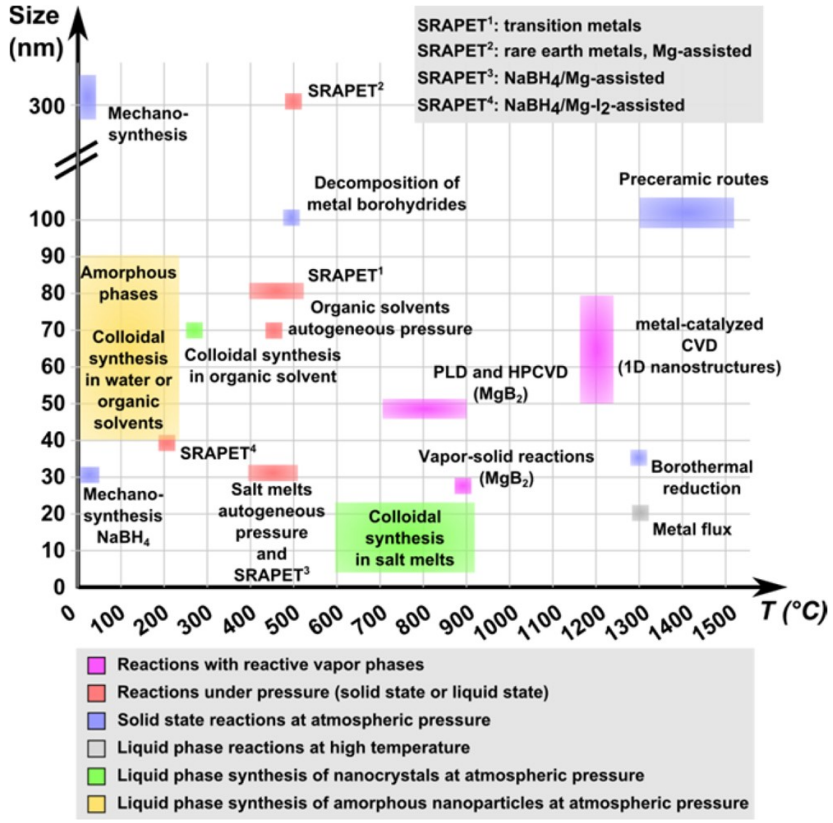


**Figure I-36. Metal boride particle size as function of the synthesis temperature. SRAPET designates solid-state reactions under autogenous pressure at elevated temperature, PVD physical vapour deposition, CVD chemical vapour deposition, HPCVD hybrid physical chemical vapour deposition.**[76]

Synthesis in water or organic solvent cannot be conducted above 400 °C, so that it leads to amorphous nano-objects, usually unstable.

Recently, Bao and co-workers reported the synthesis of three nanostructured hexaborides (namely $CaB_6$, $SrB_6$ and $BaB_6$).[116] The borides are synthesised by reacting $NaBH_4$ (used as both reductant and boron source) with calcium, strontium or barium oxide, mixed and compressed in pellets at temperatures in the 900-1150 °C range, under a $2.10^{-2}$ bar vacuum.[116] The hexaborides are reached as nanocubes *ca.* 150 nm wide for $CaB_6$, 30 nm for $SrB_6$ and 20 nm for $BaB_6$. A TEM picture of $SrB_6$ nanocubes is shown in Figure I-37. This method is single step and allows size tuning in a small range, according to the synthesis temperature. The authors report the particle size of these hexaboride as the smallest reported in the literature.

However, the synthetic route reported by Portehault *et al.* in 2011, namely synthesis in molten salts, reaches sub-10 nm crystalline borides, notably $CaB_6$.[117] This method, partially developed at the LCMCP, is a solution-based route which allows size and stoichiometry control of the borides. It has been successfully applied to several borides of various stoichiometries and various metals. It is so far the only general route toward crystalline borides with a particle size inferior to 10 nm. As

shown in Figure I-37, the particles are embedded in an amorphous matrix, composed of partially oxidised boron. Similar results have been obtained with $TiB_2$ by Terlan and co-workers, though residual amounts of other titanium borides, titanium and boron oxides are evidenced by powder XRD.[118]

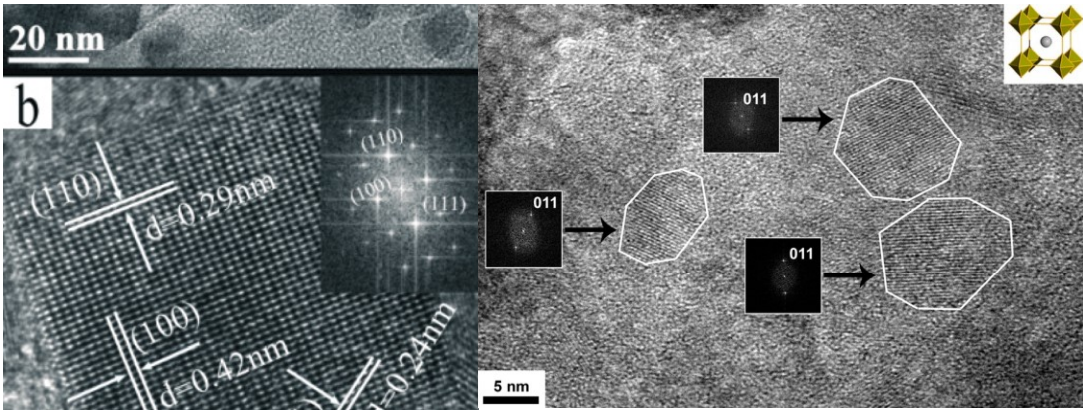


**Figure I-37. Left: TEM micrograph of $SrB_6$ nanocubes synthesised by Bao *et al.*.[116] Right: nanostructured $CaB_6$ synthesised by Portehault *et al.*, embedded in an amorphous boron matrix.[117]**

The principles and recent developments of SMS at the LCMCP will be discussed in the next chapter.

## I-4- Conclusion

To conclude on the bibliographic aspects, we have shown that nanomaterials obtained by coupled high pressure and temperature treatments are mainly limited to the development of superhard materials based on light elements, namely boron, carbon, and nitrogen. Indeed, most studies dealing with the high pressure behaviour of nanostructured oxides are conducted at room temperature. Though, note that nanostructuration of intrinsically superhard phases leads to great mechanical properties improvement, as illustrated by nanopolycristalline diamond.

The preparation of the elemental forms of boron has been discussed in this chapter. It illustrated how important the presence of potential foreign atoms can be. The latter may originate from the sample environment during synthesis or from the precursor itself. As discussed, in most boron crystallisation studies, either readily available amorphous boron or already crystalline β-B are used as precursors. These are notably bulk materials and none of the nanostructured occurrences of boron have been used as precursors for HPHT studies so far.

In this PhD work, we have studied the HPHT behaviour of non-oxides and that do not only contain light elements nanostructured materials, namely nanostructured metal borides. These were produced with a specific synthetic route, synthesis in molten salts, which also yields a unique nanostructured amorphous boron precursor.

## I-5- References

(1) Roure, F.; Rumble, J. On the Description of Nanomaterials

http://www.iupac.org/publications/ci/2012/3406/cc2_230212.html (accessed Jan 1, 2016).
(2) Nel, A.; Xia, T.; Madler, L.; Li, N. *Science* **2006**, *311*, 622–627.
(3) Helmut Mehrer. *Diffusion in Solids Fundamentals,Methods,Materials, Diffusion-Controlled Processes*; **2007**.
(4) Mehrer, H. *Defect Diffus. Forum* **2011**, *309-310*, 91–112.
(5) Irifune, T.; Kurio, A.; Sakamoto, S.; Inoue, T.; Sumiya, H. *Nature* **2003**, *421* (6923), 599–600.
(6) Brookes, C. A.; Brookes, E. J. *Diam. Relat. Mater.* **1991**, *1* (1), 13–17.
(7) Katzman, H.; Libby, W. F. *Science* **1971**, *172* (3988), 1132–1134.
(8) Kurakevych, O. O. *J. Superhard Mater.* **2009**, *31* (3), 139–157.
(9) Hall, E. O. *Proc. Phys. Soc. Sect. B* **1951**, *64* (9), 747–753.
(10) Petch, N. J. *J. Iron Steel Inst. London* **1953**, *173*, 25–28.
(11) Pande, C. S.; Cooper, K. P. *Prog. Mater. Sci.* **2009**, *54* (6), 689–706.
(12) Regueiro, M. N.; Monceau, P.; Hodeau, J.-L. *Nature* **1992**, *355*, 237–239.
(13) Irifune, T.; Kurio, A.; Sakamoto, S.; Inoue, T.; Sumiya, H.; Funakoshi, K. ichi. *Phys. Earth Planet. Inter.* **2004**, *143* (1-2), 593–600.
(14) Brazhkin, V.; Dubrovinskaia, N.; Nicol, M.; Novikov, N.; Riedel, R.; Solozhenko, V.; Zhao, Y. *Nat. Mater.* **2004**, *3* (9), 576–577.
(15) Dubrovinskaia, N.; Dubrovinsky, L.; Langenhorst, F.; Jacobsen, S.; Liebske, C. *Diam. Relat. Mater.* **2005**, *14* (1), 16–22.
(16) Dubrovinskaia, N.; Dubrovinsky, L.; Crichton, W.; Langenhorst, F.; Richter, A. *Appl. Phys. Lett.* **2005**, *87* (8), 85–88.
(17) Dubrovinskaia, N.; Dub, S.; Dubrovinsky, L. *Nano Lett.* **2006**, *6* (4), 824–826.
(18) Sumiya, H.; Irifune, T. *J. Mater. Res.* **2007**, *22* (08), 2345–2351.
(19) Sumiya, H.; Yusa, H.; Inoue, T.; Ofuji, H.; Irifune, T. *High Press. Res.* **2006**, *26* (2), 63–69.
(20) Xu, C.; He, D.; Wang, H.; Guan, J.; Liu, C.; Peng, F.; Wang, W.; Kou, Z.; He, K.; Yan, X.; Bi, Y.; Liu, L.; Li, F.; Hui, B. *Int. J. Refract. Met. Hard Mater.* **2013**, *36*, 232–237.
(21) Patterson, A. *Phys. Rev.* **1939**, *56* (10), 978–982.
(22) Ohfuji, H.; Okada, T.; Yagi, T.; Sumiya, H.; Irifune, T. *High Press. Res.* **2010**, *30* (1), 142–150.
(23) Nakamoto, Y.; Sakata, M.; Sumiya, H.; Shimizu, K.; Irifune, T.; Matsuoka, T.; Ohishi, Y. *Rev. Sci. Instrum.* **2011**, *82* (6), 82–84.
(24) Matsumoto, K.; Maruyama, H.; Ishimatsu, N.; Kawamura, N.; Mizumaki, M.; Irifune, T.; Sumiya, H. *J. Phys. Conf. Ser.* **2012**, *377*, 012039.
(25) Kurakevych, O. O. *J. Superhard Mater.* **2009**, *31* (3), 139–157.
(26) Wentorf, R. H. *J. Chem. Phys.* **1961**, *34* (3), 809.
(27) Dubrovinskaia, N.; Solozhenko, V. L.; Miyajima, N.; Dmitriev, V.; Kurakevych, O. O.; Dubrovinsky, L. *Appl. Phys. Lett.* **2007**, *90* (10), 1–4.
(28) Solozhenko, V. L.; Kurakevych, O. O.; Le Godec, Y. *Adv. Mater.* **2012**, *24* (12), 1540–1544.
(29) Solozhenko, V. L.; Kurakevych, O. O. *Acta Crystallogr. Sect. B Struct. Sci.* **2005**, *61* (5), 498–503.
(30) Tian, Y.; Xu, B.; Yu, D.; Ma, Y.; Wang, Y.; Jiang, Y.; Hu, W.; Tang, C.; Gao, Y.; Luo, K.; Zhao, Z.; Wang, L.-M.; Wen, B.; He, J.; Liu, Z. *Nature* **2013**, *493* (7432), 385–388.
(31) Dubrovinskaia, N.; Dubrovinsky, L. *Nature* **2013**, *502* (7472), E1–E2.
(32) Solozhenko, V. L.; Kurakevych, O. O.; Andrault, D.; Le Godec, Y.; Mezouar, M.

*Phys. Rev. Lett.* **2009**, *102* (1), 1–4.
(33) Zinin, P. V.; Ming, L. C.; Ishii, H. A.; Jia, R.; Acosta, T.; Hellebrand, E. *J. Appl. Phys.* **2012**, *111* (11).
(34) Solozhenko, V. L.; Andrault, D.; Fiquet, G.; Mezouar, M.; Rubie, D. C. *Appl. Phys. Lett.* **2001**, *78* (10), 1385–1387.
(35) Langenhorst, F.; Solozhenko, V. L. *Phys. Chem. Chem. Phys.* **2002**, *4* (20), 5183–5188.
(36) Zhao, Y.; He, D. W.; Daemen, L. L.; Shen, T. D.; Schwarz, R. B.; Zhu, Y.; Bish, D. L.; Huang, J.; Zhang, J.; Shen, G.; Qian, J.; Zerda, T. W. *J. Mater. Res.* **2002**, *17* (12), 3139–3145.
(37) Olsen, J. S.; Gerward, L.; Jiang, J. Z. *High Press. Res.* **2002**, *22*, 385–389.
(38) Wang, Y.; Zhao, Y.; Zhang, J.; Xu, H.; Wang, L.; Luo, S.-N.; Daemen, L. L. *J. Phys. Condens. Matter* **2008**, *20* (12), 125224.
(39) Machon, D.; Daniel, M.; Pischedda, V.; Daniele, S.; Bouvier, P.; LeFloch, S. *Phys. Rev. B* **2010**, *82* (14), 140102.
(40) MacHon, D.; Daniel, M.; Bouvier, P.; Daniele, S.; Le Floch, S.; Melinon, P.; Pischedda, V. *J. Phys. Chem. C* **2011**, *115* (45), 22286–22291.
(41) Swamy, V.; Kuznetsov, A.; Dubrovinsky, L. S.; Caruso, R. A.; Shchukin, D. G.; Muddle, B. C. *Phys. Rev. B - Condens. Matter Mater. Phys.* **2005**, *71* (18), 15–17.
(42) Chang, H.-C.; Jiang, J.-C.; Kuo, M.-H.; Hsu, D.-T.; Lin, S. H. *Phys. Chem. Chem. Phys.* **2015**, *17*, 21143–21148.
(43) Wang, Z.; Saxena, S. K.; Zha, C. S.; Pischedda, V. *Phys. Rev. B* **2002**, *66* (2), 024103.
(44) Liu, B.; Yao, M.; Liu, B.; Li, Z.; Liu, R.; Li, Q.; Li, D.; Zou, B.; Cui, T.; Chen, Z. *J. Phys. Chem. C* **2011**, No. 111, 4546–4551.
(45) Ge, M. Y.; Fang, Y. Z.; Wang, H.; Chen, W.; He, Y.; Liu, E. Z.; Su, N. H.; Stahl, K.; Feng, Y. P.; Tse, J. S.; Kikegawa, T.; Nakano, S.; Zhang, Z. L.; Kaiser, U.; Wu, F. M.; Mao, H. K.; Jiang, J. Z. *New J. Phys.* **2008**, *10*.
(46) Dogra, S.; Sharma, N. D.; Singh, J.; Poswal, H. K.; Sharma, S. M.; Bandyopadhyay, A. K. *High Press. Res.* **2011**, *31* (2), 292–303.
(47) Gonzalez, E. J.; Hockey, B.; Piermarini, G. J. *Mater. Manuf. Process.* **1996**, *11* (6), 951–967.
(48) Miyoshi, S.; Akao, Y.; Kuwata, N.; Kawamura, J.; Oyama, Y.; Yagi, T.; Yamaguchi, S. *Solid State Ionics* **2012**, *207*, 21–28.
(49) Karak, S. K.; Dutta Majumdar, J.; Witczak, Z.; Lojkowski, W.; Ciupinski, L.; Kurzydlowski, K. J.; Manna, I. *Metall. Mater. Trans. A Phys. Metall. Mater. Sci.* **2013**, *44* (6), 2884–2894.
(50) Piot, L.; Le Floch, S.; Cornier, T.; Daniele, S.; Machon, D. *J. Phys. Chem. C* **2013**, *117* (21), 11133–11140.
(51) Bera, S.; Lojkowsky, W.; Manna, I. *Metall. Mater. Trans. A Phys. Metall. Mater. Sci.* **2009**, *40* (13), 3276–3283.
(52) Bera, S.; Ghosh Chowdhury, S.; Lojkowsky, W.; Manna, I. *Mater. Sci. Eng. A* **2012**, *558*, 298–308.
(53) Zhang, J.; Lu, T.; Chang, X.; Wei, N.; Xu, W. *J. Phys. D. Appl. Phys.* **2009**, *42* (5), 052002.
(54) Zhang, J.; Lu, T.; Chang, X.; Jiang, S.; Wei, N.; Qi, J. *Nanoscale Res. Lett.* **2010**, *5*, 1329–1332.
(55) Lu, T. C.; Chang, X. H.; Qi, J. Q.; Luo, X. J.; Wei, Q. M.; Zhu, S.; Sun, K.; Lian, J.; Wang, L. M. *Appl. Phys. Lett.* **2006**, *88* (21).

(56) Kumar, M.; Chandra, U.; Parthasarathy, G. *Mater. Lett.* **2006**, *60* (17-18), 2066–2068.
(57) Parthasarathy, G. *Mater. Lett.* **2007**, *61* (21), 4329–4331.
(58) Zhang, P. E.; Zhang, J. S.; Yao, L. D.; Li, F. Y.; Bao, Z. X.; Li, J. X.; Li, Y. C.; Liu, J.; Jin, C. Q.; Yu, R. C. *J. Mater. Sci.* **2006**, *41* (22), 7374–7379.
(59) Yao, L. D.; E, P.; Zhang, J. S.; Zhang, W.; Li, F. Y.; Jin, C. Q.; Yu, R. C. *Phys. B Condens. Matter* **2008**, *403* (13-16), 2241–2245.
(60) Santoro, M.; Gorelli, F. A.; Bini, R.; Haines, J.; Van der Lee, A. *Nat Commun* **2013**, *4*, 1557.
(61) Gao, J.; Xiao, H.; Du, H. *Scr. Mater.* **2001**, *45*, 1063–1068.
(62) Qiu, L. X.; Yao, B.; Ding, Z. H.; Zheng, Y. J.; Jia, X. P.; Zheng, W. T. *J. Alloys Compd.* **2008**, *456* (1-2), 436–440.
(63) Zhou, X.; Zang, J.; Dong, L.; Cheng, X.; Li, T.; Wang, Y.; Yuan, Y.; Lu, J.; Yu, Y.; Xu, X. *Mater. Lett.* **2015**, *144*, 69–73.
(64) Valiev, R. Z.; Estrin, Y.; Horita, Z.; Langdon, T. G.; Zehetbauer, M. J.; Zhu, Y. *J. Met.* **2016**, *58* (4), 33–39.
(65) Vafaei, R.; Toroghinejad, M. R.; Pippan, R. *Mater. Sci. Eng. A* **2012**, *536*, 73–81.
(66) Gonzalez, J.; Segura, A.; Ferrer-Roca, C.; Martinez-Garcia, D.; Jose, V. M.-S.; Power, C.; Chervin, J. C.; Hamel, G.; Snoeck, E. *High Press. Res.* **2002**, *22* (2), 271–275.
(67) Kobayashi, M.; Iwata, H.; Hanzawa, H.; Yoshiue, T.; Endo, S. *Phys. Status Solidi* **1996**, *198* (1), 515–520.
(68) Gonzalez, J.; Segura, A.; Ferrer-Roca, C.; Martinez-Garcia, D.; Jose, V. M.-S.; Power, C.; Chervin, J. C.; Hamel, G.; Snoeck, E. *High Press. Res.* **2003**, *23* (1-2 SPEC. ISS.), 29–33.
(69) González, J.; Marquina, J.; Rodríguez, F.; Valiente, R. *High Press. Res.* **2009**, *29* (4), 594–599.
(70) Oganov, A. R.; Solozhenko, V. L. *J. Superhard Mater.* **2009**, *31* (5), 285–291.
(71) Albert, B.; Hillebrecht, H. *Angew. Chem. Int. Ed.* **2009**, *48* (46), 8640–8668.
(72) Solozhenko, V. L.; Kurakevych, O. O.; Oganov, A. R. *J. Superhard Mater.* **2008**, *30* (6), 428–429.
(73) Oganov, A. R.; Chen, J.; Gatti, C.; Ma, Y.; Ma, Y.; Glass, C. W.; Liu, Z.; Yu, T.; Kurakevych, O. O.; Solozhenko, V. L. *Nature* **2009**, *457* (7231), 863–867.
(74) Oganov, A. R. *Boron Rich Solids*; Orlovskaya, N., Lugovy, M., Eds.; NATO Science for Peace and Security Series B: Physics and Biophysics; Springer Netherlands: Dordrecht, 2011.
(75) Oganov, A. R.; Solozhenko, V. L.; Gatti, C.; Kurakevych, O. O.; Godec, Y. *J. Superhard Mater.* **2011**, *33* (6), 363–379.
(76) Carenco, S.; Portehault, D.; Boissière, C.; Mézailles, N.; Sanchez, C. *Chem. Rev.* **2013**, *113* (10), 7981–8065.
(77) Laubengayer, A. W.; Hurd, D. T.; Newkirk, A. E.; Hoard, J. L. *J. Am. Chem. Soc.* **1943**, *65* (10), 1924–1931.
(78) Sands, D. E.; Hoard, J. L. *J. Am. Chem. Soc.* **1957**, *79* (20), 5582–5583.
(79) McCarty, L. V.; Kasper, J. S.; Horn, F. H.; Decker, B. F.; Newkirk, A. E. *J. Am. Chem. Soc.* **1958**, *80* (10), 2592–2592.
(80) Horn, F. H. *J. Electrochem. Soc.* **1959**, *106* (10), 905.
(81) Parakhonskiy, G.; Dubrovinskaia, N.; Dubrovinsky, L.; Mondal, S.; Van Smaalen, S. *J. Cryst. Growth* **2011**, *321* (1), 162–166.
(82) Terauchi, M.; Kawamata, Y.; Tanaka, M.; Takeda, M.; Kimura, K. *J. Solid State*

*Chem.* **1997**, *133* (1), 156–159.
(83) Talley, C. P.; La Placa, S.; Post, B.; IUCr. *Acta Crystallogr.* **1960**, *13* (3), 271–272.
(84) Ma, Y.; Prewitt, C. T.; Zou, G.; Mao, H.; Hemley, R. J. *Phys. Rev. B* **2003**, *67* (17), 174116.
(85) Wentorf, R. H. *Science* **1965**, *147* (3653), 49–50.
(86) Zarechnaya, E. Y.; Dubrovinsky, L.; Dubrovinskaia, N.; Filinchuk, Y.; Chernyshov, D.; Dmitriev, V.; Miyajima, N.; El Goresy, A.; Braun, H. F.; Van Smaalen, S.; Kantor, I.; Kantor, A.; Prakapenka, V.; Hanfland, M.; Mikhaylushkin, A. S.; Abrikosov, I. A.; Simak, S. I. *Phys. Rev. Lett.* **2009**, *102* (18), 8–11.
(87) Ekimov, E. A.; Zibrov, I. P.; Zoteev, A. V. *Inorg. Mater.* **2011**, *47* (11), 1194–1198.
(88) Parakhonskiya, G.; Dubrovinskaia, N.; Bykova, E.; Wirth, R.; Dubrovinsky, L. *High Press. Res* **2013**, *33* (3), 673–683.
(89) Hoard, J. L.; Sands, D. E.; Hughes, R. E. *J. Am. Chem. Soc.* **1958**, *80* (17), 4507–4515.
(90) Kurakevych, O. O.; Le Godec, Y.; Hammouda, T.; Goujon, C. *High Press. Res.* **2012**, *32* (1), 30–38.
(91) Qin, J.; Irifune, T.; Dekura, H.; Ohfuji, H.; Nishiyama, N.; Lei, L.; Shinmei, T. *Phys. Rev. B - Condens. Matter Mater. Phys.* **2012**, *85* (1), 2–5.
(92) Kurakevych, Oleksandr O, V. L. S. *J. Superhard Mater.* **2013**, *35* (1), 60–63.
(93) Eremets, M. I.; Struzhkin, V. V; Mao, H.; Hemley, R. J. *Science* **2001**, *293* (5528), 272–274.
(94) Sanz, D. N.; Loubeyre, P.; Mezouar, M. *Phys. Rev. Lett.* **2002**, *89* (24), 245501.
(95) Boustani, I. *Phys. Rev. B* **1997**, *55* (24), 16426–16438.
(96) Mannix, A. J.; Zhou, X.-F.; Kiraly, B.; Wood, J. D.; Alducin, D.; Myers, B. D.; Liu, X.; Fisher, B. L.; Santiago, U.; Guest, J. R.; Yacaman, M. J.; Ponce, A.; Oganov, A. R.; Hersam, M. C.; Guisinger, N. P. *Science* **2015**, *350* (6267), 1513–1516.
(97) Feng, B.; Zhang, J.; Zhong, Q.; Li, W.; Li, S.; Li, H.; Cheng, P.; Meng, S.; Chen, L.; Wu, K. *Nat. Chem.* **2016**, *8*, 563–568.
(98) Zhai, H.-J.; Zhao, Y.-F.; Li, W.-L.; Chen, Q.; Bai, H.; Hu, H.-S.; Piazza, Z. a; Tian, W.-J.; Lu, H.-G.; Wu, Y.-B.; Mu, Y.-W.; Wei, G.-F.; Liu, Z.-P.; Li, J.; Li, S.-D.; Wang, L.-S. *Nat. Chem.* **2014**, *6* (8), 727–731.
(99) Komatsu, S.; Moriyoshi, Y. *J. Cryst. Growth* **1990**, *102* (4), 899–907.
(100) Wang, X.; Tian, J.; Yang, T.; Bao, L.; Hui, C.; Liu, F.; Shen, C.; Gu, C.; Xu, N.; Gao, H. *Adv. Mater.* **2009**, *19* (24), 4480–4485.
(101) Wu, Y.; Messer, B.; Yang, P. *Adv. Mater.* **2001**, *13* (19), 1487–1489.
(102) Casey, J. D.; Haggerty, J. S. *J. Mater. Sci.* **1987**, *22* (2), 737–744.
(103) Cao, L. M.; Zhang, Z.; Sun, L. L.; Gao, C. X.; He, M.; Wang, Y. Q.; Li, Y. C.; Zhang, X. Y.; Li, G.; Zhang, J.; Wang, W. K. *Adv. Mater.* **2001**, *13* (22), 1701–1704.
(104) Zhang, Y.; Ago, H.; Yumura, M.; Komatsu, T.; Ohshima, S.; Uchida, K.; Iijima, S. *Chem. Commun.* **2002**, *354* (23), 2806–2807.
(105) Wang, Z.; Shimizu, Y.; Sasaki, T.; Kawaguchi, K.; Kimura, K.; Koshizaki, N. *Chem. Phys. Lett.* **2003**, *368* (5-6), 663–667.
(106) Meng, X. M.; Hu, J. Q.; Jiang, Y.; Lee, C. S.; Lee, S. T. *Chem. Phys. Lett.* **2003**, *370* (5-6), 825–828.

(107) Bellott, B. J.; Noh, W.; Nuzzo, R. G.; Girolami, G. S. *Chem. Commun.* **2009**, No. 22, 3214–3215.
(108) Pickering, A. L.; Mitterbauer, C.; Browning, N. D.; Kauzlarich, S. M.; Power, P. P. *Chem. Commun.* **2007**, No. 6, 580–582.
(109) Bai, H.; Dai, D.; Yu, J. H.; Nishimura, K.; Sasaoka, S.; Jiang, N. *Appl. Surf. Sci.* **2014**, *292*, 790–794.
(110) Ogitsu, T.; Schwegler, E.; Galli, G. *Chem. Rev.* **2013**, *113*, 3425–3449.
(111) Slack, G. A.; Hejna, C. I.; Garbauskas, M. F.; Kasper, J. S. *J. Solid State Chem.* **1988**, *76*, 52–63.
(112) Parakhonskiy, G.; Dubrovinskaia, N.; Bykova, E.; Wirth, R.; Dubrovinsky, L. *Sci Rep* **2011**, *1* (96), 1–7.
(113) White, M. A.; Cerqueira, A. B.; Whitman, C. A.; Johnson, M. B.; Ogitsu, T. *Angew. Chem. Int. Ed.* **2015**, *54* (12), 3626–3629.
(114) Oganov, a. R.; Solozhenko, V. L.; Gatti, C.; Kurakevych, O. O.; Godec, Y. *J. Superhard Mater.* **2011**, *33* (6), 363–379.
(115) Kurakevych, O. O.; Solozhenko, V. L. *J. Superhard Mater.* **2013**, *35* (1), 60–63.
(116) Bao, L.; Qi, X.; Tana, T.; Chao, L.; Tegus, O. *CrystEngComm* **2016**, *18* (7), 1223–1229.
(117) Portehault, D.; Devi, S.; Beaunier, P.; Gervais, C.; Giordano, C.; Sanchez, C.; Antonietti, M. *Angew. Chem. Int. Ed.* **2011**, *50* (14), 3262–3265.
(118) Terlan, B.; Levin, A. A.; Börrnert, F.; Zeisner, J.; Kataev, V.; Schmidt, M.; Eychmüller, A. *Eur. J. Inorg. Chem.* **2016**, *082910* (2005), 2003–2006.

# Chapter II: Synthesis of nanostructured precursors in molten salts

The synthesis in molten salts has been mentioned in the previous chapter as a synthetic pathway toward nanostructured metal borides. First developed by Portehault and co-workers,[1] it has been reported afterwards for diboride synthesis ($VB_2$, $TiB_2$) by Terlan and co-workers.[2,3] The processes do not differ in principle, though Terlan *et al.* used a different salt mixture as solvent and different crucibles. Lately, synthesis in molten salts (SMS) has been studied in the framework of G. Gouget's PhD thesis.[4,5] During this work, the range of metal borides reachable by SMS has been extended to $HfB_2$, NiB, CoB, $YB_4$ and $YB_6$, which also exhibit the smallest reported size for these crystals, along with the highest specific area reported.[5] The easy tuning of SMS also allowed for both size and stoichiometry control. SMS cannot be applied to borides too sensitive to a necessary washing step in water. Also, the borides are obtained as nano-inclusions in a 3-D amorphous matrix containing mostly boron, which cannot be avoided so far. This matrix has been reported as partially oxidised, oxidation occurring during the washing step. In the present work, a modified synthetic pathway toward two borides was developed ($CaB_6$, $HfB_2$), using a mixture of salts soluble in solvents less oxidising than water. The synthesis outcome is similar to previous works, apart for the particle size. Herein, control of the matrix oxidation is important as the SMS-derived borides are used as precursors toward matrix crystallisation.

During his PhD work, G. Gouget also developed a new nanostructured boron-based material: a nanostructured amorphous boron that was patented.[6] It consists in *ca.* 5 nm amorphous particles with boron content above 90 at%. Residual amounts of alkaline ions are also present. As discussed in this chapter, SMS requires a chemically inert crucible. So far, a glassy carbon was used. However, recent characterisations detailed below evidence the presence of small amounts of carbon in the material (*ca.* 1 at%). In this work, the possibility to use *h*-BN as crucible material has been assessed.

The material originally synthesised by Gouget is a unique boron source, notably un-oxidised and reactive (commercially available boron is either amorphous and oxidised or crystalline and inert up to high temperatures). In this work, nanostructured amorphous boron was used as a unique boron source toward HPHT-induced crystallisation.

## II-1- Experimental set-up

The SMS of metal borides relies on the use of reactive species of metal and boron in an inorganic salt mixture. Upon heating, the salt mixture is molten, therefore acting as a liquid medium. The typical synthesis of nanoscaled borides in molten salts involves a metal source (usually a chloride, $MCl_x$) and sodium borohydride. The latter is used both as boron source and as reductant, to obtain $M^0$ in the reaction medium. The use of such precursors and of lithium and potassium salts requires working under inert atmosphere, due to the sensitivity of the mentioned chemicals to water and/or oxygen. Therefore, the precursors are handled and mixed in a glovebox under

argon. The synthesis itself is conducted under argon and not nitrogen, as the latter could react with boron species and yield boron nitride.

The requirements for the experimental set-up developed in the lab are therefore the following:

- allowing keeping the reaction media under argon atmosphere: it is done by using a quartz tube stable at the working temperatures and connected to a Schlenk line.
- allowing heating in a 300 -1000 °C range. A vertical tubular oven is used. The zone in which the desired temperature is homogeneous in the quartz tube is about 5-8 cm wide: large enough to allow homogeneous heating of the reaction media and limited enough to allow condensation of salt vapours (saturating vapour pressure is non-negligible at the working temperatures), to avoid solvent loss along the reaction. The heating rate is 10 °C/min.
- avoiding side reactions between the reaction media and the quartz tube, as alkaline ions from the salts may intercalate in oxides structures. Besides, the intercalation of alkaline ions weakens quartz, which breaks after several experiments. Oxides may also react with elemental boron, leading to contamination. Boron is also likely to react with a metal crucible. Glassy carbon is chemically inert under argon and is therefore used as crucible. The crucible is long enough to allow condensation of salts vapours in the low-temperature zone of the furnace.
- in some cases, the reaction medium is to be stirred. This is achieved using a rotating glassy carbon rod.

The set-up is displayed in Figure II-1. After the reaction, the reaction medium is let to cool down naturally. Metal borides are obtained as nanoparticles dispersed in a frozen salt bulk (Figure II-2). To remove the salts, washing/centrifugation cycles in a polar solvent (*e.g.* water or methanol) are performed, upon which a usually black powder is recovered. Among the tuneable parameters, one can distinguish the synthesis temperature, the dwell time and the initial ratio between metal and boron sources.

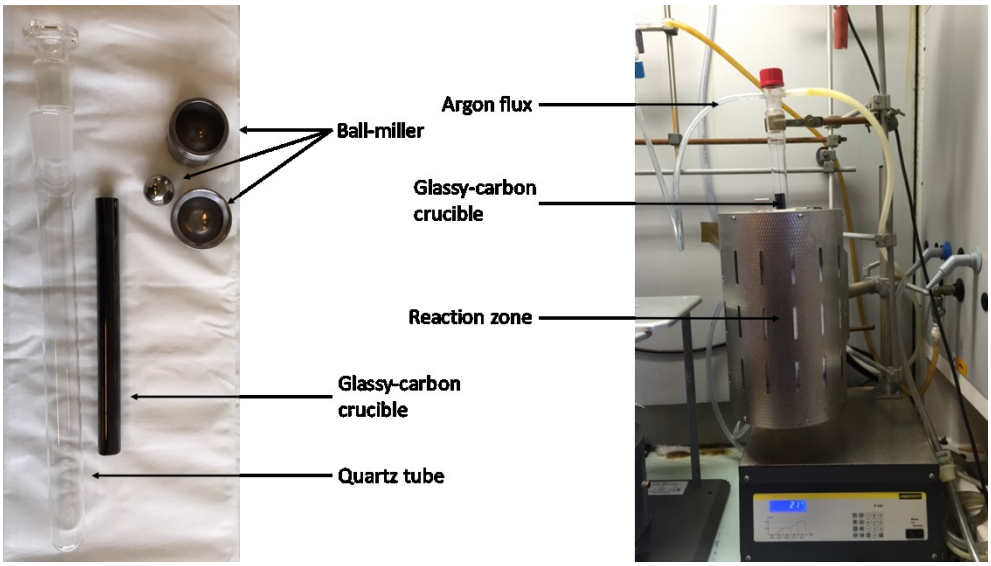


**Figure II-1. Pictures of the experimental set-up for synthesis in molten salts. The glassy carbon crucible is about 15 cm long.**

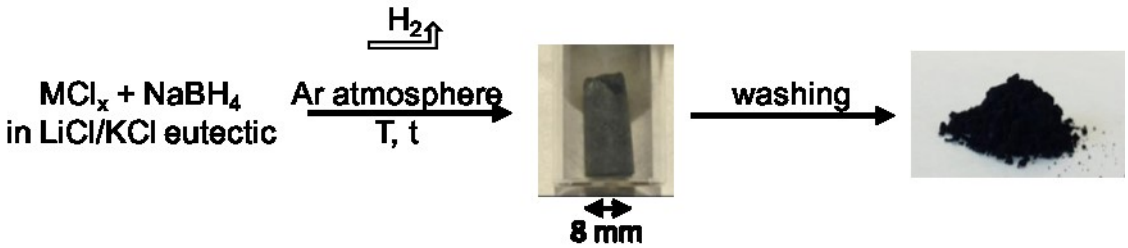


**Figure II-2. Pathway for SMS of metal borides: the heating and cooling steps yield a dispersion of black particles in a frozen eutectic salt mixture block. Washing yields a usually black, salt-free, powder.**

This PhD work has been focusing on two nanostructured metal borides: hafnium diboride and calcium hexaboride. $HfB_2$ and SMS-derived $HfB_2$ nanocomposites have already been investigated in the framework of thermoelectric materials.[4] $CaB_6$ and $HfB_2$ have no known phase transition under high pressure-high temperature and are therefore well suited for studies of the crystallisation of the amorphous phase embedding the boride particles, briefly mentioned in the previous chapter and detailed latter in the present chapter.

In this work, two salt mixtures have been used, namely the eutectic mixtures of LiCl/KCl or LiI/KI. Table II-1 summarises the densities measured at melting points and gives an order of magnitude of the volume of the reaction media, for the quantity of salts used in a standard synthesis.

**Table II-1. Density and volume of LiCl/KCl and LiI/KI eutectic mixtures used for SMS synthesis of metal borides.**[7–9]

| | Density Formula | Density at $T_{melt}$ | Volume at $T_{melt}$ |
|---|---|---|---|
| LiCl/KCl eutectic | 2.0286-5.2676E-4*T | 1.70 (at 353 °C) | 1.47 mL (for 2.5 g) |
| LiI/KI eutectic | 3.35-9.863E-4*T | 2.80 (at 285 °C) | 1.79 mL (for 5.0 g) |

## II-2- Molten salts colloidal synthesis

### II-2-1- Hafnium diboride

II-2-1-a- Synthesis in LiCl/KCl

The first syntheses of $HfB_2$ were conducted in the LiCl/KCl (45/55 wt%) eutectic mixture, for which the melting point is about 350 °C. $HfCl_4$ and $NaBH_4$ are used in a Hf:B = 1:4 molar ratio and mixed with the salt mixture. Upon heating at 900 °C for 4 h, cooling, washing with deionised water and drying under vacuum (see the appendices for experimental details), a black powder is recovered. The corresponding powder XRD pattern shows $HfB_2$ as the only crystalline phase (Figure II-3) and exhibits no reflexions corresponding nor to the solvent salts nor sodium chloride which may occur as a side product of the boride formation. Figure II-3 also shows the $HfB_2$ structure, typical of diborides, where the metal atoms are intercalated between honeycomb boron sheets.

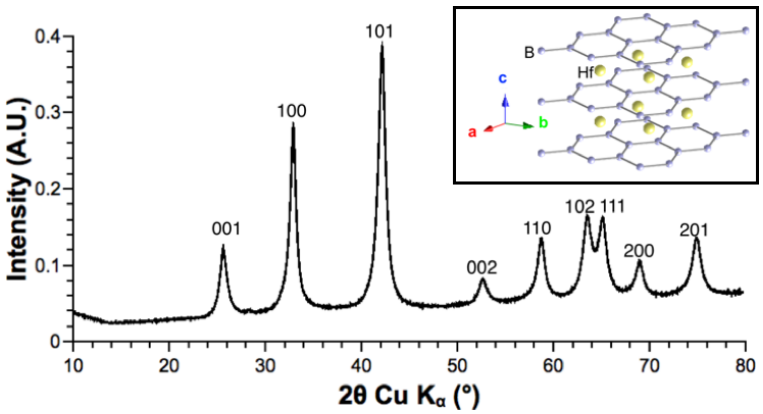


**Figure II-3. Powder XRD pattern of SMS-derived $HfB_2$ (with a 1:4 Hf:B ratio), exhibiting $HfB_2$ as the sole crystalline phase. Inset: $HfB_2$ structure. Hafnium atoms are intercalated between honeycomb boron sheets.**

According to the Scherrer formula, the particle size is 7.5(6) nm. This is confirmed by TEM (Figure II-4) and the resulting size distribution histogram (Figure II-8) showing particle sizes in the 5–12 nm range. SAED patterns and FFT of HRTEM images (Figure II-4) confirm that $HfB_2$ is the sole crystalline phase in the material and that only the nanoparticles are crystalline.

TEM also shows that the particles are surrounded by a low-contrasting, amorphous, 2–4 nm thick shell (Figure II-4b). Although observations at the aggregates' edge (Figure II-4b) call for a core-shell designation, the overall system is better described as a "nano-cookie": the particles are inclusions inside a three-dimensional amorphous matrix. Gaps between the particles are filled with a 2-4 nm thick amorphous matrix. Therefore, the matrix is also nanostructured and the material can be described as a nanocomposite.

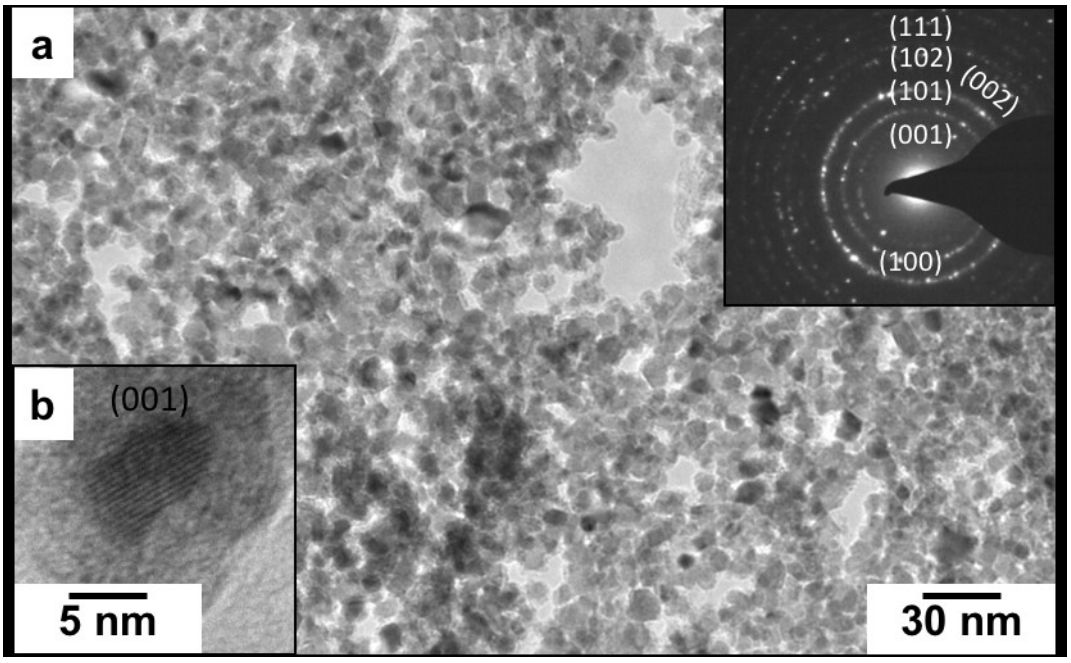


**Figure II-4. (a) TEM and (b): HRTEM images of $HfB_2$ nanocrystals, 1:4 Hf:B initial ratio. The boride is obtained as sub-10 nm crystalline particles embedded in an amorphous matrix. Inset of (a): corresponding SAED pattern indexed along the $HfB_2$ structure.**

Elemental analyses previously conducted either by SEM-EDX or ICP-OES show a similar Hf:B ratio of *ca.* 0.3, attributing the boron content exceeding the $HfB_2$ stoichiometry to the amorphous phase. Previous works on SMS-derived and similarly nanostructured metal borides (Nb- or Ca-based) showed that the matrix is composed of partially oxidised boron (based on FTIR and solid-state NMR spectroscopies).[1] Due to its high Z, hafnium displays a high TEM contrast *versus* boron which, in the first place, calls for the absence of metal in the amorphous matrix. Previous STEM-HAADF (more sensitive to Z differences) observations on cobalt boride CoB (synthesised by a similar process),[4] revealed however the presence of cobalt clusters in the amorphous phase (size inferior to 1 nm), while similar analyses ruled out the presence of metal in the matrix for NiB. In our work the hafnium-based nanocomposite has been studied with STEM-HAADF, in the framework of a collaboration with the Institut de Physique et Chimie des Matériaux de Strasbourg. The comparison of bright and dark field observations (Figure II-5) show that the presence of hafnium in the matrix around the crystalline particles is likely, as small (1-3 nm) clusters. At it is discussed later on, washing with water leads to partial oxidation of the boron matrix, though the oxidation state of the metal clusters has not been investigated yet.

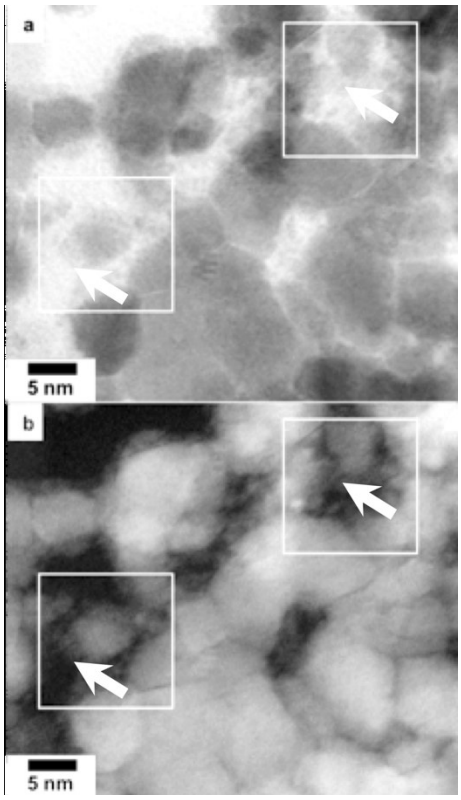


**Figure II-5. STEM (a) and STEM-dark field (b) observations of a $HfB_2$/B nanocomposite, 1:4 Hf:B initial ratio.**

The partially oxidised state of boron in the matrix has been also confirmed by XPS in the B1s energy region (Figure II-6), which shows four different environments for boron: $B^{(0)}$, $B^{(I)}$, $B^{(III)}$ and a signal corresponding to boron atoms in $HfB_2$. The oxidation is likely to occur during the washing steps in deionised water, as all previous synthetic steps are performed under strict exclusion of oxygen. However, XPS clearly indicates the presence of non–oxidised boron, meaning that only the outer surface of the matrix is oxidised.

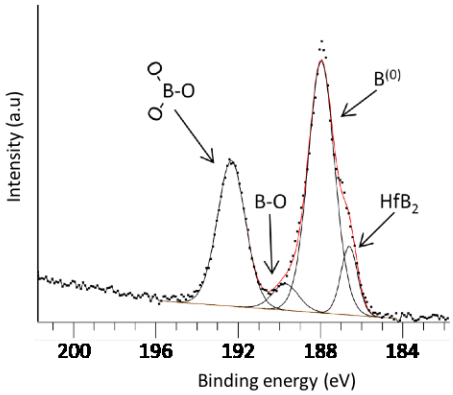


**Figure II-6. XPS spectra of SMS-derived $HfB_2$ (1:4 Hf:B initial ratio). The dotted line is the experimental signal, black curves show the deconvolution into four chemical environments, the red curve is the sum of these four contributions.**[4]

$HfB_2$ is a very representative example of the versatility offered by the molten salts synthetic pathway, as illustrated by size tuning. Indeed, the particle size can be

easily adjusted by changing the initial Hf:B ratio, as illustrated in Figure II-7 and Figure II-8.

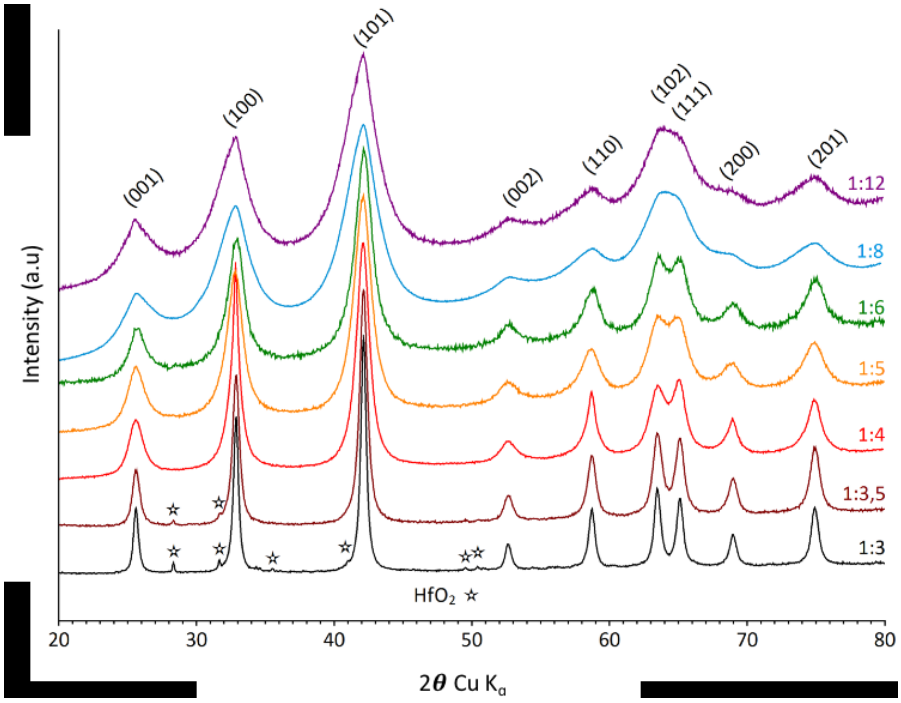


**Figure II-7. Powder XRD patterns of SMS-derived $HfB_2$, according to the initial Hf:B ratio. For ratios inferior to 1:4, only $HfB_2$ reflections are present.**[4]

The increasing width of XRD peaks shows that the particle size decreases with the Hf:B initial ratio increasing. This result is confirmed by the particle size distribution histograms obtained by TEM. As the Hf:B ratio decreases, the average particle size decreases, while the size distribution is sharpened. Moreover, XRD shows that for ratios superior to 1:4, $HfO_2$ is present as a side product, while the thickness of the amorphous matrix does not change significantly (Figure II-8). Hence, the presence of the matrix cannot be avoided, even by decreasing the Hf:B initial ratio. The size variation as a function of the initial Hf:B ratio is interpreted as a competition between nucleation and growth of the boride nanoparticles: as the concentration of boron precursor increases, the nucleation rate of the nanocrystals increases, thus yielding smaller particles.

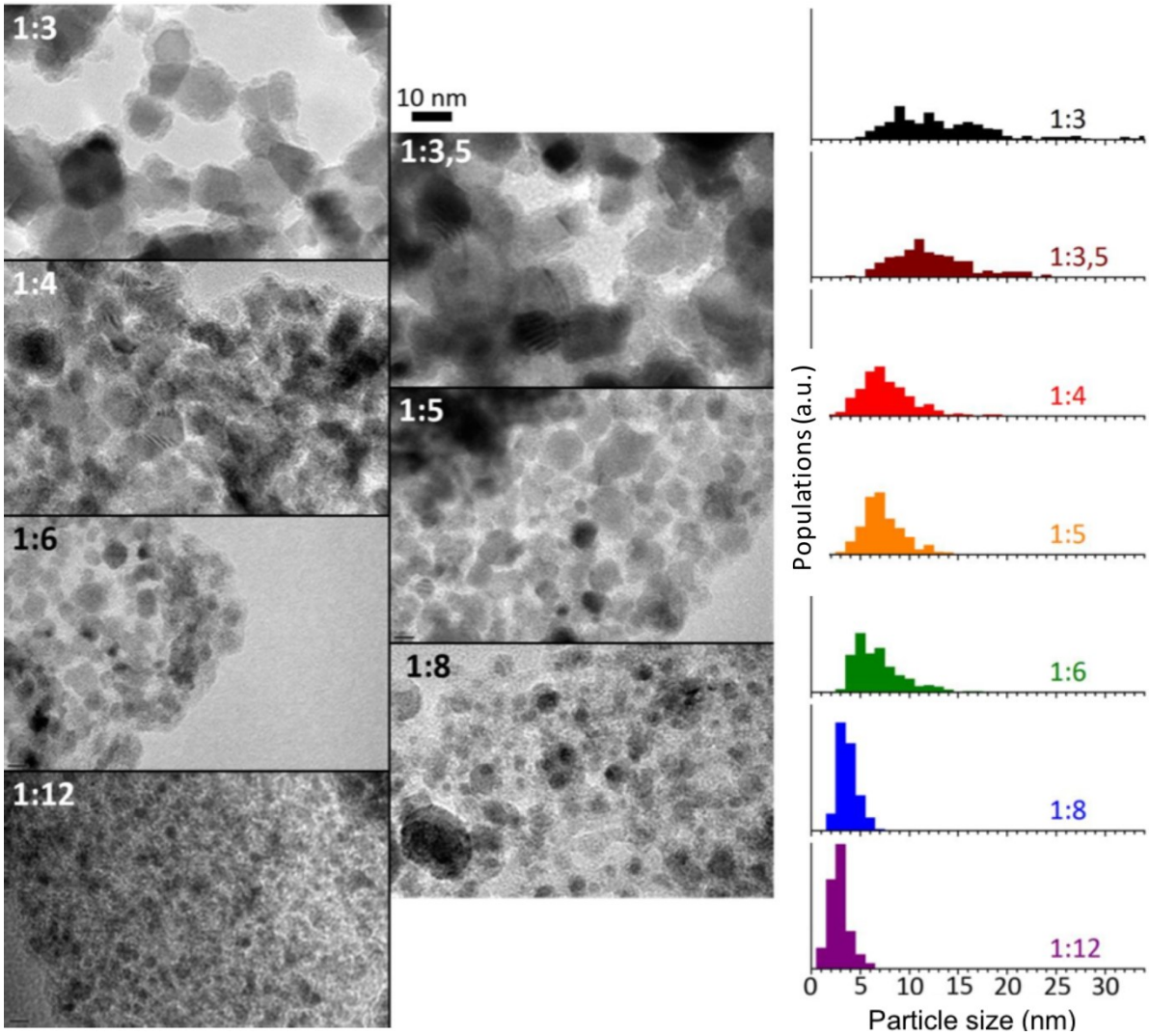


**Figure II-8. (a) TEM micrographs of SMS-derived $HfB_2$ as a function of the initial Hf:B ratio. (b) Size distribution histograms, according to the initial Hf:B ratio.**[4]

### II-2-1-b- Synthesis in LiI/KI

As discussed earlier, the amorphous boron matrix embedding the particles is partially oxidised. The oxidation likely occurs during the washing step, it could be limited by changing the washing solvent (methanol for instance). However, both components of the eutectic mixture LiCl/KCl are poorly soluble in methanol. Therefore, to avoid oxidation of the amorphous boron shell, the synthesis of $HfB_2$ was conducted in the eutectic mixture of iodine salts LiI/KI (58/42, wt%), which exhibits significant solubility in methanol. This eutectic mixture has a lower melting point than the LiCl/KCl eutectic mixture (285 °C *vs.* 353 °C). Temperature and time are kept identical and equal to 900 °C and 4 h, respectively. After four washing/centrifugation steps in methanol, the resulting black powder is dried under vacuum and then transferred to an argon-filled glovebox. The XRD pattern of the as-synthesised $HfB_2$ is shown in Figure II-9. In these conditions, $HfB_2$ is also the sole crystalline phase obtained, though the peak width indicates smaller particles, (4.4(5) nm *vs.* 7.5(6) nm, according to the Scherrer's formula).

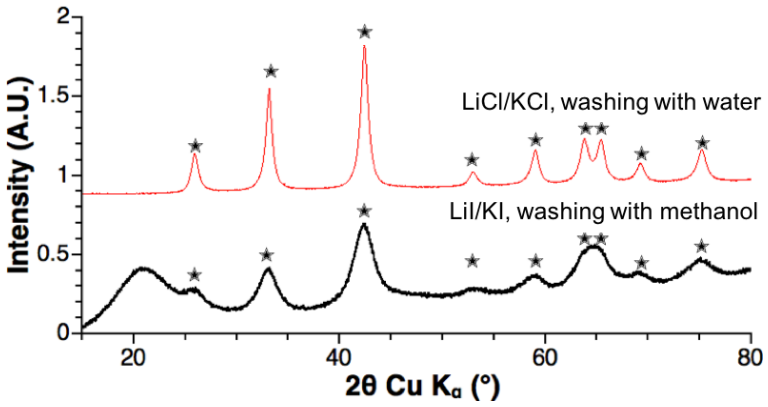


**Figure II-9. Powder XRD patterns of $HfB_2$ powders for two different molten salts and washing solvents. Black curve: 1:4 Hf:B initial ratio synthesis in LiI/KI, washed with methanol (the broad peak around 20 ° is due to the diffusion of the sample holder's plastic dome, allowing measurements under inert atmosphere). Red curve: 1:4 Hf:B synthesis in LiCl/KCl, washed with water. $HfB_2$ reflections are indexed with black stars.**

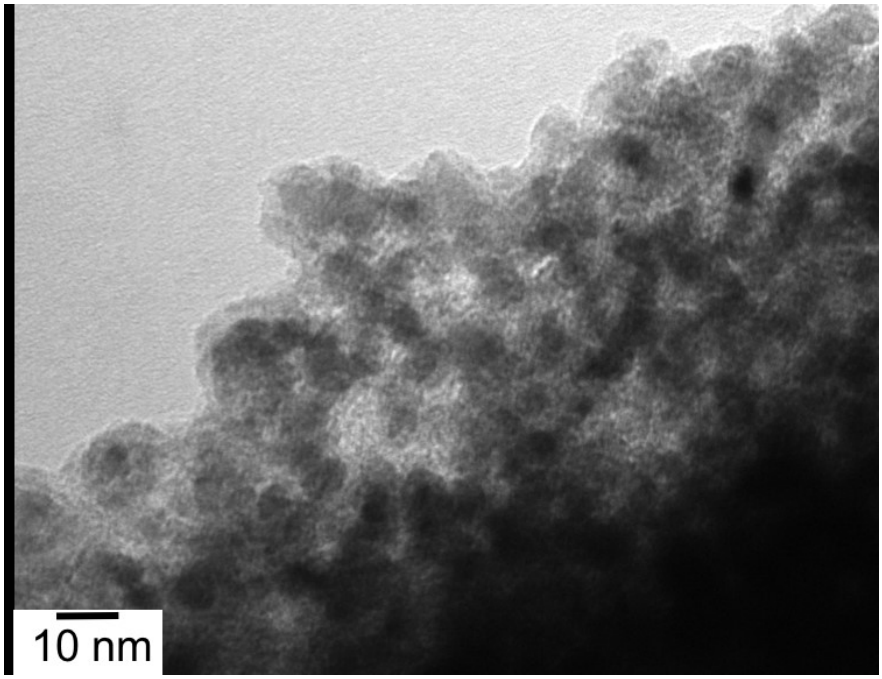


**Figure II-10. TEM micrograph of $HfB_2$ synthesised in iodide salts.**

According to TEM, the average particle size is 5 nm, in agreement with XRD. HRTEM (not shown) confirms that the particles possess the $HfB_2$ structure and that they are the only crystals present in the sample. Noteworthy, the particles obtained in molten iodides are smaller than in chlorides, with no clear explanation so far (concentrations are very close, the counter-ion may play a yet to be explained role in the mechanism). For the two molten salts and two washing solvents investigated, the overall "nano-cookie" structure is conserved.

The use of methanol as washing solvent is done to limit oxidation of the amorphous boron matrix. However, the salts are less soluble in methanol than in

water (see Table II-2 for solubility data), which may impact the final composition. Comparison of elemental analyses by SEM-EDS is shown in

Table II-3. Washing with methanol leads to residual quantities of potassium in the final material, though quantitative analysis is made difficult by the vicinity between the K-lines of boron and potassium. The possible presence of lithium cannot be investigated with EDS. The absence of oxidation has been confirmed on a metal-free boron material synthesised in conditions similar to those used for the metal borides, as detailed latter in section II-2-3.

**Table II-2. LiI and KI solubility in water and methanol (g/1000 g).**

| | LiI | KI |
|---|---|---|
| Methanol | 1710 | 160 |
| Water | 2000 | 1430 |

**Table II-3. Elemental analysis comparison for $HfB_2$/B nanocomposite, according to the synthesis and washing solvents.**

| | B (at%) | Hf (at%) | K (at%) |
|---|---|---|---|
| Washing with methanol | 65 | 13 | 0.8 |
| Washing with water | 63 | 21 | - |

All in all, both $HfB_2$-based materials exhibit similar particle size and thickness of the amorphous shell. The STEM-HAADF analyses indicate that the matrix comprises amorphous boron and hafnium clusters. Washing with water leads to partial oxidation of the matrix. Note that in cases where oxidation is not prohibited, then water washing is preferred, as it enables to reach higher purity in respect to alkaline traces. In the next chapters, both materials are used as precursors for HPHT transformations aiming at the crystallisation of the matrix.

## II-2-2- Calcium hexaboride

A second metal-based system, $CaB_6$, has been synthesised by the SMS method. In this case also, the synthesis relies on the reaction between the metal chloride ($CaCl_2$) and sodium borohydride. As for the previous system, the initial Ca:B ratio is based on the targeted stoichiometry, plus two equivalents of excess sodium borohydride (1:8 in this case).

### II-2-2-a- Synthesis in LiCl/KCl

As for $HfB_2$, the first syntheses have been conducted in the LiCl/KCl eutectic mixture.[1] During this PhD work, $CaB_6$ was synthesised from a 1:8 ratio. The XRD pattern (Figure II-11) shows that $CaB_6$ is the only crystalline phase in the final material. According to the Scherrer formula, the particle size is 12-15 nm.

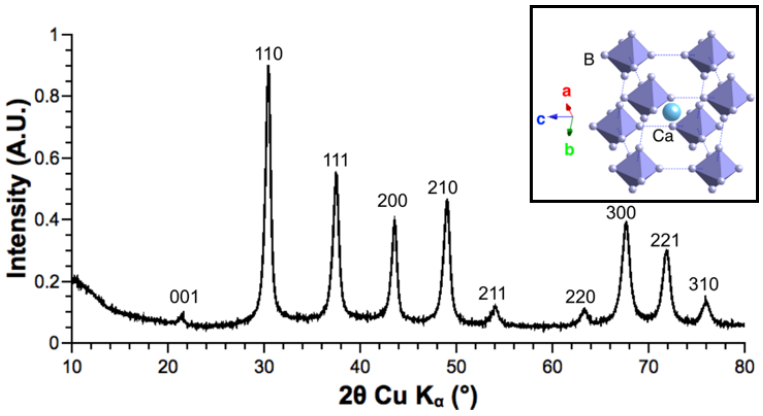


**Figure II-11. Powder XRD pattern of SMS-derived $CaB_6$, with initial Ca:B ratio of 1:8. Inset: structure of $CaB_6$: the body-centred lattice consists in boron octahedra at the vertexes and a calcium atom in the centre.**

It is difficult to perform a representative particle size analysis by TEM as the particles exhibit a low contrast *versus* the amorphous matrix due to the low atomic number of calcium. HRTEM analysis highlights the nanocrystals and confirms the "nano-cookie" structure (see Figure II-12). The particles exhibit the $CaB_6$ structure and are the only crystalline part of the sample. As mentioned in previous studies and for the hafnium-based system, the matrix embedding the particles is made of both elemental and partially oxidised boron and may comprise metal clusters, though in the case of calcium these clusters cannot be evidenced (due to the small Z difference with boron). As previously, the oxidation is likely to occur during the washing steps in water.

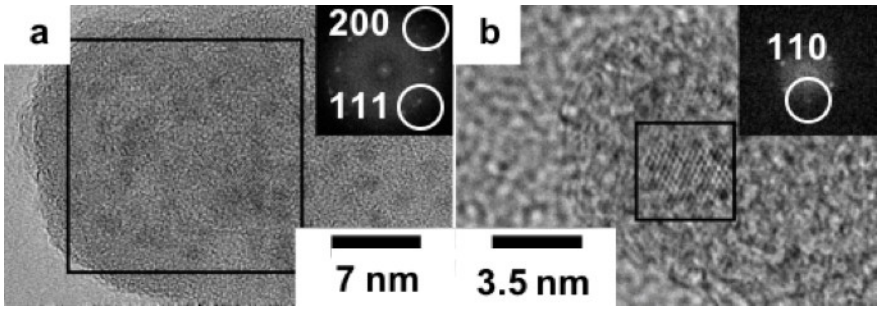


**Figure II-12. HRTEM micrographs of SMS-synthesised $CaB_6$ with initial Ca:B = 1:8. Insets: FFTs of the squared areas.**

II-2-2-b- Synthesis in LiI/KI

As for hafnium boride, using water-washed precursors for HPHT treatments may lead to crystallisation of oxidised species in the matrix, as it will be described later in chapter III. Therefore, $CaB_6$ has also been prepared in the LiI/KI eutectic mixture. The results are similar to the $HfB_2$ system discussed previously. The powder XRD pattern (Figure II-13) shows that $CaB_6$ is also the sole crystalline phase and that using LiI/KI as solvent results in smaller particles (9-11 nm according to the Scherrer formula).

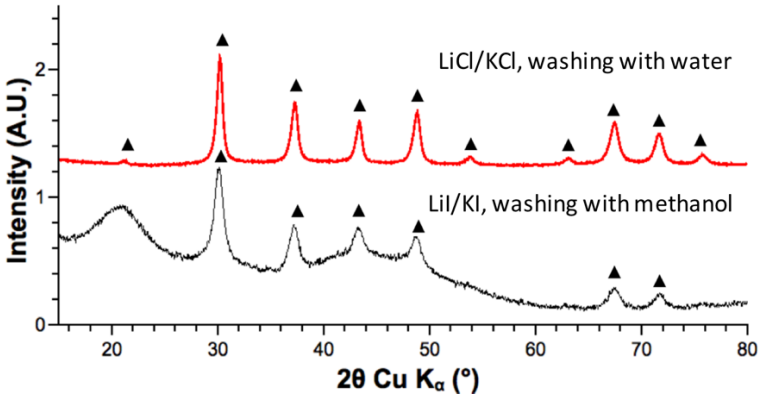


**Figure II-13. Powder XRD patterns of $CaB_6$ samples. Black curve: 1:8 Ca:B initial ratio synthesis in LiI/KI washed with methanol (the broad peak around 20 ° is due to the diffusion of the sample holder's plastic dome, allowing measurements under inert atmosphere). Red curve: 1:8 Ca:B initial ratio synthesis in LiCl/KCl, washed with water. $CaB_6$ reflections are indicated with ▲.**

TEM micrographs also show results similar to those obtained in LiCl/KCl (Figure II-14). Again, due to the contrast issue, reliable observations of particle sizes and therefore size distribution measurements are difficult to perform. The elemental analysis performed by SEM-EDS indicates a small amount of potassium for the syntheses in LiI/KI but not for syntheses conducted in LiCl/KCl (Table II-4), in agreement with the results on the $HfB_2$ system. In the case of $CaB_6$, traces of iodine (< 0.2 at%) are also detected and may be responsible for the change of colour observed: from black in the chlorides to brown in the iodides. The two $CaB_6$-based samples are also used as precursors for HPHT treatment aiming at the crystallisation of the matrix.

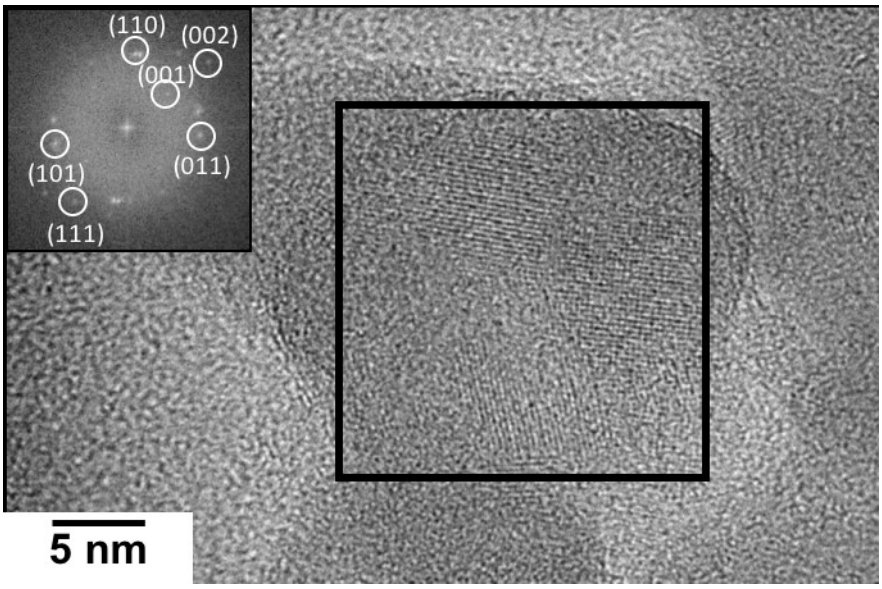


**Figure II-14. HRTEM micrograph of $CaB_6$ with initial Ca:B = 1:8, synthesised in LiI/KI and washed with methanol. Inset: FFT of the area in black square: the spots are indexed along the $CaB_6$ structure.**

**Table II-4. Elemental analysis comparison for $CaB_6$/B nanocomposite, according to the synthesis and washing solvents.**

| | B (at%) | Ca (at%) | K (at%) |
|---|---|---|---|
| Washing with methanol | 90.4 | 8.7 | 0.9 |
| Washing with water | 90.8 | 9.2 | - |

To summarise, two main metal-containing systems have been synthesised: $HfB_2$/B and $CaB_6$/B nanocomposites. Both systems consist in an intimate mixture at the nanoscale: an amorphous boron-based matrix embedding nano-inclusions of crystalline boride particles. Synthesis in molten salts (SMS) of metal borides reaches the smallest crystallite size reported for these materials. As discussed above, this method can easily be tuned to allow size control. The synthetic pathway has been successfully transferred to a different solvent that is based on iodide salts soluble in non-oxidising solvents. The resulting samples are oxygen-free but contain small residual amounts of potassium (and iodine in some cases). SMS was also extended to produce a new boron-based nanomaterial:[4,6] nanostructured amorphous boron, which is the focus of the next part.

## II-2-3- Nanostructured amorphous boron: nano Bam

The colloidal synthesis of metal borides relies on the reaction between a metal chloride and sodium borohydride. The process patented by G. Gouget and co-workers[4] uses the same experimental set-up, except for the metal chloride: the reaction consists in the decomposition of sodium borohydride in salt melts. $NaBH_4$ is synthesised in the LiI/KI eutectic mixture, heated at 800 °C with a 10 °C/min heating rate and a 1 h dwell time. The washing steps are performed in methanol, after which the powder is dried under vacuum at 60 °C for 2 h. After drying, the powder is

transferred to an argon-filled glovebox to avoid contact with air. Characterisations such as XRD and NMR spectroscopy are conducted with very limited exposure to air. The powder XRD pattern (Figure II-15) shows that the material is amorphous. Commercial amorphous boron is a brown powder, while the SMS-derived material is black (Figure II-16).

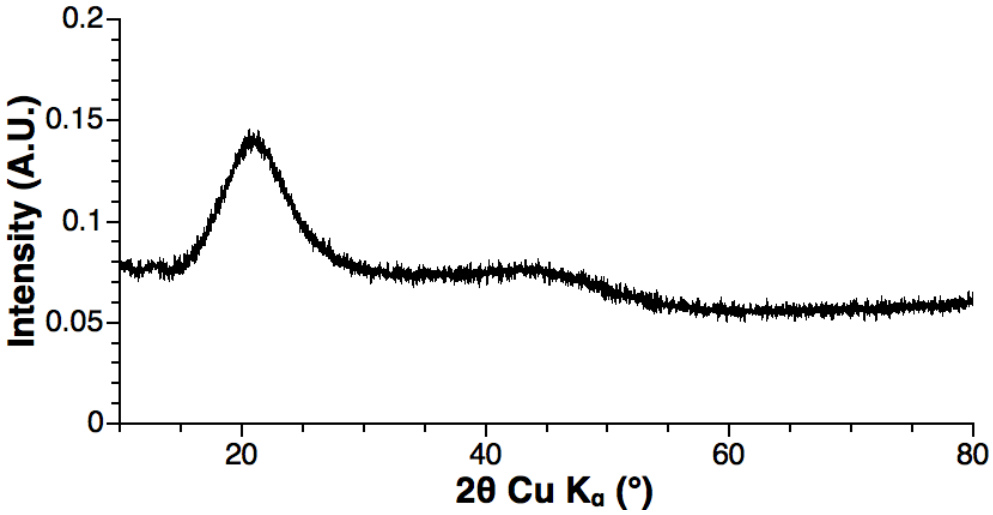


**Figure II-15. Powder XRD pattern of SMS-derived boron, showing an amorphous material. The broad signal around 20 ° is due to X-Ray diffusion by the protective dome keeping the powder under inert atmosphere.**

**Figure II-16. Left: SMS-derived amorphous boron, kept under argon atmosphere. Right: commercial amorphous boron from ABCR. Containers have a 1 cm diameter.**

The nanoscale morphology is observed by TEM. To avoid oxidation, the carbon-coated copper grid is directly dipped into the powder within the glovebox, to avoid contact with a solvent and air. The sample holder is sealed under argon atmosphere, limiting the contact with air to the transfer between an argon-sealed bag and the microscope. The observations (Figure II-17) show aggregates of *ca.* 5 nm particles. The size distribution diagram is shown in Figure II-18.

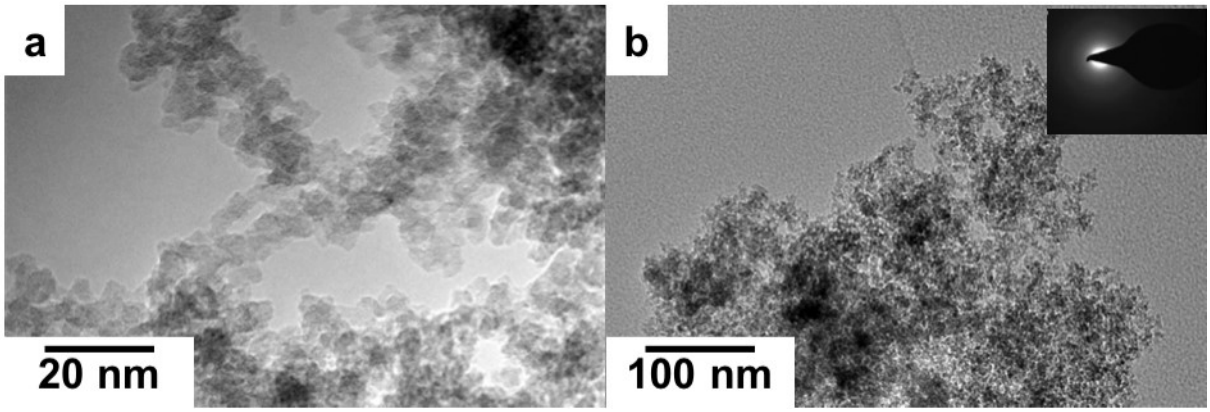


**Figure II-17. TEM micrographs of SMS-derived boron, consisting in aggregated 5 nm particles. Inset of b: SAED pattern, confirming that the material is amorphous.**

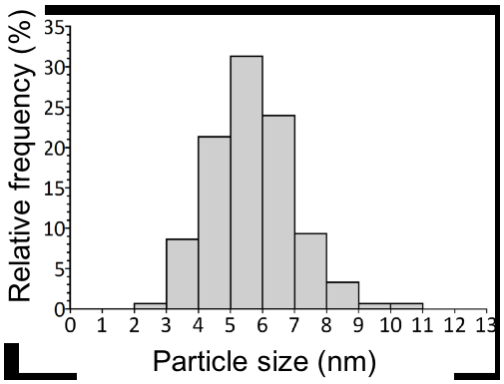


**Figure II-18. Size distribution diagram of SMS-derived amorphous boron. The statistics have been established on 150 particles.**[4]

Elemental analysis by SEM-EDS (Table II-5) shows that the material is mainly composed of boron, with a small amount of potassium, and residual amounts of sodium and iodine. The technique does not allow to quantify oxygen and carbon, as these species are always present as contaminations.

**Table II-5. SEM-EDS elemental analysis of SMS-derived boron.**

| | B (at%) | K (at%) | Na (at%) | I (at%) |
|---|---|---|---|---|
| SMS-derived B | 94.2 | 4.8 | < 0.8 | < 0.5 |

To assess the potential presence of oxygen, $^{11}B$ solid state MAS NMR spectroscopy is well suited. Indeed, the high affinity of boron for oxygen suggests that in the presence of oxygen-bearing species, B-O bonds may form readily. Note that unless otherwise stated, all the spectra shown in the manuscript were recorded on a spectrometer with a 16.3 T superconducting magnet. The spectra shown in Figure II-19 allow comparison between an oxidised form of boron, $LiBO_2,2H_2O$ (which contains both $BO_3$ and $BO_4$ units), commercial amorphous B (consisting of 1 to 2 µm particles) and nanostructured amorphous B (nano-$B_{am}$). Kept under argon and then exposed to air. The signal broadness of amorphous species is attributed to the multiplicity of boron chemical environments. Commercial amorphous B exhibits a

broad peak centred at 5 ppm, with a likely $BO_4$ contribution. When exposed to air for a few hours, nanostructured nano-$B_{am}$ shows thin peaks clearly indicating that boron has been oxidised. This calls for reactivity toward oxygen much higher than that of commercial amorphous B. When exposure to air is avoided, the peaks characteristic of B-O type environments disappear. Nano-$B_{am}$ can therefore be considered as non-oxidised.

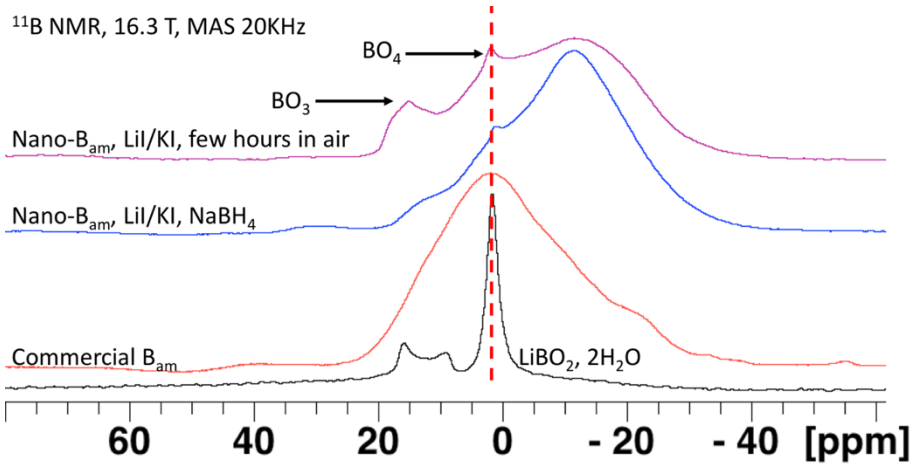


**Figure II-19. $^{11}$B solid state NMR spectra of boron samples, compared to $LiBO_2$, $2H_2O$ (black line). The red line corresponds to commercial amorphous boron from ABCR, the blue line to SMS-derived amorphous boron kept under inert atmosphere, the purple line to SMS-derived amorphous boron exposed a few hours to air.**[4]

NMR spectroscopy also shows that the chemical shift of nano-$B_{am}$ is shifted to negative values with the maximum intensity reached at -15 ppm, when compared to commercial amorphous B with maximum at 5 ppm. Consequently, the chemical environments of boron differ between these two occurrences of amorphous boron. As discussed later, the local structure of nano-$B_{am}$ is still under study. The $^{11}$B NMR spectrum of β-B has been recently studied by Turner *et al.* and show a single peak at 0 ppm (Figure II-20), pointing out the unusual boron environment in nano-$B_{am}$.

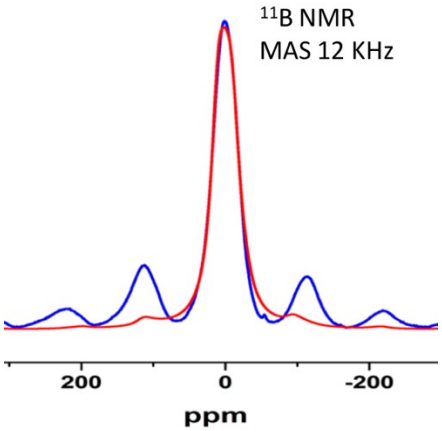


**Figure II-20. $^{11}$B solid state NMR spectrum of β-B, measured by Turner *et al.* at 7.0 T, showing a single peak centred at 0 ppm. The blue line corresponds to the experimental signal, the red line to simulated signal.**[10]

At this stage, potential carbon contamination cannot be ruled out, as carbon-containing species from the atmosphere or methanol molecules from the washing

step may adsorb at the surface of the boron particles. Carbon may also be incorporated during the synthesis from the glassy carbon crucible. To test the influence of the crucible, a similar synthesis was conducted in a high purity (AX5 grade) *h*-BN crucible. To limit the carbon contamination, the crucible was treated at 1000 °C for 1 h prior to transfer in an argon-filled glovebox where the eutectic mixture of salts and sodium borohydride were added. XRD and TEM results are similar to those obtained in glassy carbon. Elemental analysis of carbon, nitrogen and hydrogen (quantified according to the gas released conductivity after combustion) results are shown in Table II-6. With an error around 0.3 wt%, the results suggest that when the synthesis is performed in a glassy carbon crucible, small amounts of carbon (*ca.* 2 wt%, *ca.* 1 at%) are incorporated into amorphous boron. The slight amounts of carbon detected from the *h*-BN crucible are presumably due to contamination from the atmosphere during transfer of the powder to the CHN analyser, or to residual adsorbed methanol from the washing step. The comparison of the $^{11}$B NMR spectrum (Figure II-21) shows that nano-$B_{am}$ synthesised in *h*-BN has a signal similar to that of nano-$B_{am}$ synthesised in glassy-carbon but shifted: the maximum intensity is reached around 5 ppm, as for commercial amorphous B. The difference in chemical shifts between the two nano-$B_{am}$ samples is interpreted as a consequence of the carbon content introduced when the synthesis is performed in glassy carbon, which would therefore be integrated in the structure rather than simply adsorbed.

**Table II-6. CHN elemental analysis: comparison of synthesis in glassy carbon or *h*-BN.**

| | C (wt%) | H (wt%) |
|---|---|---|
| Glassy carbon | 2.7 | 4 |
| *h*-BN | 1.0 | 2.3 |

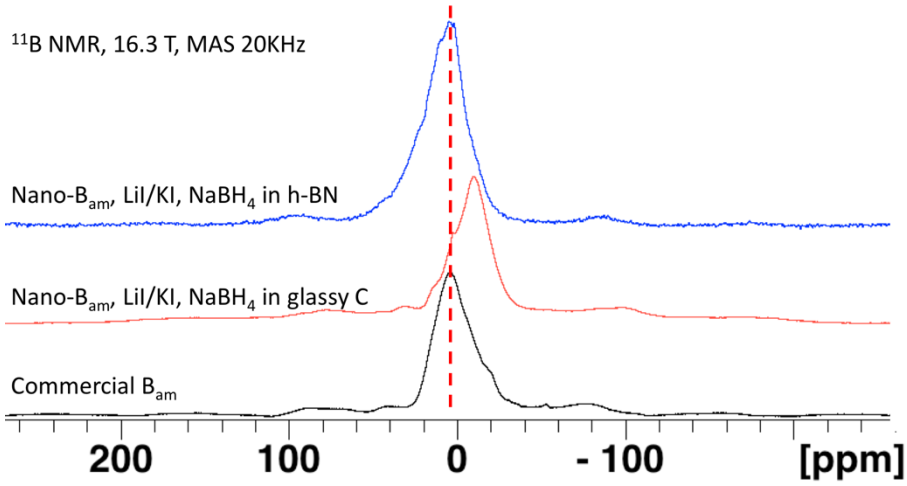


**Figure II-21. $^{11}$B solid state NMR spectra of nanostructured amorphous boron powders, for two different synthesis crucibles: *h*-BN and glassy carbon. Commercial amorphous B is plotted as a reference.**

As discussed in the first chapter, boron is extremely sensitive to carbon impurities. The slight amounts of carbon may strongly impact crystallisation processes described in chapter V.

Similarly, the alkali content may impact crystallisation under HPHT conditions. As potassium salts are the less soluble in organic solvents and then the most important impurities, MS syntheses have been conducted by using more soluble lithium salts instead of $K^+$ salts. The starting material was lithium borohydride and the eutectic mixture LiI/LiCl (85/15 wt%) was used as solvent. The reaction and methanol washing conditions were identical to those described previously. $^{11}$B NMR does not show significant difference between samples obtained in different solvents (Figure II-22), while TEM indicates the usual nanostructure described above (Figure II-23). Elemental analysis by ICP-OES, sensitive to lithium, is shown in Table II-7. Again, no difference is observed with other SMS-derived amorphous boron samples. The presence of sodium is due to the initial commercial $LiBH_4$ fabricated from $NaBH_4$ and that is not available with purity superior to *ca.* 95 %. Elemental analysis shows that the presence of alkaline ions cannot be totally avoided. Syntheses in NaI starting from $NaBH_4$ (not shown) confirm this result.

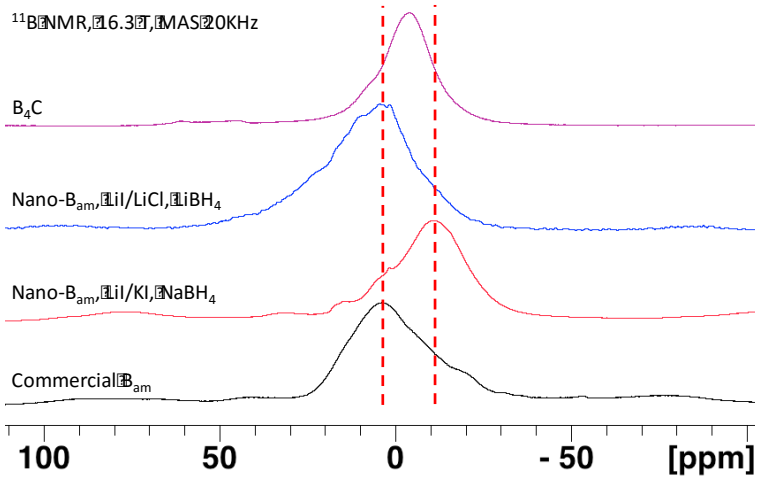


**Figure II-22. $^{11}B$ solid state NMR of $B_4C$ (purple line), nano-$B_{am}$, synthesised from $LiBH_4$ in LiI/LiCl in a glassy carbon crucible (blue line), synthesised from $NaBH_4$ in LiI/KI in a glassy carbon crucible (red line) and commercial amorphous boron (black line).**

**Table II-7. ICP-OES elemental analysis of SMS-derived boron, synthesied from $LiBH_4$ in LiI/LiCl.[4]**

| | B (at%) | K (at%) | Na (at%) | Li (at%) |
|---|---|---|---|---|
| Amorphous B from $NaBH_4$ | 95.0 | 4.9 | < 0.07 | < 0.01 |
| Amorphous B from $LiBH_4$ | 93.5 | < 0.3 | 2.4 | 3.8 |

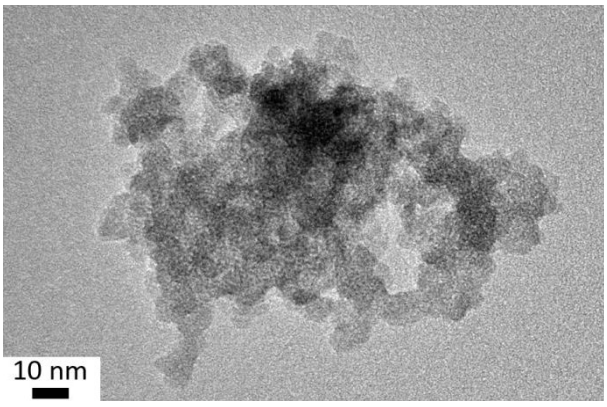


**Figure II-23. TEM picture of nanostructured amorphous boron synthesised in LiCl/LiI from $LiBH_4$.[4]**

The $^{11}B$ solid state NMR signal from carbon-contaminated nano-$B_{am}$ differs from that of commercial bulk amorphous boron (Figure II-21 and Figure II-22), which is usually described as randomly oriented $B_{12}$ icosahedra. All currently known bulk structures of boron are based on that building block, while recently discovered single-layer boron, so-called “borophene”, is constructed on $B_7$ clusters.[11,12] Note also that the $^{11}B$ solid state signal differs from boron carbide $B_4C$ (Figure II-22).

As NMR spectroscopy signs local organisation, the local structure of nano-$B_{am}$ has been further studied. Pair-distribution-function obtained from X-ray scattering

characterises short range order in materials. The comparison between nano-$B_{am}$ and commercial bulk amorphous boron shows (Figure II-24) that the first distances signing nano-$B_{am}$ (1.66 and 2.97 Å) are lower (1.82 and 3.00 Å). The difference is more important for larger distances (4.12 Å and 5.13 Å for nano-$B_{am}$ *vs.* 4.52 Å and 5.80 Å for the bulk). The PDF of commercial amorphous boron is very close to that of beta-boron, calculated from the known structure, confirming the presence of $B_{12}$ units. The B-B distance in $B_{12}$ is around 1.78 Å, superior to the smallest distance found in nano-$B_{am}$, which again raises questions about the presence of this structural building block in nano-$B_{am}$. Interestingly, Pallier *et al.* reported an amorphous $B_4C$ ceramic in 2013: the B-C distance in C-B-C chains is 1.42 Å, much shorter than our experimental result for nano-$B_{am}$ ruling out the presence of chain-type B-C structures, in agreement with $^{11}B$ NMR data (Figure II-22).[13] Note that Aydin and Simsek simulated $B_4C$-type structures with $B_{11}C$ icosahedra.[14] In this case, the B-C distance would be in the 1.63-1.68 Å range in icosahedra (around 1.4 Å in the inter-icosahedra chains), close to the 1.66 Å distance in nano-$B_{am}$.[14] However, in such an environment, B-B distances in the icosahedra would be at least 1.73 Å, not detected in the PDF of nano-$B_{am}$, hence ruling out the presence of icosahedral-type B-C distance in nano-$B_{am}$.[14]

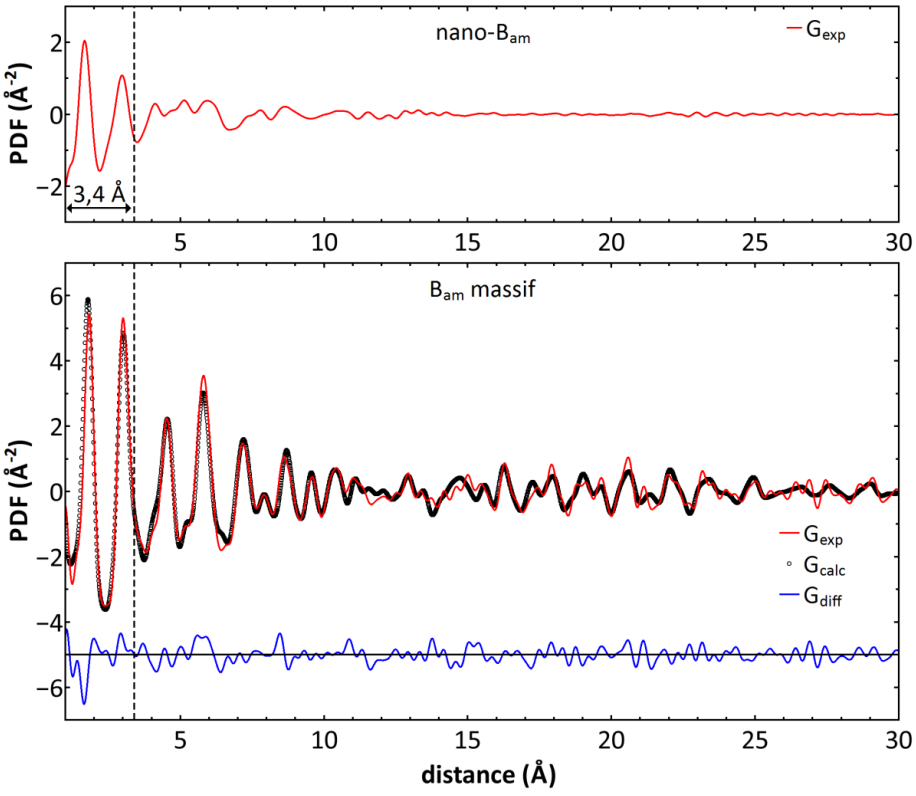


**Figure II-24. PDF diagrams of nano-$B_{am}$ (top) and commercial amorphous B (bottom).**[4]

Simulation experiments aiming at generating boron structures compatible with both density and PDF data are ongoing to assess the local structure of nano-$B_{am}$. Moreover, comparing the PDF of samples synthesised in glassy carbon and in *h*-BN is possibly a way to determine the nature of the carbon impurities, such as the presence of B-C bonds.

The original local structure of nano-$B_{am}$ is a particularly interesting feature when it comes to its crystallisation, as the phase diagram of boron has mainly been investigated from already crystalline samples, all exhibiting $B_{12}$-based structures. Crystallisation of nano-$B_{am}$ under HPHT techniques is the object of the chapter V.

## II-3- Conclusions

This chapter aimed at an in-depth description of the materials that will be used for HPHT studies in the next chapters.

These precursors are synthesised in molten salts from molecular precursors, a general and versatile route toward metal-boron alloys. The boride/boron materials for which this synthetic pathway has been developed in the first place are unique nanocomposites. In the course of this PhD work, the route toward nanostructured borides has been extended to another reaction medium, namely the LiI/KI eutectic mixture. While conserving the benefits of molten salts media (low vapour pressure, high temperature stability and oxygen/water free), these iodine-based salts are soluble in methanol, which is not the case of LiCl/KCl. Using methanol as washing solvent instead of water enables limiting oxidation of the final material. However, note that the use of methanol leads to residual amounts of alkaline ions in the final composite, which may impact further transformation under HPHT conditions.

Besides borides, a new nanostructured amorphous boron material, nano-$B_{am}$, can be reached through SMS.[4,6] This material exhibits unique properties such as high specific area, high reactivity, original local structure and is un-oxidised, as confirmed by $^{11}$B solid state NMR, unlike commercial amorphous boron. Hence, nano-$B_{am}$ is a unique boron source. In this PhD work, the carbon content in this new material has been especially investigated. Changing the synthesis crucible's nature has been shown to modify the carbon content, thus evidencing that glassy carbon is not totally inert and contributes to a carbon content of *ca.* 2 wt%. Among possible crucible materials, *h*-BN has been tested and efficiently decreases carbon contamination. Metal crucibles could as well be envisaged but would need passivation first (by first synthesising a metal boride on the inner surface of the crucible). As underlined before, the composition control is of prime importance when studying boron, due to its alloying capability with most elements, even in low amounts.

SMS-derived products represent unique precursors for high pressure studies on nanostructured occurrences of both metal borides and elemental boron. Such HPHT studies are discussed in the next chapters.

## II-4- References


(1) Portehault, D.; Devi, S.; Beaunier, P.; Gervais, C.; Giordano, C.; Sanchez, C.; Antonietti, M. *Angew. Chem. Int. Ed.* **2011**, *50* (14), 3262–3265.

(2) Terlan, B.; Levin, A. A.; Börrnert, F.; Zeisner, J.; Kataev, V.; Schmidt, M.; Eychmüller, A. *Eur. J. Inorg. Chem.* **2016**, *082910* (2005), 2003–2006.

(3) Terlan, B.; Levin, A.; Börrnert, F.; Simon, F.; Oschatz, M.; Schmidt, M.; Cardoso-Gil, R.; Lorenz, T.; Baburin, I.; Joswig, J.-O.; Eychmueller, A. *Chem. Mater.* **2015**, *27*, 5106–5115.

(4) Gouget, G. Approche moléculaire vers des nanomatériaux inorganiques composés de bore : nouvelles nanostructures fonctionnelles, **2016**.

(5) Gouget, G.; Beaunier, P.; Portehault, D.; Sanchez, C. *Faraday Discuss.* **2016**, 10.1039/C6FD00053C

(6) Portehault, D.; Gouget, G.; Gervais-Stary, C.; Sanchez, C. Matériau nanostructuré de bore amorphe **2016**, 15/55878

(7) Johnson, C. E.; Cairns, E. J.; Sridhar, R. *J. Chem. Eng. Data* **1970**, *15* (2), 244–245.

(8) Basin, A. S.; Kaplun, A. B.; Meshalkin, A. B.; Uvarov, N. F. *Russ. J. Inorg. Chem.* **2008**, *53* (9), 1509–1511.

(9) Liu, C. H.; Lieto, L. R. *J. Chem. Eng. Data* **1969**, *14* (1), 83–84.

(10) Turner, C. L.; Taylor, R. E.; Kaner, R. B. *J. Phys. Chem. C* **2015**, *119* (24), 13807–13813.

(11) Mannix, A. J.; Zhou, X.-F.; Kiraly, B.; Wood, J. D.; Alducin, D.; Myers, B. D.; Liu, X.; Fisher, B. L.; Santiago, U.; Guest, J. R.; Yacaman, M. J.; Ponce, A.; Oganov, A. R.; Hersam, M. C.; Guisinger, N. P. *Science* **2015**, *350* (6267), 1513–1516.

(12) Feng, B.; Zhang, J.; Zhong, Q.; Li, W.; Li, S.; Li, H.; Cheng, P.; Meng, S.; Chen, L.; Wu, K. *Nat. Chem.* **2016**, *8*, 563–568.

(13) Pallier, C.; Leyssale, J.-M.; Truflandier, L. A.; Bui, A. T.; Weisbecker, P.; Gervais, C.; Fischer, H. E.; Sirotti, F.; Teyssandier, F.; Chollon, G. *Chem. Mater.* **2013**, 25 (13), 2618-2629

(14) Aydin, S.; Simsek, M. *Phys. Status Solidi Basic Res.* **2009**, *246* (1), 62–70.

# Chapter III: HPHT treatments on oxygen-containing nanocomposites

This chapter focuses on the HPHT treatment performed on the two nanocomposites systems $HfB_2$/B and $CaB_6$/B synthesised in the LiCl/KCl eutectic mixture and washed with water. This work aims at demonstrating the possibility to crystallise the amorphous matrix embedding the nanoparticles. Moreover, this transformation is accompanied by conservation of the nanostructure of the material as grain growth remains very limited. As a consequence of the oxygen content in the precursors, the amorphous matrix crystallises in the matrix as $HfB_2O_5$,[1] the first ternary hafnium borate and $CaB_2O_4$-IV,[2] a high-pressure modification of calcium borate. We also demonstrate below that these phases are nanostructured so that the nanocomposite nature of the synthesised materials is conserved. As this work is submitted for publication in peer-reviewed journal, it is integrated to this manuscript as submitted. As a consequence the precursors synthesis in molten salts presented in part III-3-1- has already been described in the previous chapter.

## III-1- Introduction

While numerous works describe the behavior of preformed inorganic nanoparticles under high pressures and temperatures (HPHT) ranging from 1 to 35 GPa and from 500 to 1500 °C,[3–7] respectively, reports on nanoscaled inorganic compounds crystallised under such extreme conditions are much scarcer. Notably, most studies on oxide nanoparticles apply high pressure transformation only and no heating.[8–11] Note studies combining both high pressure and high temperature treatment of nanomaterials are mostly limited to the synthesis on light elements based nanomaterials, as nanostructuration enhances the hardness properties of these materials (*e.g.* nanostructured polycrystalline diamond or *c*-BN).[8,12–18] Indeed, HPHT phase transformations are often accompanied by extensive crystal growth in inorganic phases,[19] except for a few compounds, most of them containing strong covalent bonds involving boron incorporated in boron nitrides or metal-boron alloys, so-called metal borides.[8–11]

Another wide family of high pressure boron-based phases for which nanostructuration has not been reported yet is borates. In all its natural occurrences, boron is found covalently bound with oxygen to form borates, as a consequence of the B-O bond strength.[20] Besides the direct use of these minerals as boron source, borates are widely used in the glass and fiber glass insulation industry.[20] Borates are also actively scrutinised for their non-linear optical properties.[20] All in all, the global borates production reached 3.7 million metric tons in 2014 (estimated, excluding U.S.A.'s production).[21] Flux[20] and hydrothermal[22] syntheses as well as crystal growth methods[20,23] are used to produce borates, especially single crystals highly sought for optics. These compounds can also be synthesised by sol-gel processes to yield glasses and glass-fibers.[24–26] However, high pressures appear among the most versatile approaches toward complex borates, and lead to regular discovery of new crystal structures.[1,27–31] Indeed, such extreme conditions yield a wide variety of new compounds and novel polymorphs,[27] sometimes with intriguing structural motifs, such as edge-sharing $BO_4$ octahedra,[28,30,32–34] or the first members of compounds families,

such as the first ternary hafnium borate β-$HfB_2O_5$.[1] Again, these phases obtained only after HPHT treatment have been reported only in the bulk state without any occurrence of nanostructuration. Furthermore, these compounds have not been combined with other materials into original nanocomposites that could yield multifunctionality and new properties.

Herein we present the first cases of nanocomposites based on high pressure-derived borates of hafnium or calcium. These phases contain nano-inclusions of metal-boron alloys separated from each other by few nanometres, so that the borate matrix is also nanostructured. To reach these novel materials, we have developed a procedure relying on the original combination of liquid phase chemical synthesis of nanoscaled metal boride precursors,[35,36] and of treatment of these powders under extreme conditions of pressure and temperature. Metal boride nanocrystals exhibit a wide range of fundamentally and technologically relevant properties, for instance in field emission, thermoelectricity, superconductivity, hardness and magnetism.[37–39] Hence, combining such nanoparticles with high pressure borates should pave the way to innovative multifunctional nanocomposites. The process is presented in Figure III-1.

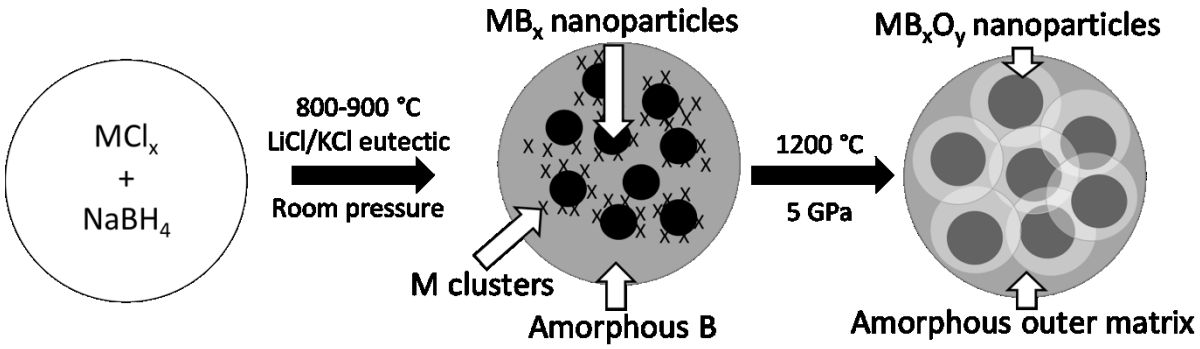


**Figure III-1. Schematic overview of whole process, involving liquid phase synthesis and HPHT treatment of metal boride-based nanocomposites, yielding boride/borate nanocomposites.**

## III-2- Experimental

**Synthesis of borides/oxidised boron nanocomposites.** The synthesis of the nanostructured precursors was performed according to a previously reported procedure.[35] Before heating, all powders were handled into an argon filled glovebox. Anhydrous $HfCl_4$ (Alfa Aesar), anhydrous $CaCl_2$ (Alfa Aesar) and sodium borohydride (Alfa Aesar) were used as received. Prior to synthesis, LiCl and KCl (Aldrich) were previously mixed at the eutectic composition LiCl:KCl = 45/55 wt% and finely ground in a mortar. The resulting mixture was evacuated at 200 °C for 4 days and transferred into the glovebox. Before heating, anhydrous metal chlorides, sodium borohydride and the eutectic salt mixture LiCl:KCl (2.5 g) were finely ground together with a Retsch MM400 ballmiller (airtight vials of 50 mL, one steel ball of 62.3 g and a diameter of 23 mm) for 2 minutes at 20 Hz. The mixture was transferred into a glassy carbon crucible which was then heated under argon flow in a tube oven at 10 °C·min$^{-}$

[1]. For $HfB_2$, 1 mmol of hafnium (IV) chloride and 4 mmol of sodium borohydride were used. The reaction medium was heated at 900 °C for 4 h. For $CaB_6$, 1 mmol of calcium (II) chloride and 8 mmol of sodium borohydride were used. The medium was heated at 800 °C for 4 h. After cooling, the metal boride powders were recovered by dissolution of the frozen eutectic in water and four washing-centrifugation cycles (in 10 mL polycarbonate centrifugation tubes, at 16500 rpm for 20 min), then dried under vacuum at 60 °C overnight. Finally, the powders were exposed to air for 7 days to ensure oxidation of the boron shell.

**High Pressure High Temperature (HPHT) experiments.** Before building the high pressure assemblies, the powders (~ 60 mg) were compacted into 2 mm diameter pellets, which were placed into a Paris-Edinburgh cell assembly as described by Besson and co-workers.[40] Briefly, the pellets were loaded into a hexagonal boron nitride capsule, in turn loaded into a graphite capsule. The set-up was then loaded in a 10 mm baked pyrophyllite gasket that was compressed between two tungsten carbide conical anvils with a specially designed bottom part to improve mechanical strength and compression.[40,41] The high-resistivity graphite inside the assembly was used as heater by injecting electrical current from the anvils through the assembly. The samples were compressed at 5 GPa for 3 h in a 2 columns VX3 Paris-Edinburgh press. Once at the desired pressure, the samples were heated at 1200 °C at a *ca.* 25(5) °C·min$^{-1}$ rate with a dwell time of 90 min before quenching. After cooling, the samples were slowly decompressed over 6 h.

**Characterisations.** The precursors and products were characterised with a Bruker D8 X-ray diffractometer operating in the Bragg-Brentano reflection mode equipped with a nickel filter to select the Cu-$K_\alpha$ radiation. The data were collected in the $2\theta$ = 10-80 ° range with 0.05 ° steps. For samples recovered after HPHT treatment, crystalline silicon low-background sample holders from Bruker were used for XRD analysis. The morphology and the average particle size of the samples were analysed by transmission electron microscopy (TEM) using a *Tecnai spirit G2* apparatus ($LaB_6$, operating at 120 kV). HRTEM analyses were performed on a JEOL JEM 2011 ($LaB_6$, operating at 200 kV) apparatus at the Microscopy Centre of Institut of Materials of Paris Centre, Sorbonne Universités-UPMC, Paris. The STEM-HAADF and STEM-DF observations were performed on a JEOL 2100 F operating at 200 kV and equipped with aberration correction on the electronic probe at the Institut de Physique et Chimie de la Matière de Strasbourg. All samples were prepared by evaporating a drop of diluted suspension in ethanol on a carbon-coated copper grid. For infrared spectroscopy, a Perkin-Elmer spectrum 400 FT-IR apparatus equipped with ATR FT-IR was used.

## III-3- Results and discussion

### III-3-1- Synthesis of metal borides-boron nanoparticles in molten salts

The synthesis of the nanoscaled precursors was performed by precipitation in the inorganic molten eutectic mixture LiCl:KCl with high thermal stability, which enables reaching temperatures up to 900 °C within the liquid medium at room pressure.[35,42] After the synthesis and to ensure subsequent evolution under HPHT of the amorphous matrix toward borates and not boron polymorphs, the powders were exposed to air for 7 days to allow oxidation of the boron matrix and incorporation of B-O bonds. The presence of B-O bonds characteristic vibrations is evidenced by bands at 1350 $cm^{-1}$ on the infrared spectra (Supplementary information Figure III-S1**)**. XRD shows that hafnium diboride is obtained at 900 °C as a pure crystalline phase (Figure II-3). The crystallite size is 7.5(6) nm according to the Scherrer's formula.[43] It is consistent with the particle diameter observed by TEM (Figure III-3a), which exhibits sizes ranging from 5 to 10 nm range in agreement with our previous report.[35] The particles are single-crystals and isotropic. To our knowledge, this molten salt method yields the smallest particle size reported for crystalline metal borides. As previously reported,[35,36] these particles are embedded in an amorphous matrix which was shown to consist mainly in slightly oxidised boron, where oxygen arises from the washing step when the powders are exposed to water and air. The nature of the matrix was also assessed by the mean of Scanning Transmission Microscopy-High Angle Annular Dark Field (STEM-HAADF), more sensitive to difference in atomic numbers than bright field TEM. For the Hf-based system, the comparison of bright and dark field observations (Figure III-4) shows that the matrix around the particles does contain small clusters (*ca.* 2 nm) contrasting with the rest of the matrix. This shows the presence of hafnium atoms within the matrix. The thickness of this amorphous phase is about 2 nm. Consequently, between two adjacent nanocrystals, a 4 nm gap is filled with amorphous boron doped with Hf atoms and clusters. As two adjacent particle shells are fused together, then the system is best described as "nano-cookie dough": the boride particles are inclusions within the amorphous boron nanostructured three-dimensional matrix. Therefore, both components are nanostructured (Figure III-3a): the crystalline phase as nanoscale inclusions and the amorphous phase consisting in nanoscale walls between the crystalline inclusions. The nanostructure is illustrated in the scheme in Figure III-3b.

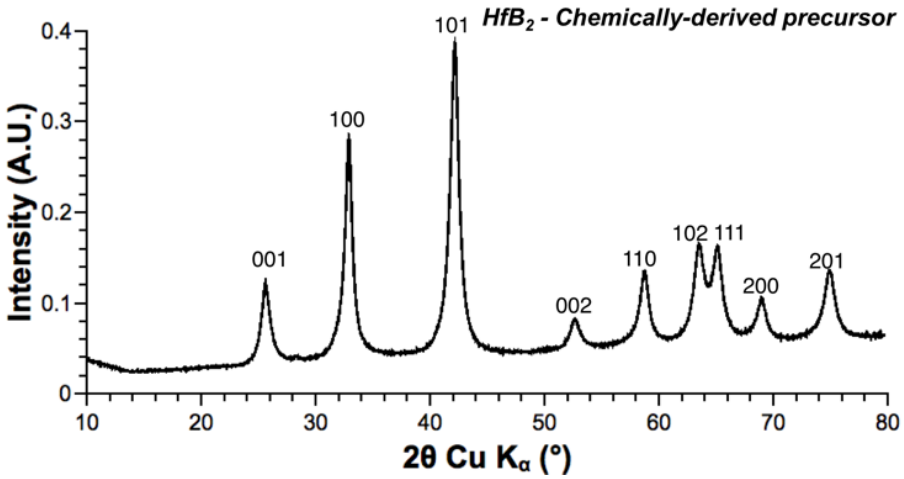


**Figure III-2. XRD powder pattern of $HfB_2$/amorphous boron nanocomposite.**

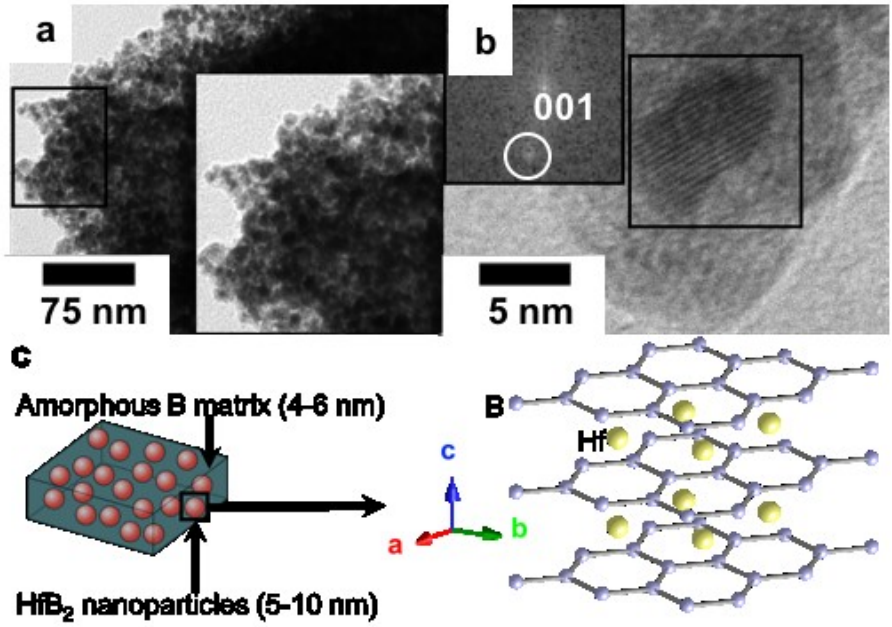


**Figure III-3. (a) and (b) (HR)TEM micrographs showing the composite "nano-cookie" structure and the particle crystal structure. The latter is consistent with a crystalline $HfB_2$ particle (inset of b: Fast Fourier Transform (FFT) pattern of the area in black square and indexed along the $HfB_2$ structure) embedded in amorphous B. (c) Scheme of the chemical synthesis-derived nanostructured precursor for HPHT treatments and $HfB_2$ structure typical of metal diboride: honeycomb boron sheets with metal atoms intercalated in the interlayer space.**

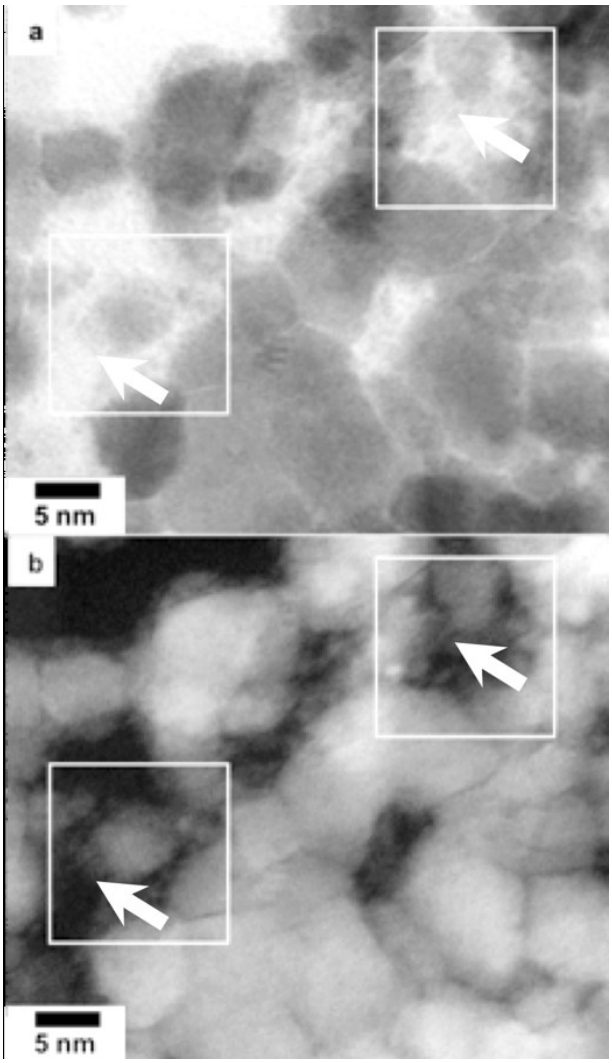


**Figure III-4. (a) STEM picture of $HfB_2$/B nanocomposite. (b) STEM-HAADF picture of $HfB_2$/amorphous boron nanocomposite. Comparison of the matrix around the particles shows the presence of Hf clusters, about 2 nm big.**

For calcium hexaboride, XRD (Figure II-5) shows again a sole crystalline phase. Here, the crystallite size is 15 nm according to the Scherrer's formula. Calcium has an atomic number much lower than hafnium, which makes it less contrasting in TEM *vs.* boron and carbon. Nevertheless, TEM analysis, these samples exhibit a size between 5 and 10 nm **(**Figure III-6a, b). High-resolution micrographs show single crystal particles, as seen for $HfB_2$ (Figure III-6a, b). The amorphous gap between two adjacent nanoparticles consists in 4-6 nm-thick amorphous matrix (Figure III-6a, b, c), as for the Hf-based system.

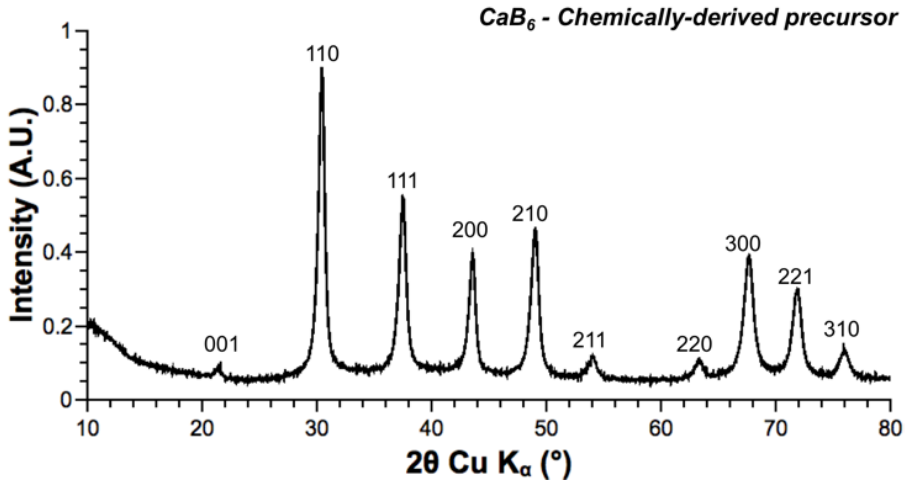


**Figure III-5. XRD powder pattern of $CaB_6$/amorphous boron nanocomposite.**

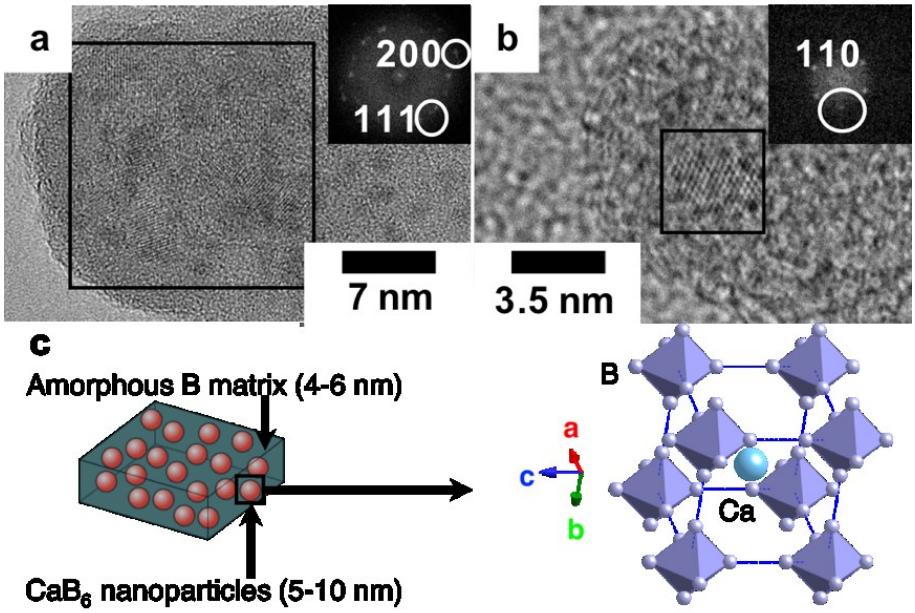


**Figure III-6. (a) and (b) (HR)TEM micrographs showing the composite "nano-cookie" structure and the particle crystal structure. The latter is consistent with $CaB_6$ particles embedded in amorphous B matrix (insets: FFT patterns of the zones in black squares and indexed along the $CaB_6$ structure). (c) Scheme of the chemical synthesis-derived nanostructured precursor for HPHT treatments and $CaB_6$ structure: as a body centered crystal, with boron octahedra at the cubes' vertexes and a calcium atom in the center.**

### III-3-2- High Pressure-High Temperature (HPHT) treatments

The oxidised composites were placed in Paris-Edinburgh cell assemblies, producing 1.5 mm diameter by 1-2 mm height pellets after HPHT treatments. The conditions were identical for both $HfB_2$ and $CaB_6$ samples: 1200 °C at 5 GPa with a 45 min-long slope from room temperature and a 90 min dwell time. The pressure was applied prior to heating. After the HPHT treatment, the samples were quenched by cooling

down the temperature and then slowly releasing the pressure. The assemblies were opened in air and the samples recovered.

For the hafnium-based system, the XRD pattern (Figure II-11) first shows that hafnium diboride is conserved upon HPHT treatment. Crystallite size analysis with the Scherrer's formula evidences slight particle growth, although the nanoscale is preserved with an average size of 25 nm. XRD also indicates crystallisation of another crystalline phase which is identified as hafnium borate β-$HfB_2O_5$. This phase was first prepared by Huppertz *et al*. from $HfO_2$ and $B_2O_3$ at 7.5 GPa and 1100 °C.[1] To our knowledge, we provide in this report the second occurrence of this crystalline ternary hafnium borate. TEM micrographs (Figure II-12a, b) and particle size distributions (Figure III-9) confirm the very limited grain growth and sintering: the particle size does not exceed 30 nm after a treatment at 1200 °C. Yet, after the HPHT treatment, the matrix is crystallised and several interplanar spaces characteristic of β-$HfB_2O_5$ can be seen (Figure II-12b, c). These fringes run over several dozens of nanometers, thus highlighting the extensive crystallisation of the matrix. Consequently, the amorphous matrix crystallised upon HPHT while preserving the interparticle gap, leading to nanostructured $HfB_2$/β-$HfB_2O_5$ composite monoliths, which may be described again as a "nano-cookie": a crystalline β-$HfB_2O_5$ matrix embedding nano-inclusions of $HfB_2$ and containing nanoscaled walls separating the inclusions (Figure II-12b). The particle size distribution of $HfB_2$ compared before and after treatment is shown in Figure III-9c and confirms the limited grain growth.

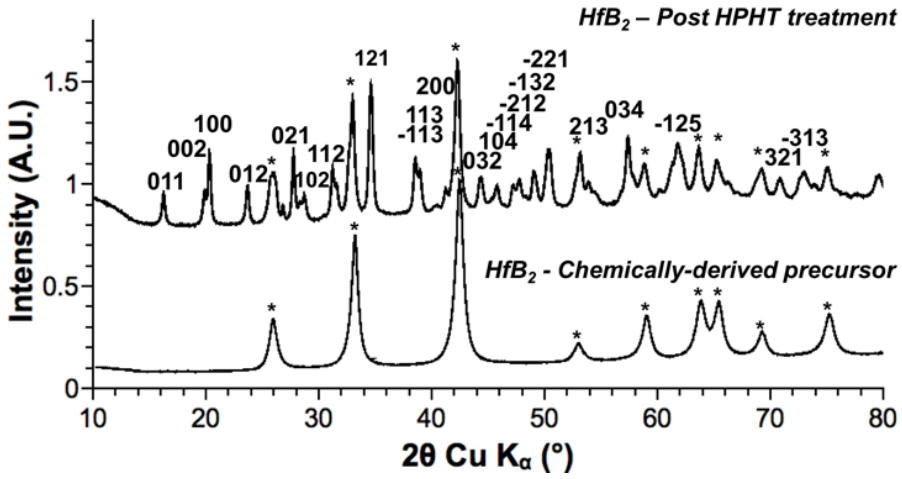


**Figure III-7. (a) XRD powder patterns of the initial composite precursor and of the $HfB_2$/$HfB_2O_5$ nanocomposite obtained after HPHT treatment, evidencing the hafnium borate crystallisation while conserving nanoscaled hafnium boride. For legibility sake, only main β-$HfB_2O_5$ peaks are indexed and $HfB_2$ peaks are highlighted as black stars.**

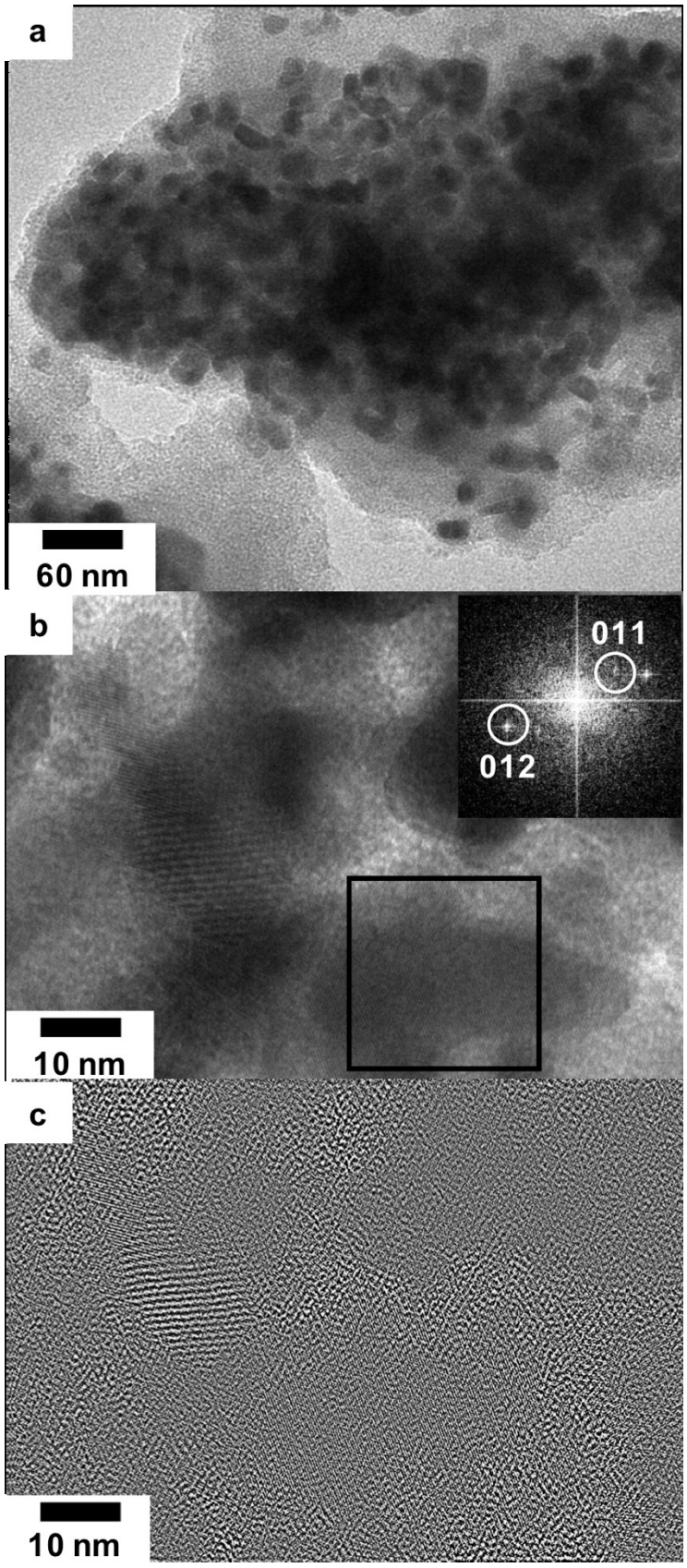


**Figure III-8. (a) and (b) (HR)TEM micrographs showing the composite "nano-cookie" structure, the hafnium borate nanostructure and limited grain growth. Inset of (d): FFT pattern of the zone inside the black square). (c) Filtered Fourier Transform of (b).**

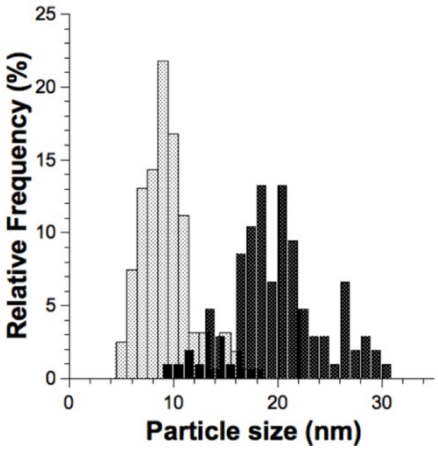


**Figure III-9. $HfB_2$ particle size distribution before (black-dotted white) and after (white-dotted black) HPHT treatment.**

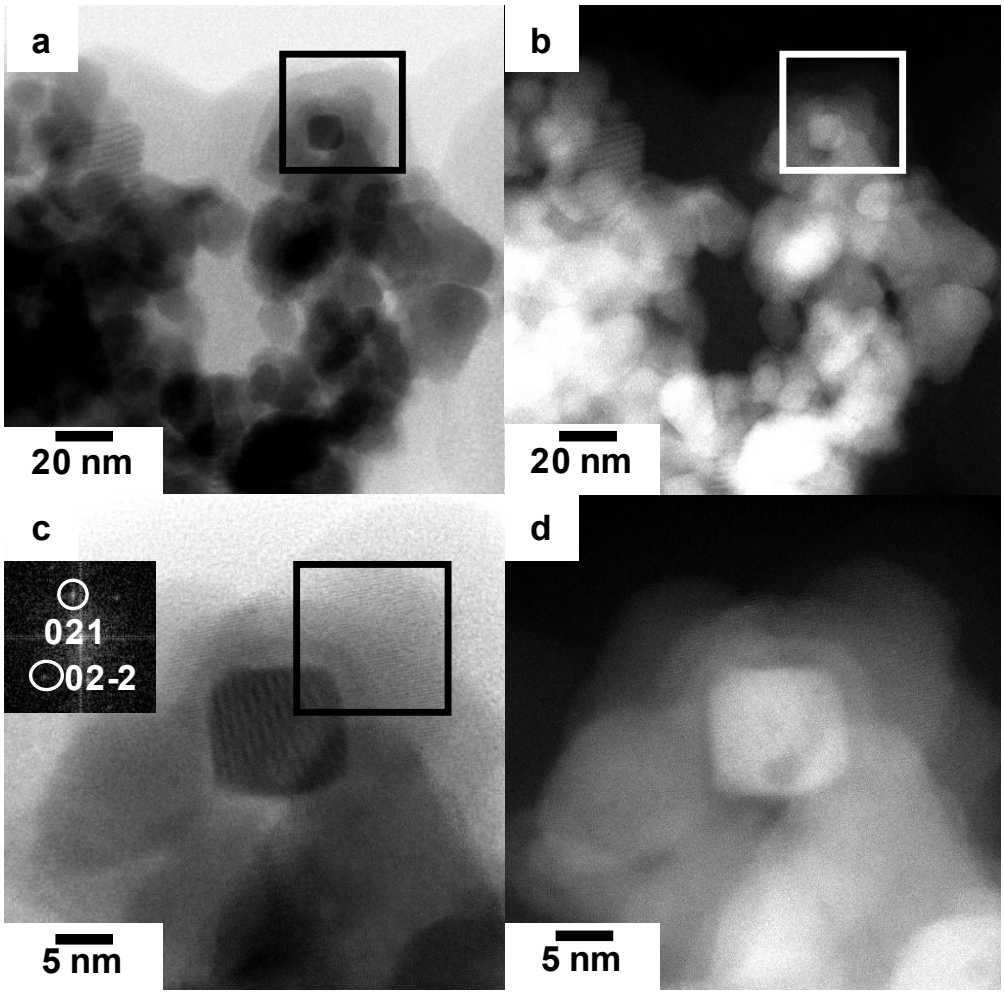


**Figure III-10. (HR)STEM bright (a), (c) and dark (b), (d) field micrographs of the $HfB_2/HfB_2O_5$ nanocomposite. Inset of (c): FFT of zone inside the black square, indexed along the $HfB_2O_5$ structure.**

Note that comparison of HR-STEM bright and dark field observations on the $HfB_2/HfB_2O_5$ nanocomposite (Figure III-9) clearly shows a decrease in contrast,

hence in hafnium content as the distance to the $HfB_2$ inclusions is increased. This indicates that $HfB_2O_5$ likely nucleates at the surface of the inclusions.

For the Ca-based composite, XRD patterns also show the conservation of the initial boride crystalline phase, calcium hexaboride (Figure III-11). Again, another phase crystallised besides the boride: $CaB_2O_4$ (IV). This borate has been previously prepared by Marezio and co-workers in the first place, by HPHT treatment of the ambient pressure phase $CaB_2O_4$ (I).[2] TEM micrographs of the recovered sample show again very limited grain growth with borides particles smaller than 30 nm (Figure III-12a). Here again, the “nano-cookie” structure is preserved (Figure III-12b). Extensive crystallisation of the matrix into $CaB_2O_4$ (IV) is evidenced by TEM micrographs (Figure III-12b, c) with lattice fringes running over long distances of more than 80 nm.

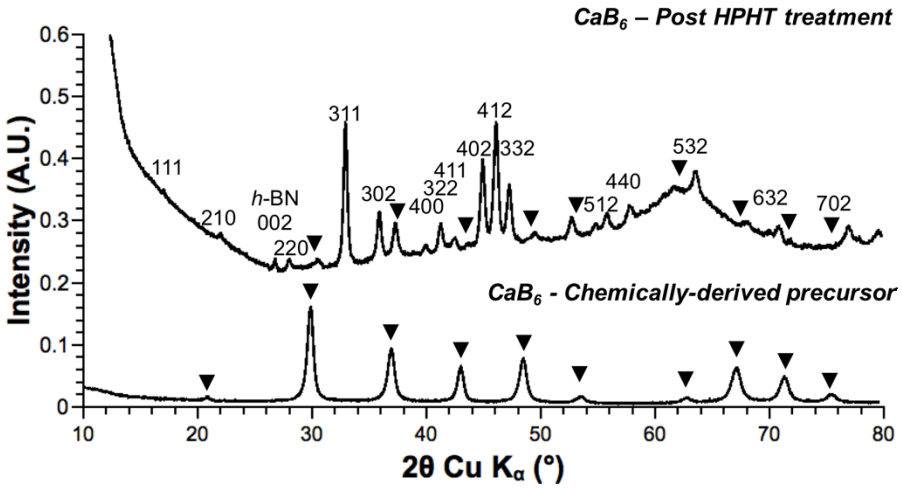


**Figure III-11. XRD powder patterns of the initial composite precursor and of the $CaB_6/CaB_2O_4$ (IV) nanocomposite material after HPHT treatment, evidencing the calcium borate (IV) crystallisation with preservation of the nanoscale calcium hexaboride phase. Only main $CaB_2O_4$ (IV) peaks are indexed and $CaB_6$ peaks are highlighted as black triangles.**

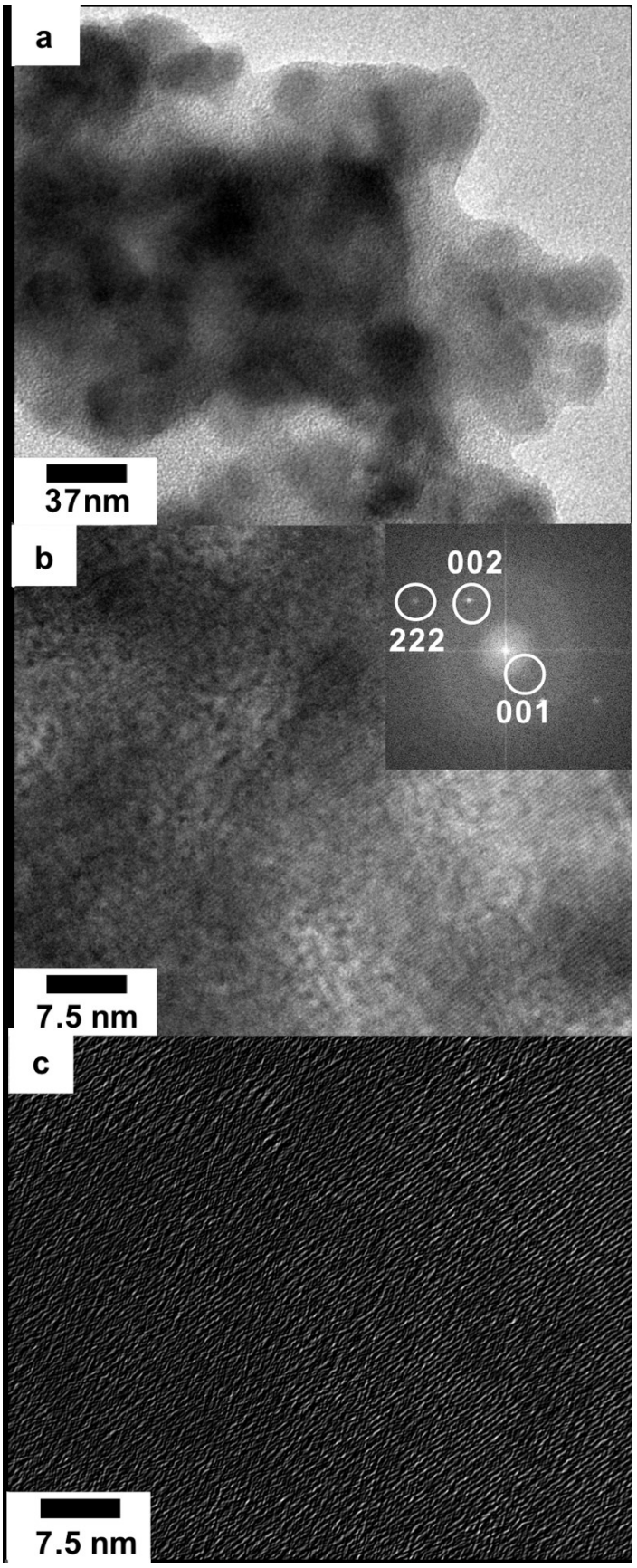


**Figure III-12. (a) and (b) (HR)TEM micrographs showing the composite "nano-cookie" structure, the calcium borate nanostructure and limited grain growth. Inset of (b): FFT pattern of the zone inside the black square. (c) Filtered Fourier of (b).**

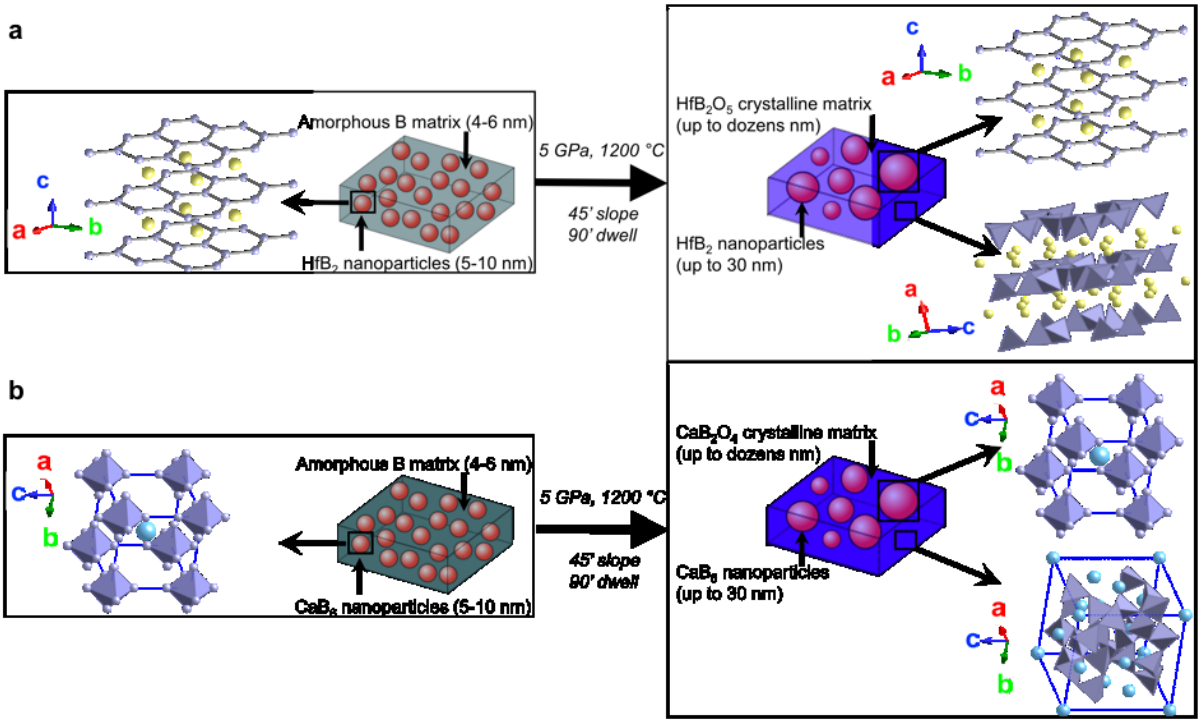


**Figure III-13. (a) Schematic representation of $HfB_2$ (a) and $CaB_6$ (b) nanocomposites evolution upon HPHT treatment. The matrix is crystallised into the nanostructured borate, while conserving the initial particles' nature and nanostructure.**

In both cases, the high temperature treatment (1200 °C) of the sample preserves the nanostructure, with very limited grain growth and sintering of the initial nanoparticles. A scheme summarising the overall evolution of the materials is shown in Figure III-13. Hence, nanoparticles are obtained at extreme conditions. Remarkably, up to now only scarce reports have related the synthesis of nanostructured inorganic materials under HPHT conditions.[3,6,44–46] Indeed, such treatments usually yield thermodynamically stable states, hence reduced interfaces by large crystal growth. Our striking result arises from two factors. First, high pressure limits atomic diffusion,[47] thus increasing the activation barrier for grain growth. Second, particle migration is likely restrained by the matrix they are embedded in. Noteworthy, the crystallisation of ternary borates in the matrix suggests that calcium and hafnium atoms diffuse within the matrix. The case study of the hafnium-based system, the STEM-HAADF observations show the plausible presence of metal atoms within the matrix, which are likely incorporated in $HfB_2O_5$ upon HPHT treatment.

## III-4- Conclusions

To conclude, we have demonstrated the original combination of chemically-derived precursors with HPHT treatments for the preparation of innovative nanostructured

composites produced by the high pressure crystallisation of ternary borates $HfB_2O_5$ and $CaB_2O_4$-(IV) containing $HfB_2$ and $CaB_6$ nanoinclusions, respectively. The initial nanoscaled precursors are derived from molten salt syntheses and consist in metal borides nanoparticles embedded in an amorphous oxidised matrix mainly containing boron. Hence, all the components, *i.e.* metal borides and oxidised boron, are confined at the nanoscale in the precursor. This nanostructuration is preserved upon crystallisation of the matrix into the high pressure borate phases under HPHT conditions using a large-volume Paris-Edinburgh press. Especially, after treatment at 1200 °C and 5 GPa, the diameter of the metal boride inclusions does not exceed 30 nm. These results demonstrate the validity of the approach combining solution-phase synthesis of inorganic nanomaterials and treatments under extreme conditions to yield nanocomposites containing phases not reachable at ambient conditions. The resulting heterostructures combine compounds with metal and insulator behaviours. Thermal and electronic properties may then be thoroughly influenced within these intimate mixtures, thus paving the way to exciting functional nanocomposites.

## III-5- Associated content

**Supporting Information**. Figure III-S1: FTIR spectra of the precursors.

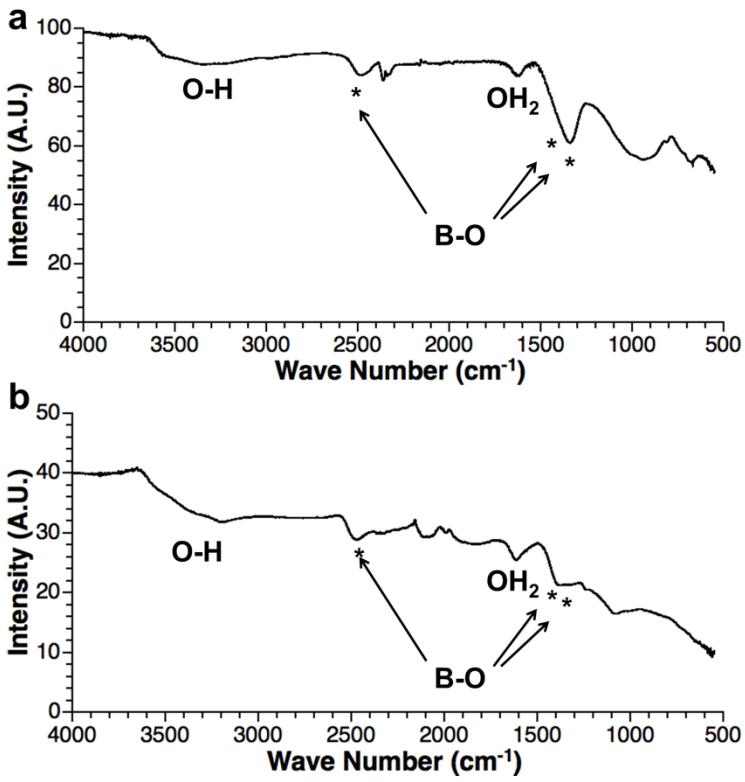


**Figure III-S1. Fourier Transform Infrared spectra of the (a) $HfB_2$/amorphous boron and (b) $CaB_6$/amorphous boron nanocomposites after exposure to air during seven days.**

## III-6- References


(1) Knyrim, J. S.; Huppertz, H. *J. Solid State Chem.* **2007**, *180* (2), 742–748.
(2) Marezio, M.; Remeika, J. P.; Dernier, P. D. *Acta Crystallogr. Sect. B Struct. Crystallogr. Cryst. Chem.* **1969**, *25* (5), 965–970.
(3) Gonzalez, E. J.; Hockey, B.; Piermarini, G. J. *Mater. Manuf. Process.* **1996**, *11* (6), 951–967.
(4) Olsen, J. S.; Gerward, L.; Jiang, J. Z. *High Press. Res.* **2002**, *22*, 385–389.
(5) Chang, H.-C.; Jiang, J.-C.; Kuo, M.-H.; Hsu, D.-T.; Lin, S. H. *Phys. Chem. Chem. Phys.* **2015**, *17*, 21143–21148.
(6) Liu, B.; Yao, M.; Liu, B.; Li, Z.; Liu, R.; Li, Q.; Li, D.; Zou, B.; Cui, T.; Chen, Z. *J. Phys. Chem. C* **2011**, No. 111, 4546–4551.
(7) Shahabuddin Shah, M.; Shahabuddin, M.; Parakkandy, J. M.; Alzayed, N. S.; Madhar, N. A.; Batoo, K. M. *J. Supercond. Nov. Magn.* **2014**, *28* (2), 481–485.
(8) Solozhenko, V. L.; Kurakevych, O. O.; Le Godec, Y. *Adv. Mater.* **2012**, *24* (12), 1540–1544.
(9) Dubrovinskaia, N.; Solozhenko, V. L.; Miyajima, N.; Dmitriev, V.; Kurakevych, O. O.; Dubrovinsky, L. *Appl. Phys. Lett.* **2007**, *90* (10), 1–4.
(10) Nagakubo, A.; Ogi, H.; Sumiya, H.; Hirao, M. *Appl. Phys. Lett.* **2014**, *105* (8), 081906.
(11) Liang, B.; Xie, Y.; Li, W.; Wu, W.; Zhang, X. *J. Phys. D. Appl. Phys.* **2008**, *41* (19), 195010.
(12) Irifune, T.; Kurio, A.; Sakamoto, S.; Inoue, T.; Sumiya, H. *Nature* **2003**, *421* (6923), 599–600.
(13) Dubrovinskaia, N.; Dubrovinsky, L.; Langenhorst, F.; Jacobsen, S.; Liebske, C. *Diam. Relat. Mater.* **2005**, *14* (1), 16–22.
(14) Zhao, Y.; He, D. W.; Daemen, L. L.; Shen, T. D.; Schwarz, R. B.; Zhu, Y.; Bish, D. L.; Huang, J.; Zhang, J.; Shen, G.; Qian, J.; Zerda, T. W. *J. Mater. Res.* **2002**, *17* (12), 3139–3145.
(15) Solozhenko, V. L.; Andrault, D.; Fiquet, G.; Mezouar, M.; Rubie, D. C. *Appl. Phys. Lett.* **2001**, *78* (10), 1385–1387.
(16) Tian, Y.; Xu, B.; Yu, D.; Ma, Y.; Wang, Y.; Jiang, Y.; Hu, W.; Tang, C.; Gao, Y.; Luo, K.; Zhao, Z.; Wang, L.-M.; Wen, B.; He, J.; Liu, Z. *Nature* **2013**, *493* (7432), 385–388.
(17) Solozhenko, V. L.; Dub, S. N.; Novikov, N. V. *Diam. Relat. Mater.* **2001**, *10* (12), 2228–2231.
(18) Wentorf, R. H. *J. Chem. Phys.* **1961**, *34* (3), 809.
(19) Zhou, X.; Zang, J.; Dong, L.; Cheng, X.; Li, T.; Wang, Y.; Yuan, Y.; Lu, J.; Yu, Y.; Xu, X. *Mater. Lett.* **2015**, *144*, 69–73.
(20) Huppertz, H.; Keszler, D. A. In *Encyclopedia of Inorganic and Bioinorganic Chemistry*; Wiley, **2014**; pp 1–12.
(21) U.S. Geological Survey. *US Geol. Surv.* **2015**, 196.
(22) Demianets, L. N. *Prog. Cryst. Growth Charact. Mater.* **1991**, *21* (1-4), 299–355.
(23) Kouta, H.; Kuwano, Y.; Ito, K.; Marumo, F. *J. Cryst. Growth* **1991**, *114* (4), 676–682.
(24) Brinker, J. *Silica Glass and its Application*; Glass Science and Technology; Elsevier, **1991**; Vol. 11.
(25) Venkatasubramanian, N.; Wade, B.; Desai, P.; Abhiraman, A. S.; Gelbaum, L. T. *J. Non. Cryst. Solids* **1991**, *130* (2), 144–156.
(26) Snowman, H. G. *Sol-gel technology for thin films, fibers, preforms, electronics,*

*and specialty shapes*; Klein, L. C., Ed.; **1988**.
(27) Huppertz, H. *Chem. Commun.* **2011**, *47* (1), 131–140.
(28) Emme, H.; Huppertz, H. *Acta Crystallogr. Sect. C* **2005**, *3*, 29–31.
(29) Emme, H.; Huppertz, H. **2002**, *204* (2), 69451.
(30) Emme, H.; Huppertz, H. *Chemistry* **2003**, *9* (15), 3623–3633.
(31) Sohr, G.; Ciaghi, N.; Schauperl, M.; Wurst, K.; Liedl, K. R.; Huppertz, H. *Angew. Chemie Int. Ed.* **2015**, *5*,
(32) Emme, H.; Valldor, M.; Po, R.; Huppertz, H. *Chem. Mater.* **2005**, *17* (1), 2707–2715.
(33) Huppertz, H.; von der Eltz, B. *J. Am. Chem. Soc.* **2002**, *124* (32), 9376–9377.
(34) Knyrim, J. S.; Roessner, F.; Jakob, S.; Johrendt, D.; Kinski, I.; Glaum, R.; Huppertz, H. *Angew. Chem. Int. Ed.* **2007**, *46* (47), 9097–9100.
(35) Portehault, D.; Devi, S.; Beaunier, P.; Gervais, C.; Giordano, C.; Sanchez, C.; Antonietti, M. *Angew. Chem. Int. Ed.* **2011**, *50* (14), 3262–3265.
(36) Carenco, S.; Portehault, D.; Boissière, C.; Mézailles, N.; Sanchez, C. *Chem. Rev.* **2013**, *113* (10), 7981–8065.
(37) Ji, X. H.; Zhang, Q. Y.; Xu, J. Q.; Zhao, Y. M. *Prog. Solid State Chem.* **2011**, *39* (51).
(38) Mori, T. *J. Phys. Conf. Ser.* **2009**, *176* (1), 012036.
(39) Levine, J. B.; Tolbert, S. H.; Kaner, R. B. *Adv. Funct. Mater.* **2009**, *19* (22), 3519–3533.
(40) Godec, Y. Le; Dove, M. T.; Redfern, S. A. T.; Tucker, M. G.; Marshall, W. G.; Syfosse, G.; Besson, J.-M. *High Press. Res.* **2001**, *21* (5), 263–280.
(41) Besson, J. M.; Nelmes, R. J. *Phys. B Condens. Matter* **1995**, *213-214*, 31–36.
(42) Gouget, G.; Beaunier, P.; Portehault, D.; Sanchez, C. *Faraday Discuss.* **2016**.
(43) Patterson, A. *Phys. Rev.* **1939**, *56* (10), 978–982.
(44) Olsen, J. S.; Gerward, L.; Jiang, J. Z. *High Press. Res.* **2002**, *22*, 385–389.
(45) Chang, H.-C.; Jiang, J.-C.; Kuo, M.-H.; Hsu, D.-T.; Lin, S. H. *Phys. Chem. Chem. Phys.* **2015**, *17*, 21143–21148.
(46) Dogra, S.; Sharma, N. D.; Singh, J.; Poswal, H. K.; Sharma, S. M.; Bandyopadhyay, A. K. *High Press. Res.* **2011**, *31* (2), 292–303.
(47) Helmut Mehrer. *Diffusion in Solids Fundamentals,Methods,Materials, Diffusion-Controlled Processes*; **2007**.

# Chapter IV: HPHT formation of non-oxidised nanocomposites

The experiments described in the previous chapter used nanocomposite boride/boron precursors washed with water and exposed to air, so that the boron-rich matrix was oxidised. Here, the precursors have been synthesised in iodine-based salts washed with methanol and kept under argon, to limit oxidation of the boron matrix. The assemblies were prepared in an argon-filled glovebox, then sealed under argon and exposed to air only a few seconds when placed immediately in-between the anvils, prior to compression. After decompression, the assemblies were transferred and opened in an argon-filled glovebox. To limit air exposure, the samples were sealed in glass capillaries under argon prior XRD measurements for *ex situ* experiments. Note that TEM however requires dispersion in a solvent, which was done under air in ethanol. All in all, the methodology presented in this chapter has been developed to minimise potential oxidation effects.

As for Chapter III, the two systems of interest are the nanocomposites $CaB_6$/B and $HfB_2$/B. In both cases, *in situ* XRD experiments have been performed on synchrotron beamlines in order to readily identify the pressure and temperature domains of interest where phase transitions occur. Then, *ex situ* HPHT treatments have been conducted in these areas for more advanced characterisation of the products.

## IV-1- Experimental set-ups

Most experiments were conducted in Paris-Edinburgh cells, mainly using 10/3.5 mm assemblies, unless stated otherwise, described in the general introduction. The initial sample volume is a 2.1 mm diameter/3 mm height cylinder. Some experiments were carried out using *in situ* XRD on synchrotron beamlines.

At ESRF's ID27 beamline, an angle-dispersive set-up is used: a monochromatic beam is diffracted on the sample and the signal collected on a 2-D detector for all angles (Figure IV-1). To increase the signal-to-noise ratio and decrease the axial divergence, a pair of Soller slits is used, consisting in tungsten carbide strips. However, at low angles (close to the beamstop), their lower efficiency superimposes the diffraction signal of the gasket to the experimental data. For these experiments, the gasket is made from epoxy resin and commercial boron, qualified as "amorphous" but that exhibits Bragg peaks at low diffraction angles. A motorised table supports the press and allows sample's alignment with the X-Ray beam and the Soller slits.

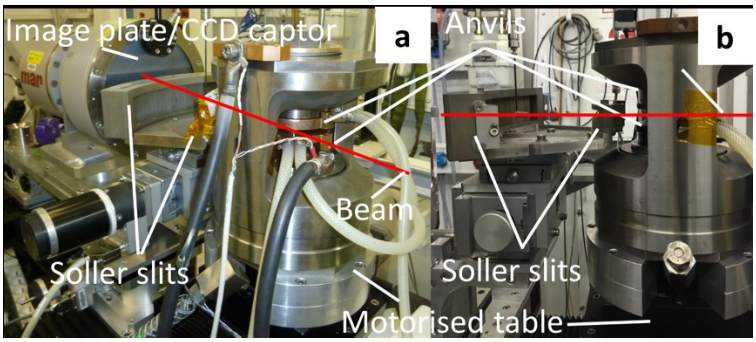


**Figure IV-1. ESRF's ID27 set-up for Paris-Edinburgh cell. (a): top view. (b) side view.**

At SOLEIL Synchrotron's PSICHE beamline, an energy-dispersive set-up is used: a polychromatic "white" beam is diffracted by the sample and the signal collected at a single angle on a germanium detector (Figure IV-2), which allows fast measurements but at the price of relative intensity accuracy, as the emission profile is not constant over the energy range used.

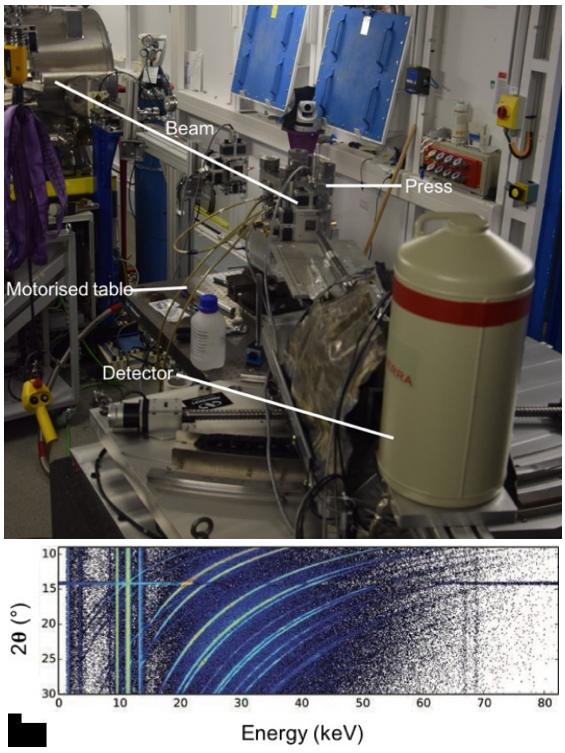


**Figure IV-2. Top: PSICHE beamline set-up for Paris-Edinburgh cell. Bottom: gold leaf diffraction acquired with the CAESAR system.**

The detector is mobile, allowing changing the Bragg's angle according to the d-spacing region of interest. It is therefore possible to record three-dimensional diagrams (plotted for intensity, angle and energy, Figure IV-2), which can be read either at fixed angle or fixed energy. However, in the course of the project, all data have been recorded at fixed angle, in energy dispersive mode only. Indeed, because the detector must be moved with very high precision (about 2 "), it moves very slowly. Hence, the so-called CAESAR system at varying angle is not suitable for samples exhibiting preferred orientation and to probe phenomena in time scales inferior to 1 h. Data recording with the CAESAR system requires about at least an hour, compared

to few seconds for the energy dispersive mode only (at fixed angle). As previously, the press is placed on a motorised table, allowing sample's alignment with the X-Ray beam.

As reference experiments, *in situ* XRD was also performed at "low" pressure (*ca.* 400 MPa, enough to establish electrical contact in the assembly) to probe crystallisation upon heating at close-to-atmospheric pressure. For both systems, $HfB_2$/B and $CaB_6$/B, no crystalline phase is detected besides the boride up to 1400 °C, temperature at which the assembly systematically blows-out, causing loss of the totality of the samples. The synthesis conditions are in the range of that developed for bulk boron crystallisation, as mentioned in Chapter I.[1–12]

## IV-2- Calcium hexaboride

### IV-2-1- *In situ* XRD in Paris-Edinburgh cell

#### IV-2-1-a- Experiment at ID27/ESRF

This first experiment has been conducted on the ID27 beamline at ESRF described above. A 7/2.4 mm assembly was used, with an amorphous boron/epoxy gasket instead of pyrophilite, which absorbs too much X-Rays.[13,14] The diffraction data along compression and heating are presented in Figure IV-3. The reflections in the 8-12° and 18-22° (2θ) regions correspond to commercial "amorphous" boron. It is clear from XRD along compression (up to 5 GPa) that the composite system does not exhibit phase transition under pressure at room temperature. Starting from 1150 °C (reached within 75 min), a second phase crystallises besides $CaB_6$. The reflections corresponding to this second phase named $X_1$ (labelled with ■) have not been identified. They do not match known phases, including boron allotropes, calcium borates, boron (hydr)oxides, alkali borides or borates. The crystallisation of this second phase continues upon further heating, up to 1650 °C (reached within 135 min, Figure IV-3). At this temperature, reflections matching the high-pressure phase $CaB_2O_4$-IV appear (Figure IV-3) and grow upon heating to 1700 °C (dwell time of 30 min). The crystallised phases are conserved upon decompression (Figure IV-3). Notably, based on Scherrer's formula, the crystallite size of $CaB_6$ is estimated to *ca.* 15-20 nm, a small size considering the high temperature treatment and relatively small grain growth compared to the initial sample (12-15 nm crystallite size). The XRD pattern recovered after return at room temperature and pressure is magnified in Figure IV-4. Note that the reflections shift to lower angles due do decompression, as expected.

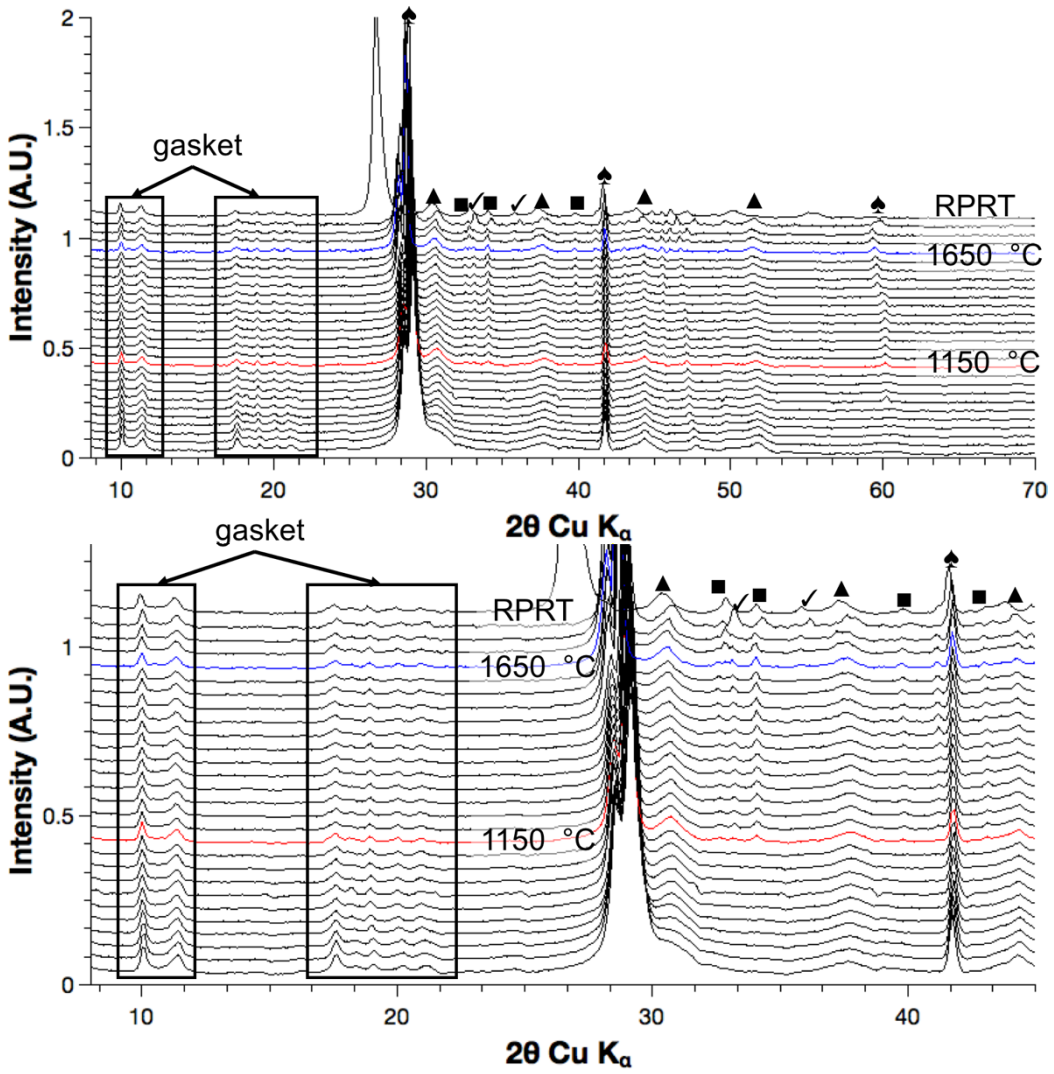


**Figure IV-3.** ***In situ*** **XRD patterns of $CaB_6$/B nanocomposite, methanol washed, and treated at 5 GPa and maximum 1700 °C. Top: overview. Bottom: enlargement of the area of interest.** ***h*****-BN is labelled with ♠, $CaB_6$ with ▲, $CaB_2O_4$-IV with black ✓ and $X_1$ with ■. The black frames indicate the reflections corresponding to the gasket. The bottom pattern corresponds to room temperature at 5 GPa. The pattern in red corresponds to the onset of $X_1$ crystallisation, the pattern in blue to the onset of $CaB_2O_4$-IV crystallisation.**

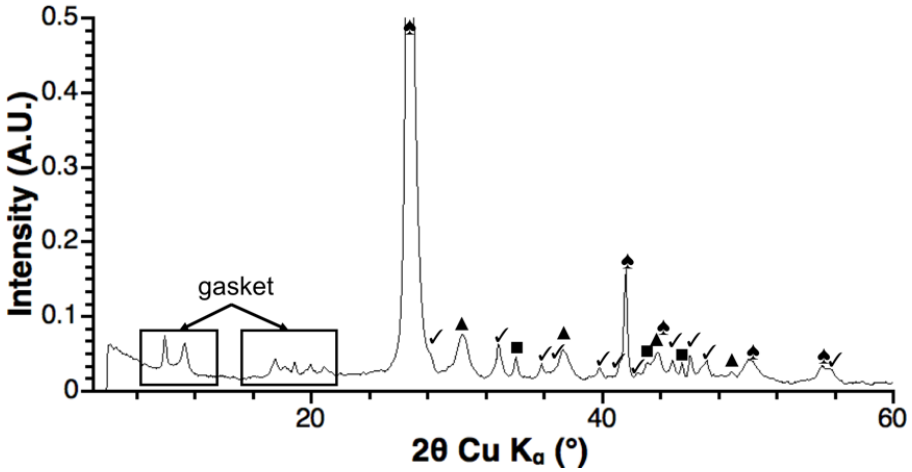


**Figure IV-4. Powder XRD pattern of a $CaB_6$/B nanocomposite washed with methanol and treated at 5 GPa and 1700 °C, after cooling and decompression (but still in its amorphous gasket) following an *in situ* experiment. *h*-BN is labelled with ♠, $CaB_6$ with ▲, $CaB_2O_4$-IV with ✓ and $X_1$ with ■. The black frames indicate the reflections corresponding to the gasket.**

Although the reflections corresponding to $X_1$ could not be indexed, HRTEM analysis shows interesting results. In first place, the conservation of $CaB_6$ is shown: numerous zones show lattice fringes consistent with the $CaB_6$ structure (Figure IV-5). The nanostructure preservation is confirmed, as most particles have a size under 30 nm (Figure IV-5). As described in Chapter III, nanostructure conservation is attributed to the diffusion-limiting role of both high pressure and the matrix. At the edges of the matrix, some regions also show particles (20-60 nm) exhibiting the structure of β-B (HRTEM Figure IV-6). The small proportion of these particles would presumably be responsible for the absence of β-B-associated reflections on the XRD pattern.

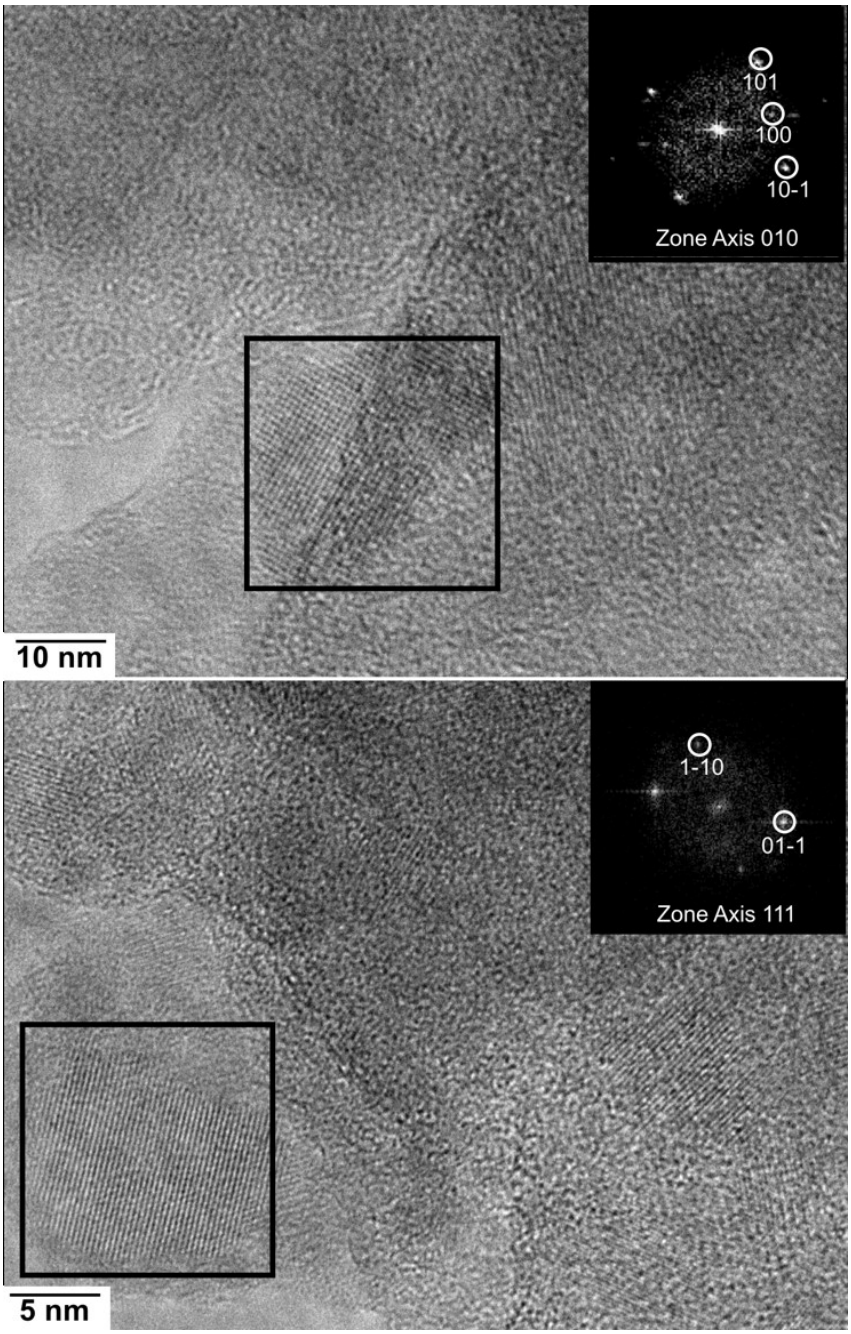


**Figure IV-5. HRTEM pictures of a $CaB_6$/B nanocomposite washed with methanol and treated at 5 GPa and 1700 °C. Insets show the FFT patterns of zones in black squares. Indexation is made on the $CaB_6$ structure.**

Based on XRD and TEM, we therefore describe a three-components nanocomposite composed of sub-30 nm particles of $CaB_6$, $CaB_2O_4$-IV (in much smaller amounts than in the nanocomposite described in Chapter III) of unknown morphology, and sub-100 nm particles of β-B. Note that β-B could not be detected by XRD, presumably because of its low amount and/or because the most intense corresponding reflections are located in the same region than the gasket's signal. The surprising occurrence of the $CaB_2O_4$-IV phase could originate from the small oxygen amounts provided by adsorbed methanol after purification of the precursor or to sub-optimal transfer conditions leading to accidental air exposure.

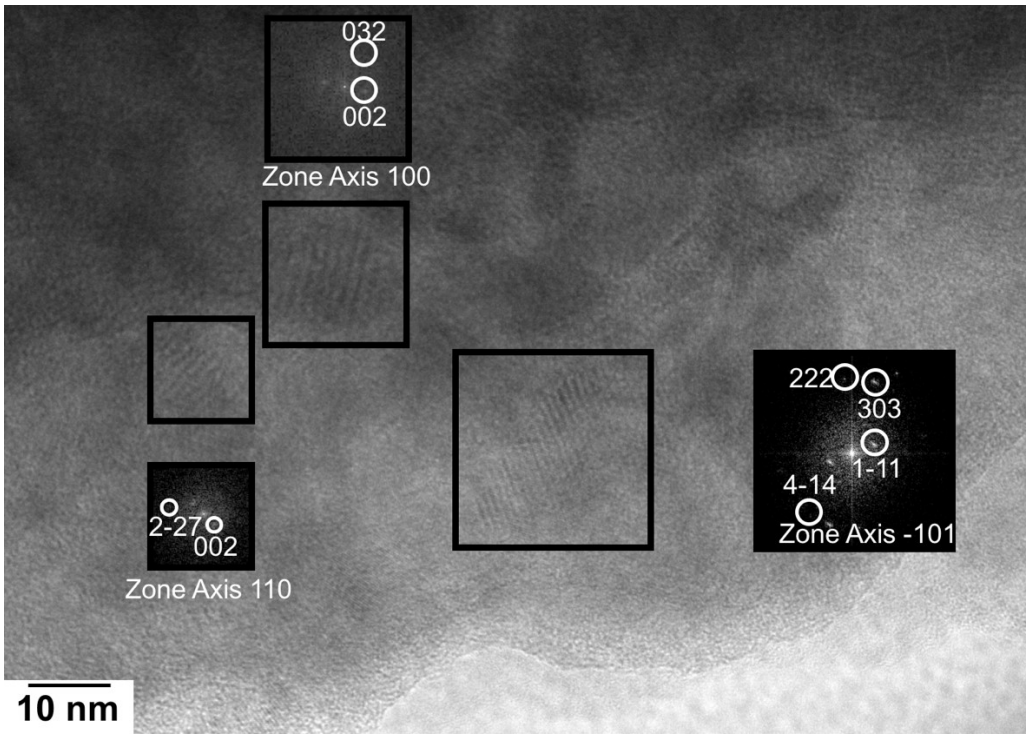


**Figure IV-6. HRTEM picture of $CaB_6$/B nanocomposite washed with methanol and treated at 5 GPa and 1700 °C. Insets show the FFT patterns of zones in black squares. The indexation is made on the β-B structure.**

IV-2-1-b- Experiment at PSICHE/SOLEIL Synchrotron

A similar experiment has been conducted on the PSICHE beamline at SOLEIL Synchrotron, from a different precursor batch. As described earlier, this beamline has a set-up slightly different from that of ID27. The use of a non-monochromatic beam allows fast measurements, but as the emission profile in not homogeneous all-over the energy range considered, the relative intensities cannot be relied on. The XRD patterns upon heating at 5 GPa are shown in Figure IV-7. $CaB_6$ is identified and conserved on the course of the experiment. The two peaks at 24.2 ° and 24.8 ° correspond to the fluorescence of iodine (traces of iodine from the solvent salts are present, as discussed in Chapter II), due to the use of a white beam. Crystallisation of a second phase starts around 1000 °C, at lower temperature than in the previous experiment (1150 °C). This phase is conserved up to 1400 °C (total time to reach temperature: 45 min, dwell time: 45 min) It cannot be indexed in this case too and is named $X_2$ (labelled with □), the reflections of which differ from that of $X_1$ (■). Note that this sample does not exhibit $CaB_2O_4$-IV, the occurrence of which in previous experiment at ESRF is then attributed to sub-optimal transport conditions leading to contamination with air. According to the Scherrer's formula, the particle size of $CaB_6$ after treatment is 16-20 nm in agreement with the previous experiment at ESRF, thus confirming the very limited grain growth in these composite systems. Further phase identification with the help of HRTEM was impeded by strong contamination under the electron beam.

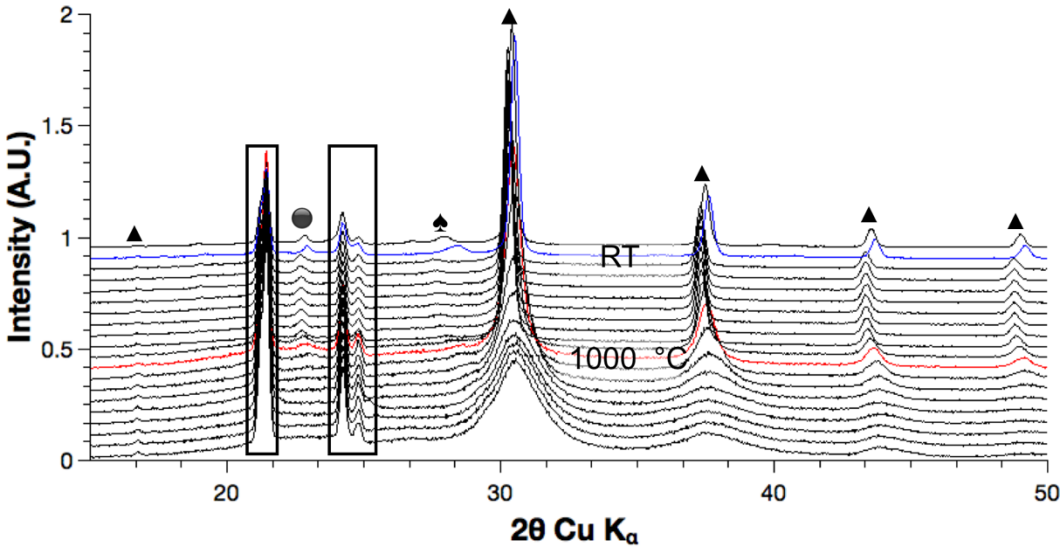


**Figure IV-7 *In situ* XRD patterns of a $CaB_6$/B nanocomposite washed with methanol and treated at 5 GPa and maximum 1400 °C. *h*-BN is labelled with ♠, $CaB_6$ with ▲ and $X_2$ with □. The black frames indicate the iodide fluorescence signal and associated artifacts. The pattern in red corresponds to the onset of the $X_1$ crystallisation, the pattern in blue to post-quenching to room temperature, the top pattern after recovery at room pressure and room temperature.**

Although *in situ* experiments did not enable phase identification, they unveiled the domains of pressure and temperature where phase transitions occur. Some discrepancies between both experiments, such as the occurrence or not of a calcium borate, call for more precise structural characterisations. Hence, the next part focuses on experiments carried out in the (P, T) conditions identified in the *in situ* experiments but with no *in situ* control and only "*post mortem*" characterisation: the samples are characterised after gasket opening under inert atmosphere. The experiments are compared in Table IV-1, table that will be filled along this chapter.

**Table IV-1. Comparison of *in situ* HPHT experiments on a $CaB_6$/B nanocomposite.**

| Experiment | XRD | HRTEM |
|---|---|---|
| 1350 °C 45/90 | $CaB_6$ +$X_2$ | β-B |
| 1350 °C 8/90 | $CaB_6$+$X_2$ | β-B |
| 1400 °C 45/45 (PSICHE) | $CaB_6$+$X_2$ | N/A |
| 1550 °C 8/90 | $CaB_6$+$CaB_2O_4$-IV+$X_2$ | β-B+$CaB_2O_4$-IV |
| 1700 °C 75/30 (ID27) | $CaB_6$+$CaB_2O_4$-IV+$X_1$ | $CaB_6$+β-B+$CaB_2O_4$-IV |
| 1750 °C 8/10 | $CaB_6$+$X_2$ | β-B |

### IV-2-2- *Ex situ* experiments

All the following experiments were conducted at 5 GPa in a Paris-Edinburgh cell, using 10 mm assemblies, loaded and opened under argon as described earlier.

#### IV-2-2-a- Heating at 1350 °C

At 5 GPa, heating at 1350 °C (45 min ramping, 90 min dwell time before quenching, described as “1350 °C, 45/90” in the following) leads to crystallisation of the matrix, as shown by XRD (Figure IV-8). The phase crystallised is similar to that obtained during the *in situ* experiment at PSICHE, the so-called $X_2$ phase, thus confirming that extended oxidation was an artifact in the ESRF experiment. No evidence of the borate $CaB_2O_4$-IV is detected. Another experiment with a 8 min heating ramping (1350 °C, 8/90) yields the same $X_2$ phase, so that the influence of the heating rate is limited. The $CaB_6$ particle size is in the 15-20 nm range for both experiments according to the Scherrer’s formula, although no $CaB_6$ particles could be identified by (HR)TEM (Figure IV-9). Yet, HRTEM pictures show objects from 40 to 150 nm in size, exhibiting lattice fringes consistent with a β-B structure, though not detected on the XRD patterns, probably due to the small proportion of β-B. The boride particles are probably hidden by the crystalline matrix, as calcium exhibits a low electron contrast versus boron. Hence, the samples obtained at 1350 °C in the course of the *ex situ* experiment and the *in situ* study at SOLEIL are similar and exhibit nanocrystalline β-B, $CaB_6$ and a presumably new phase called $X_2$, which structure could not be determined in the framework of this PhD work. Note that the similar experiment monitored *in situ* at ID27 (ESRF) but with air contamination yields β-B, $CaB_6$, but also $CaB_2O_4$-IV and another unreported phase $X_1$, with XRD reflections different from $X_2$ (Figure IV-10).

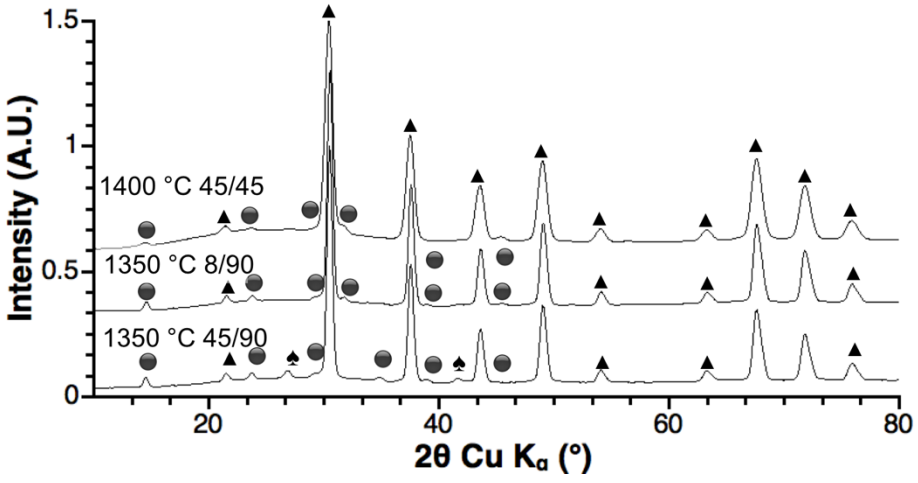


**Figure IV-8. XRD patterns of the $CaB_6$/B nanocomposite, after HPHT treatment at 5 GPa and various thermal treatments. The experiment at 1400 °C 45/45 is the experiment conducted at SOLEIL. *h*-BN is labelled with ♠, $CaB_6$ with ▲ and $X_2$ with □.**

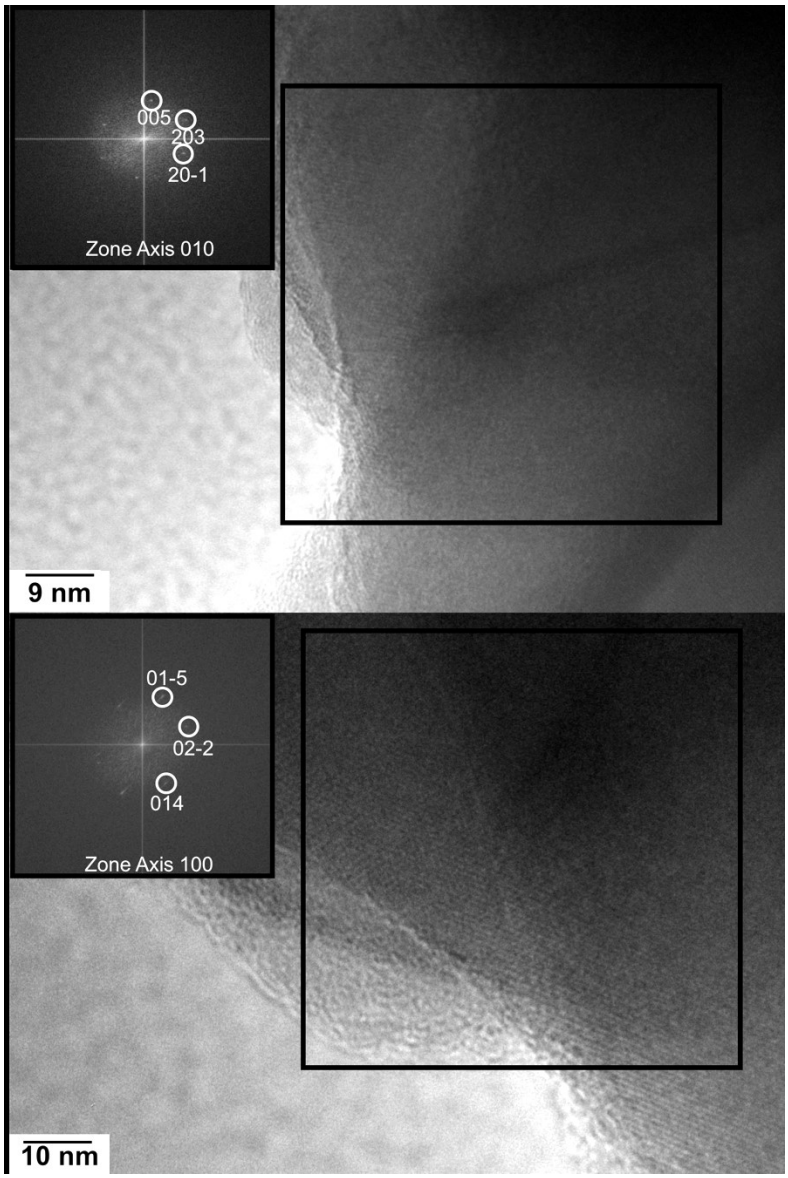


**Figure IV-9. HRTEM pictures of the sample heated at 1350 °C (45 min/90 min). Insets show FFT of zones in black squares, indexed along the β-B structure.**

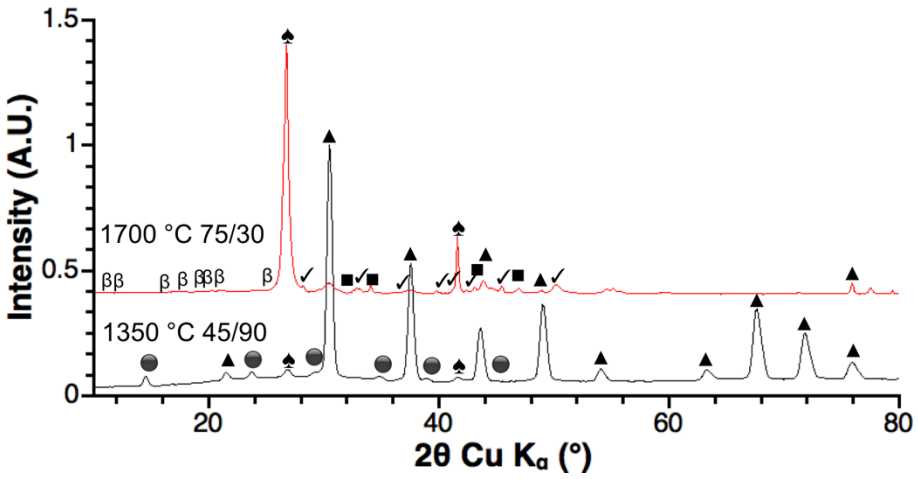


**Figure IV-10. XRD pattern of a $CaB_6$/B nanocomposite treated at 1350 °C (8 min/90 min), compared to the sample obtained at ESRF's ID27 (heated at 1700 °C). *h*-BN is labelled with ♠, $CaB_6$ with ▲ and $X_2$ with □. As reference, the main β-B expected reflections are indicated with β.**

IV-2-2-b- Heating at 1550 °C

For a sample heated at 1550 °C (8 min, 90 min), the XRD pattern (Figure IV-11) also shows conservation of nanostructured $CaB_6$. Reflections corresponding to the $X_2$ phase identified at 1350 °C are present, along with reflections associated to $CaB_2O_4$-IV (notably the most intense at 33 °). This is confirmed by HRTEM (Figure IV-12), which shows $CaB_2O_4$-IV nanoparticles in the outer parts of the matrix (Figure IV-12a). In the inner part, crystalline structures can be indexed as β-B (Figure IV-12b), though again it is not seen on the XRD pattern.

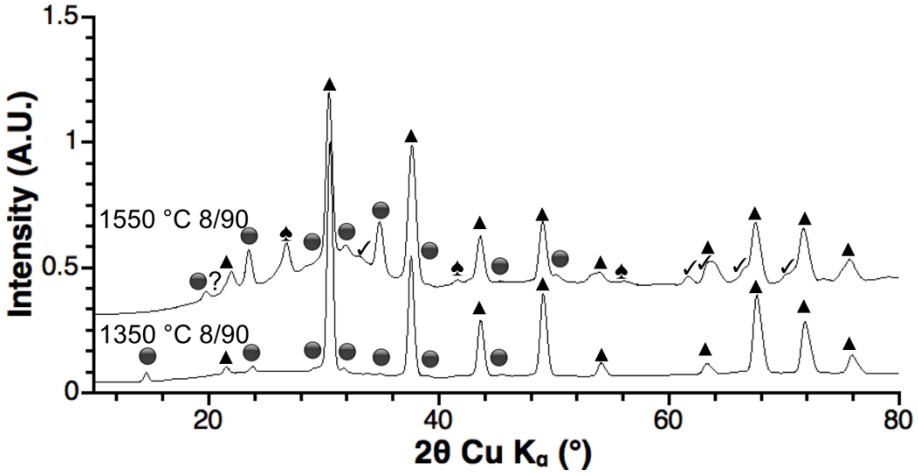


**Figure IV-11. XRD pattern of $CaB_6$/B nanocomposite, treated at 1350 °C (8 min/90 min) and treated at 1550 °C (8 min/90 min). *h*-BN is labelled with ♠, $CaB_6$ with ▲ and $X_2$ with □.**

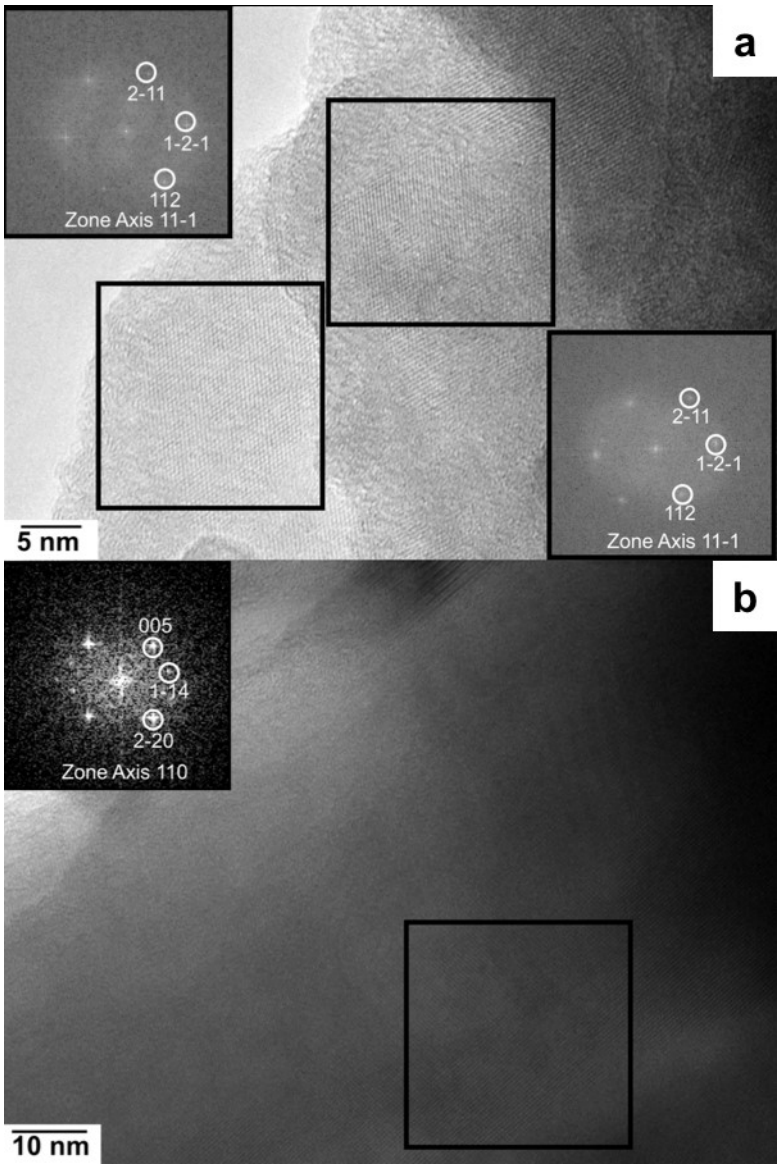


**Figure IV-12. HRTEM pictures of a $CaB_6$/B nanocomposite treated at 1550 °C (8 min/90 min). Insets: FFT of zones in black squares, indexed either along $CaB_2O_4$-IV (a) or β-B (b) structures.**

The results obtained for the $CaB_6$/B nanocomposite are summarised in Table IV-1 and based on HRTEM observations, $X_2$ is attributed to β-B.

IV-2-2-c- Heating at 1750 °C

Heating was also performed at 1750 °C (8 min, 10 min). $CaB_6$ is again conserved, as shown by the XRD pattern (Figure IV-13). According to the Scherrer's formula, the particle size is *ca.* 15-20 nm. The XRD pattern exhibits reflections corresponding to the $X_2$ phase, along with two other reflections (identified as hollow circles in Figure IV-13).

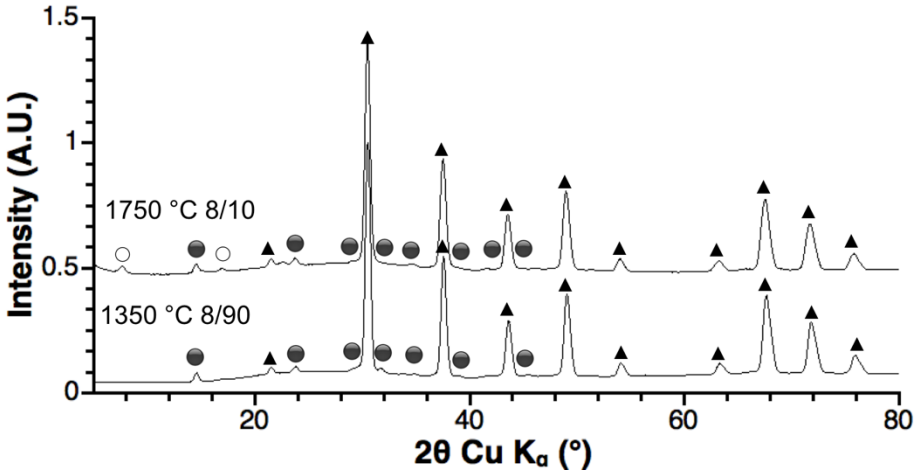


**Figure IV-13. XRD pattern of a $CaB_6$/B nanocomposite treated at 1350 °C (8 min/90 min) and treated at 1750 °C (8 min/10 min). *h*-BN is labelled with ♠, $CaB_6$ with ▲, $CaB_2O_4$-IV with ✓, $X_2$ with □ and reflections associated to β-B with ○.**

In this case again, the size and morphology of $CaB_6$ particles cannot be investigated upon TEM/HRTEM analysis as all pictures show strongly faceted crystalline particles (Figure IV-14) that do not match the $CaB_6$ structure, likely hiding boride particles with low contrast. However, the XRD pattern exhibits a reflection at 7.68 ° (which corresponds to a d-spacing of 11.5 Å), relatively close to the (002) distance of β-B (11.89 Å). Considering the structure of β-B (**a** = 10.1 Å, **c** = 23 Å in the hexagonal setting, based on the ICSD entry by Callmer)[15], it is possible to index the FFT patterns along β-B (Figure IV-15) with about 6 % and 4 % reduction for **a** and **c** parameters respectively. Hence, distorted β-B is obtained as nanoparticles, in a nanocomposite containing also $CaB_6$ nanocrystals. The small particle size of β-B is particularly interesting when it comes to mechanical properties. In virtue of the HPE, the hardness should be higher than that of bulk β-B, keeping in mind that the critical particle size for β-B in the framework of the HPE detailed in chapter I remains unknown, due to the lack of nanostructured occurrences of β-B. The absence of the corresponding XRD reflections is interpreted as a consequence of the limited size of the β-B particles, yielding a low number of unit cells in each crystal and possibly numerous defects.

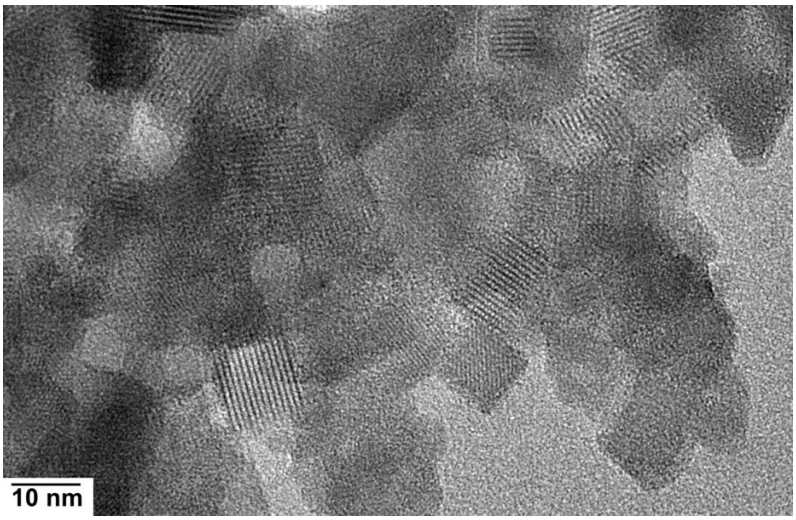


**Figure IV-14. HRTEM picture of β-B nanoparticles in a $CaB_6$/B nanocomposite treated at 1750 °C (8 min/10 min).**

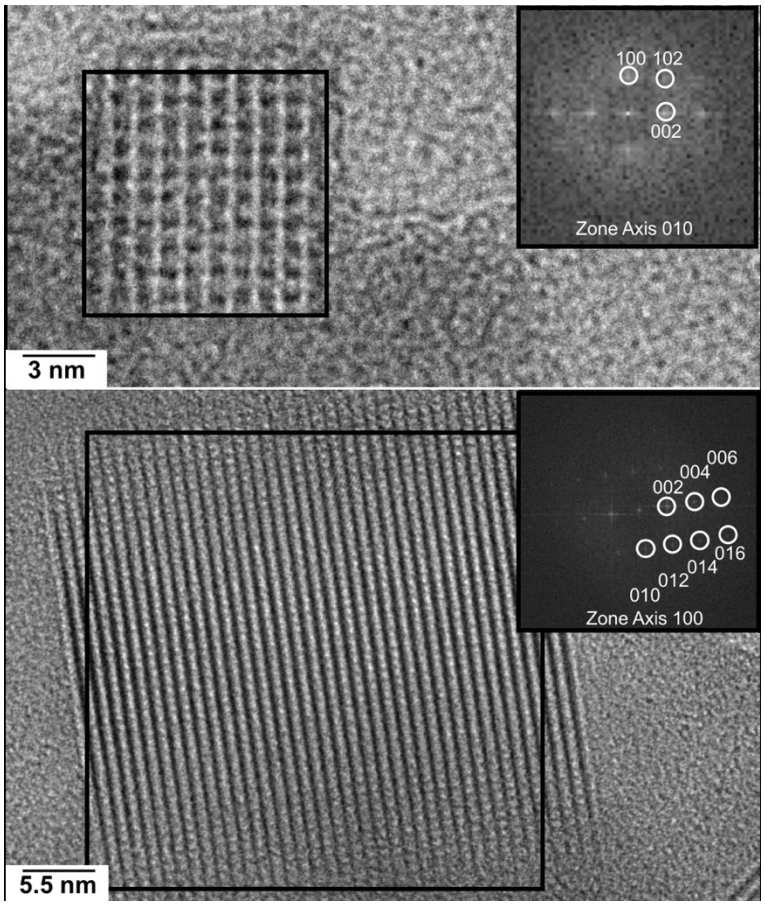


**Figure IV-15. HRTEM picture of β-B nanoparticles in a $CaB_6$/B nanocomposite treated at 1750 °C (8 min/10 min). Inset: FFT of the zone in black square. The d-spacings are indexed along the structure of β-B.**

Considering the high temperature treatment and results detailed in chapter III, the crystallisation of $CaB_2O_4$-IV could be envisaged but this phase is not detected nor on XRD patterns nor on HRTEM micrographs. The crystallisation of $CaB_2O_4$-IV is presumably favoured by long thermal treatments, as it is crystallised in the experiment at 1550 °C, 8/90. Note that all *ex situ* experiments were conducted from the same precursor batch.

The possibility to crystallise the matrix while conserving a nanostructured boride is confirmed. In the case of $CaB_6$/B, the use of a precursor with limited oxygen content allows avoiding borate crystallisation in most cases as $CaB_2O_4$-IV is only crystallised at 1550 °C (8/90) for *ex situ* experiments at long dwell time. The crystallisation of $CaB_2O_4$-IV can be envisaged as the consequence of (i) air contamination (ii) oxygen contamination from residual adsorbed methanol. Based on HRTEM observations, the matrix is crystallised into nanoparticles with a distorted β-B structure. However, this phase is not identified on XRD patterns, which may be due to the small amount crystallised *vs.* $CaB_6$, to the small particle size compared to that of the unit cell or to numerous defects in the particles. The results of the $CaB_6$/B nanocomposite are summarised in Figure IV-16.

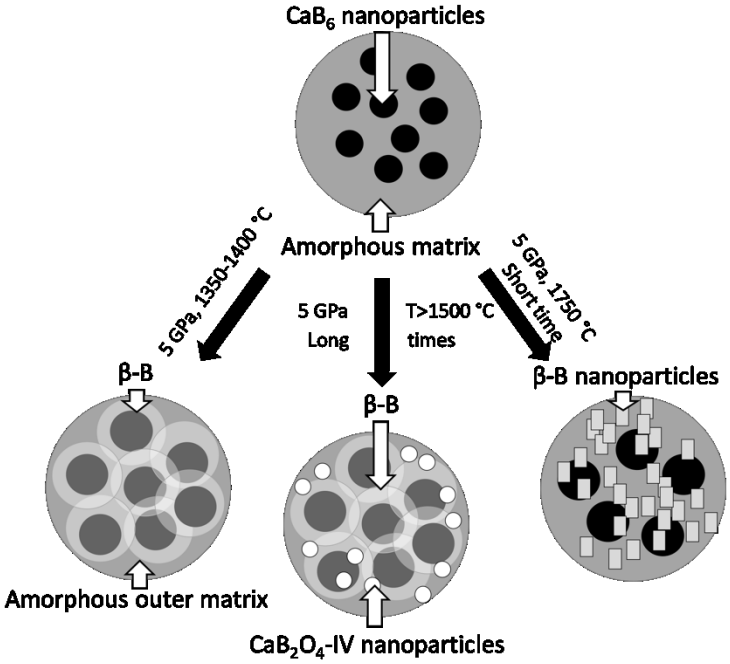


**Figure IV-16. Matrix evolution scheme for the $CaB_6$/B nanocomposite.**

Among prospects, one can envisage to heat for much longer dwell times, in order to allow particle growth and facilitate structural characterisation.

## IV-3- Hafnium diboride

### IV-3-1- *In situ* XRD in Paris-Edinburgh cell

This experiment was conducted at ESRF's ID27 beamline, at 5 GPa, using a 7/2.4 mm assembly. A $HfB_2$/B composite precursor, synthesised in iodide salts and washed with methanol was studied with *in situ* XRD. As for the calcium-based composite, XRD (Figure IV-17) shows no phase transition upon compression. The behaviour upon heating is however different. Indeed, crystallisation of $HfB_2O_5$ starts at 900 °C. On the opposite, the calcium borate in the $CaB_6$/B system crystallised only as third phase at much higher temperature (1550 °C for 90 min dwell times, 1650 °C for few minutes dwell time). $HfB_2O_5$-associated reflections continue growing up to 1270 °C, then start to diminish. At 1500 °C, all $HfB_2O_5$ peaks disappear, in agreement with the absence of $HfB_2O_5$ lattice fringes on HRTEM pictures (Figure IV-18). Keeping the temperature at 1500 °C for 30 min does not further modify the XRD pattern (Figure IV-17).

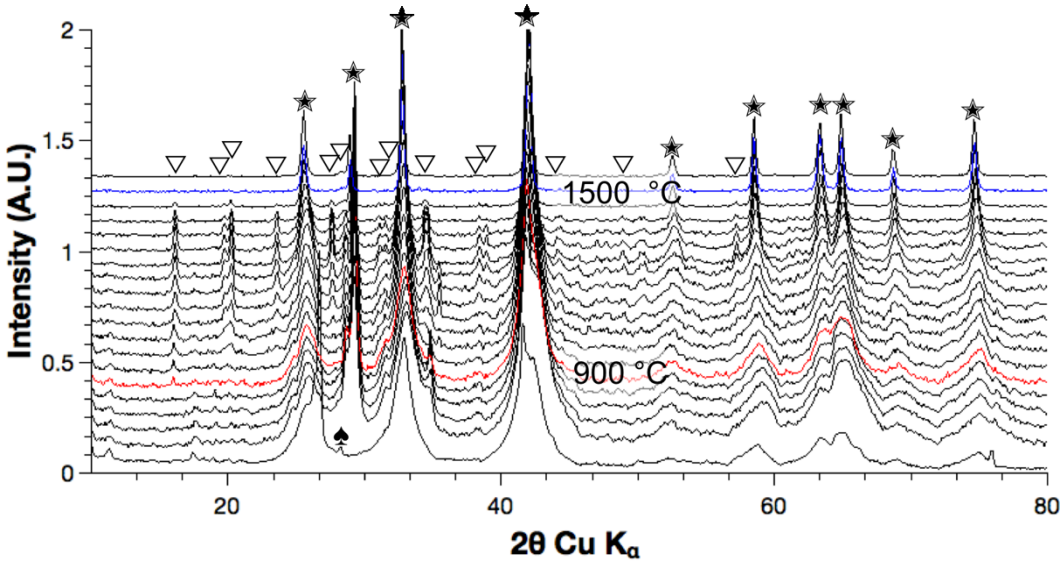


**Figure IV-17. *In situ* XRD patterns recorded during HPHT treatment of a $HfB_2$/B nanocomposite. The bottom XRD pattern is taken after compression at 5 GPa at room temperature, the pattern in red at 5 GPa and 900 °C, where matrix crystallisation starts. The pattern in blue corresponds to 1500 °C, where $HfB_2O_5$ reflections have completely disappeared. The pattern in black at the top corresponds to the return to room temperature (quench). *h*-BN are indicated with ♠, $HfB_2$ with ★, $HfB_2O_5$ with ▽.**

The original synthesis of $HfB_2O_5$ by Huppertz *et al.* was done at 7.5 GPa and 1100 °C.[16] Afterward, the authors tested the thermal stability at room pressure of the borate by heating in a quartz capillary.[16] The XRD patterns (Figure IV-19) show that above 800 °C, $HfB_2O_5$ decomposes into $HfO_2$ and supposedly $B_2O_3$.[16] Further heating (above 1000 °C) causes side reactions with the quartz capillary, leading to the formation of $HfSiO_4$. Accordingly, in the present *in situ* experiment at 5 GPa, thermal decomposition of $HfB_2O_5$ is likely to start at 1270 °C. Indeed, the onset temperatures of reactions or phase transitions are usually shifted to higher values under high pressure.[17]

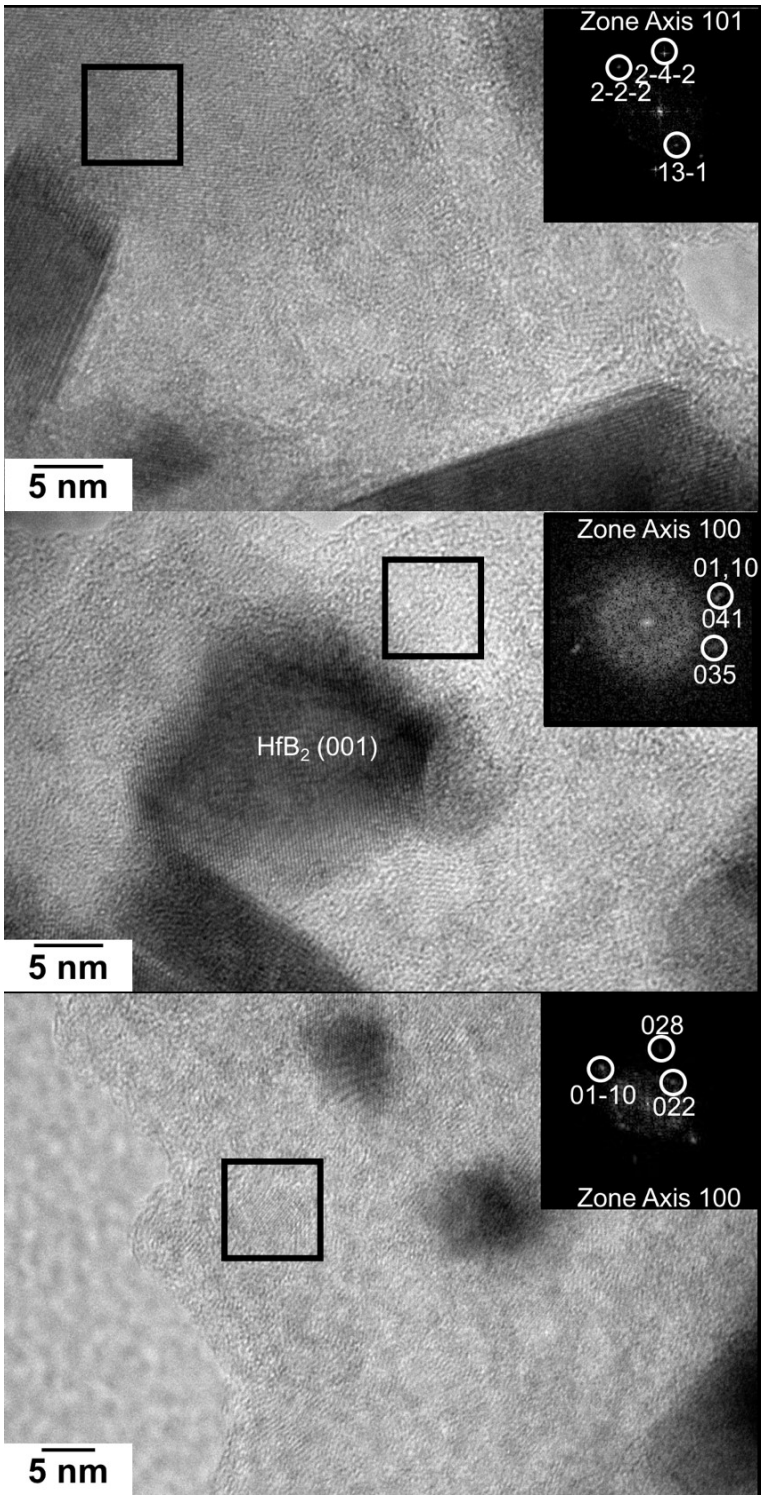


**Figure IV-18. HRTEM pictures of a $HfB_2$/B nanocomposite treated at 5 GPa and 1500 °C (30 min dwell). The insets correspond to FFT of black squares, indexed along the β-B structure.**

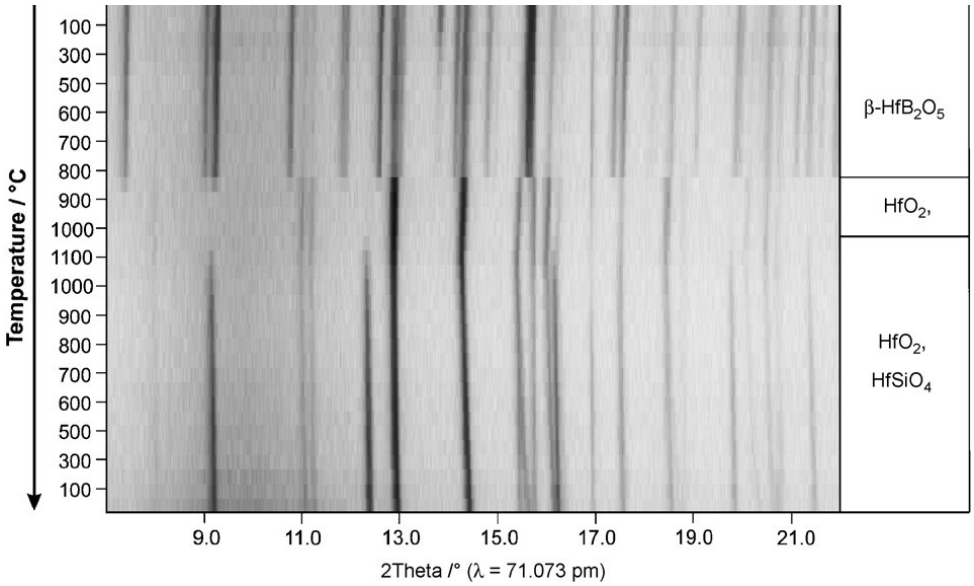


**Figure IV-19. XRD powder patterns of $HfB_2O_5$ under heating at room pressure in a quartz capillary from ref [16]. No changes but thermal dilatation occur up to 800-850 °C. Above $HfB_2O_5$ is decomposed into $HfO_2$ and supposedly $B_2O_3$. From 1000 °C, $HfO_2$ reacts with the quartz tube, forming $HfSiO_4$.[16]**

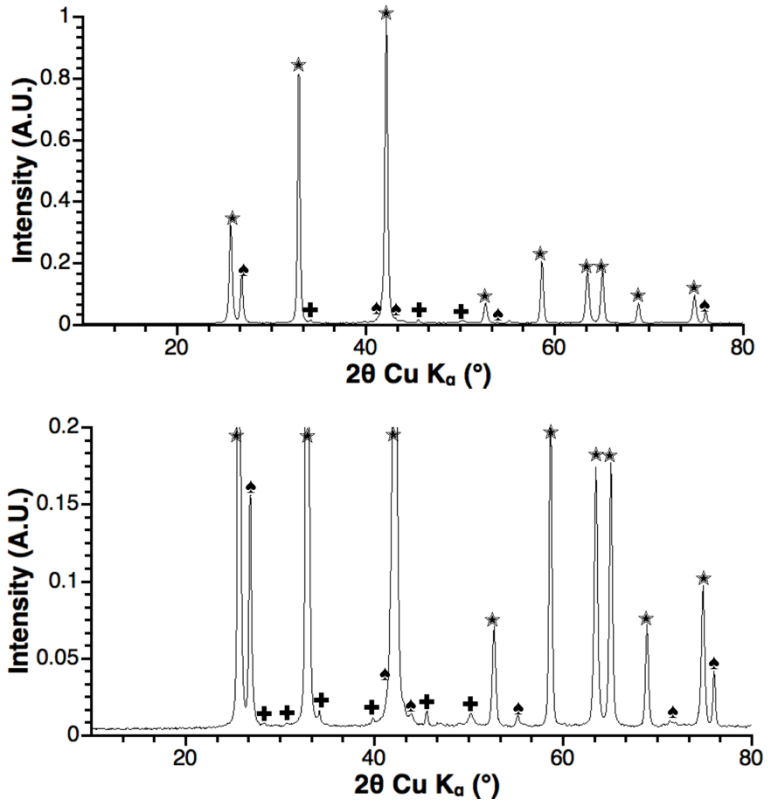


**Figure IV-20. XRD pattern of a $HfB_2$/B nanocomposite treated at 5 GPa and 1500 °C (30 min dwell). Top: full pattern. Bottom: zoom in on low intensities. *h*-BN reflections are indicated with ♠, $HfB_2$ with ★ and $Y_1$with ✚.**

For the $HfB_2$/B nanocomposite, heating above the temperature of complete decomposition of the borate and up to 1500 °C produces reflections that cannot be indexed on known phases, notably $HfO_2$ nor boron oxides, boron allotropes, hafnium borides and borates nor alkali borides and borates (Figure IV-20). The corresponding peaks are conserved upon temperature quenching and decompression (the absence of $HfB_2O_5$ after return to room pressure and temperature is also confirmed) and associated to a solid named $Y_1$ (Figure IV-20). After HPHT treatment, the size of the $HfB_2$ crystallites is 35-40 nm according to the Scherrer's formula. HRTEM observations (Figure IV-18) show indeed $HfB_2$ particles with a size in the 30-40 nm range, along with smaller particles of the 10-15 nm diameter, close to the initial particle size. In this size range, HRTEM also shows numerous crystalline domains, matching the structure of β-B (Figure IV-18). The absence of β-B-associated reflections on the XRD patterns can be attributed to two causes: the small proportion of β-B *vs.* $HfB_2$ and the atomic form factor, largely in favour of $HfB_2$: a boron only phase would exhibit very small relative intensities. The origin of two populations of $HfB_2$ particles can be tentatively explained as follows: bigger particles should be the outcome of initial particles sintering, which is consistent with the particle size reached in Chapter III; while the smaller particles may correspond to particles crystallised after $HfB_2O_5$ decomposition. Indeed, the latter results in boron oxide released as gas species.[16] The matrix is then likely crystallised into $HfB_2$ and β-B. As in the $HfB_2O_5$/$HfB_2$ composite, part of the matrix is still amorphous and may act as boron reservoir. The occurrence of a gas release along heating is also supported by the inside-to-outside deformation of experimental *h*-BN capsules and graphite heater recovered.

In brief, the material obtained after the *in situ* experiment à 5 GPa up to 1500 °C is described as a $HfB_2$/β-B nanocomposite obtained through a $HfB_2$/$HfB_2O_5$ intermediate, where both components are nanostructured. The overall "nanocookie" structure is conserved after the HPHT treatment, while part of the matrix is likely still amorphous (Figure IV-18). The nature of $Y_1$ is yet to be determined.

### IV-3-2- *Ex situ* experiments

As for the $CaB_6$/B nanocomposite, many experiments have been conducted with *ex situ* characterisations. The XRD pattern of the $HfB_2$/B sample treated at 5 GPa and 1550 °C (8 min/90 min) (Figure IV-21) does not show any other reflections besides $HfB_2$ and *h*-BN (the sample capsule). Notably the reflections associated to $Y_1$ are not detected. $HfB_2$ is obtained with a particle size in the 15-20 nm range, according to the Scherrer's formula.

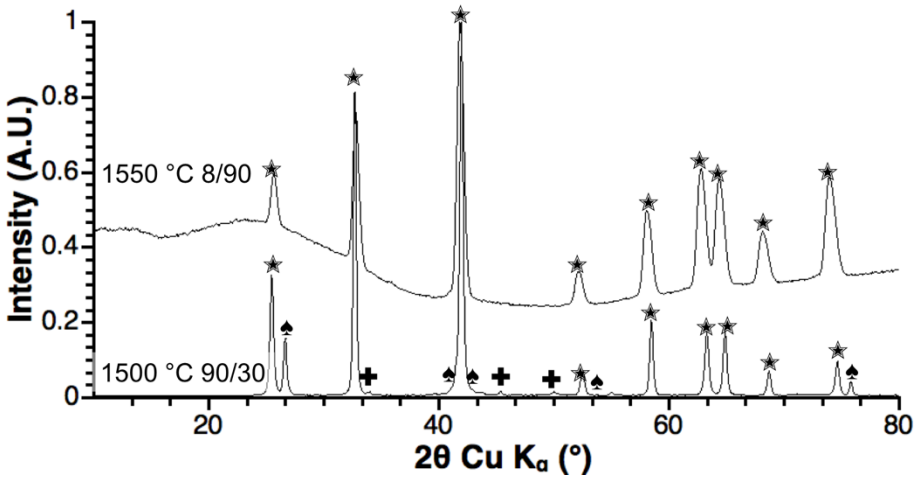


**Figure IV-21. XRD patterns of a $HfB_2$/B nanocomposite *ex situ* HPHT treatments at 5 GPa: 1550 °C (8 min/90 min) and 1500 °C (90 min/30 min). *h*-BN is indicated with ♠, $HfB_2$ with ★ and $Y_1$with ✚.**

TEM observations (Figure IV-22) show particles 8-15 nm in size, in agreement with XRD. These particles, attributed to $HfB_2$, are surrounded by particles (Figure IV-22) in the 50-80 nm size range that exhibit a “hourglass/bow tie” motif. They match the structure of β-B, with reduced cell parameters close to those seen in the case of $CaB_6$/B (**a** = 10.1 Å, **c** = 23 Å, hexagonal setting). Moreover, as the lattice fringes constituting the chevron pattern correspond all to (001) lattice planes, these particles are polycrystalline. As for the Ca-based system, the absence of XRD reflections impedes more accurate determination of the cell parameters. The reduction of the β-B cell parameters may be attributed to the small size of individual crystallites constituting the “hourglass particles” or to numerous defects.

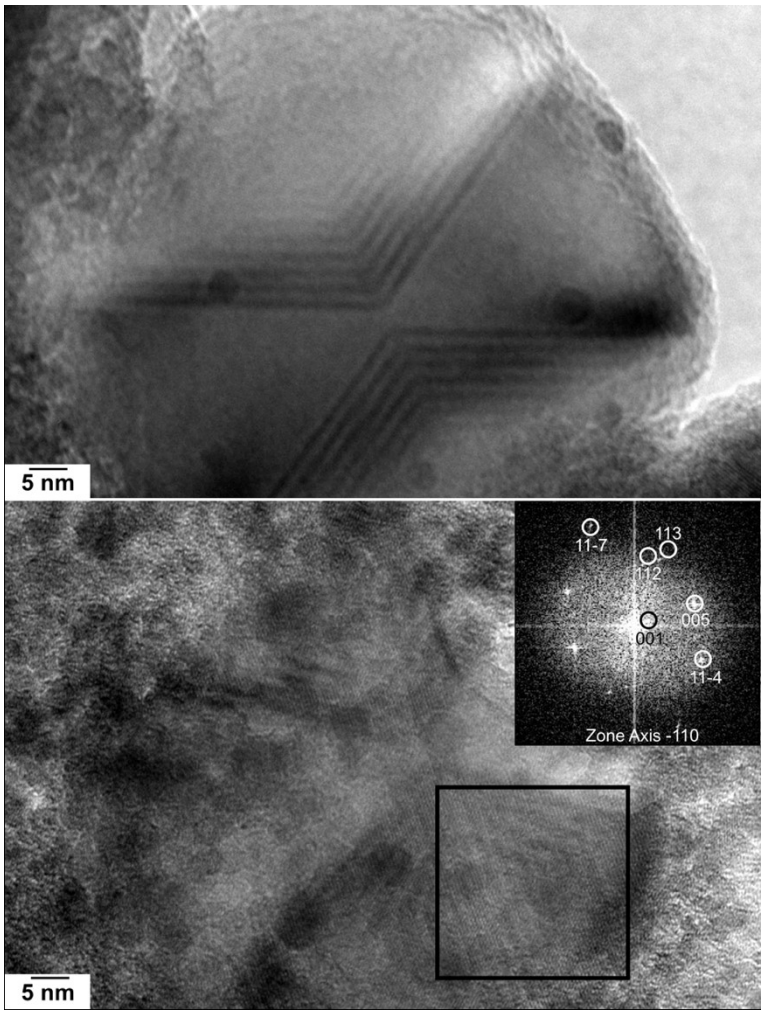


**Figure IV-22. HRTEM pictures of a $HfB_2$/B nanocomposite treated at 5 GPa and 1550 °C 8/90. Both pictures show crystalline objects that have the structure of β-B. Bottom inset: FFT of zone in black square (enlarged).**

The same precursor was treated at 5 GPa and 1750 °C (8 min/10 min). The XRD pattern (Figure IV-23) shows conservation of $HfB_2$, with a particle size in the 14-19 nm range. Unlike the previous experiment, other reflections are present, though they cannot be indexed on known phases nor they match the solid $Y_1$. They are associated with a solid $Y_2$. The crystallite size associated to these reflections is 20-22 nm according to the Scherrer's formula, which is consistent with HRTEM observations (Figure IV-24) that show numerous particles with a size inferior to 25 nm. According to HRTEM, these particles display the structure of β-B, with reduced cell parameters (**a** = 10.9 Å, **c** = 23.5 Å) that are consistent with the peaks at 14.7 ° ((103), 6.042 Å) and 28.1 ° ((300), 3.164 Å) on the XRD pattern (Figure IV-23). However, these reflections have null (103) or very weak intensities (6 % for (300)) on reference β-B patterns, thus pointing out slight symmetry or site occupancies changes. Therefore, on the base of HRTEM, the $Y_2$ phase is associated to distorted β-B.

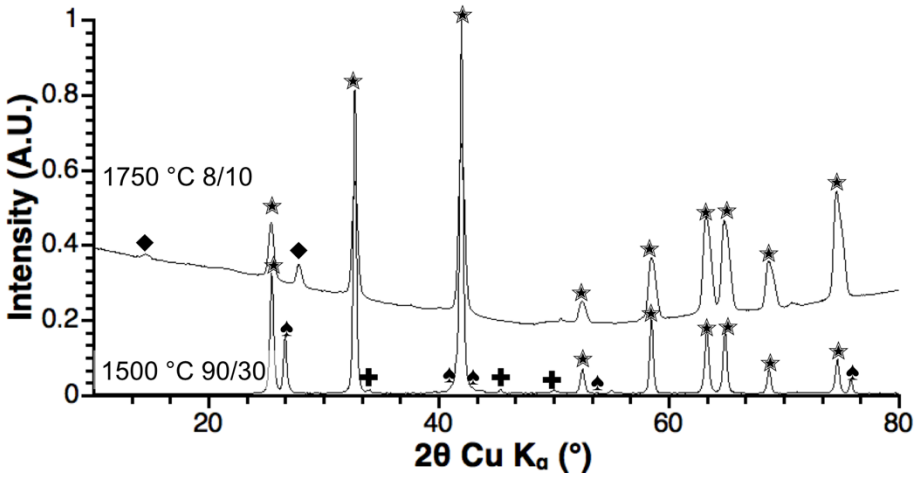


**Figure IV-23. XRD patterns of a $HfB_2$/B nanocomposite treated at 5 GPa: 1750 °C 8/10 and 1500 °C 90/30. *h*-BN is indicated with ♠, $HfB_2$ with ★, $Y_1$ with ✚ and $Y_2$ with ♦.**

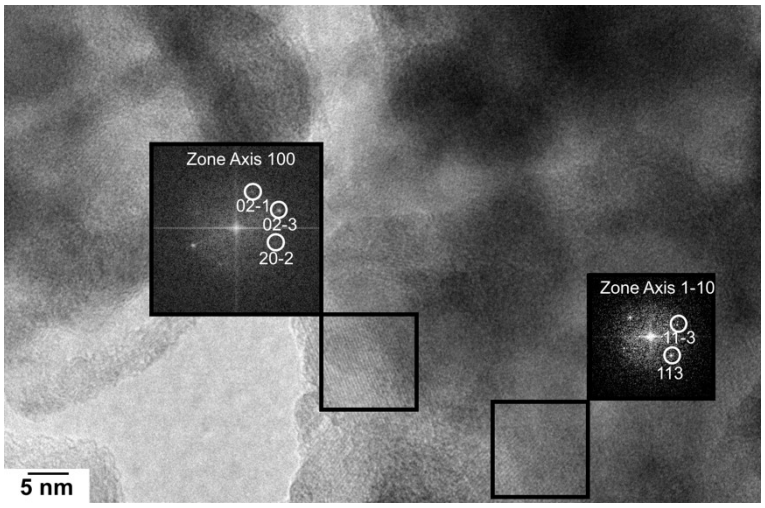


**Figure IV-24. HRTEM picture of a $HfB_2$/B nanocomposite, treated at 5 GPa and 1750 °C 8/10. Insets: FFT of black square areas, matching the structure of β-B with reduced cell parameters.**

Along with the sub-25 nm particles, bigger particles are observed (Figure IV-25) with a size up to 60 nm. They are again indexed along the β-B structure. These particles exhibit a hourglass/bow tie motif, close to the particles obtained at 1550 °C (8 min/90 min), yet smaller. Therefore, longer thermal treatments, even at lower temperature, likely favour the growth of the “hourglass particles” at the cost of smaller particles. The latter would therefore act as precursors for the bigger facetted polycrystalline particles.

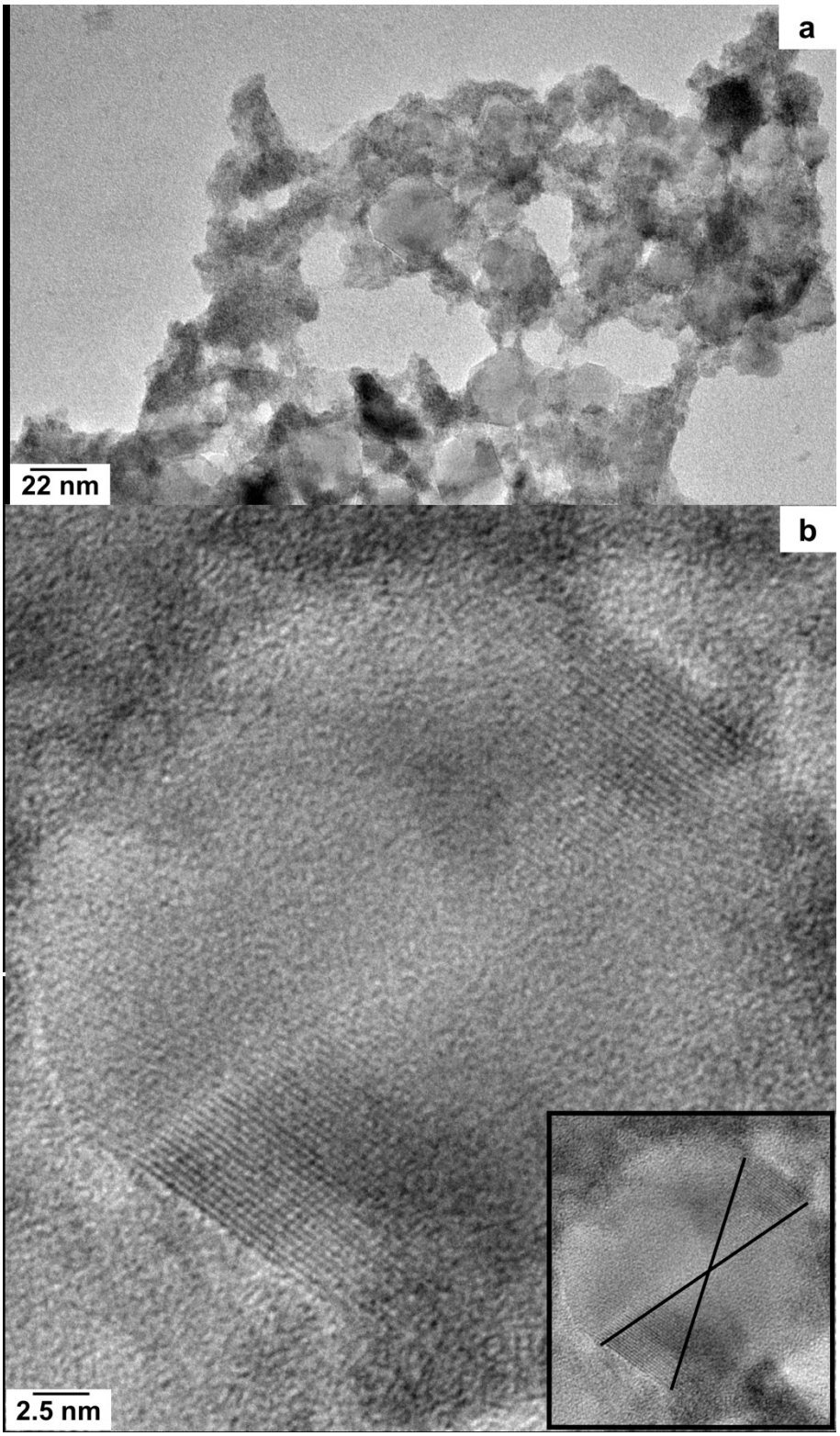


**Figure IV-25. (a) TEM picture of a $HfB_2$/B nanocomposite treated at 5 GPa and 1750 °C 8/10. (b) HRTEM picture of a $HfB_2$/B nanocomposite, treated at 5 GPa and 1750 °C 8/10, the lattice fringes match interplanar spaces of β-B (with reduced cell-parameters). The hourglass-bowtie motif is seen on the crystalline particle and is highlighted with black lines in inset of (b).**

The schematic evolution of the phases in the matrix is shown in Figure IV-26. In the initial nanocomposite, HPHT treatment first leads to the crystallisation of $HfB_2O_5$, accompanied with slight $HfB_2$ particle growth. At higher temperature, the hafnium borate is decomposed, likely into $HfB_2$ and β-B. The latter is obtained with two different morphologies: small isotropic particles and bigger hourglass particles which are favoured for long dwell times. Note that $HfB_2O_5$ has not been obtained in recovered samples from *ex situ* experiments (starting from methanol-washed precursors). Anyway, the experiment at ESRF's ID27 showed that even if the borate is obtained (possibly from accidental exposure to air), it is possible to get rid of the latter, by simply performing thermal treatment above 1500 °C (at 5 GPa).

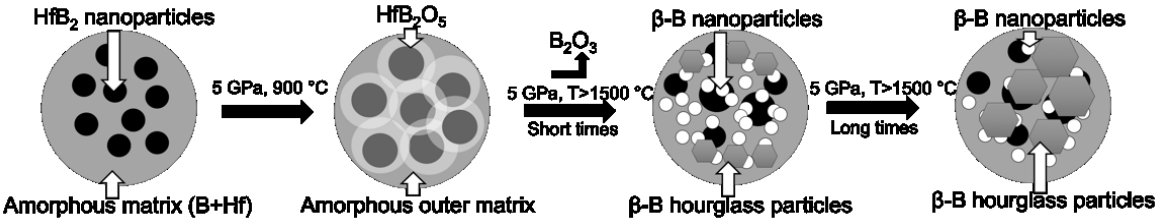


**Figure IV-26. Matrix evolution scheme for the $HfB_2$/B nanocomposite.**

## IV-4- Conclusions & Prospects

This chapter focused on HPHT transformations of precursors with a limited oxygen content. The possibility is demonstrated to crystallise the matrix into a nanostructured material while conserving the boride inclusions both in nature and nanostructure. So far, this approach has been applied to two systems, $HfB_2$/B and $CaB_6$/B. In both cases, the crystallisation of the matrix into nanostructured β-B is demonstrated by the mean of HRTEM, with various particle size (from 20 to 80 nm). In addition to the new boride/borate nanocomposites described in Chapter III, new boride/β-B nanocomposites have been produced. As an ultrahard material, exploiting the Hall-Petch effect on β-B paves the way toward strong improvement of the mechanical properties. Such studies are underway. As nanocomposites are reached, properties investigation is also to be conducted considering the borides' properties, as the intimate mixture of the composites' components may allow combination of their respective properties.

However, numerous questions are yet to be solved. First of all, the behaviour difference regarding borate crystallisation of the two systems: starting from precursors synthesised in chlorine-based salts and washed with water, the two borates $CaB_2O_4$-IV and $HfB_2O_5$ are synthesised in similar conditions (Chapter III). However, using precursors synthesised in iodine-based salts, if $HfB_2O_5$ is crystallised in similar conditions, $CaB_2O_4$-IV is not crystallised before 1550 °C, and only after the crystallisation of a first phase in the matrix, underlining the initial metal's influence in the SMS-derived systems. As discussed in Chapter II, changing the metal has an influence on the nature of the matrix. For cobalt and hafnium for instance, STEM-HAADF shows that the matrix comprises metal clusters, unlike nickel. The

presence of metal clusters in the matrix is likely to impact the crystallisation process at high pressure and temperature. The metal influence is also clearly illustrated by the different β-B particles morphologies obtained: no “hourglass particles” are seen for the calcium-based system. Therefore, using different initial borides to generalise the approach is interesting, to span the wide range of properties displayed by the metal boride family and to study the influence of the boride on boron crystallisation. The stability toward oxidation of samples transformed under HPHT is also to be tested. Indeed, it is clear that the initial amorphous matrix is sensitive to oxidation in air or water. However, boron allotropes share a high chemical inertness (unlike commercial amorphous boron) that stands for bulk materials, as nanostructured boron allotropes are rarely mentioned in the literature, so that once crystallised, the matrix is presumably less sensitive to oxidation. The samples synthesised along this work have been kept in the strict exclusion of air so far, to allow full characterisation before exposure. The exact nature of distorted β-B is also to be examined, notably with careful local composition analysis, to establish if foreign atoms can be responsible for the distortions observed.

Using the same initial nanocomposites, the use of higher pressure (> 10 GPa) is also an axis for future developments, as boron allotropes crystallised in this higher pressure region are harder than β-B.

The last two chapters focused on the nanocomposites systems. The next chapter focuses on HPHT treatment of nanostructured amorphous boron.

## IV-5- References


(1) Oganov, A. R.; Chen, J.; Gatti, C.; Ma, Y.; Ma, Y.; Glass, C. W.; Liu, Z.; Yu, T.; Kurakevych, O. O.; Solozhenko, V. L. *Nature* **2009**, *457* (7231), 863–867.

(2) Oganov, A. R. *Boron Rich Solids*; Orlovskaya, N., Lugovy, M., Eds.; NATO Science for Peace and Security Series B: Physics and Biophysics; Springer Netherlands: Dordrecht, **2011**.

(3) Yu Zarechnaya, E.; Dubrovinsky, L.; Dubrovinskaia, N.; Miyajima, N.; Filinchuk, Y.; Chernyshov, D.; Dmitriev, V. *Sci. Technol. Adv. Mater.* **2009**, *9* (2008), 044209.

(4) Zarechnaya, E. Y.; Dubrovinsky, L.; Dubrovinskaia, N.; Filinchuk, Y.; Chernyshov, D.; Dmitriev, V.; Miyajima, N.; El Goresy, A.; Braun, H. F.; Van Smaalen, S.; Kantor, I.; Kantor, A.; Prakapenka, V.; Hanfland, M.; Mikhaylushkin, A. S.; Abrikosov, I. A.; Simak, S. I. *Phys. Rev. Lett.* **2009**, *102* (18), 8–11.

(5) Oganov, a. R.; Solozhenko, V. L.; Gatti, C.; Kurakevych, O. O.; Godec, Y. *J. Superhard Mater.* **2011**, *33* (6), 363–379.

(6) Wentorf, R. H. *Science* **1965**, *147* (3653), 49–50.

(7) Slack, G. A.; Hejna, C. I.; Garbauskas, M. F.; Kasper, J. S. *J. Solid State Chem.* **1988**, *76* (1), 52–63.

(8) Horn, F. H. *J. Electrochem. Soc.* **1959**, *106* (10), 905.

(9) Parakhonskiya, G.; Dubrovinskaia, N.; Bykova, E.; Wirth, R.; Dubrovinsky, L. *High Press. Res* **2013**, *33* (3), 673–683.

(10) Parakhonskiy, G.; Dubrovinskaia, N.; Dubrovinsky, L.; Mondal, S.; Van Smaalen, S. *J. Cryst. Growth* **2011**, *321* (1), 162–166.

(11) Parakhonskiy, G. Synthesis and investigation of boron phases at high pressures and temperatures, **2012**.

(12) Kurakevych, O. O.; Solozhenko, V. L. *J. Superhard Mater.* **2013**, *35* (1), 60–63.

(13) Besson, J. M.; Nelmes, R. J. *Phys. B Condens. Matter* **1995**, *213-214*, 31–36.

(14) Godec, Y. Le; Dove, M. T.; Redfern, S. A. T.; Tucker, M. G.; Marshall, W. G.; Syfosse, G.; Besson, J.-M. *High Press. Res.* **2001**, *21* (5), 263–280.

(15) Callmer, B. *Acta Crystallogr., Sect. B* **1977**, *33* (6), 1951–1954.

(16) Knyrim, J. S.; Huppertz, H. *J. Solid State Chem.* **2007**, *180* (2), 742–748.

(17) Jiang, J. Z.; Rozeker, W.; Sikorski, M.; Cao, Q. P.; Xu, F. *App. Phys. Lett.* **2004**, *84* (11), 1871–1873.

# Chapter V: HPHT treatments of nanostructured amorphous boron

As discussed in Chapter I, HPHT studies on boron aim at crystallising the different allotropes, though occurrences of most allotropes remain scarce (notably γ[1,2], ε[3] and β-T boron[4]). Also, at the notable exception of the work by Ekimov *et al.* (δ-B synthesis by decaborane decomposition)[5], boron crystallisation studies use either commercial amorphous boron or already crystalline β-B as precursors, though the amorphous character of commercial "amorphous" boron is never assessed. Its XRD pattern (Figure V-1)[6] shows that it is at least partially crystallised along the β-B structure. Yet, the SMS-derived nanostructured boron (nano-$B_{am}$) is genuinely amorphous, as shown by XRD and HRTEM in Chapter II.

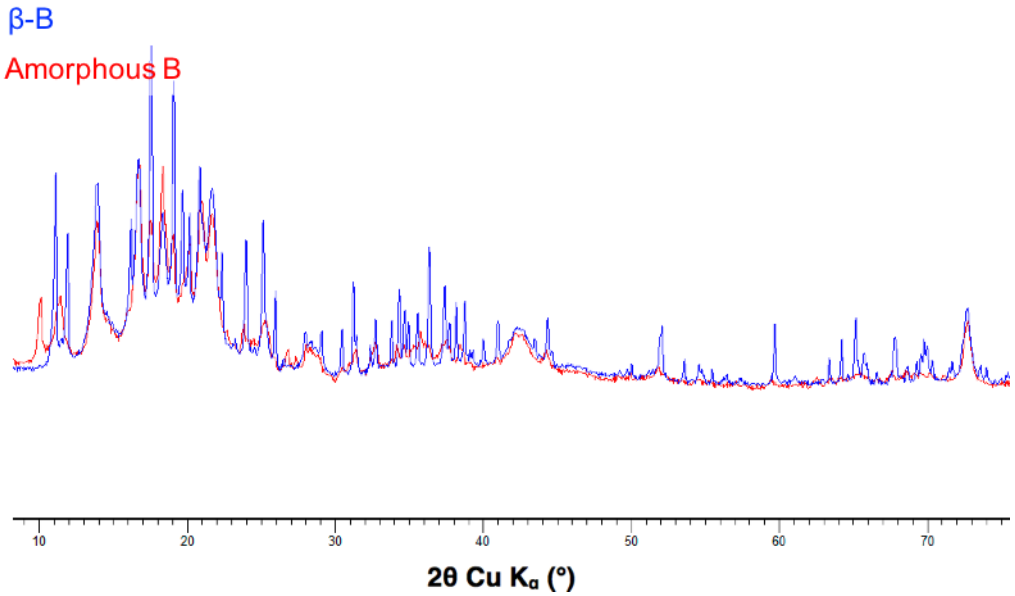


**Figure V-1. XRD patterns of β-B (blue) and commercial "amorphous" boron (red).**[6]

Considering the non-negligible crystallinity of commercially available "amorphous" boron, using nano-$B_{am}$ as precursor represents a unique opportunity to study the crystallisation of boron from a "truly" amorphous precursor. Also, as stated in Chapter I, only few nanostructured occurrences of boron are reported.[7–17] So far, none of the nanostructured forms of boron has been used as boron precursor, which also makes the use of nano-$B_{am}$ as precursor a new pathway toward boron allotropes.

This chapter aims at obtaining crystalline products from nano-$B_{am}$, and to characterise those in terms of structure and morphology. The transformation parameters such as pressure, temperature and thermal treatment duration are investigated.

As for the previous chapter, *in situ* experiments were conducted on a synchrotron beamline, object of the first part. The focus then shifts toward experiments conducted with *ex situ* characterisations, at 5 or 14 GPa.

This chapter is dealing with the crystallisation of nanostructured amorphous boron under high pressure and high temperature. If not mentioned otherwise, the experiments described in this chapter use nanostructured amorphous boron synthesised in LiI/KI, in a glassy carbon crucible and washed with methanol.

Noteworthy, the use of this precursor may introduce carbon (carbide) impurities. This point is also discussed. Due to the sensitivity of the powder to oxidation in air, the preparation of the high (P,T) set-up assembly was carried out in an argon-filled glovebox, the loaded assembly sealed under argon and exposed to air only a few seconds when placed immediately in-between the press anvils, prior to compression. After decompression, the assemblies were transferred and finally opened in an argon-filled glovebox. To limit exposure to air for *ex situ* experiments, the samples were sealed in glass capillaries under argon prior to XRD measurements, solid state NMR rotors were also loaded and unloaded in an argon filled glovebox. Note that TEM requires dispersion in a solvent, which is done under air in ethanol.

Experiments at 5 GPa were carried-out in a Paris-Edinburgh press, experiments at 14 GPa in a multi-anvil press, in which case the assembly was exposed to air for a few minutes, as the octahedra must be placed between cubic anvils before their introduction in the press itself.

## V-1- *In situ* XRD in Paris-Edinburgh cell

This experiment was conducted on the PSICHE beamline at synchrotron SOLEIL, using a 10/3.5 mm HPHT Paris-Edinburgh cell assembly. The corresponding XRD patterns are shown in Figure IV-3. As described in chapter IV, the use of energy dispersive diffraction does not allow comparison of relative intensities. Besides, the diagrams show the presence of fluorescence peaks from residual iodine. As for the nanocomposite systems in chapter IV, XRD does not show crystallisation upon compression at room temperature (Figure IV-3). Upon heating, a first phase crystallises at 1150 °C (temperature reached within 20 min, Figure IV-3, phase A), though the narrow 2θ range accessible and the intrinsic limitations of energy dispersive analysis (poor reliability of relative intensities, as discussed in Chapter IV) does not allow phase identification. Further heating up to 1250 °C leads to crystallisation of a second phase (phase B, Figure IV-3) while the peaks associated with A grow. Both reflections increase during the dwell time (total dwell time: 4 h). These two phases are conserved after temperature quench (at 4 GPa and room temperature, Figure IV-3). However, an additional non-indexed peak is observed (Figure IV-3), which is conserved along with A and B after pressure release (Figure IV-4). Based on the XRD pattern obtained at room pressure and temperature, neither A nor B can be indexed on known boron compounds, including boron allotropes, boron oxides, alkaline borides or borates or known boron carbides. Due to strong sample contamination, no HRTEM observations were possible.

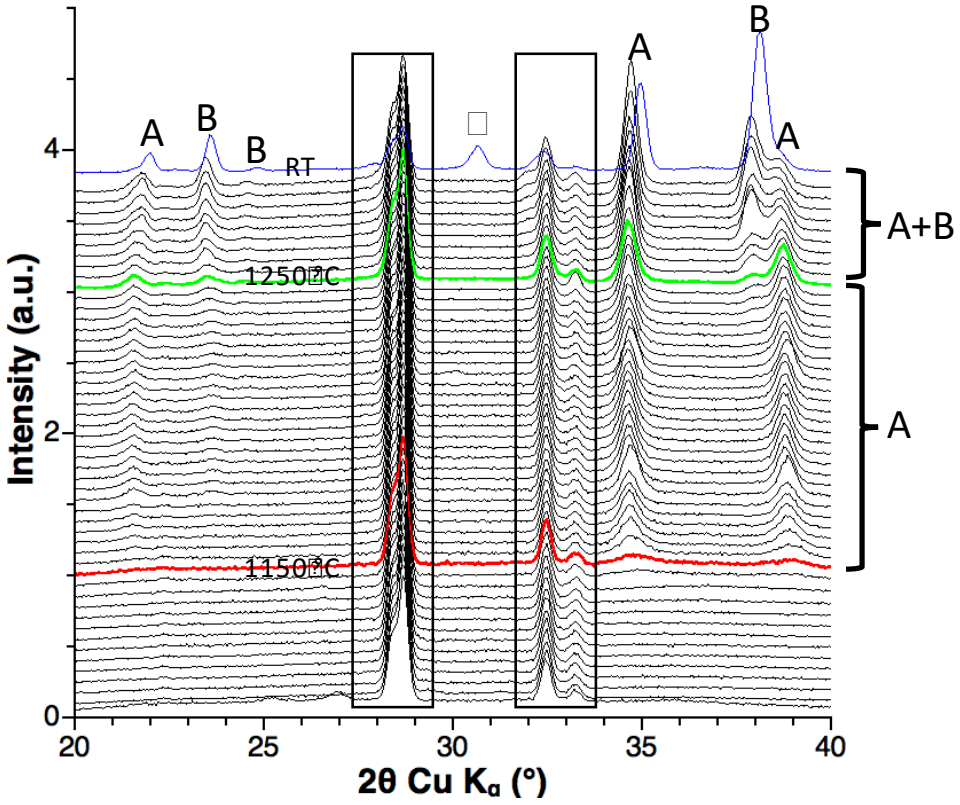


**Figure V-2. *In situ* XRD patterns of nano-$B_{am}$ treated at 5 GPa during progressive heating up to maximum 1250 °C. The first pattern at the bottom corresponds to the end of the compression (5 GPa, room temperature). The pattern in red corresponds to the beginning of the first phase crystallisation (A phase), at 1150 °C. The pattern in green corresponds to the beginning of the second phase crystallisation (B phase). The top pattern in blue corresponds to quenching to room temperature at 5 GPa. The two black frames indicate artefacts from iodine fluorescence or detector. The additional reflection seen after temperature quench is indicated with □.**

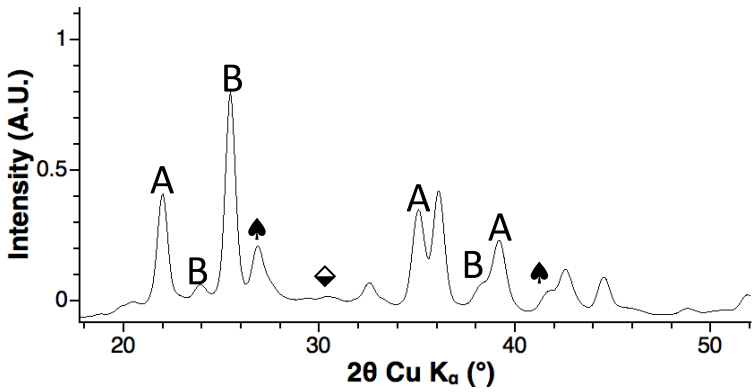


**Figure V-3. *Ex situ* XRD patterns of nano-$B_{am}$ treated at 5 GPa and maximum 1250 °C for 4 h after *in situ* experiment. *h*-BN is indicated with ♠. □ indicates the additional reflection appearing after temperature quench in the *in situ* experiment.**

This experiment allowed identification of the onset temperature of crystallisation for two crystalline phases, 1150 °C and 1250 °C. The corresponding (*P*,*T*) conditions

have then been explored by *ex situ* experiments in next parts, in order to allow for more in-depth phase characterisation.

## V-2- *Ex situ* experiments

### V-2-1- 5 GPa experiments

The following experiments reproduced the synthesis conditions obtained with the previous *in situ* experiment. Note that none of the phases crystallised from nanostructured amorphous boron match phases crystallised in the matrix of borides/boron nanocomposites (chapter IV).

At 5 GPa, the thermal treatments performed for *ex situ* studies are summarised in Table IV-1.

**Table V-1. HT treatments of nano-$B_{am}$ at 5 GPa. For all experiments, the desired temperature was reached in 8 min.**

| Experiment | Temperature (°C) | Dwell (min) |
|---|---|---|
| 1 | 1350 | 10 |
| 2 | 1350 | 90 |
| 3 | 1550 | 10 |
| 4 | 1550 | 90 |
| 5 | 1750 | 10 |
| 6 | 1750 | 90 |
| 7 | 1800 | 10 |
| 8 | 1800 | 90 |

The composition obtained by EDS-SEM is shown in Table V-2. Measurements have been performed without sample metallisation to allow non-destructive analysis. The exposition to air is however unavoidable but kept as short as possible, in the minute scale. The sample composition after HPHT experiments is constant among the synthesised samples according to EDS-SEM (values are detailed in the appendices, the mean value is indicated in Table V-2), though carbon and oxygen contents cannot be assessed with this technique. However, ICP-OES and CHN analysis fail on the samples crystallised under HPHT because they cannot be entirely dissolved in nitric acid or *aqua regia*, so that carbon and oxygen contents are not reported in this chapter.

**Table V-2. Composition of nanostructured amorphous boron, before and after HPHT.**

| | B (at%) | K (at%) | Na (at%) | I (at%) |
|---|---|---|---|---|
| SMS-derived B | 94.2 | 4.8 | < 0.8 | < 0.5 |
| Post HPHT | 96.75 | 3.25 | < 0.1 | < 0.1 |

The *ex situ* experiments lead to the construction of a speciation diagram at 5 GPa, shown in Figure V-4, which will be detailed in this part. Note that in addition to the A and B phase, these experiments unveiled a third phase, C, and reached a known boron allotrope, ε-B.

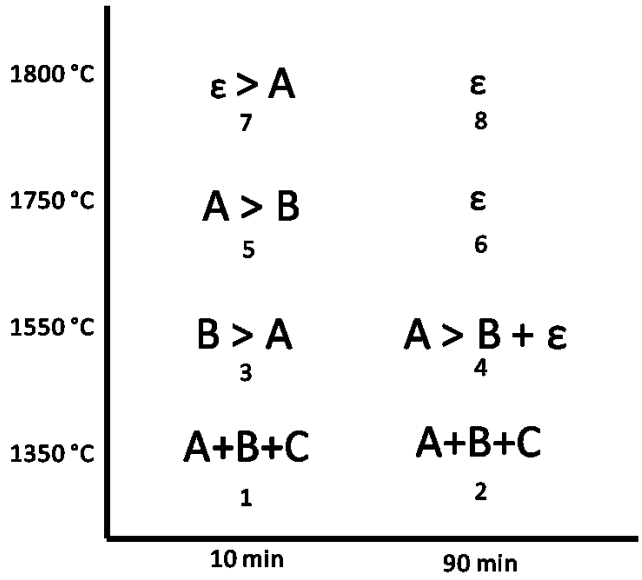


**Figure V-4. Speciation diagram of the phases obtained by HPHT treatments of nanostructured amorphous boron at 5 GPa, according to the thermal treatment (temperature, dwell time). “>” symbols indicate qualitatively the major and minor phases. The numbers correspond to the respective experiments (see Table V-1).**

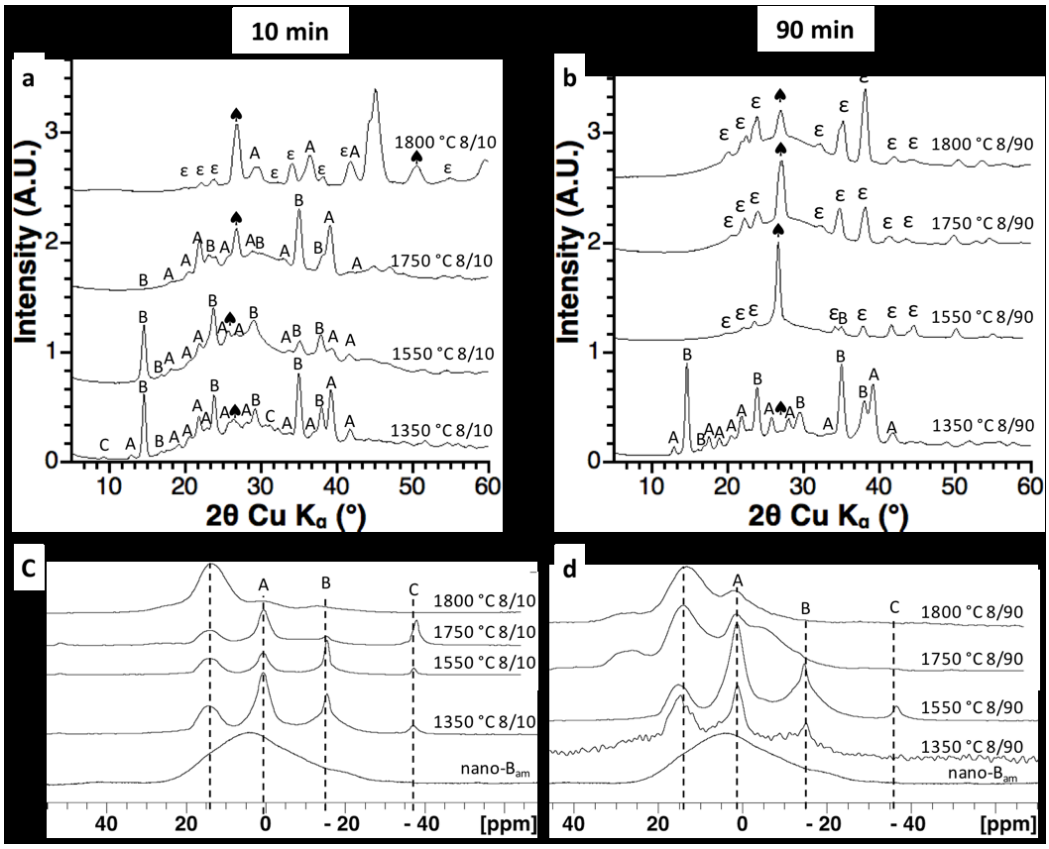


**Figure V-5. (a) XRD patterns of samples obtained at 10 min (1, 3, 5 and 7). (b) XRD patterns of samples obtained at 90 min (2, 4, 6 and 8). (c) $^{11}$B NMR spectra (MAS 20 kHz) of samples obtained at 10 min (1, 3, 5 and 7). (d) $^{11}$B NMR spectra (MAS 20 kHz) of samples obtained at 90 min (2, 4, 6 and 8). Note that this figure is reproduced on the Chapter V bookmark.**

At 1350 °C (*i.e.* experiments 1 and 2), the XRD patterns show reflections associated with the two phases A and B (Figure V-5 and Figure V-6) and a strong similarity between the two samples obtained at varying dwell time. The $^{11}$B NMR spectra are shown in Figure V-5 and Figure V-6. Both spectra exhibit peaks at 14, 0.5 and -15 ppm. The sample 1 exhibits an additional small peak at -38 ppm, tentatively associated with the additional XRD reflection around 10 ° (phase C) as both the XRD reflection and the NMR peak are absent in data from sample 2. In order to further index the $^{11}$B solid state NMR signals, the $^{11}$B NMR parameters of several boron-based materials were calculated (NMR data are not available in the literature for most boron allotropes and the samples are not readily available), in the framework of an internal collaboration with C. Gervais (Table V-3), with limitations for some boron allotropes that exhibit either partial occupation of crystallographic sites or odd numbers of boron atoms in the unit cell. For instance, NMR parameters for $^{11}$B could not be calculated for ε-B and isostructural $B_{13}C_2$. Although the signal at 14 ppm (Figure V-5) could be consistent with a $B_2O_3$-type environment, $B_2O_3$ cannot be detected on XRD patterns. In the same way, the signal around 0.5 ppm could correspond to β-B, but is also absent from XRD patterns. No known phases of boron could be associated to the peaks at *ca.* -15 ppm and at *ca.* -38 ppm.

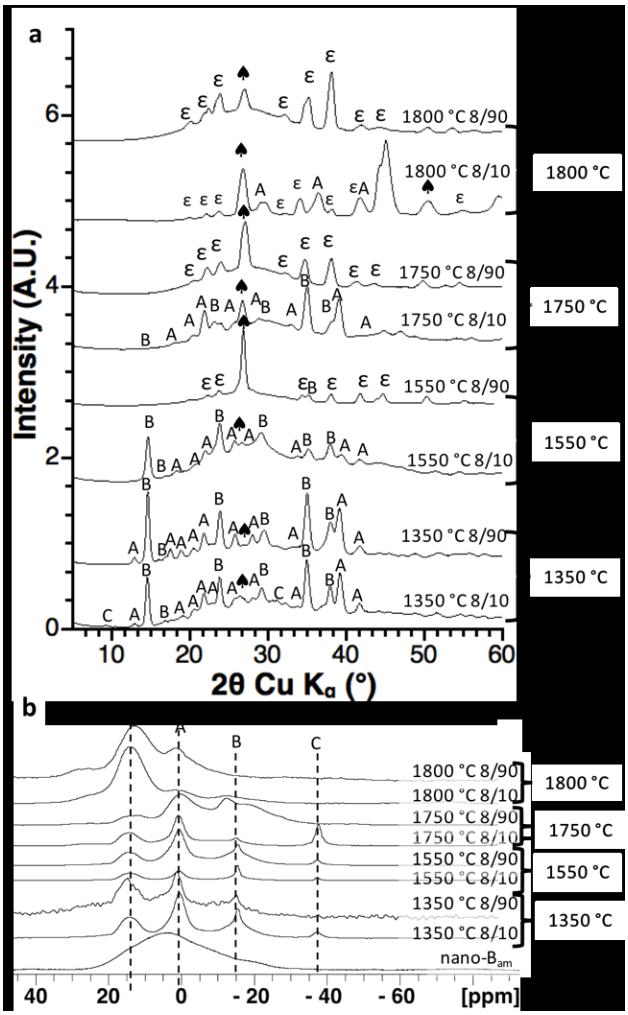


**Figure V-6. (a) XRD patterns of samples 1 to 8. (b) $^{11}$B NMR spectra of samples 1 to 8. This figure is also available on the Chapter V bookmark.**

**Table V-3. Calculated $^{11}$B NMR parameters for several boron-based materials.**

| Material | $\delta_{iso}$ (ppm) | $C_Q$ (MHz) | η |
|---|---|---|---|
| **γ-B** | | | |
| $B_1$ | 2.3 | 0.35 | 0.37 |
| $B_2$ | 3.4 | 1.57 | 0.04 |
| $B_3$ | -0.6 | 1.55 | 0.01 |
| $B_4$ | -10.8 | 0.40 | 0.77 |
| $B_5$ | 7.2 | 3.02 | 0.60 |
| **α-B** | | | |
| $B_1$ | 6.5 | 1.48 | 0.19 |
| $B_2$ | 8.9 | 0.75 | 0.39 |
| **$B_2O_3$** | | | |
| $B_1$ | 14.6 | 2.73 | 0.14 |
| $B_2$ | 15.0 | 2.71 | 0.18 |
| **$B_2O_3$-HP** | | | |
| $B_1$ | -1.1 | 1.09 | 0.12 |
| **$B_6O$** | | | |
| $B_1$ | 3.2 | 1.09 | 0.35 |
| $B_2$ | -9.9 | 1.66 | 0.08 |

HRTEM observations are similar for both 1350 °C samples and show two distinct families of particles, in size, morphology and structure (Figure V-7). The smaller (20-60 nm) particles exhibit d-spacing matching XRD reflections associated with A, while the bigger faceted particles (60-150 nm) match XRD reflections associated with B. TEM also shows that the particles are surrounded by an amorphous shell, 2 to 5 nm wide, which composition has not been assessed up to now.

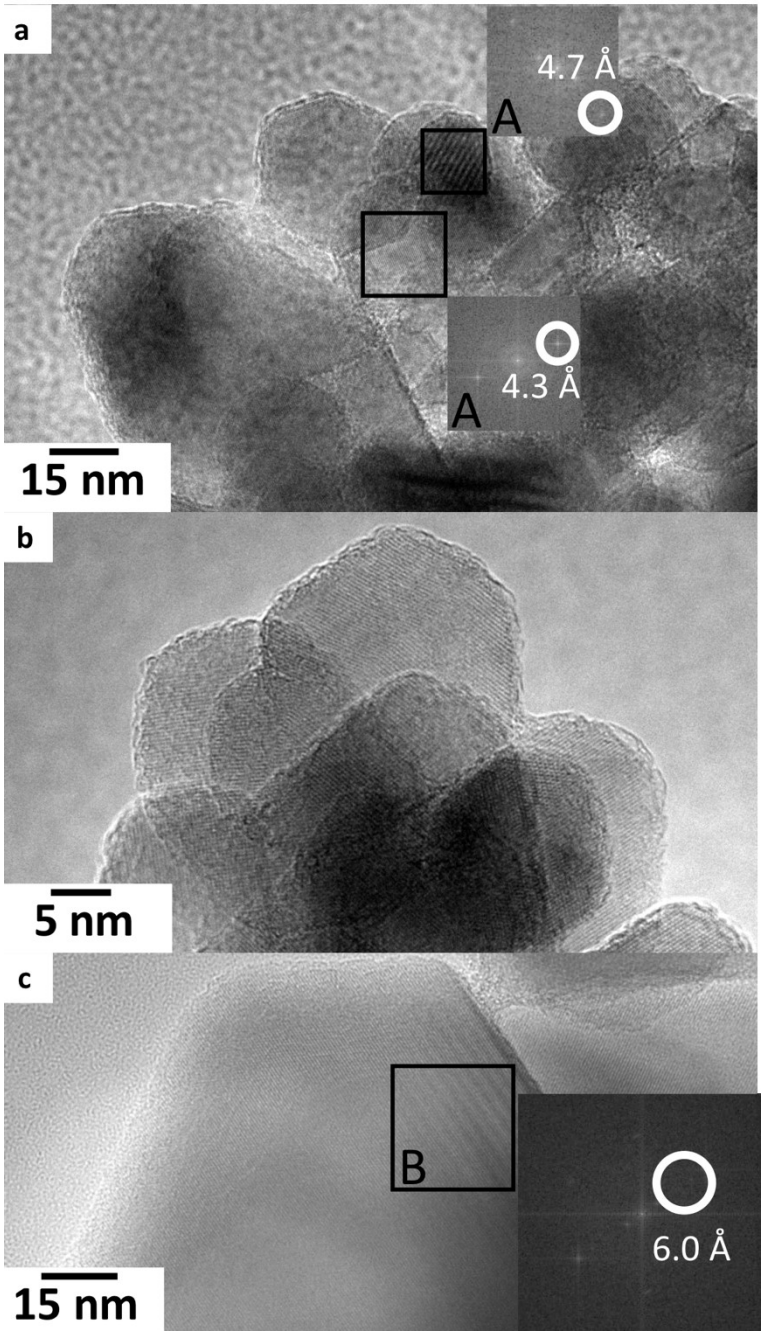


**Figure V-7. (a) HRTEM pictures of sample 1. (b) and (c) HRTEM pictures of sample 2. Insets correspond to the FFT of the zone in black squares.**

The comparison of the XRD patterns (Figure V-5) of experiments 1 (1350 °C, 8/10) and 3 (1550 °C, 8/10) shows that at higher temperature the two

phases previously identified (A and B) are still present, though the relative intensities indicate that the proportion of phase B increased. This result is confirmed by comparison of the $^{11}$B NMR spectra (Figure V-5), where the relative area of the peak at *ca.* -15 ppm increased from 1350 to 1550 °C. This confirms assignment of this peak to the B phase.

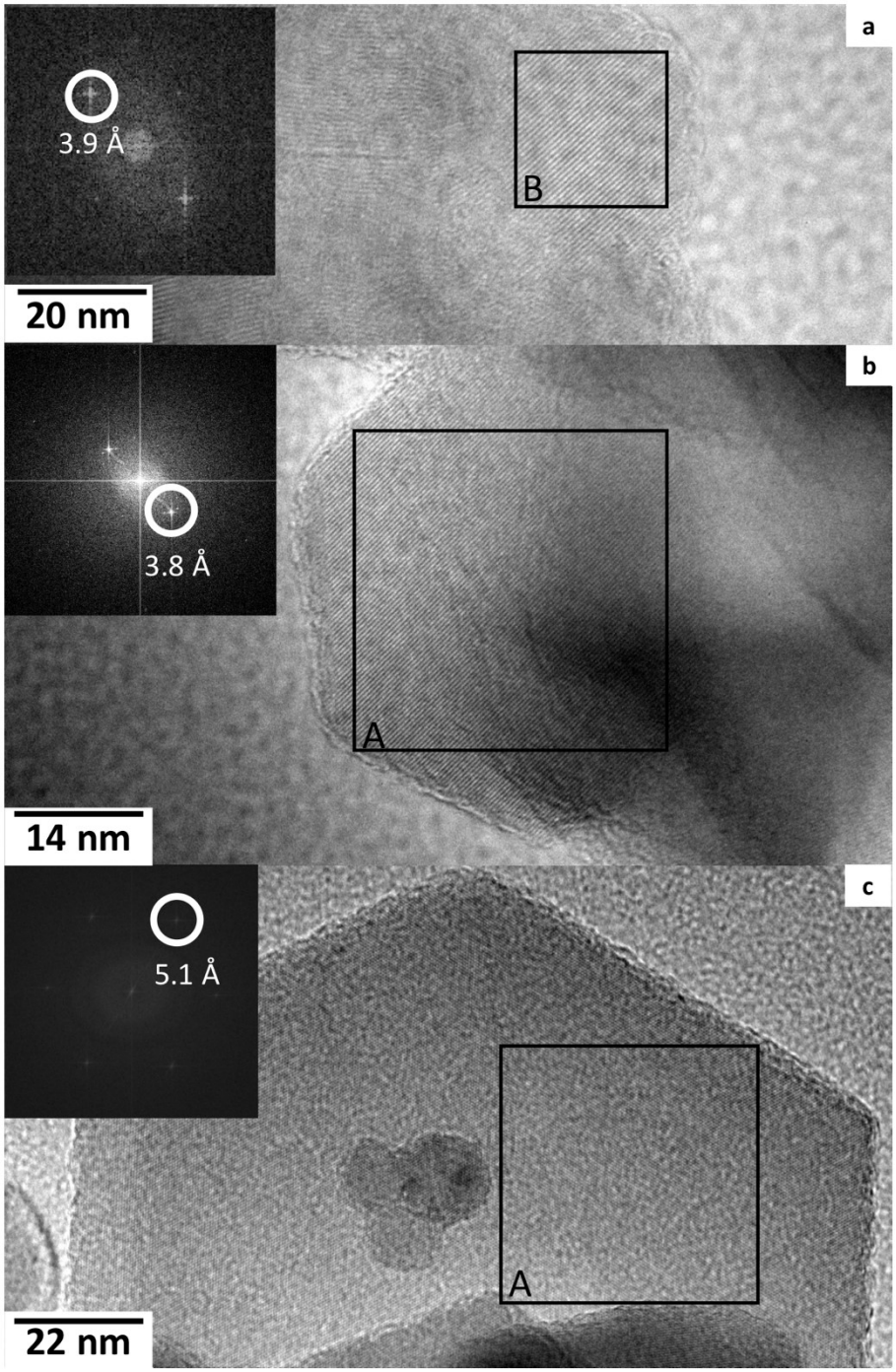


**Figure V-8. HRTEM pictures of sample 3 (1550 °C, 8/10). Insets correspond to the FFT of the zones in black squares.**

HRTEM pictures of sample 3 (Figure V-8) show two particles families, in agreement with the occurrence of two phases. In this case as well, based on the

d-spacings observed by HRTEM on both particles, smaller particles are associated to A, while the bigger faceted particles are associated with B.

At 1550 °C, longer heating (8/90, experiment 4), the XRD pattern of the recovered sample (Figure V-6) shows two crystalline phases: B and reflections matching ε-B, in addition to unavoidable *h*-BN (sample capsule). According to the Scherrer's formula, the isotropic crystallite size of ε-B is 60 nm. This remarkable result represents the second occurrence of the ε-B phase and the first nanostructured occurrence of ε-B. However, the exact nature of the crystallised phase raises questions. Indeed, as discussed in Chapter II, nano-$B_{am}$ synthesised in glassy carbon contains a few atomic percent of carbon (*ca.* 1 at%). Considering that $B_{13}C_2$ (*ca.* 14 at% of carbon) is isostructural to ε-B, the possibility of a solid solution of both phases is to be taken into account. Interestingly, ε-B is obtained in our work at lower pressure than Parakhonsky *et al.*[3] (5 *vs.* 9 GPa). Note that boron carbides can be crystallised at room pressure and high temperature, in the solid-solution domain comprised between *ca.* 9 and 22 at% of carbon.[18] At lower carbon content, a mixture of β-B and $B_4C$ is obtained.[18] At 5 GPa, the solid-solution domain is possibly extended, so that C-doped ε-B could be obtained. The $^{11}$B NMR spectrum (Figure V-5, Figure V-6) shows peaks similar to those obtained at 1350 and 1550 °C for 10 min dwell, which calls for the likely presence of small amounts of ε-B in previous experiments (though not seen on XRD patterns). The related spectra also enable attributing the peak at *ca.* 15 ppm to ε-B. The strong contamination under the electron beam precludes any HRTEM observation.

Comparison of the XRD patterns of samples 3 (1550 °C, 8/10) and 5 (1750 °C, 8/10) (Figure V-5) show the presence of phases A and B. XRD patterns (Figure V-5) show neither ε-B nor the C phase. The $^{11}$B NMR spectra of both samples show peaks at *ca.* 15, 0, -15 and -38 ppm, which indicate a mixture of A, B, C and ε-B. The relative amounts of phases A and B indicated by both $^{11}$B NMR and XRD are consistent (Figure V-5) and show that the A phase is favoured *vs.* B above 1550 °C for short dwell times.

Still at 1750 °C but for longer dwell time (90 min, experiment 6), XRD indicates the formation of a single crystalline phase: ε-B (Figure V-5 and Figure V-6). No reflections associated to the phases A, B and C are seen on the XRD pattern (Figure V-5). The $^{11}$B NMR spectrum (Figure V-6) displays an intense peak at *ca.* 15 ppm, associated with ε-B. An additional broad peak (or two superimposed peaks) is seen at *ca.* 26 ppm, which may also be assigned to ε-B. The $^{11}$B NMR spectrum also indicates low amounts of the A phase. The absence of the phase A on the XRD pattern is likely due to the small amounts present. HRTEM (Figure V-9) shows a *ca.* 200 nm particle with the ε-B structure. Note that significant contamination from the sample impedes exhaustive analysis of the sample.

Two experiments were conducted at higher temperature (1800 °C, experiments 7 and 8 with respectively 10 and 90 min dwells). The outcome is similar to that obtained at 1750 °C: for short dwell times, the XRD patterns show a mixture of

ε-B with the A phase (Figure V-5 and Figure V-6), as attested by the $^{11}B$ NMR spectrum (Figure V-6).

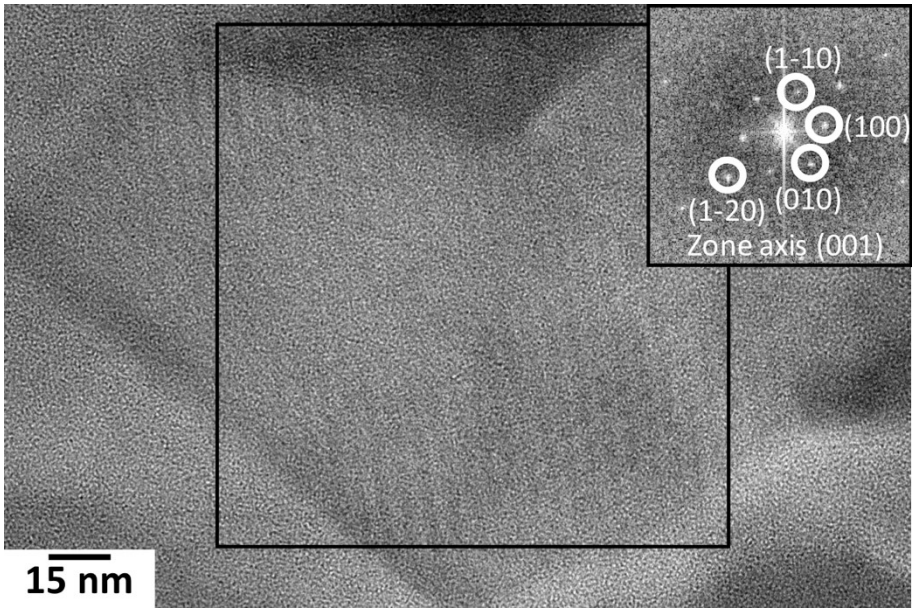


**Figure V-9. HRTEM picture of sample 6. Inset: FFT of black square area, indexed along the structure of ε-B.**

The experiment 8 (1800 °C, 8/90) leads to the crystallisation of ε-B as well, as evidenced by the XRD pattern (Figure V-5). Moreover, clear shouldering of the XRD peaks can be seen. As discussed in Chapter I, ε-B is isostructural to $B_{13}C_2$. This observation, coupled to the carbon content (1-1.5 at%) measured by elemental analysis of the amorphous precursor, indicates that the crystallised phase possibly contains small amounts of boron carbide, whether $B_{13}C_2$ or a solid solution between isostructural $B_{13}C_2$ and ε-B.

The outcome of experiments 1 to 8 is summed up in Figure V-10, recall of Figure V-4. It shows that A and B can be crystallised together at temperatures below up to 1550 °C. However, at 5 GPa, B cannot be obtained as sole crystalline phase. Heating above 1550 °C tends to favour the crystallisation of ε-B, the whole system evolving toward this phase for 90 min dwell times above 1750 °C, thus underlining the metastability of the A and B phases. ε-B is also a metastable allotrope,[3] but seems to correspond to a deeper energy well.

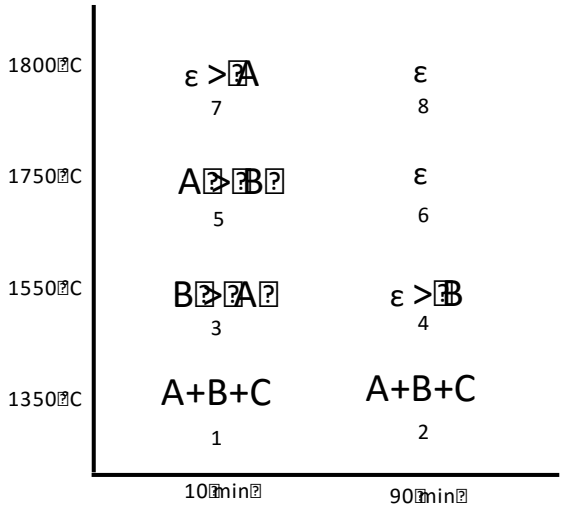


**Figure V-10. Recall of Figure V-4. Speciation diagram of the phases obtained by HPHT treatments of nanostructured amorphous boron at 5 GPa, according to the thermal treatment (temperature, dwell time). ">" symbols indicate qualitatively the major and minor phases. The numbers correspond to the respective experiments (see Table V-1).**

In this work, we have demonstrated the crystallisation of nanostructured amorphous boron into various products: two unknown solids (A and B) and ε-B, at 5 GPa. Notably, ε-B crystallises herein at 5 GPa, a lower pressure than that reported in the first ε-B occurrence (9 GPa)[3], thus underlining the influence of the boron precursor on crystallisation phenomena. The microstructure of ε-B has not been extensively investigated so far, due to strong aggregation of the particles or strong contamination under electron beam, which does not allow comparison of microscopy data with the particle size calculated with the Scherrer's formula. If nanostructuration is confirmed, then particle size reduction of ε-B is particularly interesting for mechanical properties, as microcrystalline ε-B has been reported as one of the hardest boron allotropes ($H_v$ = 55-60 GPa)[3] and is therefore a good candidate for hardness increase by the Hall-Petch effect. However, the possibility that the nanostructured ε-B contains small carbon amounts or is obtained as a solid solution with isostructural $B_{13}C_2$ cannot be ruled out. Besides this known phase, two new phases are clearly identified, whose structure need to be resolved. To do so, samples as pure as possible are required. However, at 5 GPa, the B phase could not be isolated. The next part focuses on experiments at higher pressure as a tentative to assess this issue.

### V-2-2- 14 GPa experiments

Several experiments of HPHT crystallisation of nanostructured amorphous boron were conducted at 14 GPa, by using a Multi-Anvil Press (MAP) in the framework of a collaboration with the Laboratoire Magma et Volcans in Clermont-Ferrand. All these experiments were carried out at 1800 °C (reached within 8 min) with various dwell times. The experimental conditions are summarised in Table V-4. Note that for experiments 9 to 12, heating was stopped due to failure of the $LaCrO_3$ heater, which exhibited abnormal electric behaviour, therefore assemblies were quenched to avoid

blow out and sample loss. For experiments above 10 GPa, the capsule and heater materials differ from that used at lower pressure. Indeed, graphite heaters used under 10 GPa would undergo transition toward diamond at high temperature, as for *h*-BN (into *w*-BN). Both phase transitions are accompanied with strong volume reduction, which challenges the mechanical stability of the assembly at high pressure. Therefore, a $LaCrO_3$ heater is used, along with a MgO capsule. For these experiments, both the heater and the capsule are strongly deformed from the inside, which likely causes the heater failure and is interpreted as a consequence of gas release during heating. Except for experiment 10, the sample environment is recovered broken, which exposes the samples to air, hence impeding opening in an argon-filled glovebox.

**Table V-4. Various HT treatments of nano-$B_{am}$ at 14 GPa. For all experiments, the desired temperature was reached in 8 min. The dwell times indicated are the effective one.**

| Experiment | Temperature (°C) | Dwell (min) |
|---|---|---|
| 9 | 1800 | 32 |
| 10 | 1800 | 46 |
| 11 | 1800 | 60 |
| 12 | 1800 | 90 |

All 14 GPa experiments show crystallisation of the A and B phases, as evidenced by the XRD patterns (Figure V-11) and the peaks at *ca.* 0 ppm (resp. *ca.* -15 ppm) on the $^{11}B$ NMR spectra (Figure V-12). For short dwell times up to 45 min, the system evolves from a partially amorphous state evidenced by the broad bump of the XRD pattern backgrounds to a fully crystalline state. The phase C appears at short dwell time but disappears afterward, in agreement with the evolution of the -38 ppm peak on $^{11}B$ NMR spectra (Figure V-12). The A phase appears as the minor product according to the XRD (Figure V-11), in agreement with the low relative intensity of the *ca.* 0 ppm signal on $^{11}B$ NMR spectra. The relative intensities of the A phase signals on $^{11}B$ NMR spectra and XRD patterns decreases at long dwell times.

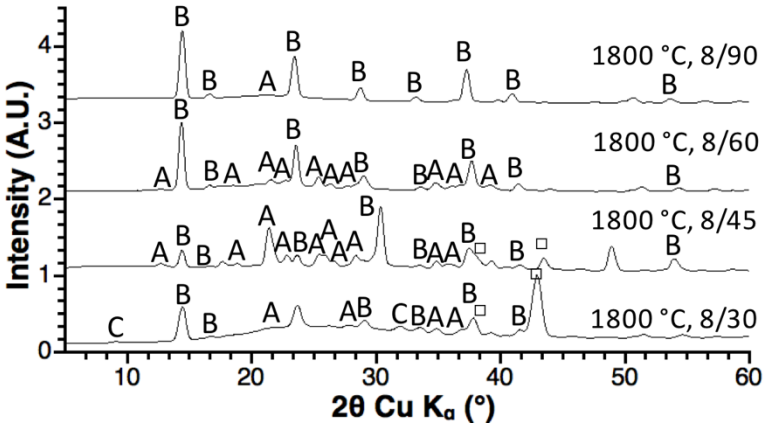


**Figure V-11. XRD patterns of samples 9, 10, 11 and 12. All reflections of phases previously mentioned are indicated with their respective symbol, residual MgO (sample capsule) reflections from sample-containing capsule are indicated with ▫.**

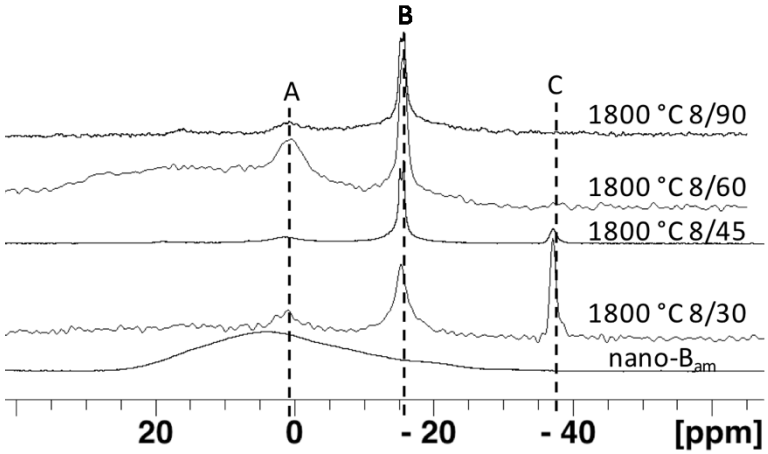


**Figure V-12. $^{11}$B MAS NMR spectra of nano-$_{Bam}$, samples 9 (1800 °C 8/30), 10 (1800 °C 8/45), 11, (1800 °C 8/60) and 12 (1800 °C 8/90).**

The C phase was already detected in experiment 1. Its absence in all other 5 GPa experiments while it is more frequent at 14 GPa, according to $^{11}$B NMR, is interpreted as a consequence of the faster kinetics at lower pressure: this high energy metastable phase may quickly evolve at 5 GPa, thus precluding its detection. Also, as the decrease of the intensity of the $^{11}$B NMR peak associated with C corresponds to an increase in the intensity of the peak associated with A, A is possibly crystallised from C (Figure V-12). HRTEM observations of sample 10 (1800°C/45min) are presented in Figure V-13. Faceted particles (50-250 nm) are observed. The SAED pattern (Figure V-13) exhibits d-spacings that correspond only to A, no object exhibits d-spacings corresponding to B. Some particles exhibit elongated shape (Figure V-13, bottom right corner). Note that the pattern has a symmetry close to hexagonal (Figure V-13).

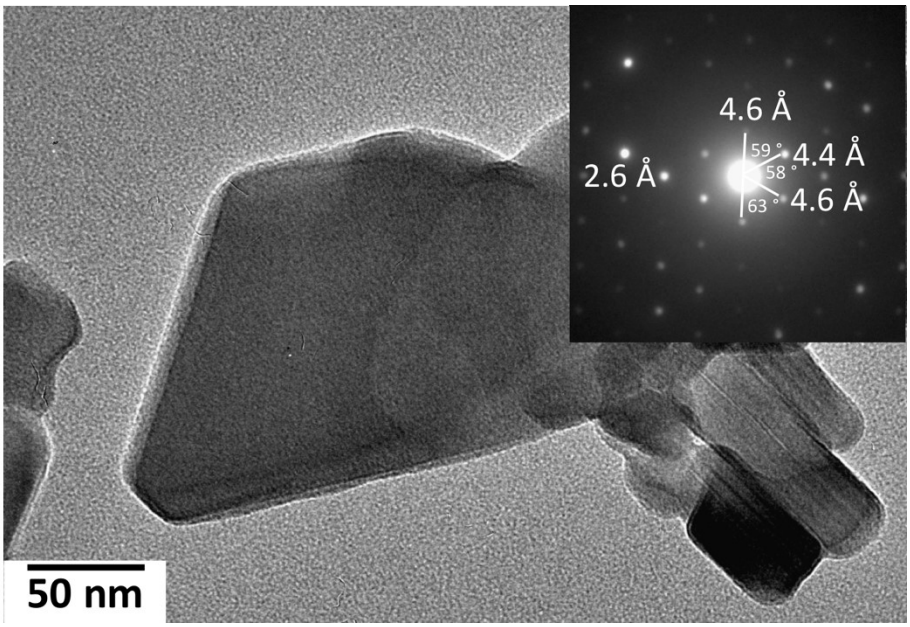


**Figure V-13. HRTEM pictures of sample 10 (1800°C/45min). Inset: SAED patterns highlighting d-spacings typical of the A phase.**

The HRTEM observations of sample 11 (1800°C/60min) are shown in Figure V-14. It shows particles with size in the 60-300 nm range, exhibiting d-spacings consistent with the XRD reflections associated to the A phase (Figure V-14).

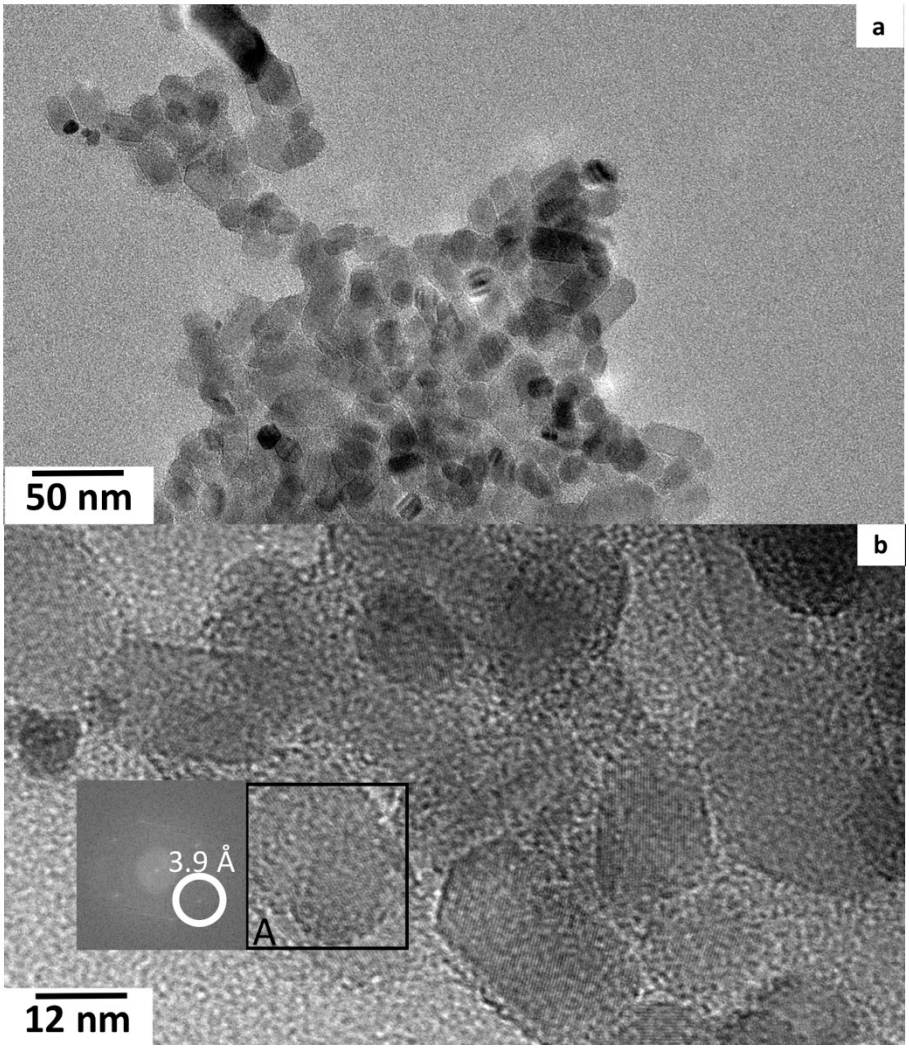


**Figure V-14. (a) TEM picture of sample 11 (1800 °C/60 min). (b) HRTEM picture of sample 11 (1800 °C/60 min). The inset is the FFT of the squared zone.**

In experiment 12 (1800°C/60min), both XRD (Figure V-11 and Figure V-15) and $^{11}B$ NMR (Figure V-12) show that the B phase is obtained almost pure with a residual amount of A. As for previous experiments at 5 GPa, the K/B ratio estimated by EDS-SEM is very similar to that of the initial powder: $K_{0.06}B$.

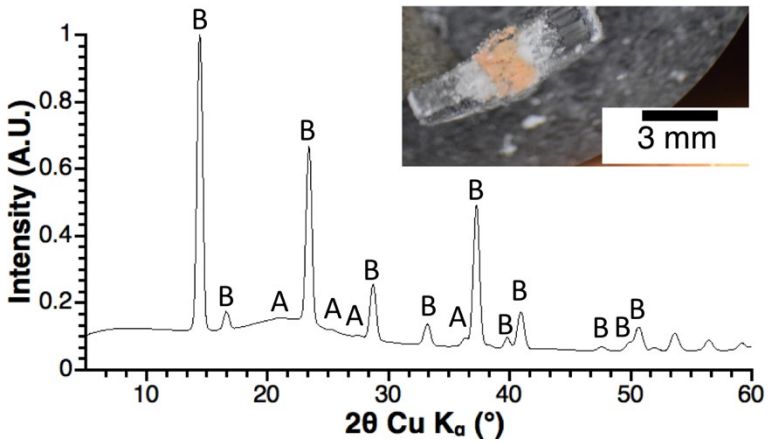


**Figure V-15. XRD pattern of sample 12. Inset: picture of the cut assembly, with the sample in its centre.**

HRTEM (Figure V-16) shows faceted particles, exhibiting a hourglass motif, with a size in the 50-300 nm range. According to the Scherrer's formula, the crystallite size is 16-20 nm. In this case also, the particles are surrounded by an amorphous matrix 2-10 nm wide, which nature remains unknown. Indeed, to assess the presence of carbon, STEM-EELS experiments were performed, but again impeded by the strong contamination of the samples. The faceted particles exhibit some lattice fringes which d-spacing matches XRD reflections of the B phase (Figure V-16). Other d-spacings may correspond to reflections of null intensity in XRD. After HPHT treatment at 14 GPa, the initially black powder is orange, as shown in Figure V-15.

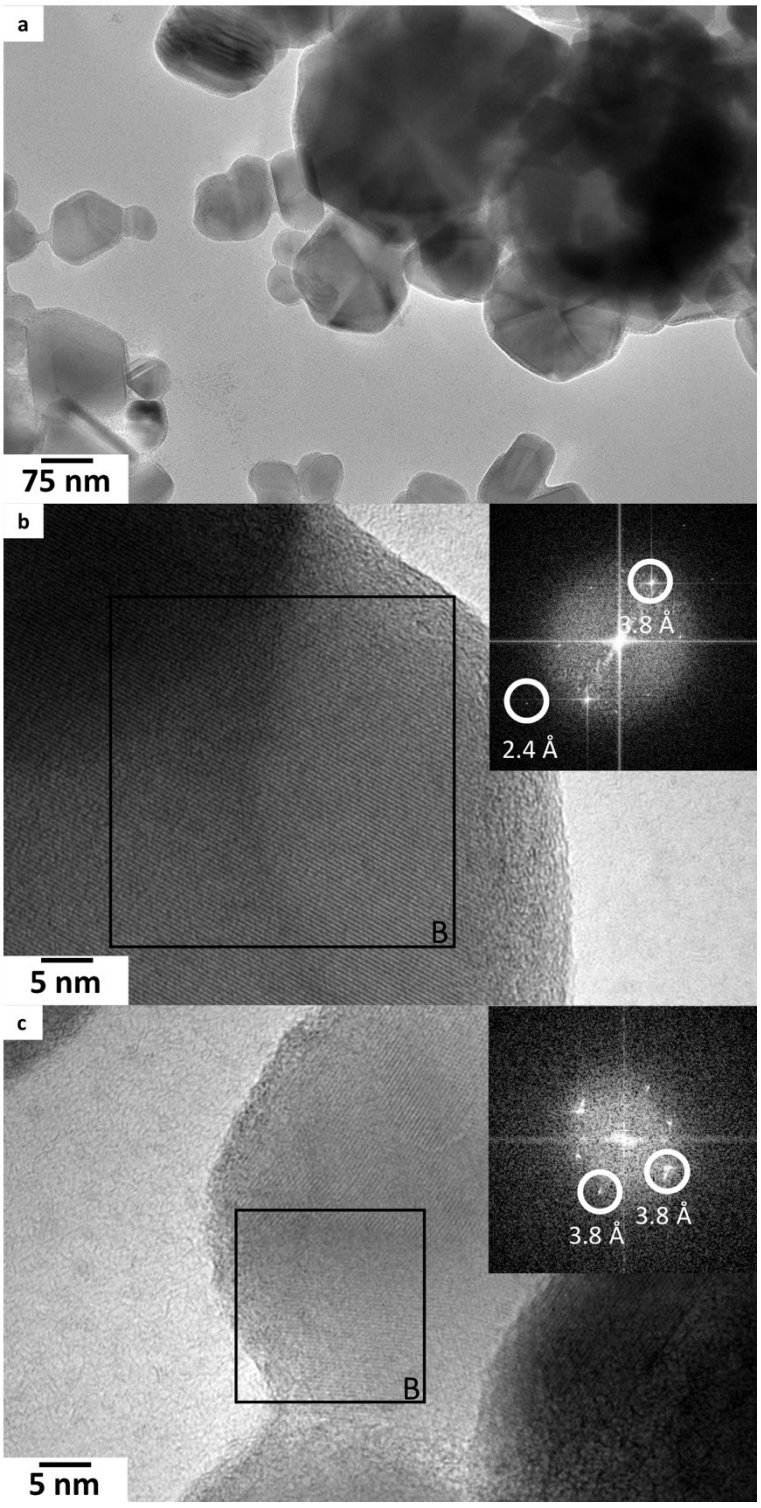


**Figure V-16. (a) TEM and (b, c) HRTEM pictures of sample 12 (1800 °C/90 min). Insets: FFT of squared zones.**

Note that the phases obtained at 14 GPa are similar to those obtained at 5 GPa, which rules out possible side reactions with the MgO sample-containing capsules used at 14 GPa. Besides, an 1800 °C experiment has been attempted using a *h*-BN capsule at 14 GPa, but failed due to the *h*-BN to *w*-BN phase transition, causing heater collapse and failure. The new phase B, obtained with low amounts of crystalline impurities according to XRD, is the object of structure resolution, in the

framework of a collaboration with B. Albert and K. Hofmann in Technische Universität Darmstadt, still ongoing.

Experiments at 14 GPa showed that also at pressure higher than 5 GPa, nanostructured amorphous boron does not crystallise into known allotropes (γ-B would be expected in this P,T domain) in the first place. However, contrary to 5 GPa transformations, no crystallisation into ε-B was observed in the time frame studied. Transformation into ε-B may be impeded by slower kinetics at higher pressure. Hence, longer thermal treatments are envisaged for two purposes: isolation of pure, B phase (without A impurities) and to investigate the possibility to evolve the system toward a known allotrope.

## V-3- Conclusion and prospects

The HPHT studies on nano-$B_{am}$ demonstrated crystallisation into various products, notably two new phases A and B. The synthetic conditions explored so far did not yield the boron allotropes expected in such conditions: β-B for experiments at 5 GPa and γ-B for experiments at 14 GPa. This shows the strong influence of the initial boron source on crystallisation processes. Interestingly, all phases evolve toward ε-B, evidencing their metastability. ε-B presumably exhibits a deeper energy well. The crystallisation of nanostructured ε-B is a striking result, as nanostructured occurrences of crystalline boron have rarely been reported (as discussed in Chapter I), notably never for ε-B. Mechanical properties of this nanostructured material are to be tested, though it could not have been done along the course of this work.

Yet, if striking, this result also rises questions. Indeed, the initially present carbon, even of low content (*ca* 1 at%), can be easily integrated into boron-based structures (as in $B_{50}C_2$ or $B_{13}C_2$). At this point, ε-B crystallised from nano-$B_{am}$ may contain small amounts of carbon, or even consist of a solid solution between ε-B and the isostructural boron carbide.

The latest developments in MS synthesis pave the way toward the decrease in carbon content. Indeed, it can be limited by switching to a *h*-BN synthesis crucible. Also, preliminary results have paved the way to use argon-saturated water as washing solvent. This is particularly interesting in the light of the results obtained with the nanocomposite systems, for which the use of methanol leads to residual potassium amounts. Notably, slight shifts of cell parameters for crystalline phases could indicate the integration of foreign elements in the structures. Therefore, the possibility to wash with water opens the possibility to compare the influence of (i) the crucible material (ii) the synthesis solvent (as the LiCl/KCl eutectic mixture cannot be washed with methanol) and (iii) the washing solvent on the crystallisation processes and the phases crystallised.

The comparison with the nanocomposite systems shows that thoroughly different phases are crystallised within the matrix, unveiling the role of the crystalline nano-inclusions.

As underlined before, the issue of composition is of particular importance in the case of boron rich phases. For the nanostructured crystalline phases, if the global material composition is important, the local composition is also. Indeed, as most crystallised particles are surrounded by an amorphous matrix a few nm thick. Establishing the composition of this outer shell, notably regarding the foreign atoms content is of interest, especially if it differs from that of the crystalline particles. It would require a technique with (i) sufficient spatial resolution and (ii) suited to light elements, such as STEM-EELS.

Experiments at pressure above 10 GPa are particularly interesting, as their optimisation is likely to allow the isolation of all A, B and C phases. Future works should test the possibility to evolve the system toward known metastable phases, with long thermal treatments.

$^{11}B$ solid state NMR has proven to be a useful tool for phase identification, notably because of its superior sensitivity compared to XRD. Future developments should include synthesis of known boron allotropes (from usual precursors), in order to produce reference spectra of known phases. Indeed, the local structure of boron in both the precursor and crystallised phases is still unknown. It may be non $B_{12}$-based, a very uncommon feature in boron-rich solids.

## V-4- References


(1) Oganov, A. R.; Chen, J.; Gatti, C.; Ma, Y.; Ma, Y.; Glass, C. W.; Liu, Z.; Yu, T.; Kurakevych, O. O.; Solozhenko, V. L. *Nature* **2009**, *457* (7231), 863–867.

(2) Yu Zarechnaya, E.; Dubrovinsky, L.; Dubrovinskaia, N.; Miyajima, N.; Filinchuk, Y.; Chernyshov, D.; Dmitriev, V. *Sci. Technol. Adv. Mater.* **2009**, *9* (2008), 044209.

(3) Parakhonskiya, G.; Dubrovinskaia, N.; Bykova, E.; Wirth, R.; Dubrovinsky, L. *High Press. Res* **2013**, *33* (3), 673–683.

(4) Talley, C. P.; La Placa, S.; Post, B.; IUCr. *Acta Crystallogr.* **1960**, *13* (3), 271–272.

(5) Ekimov, E. A.; Zibrov, I. P.; Zoteev, A. V. *Inorg. Mater.* **2011**, *47* (11), 1194–1198.

(6) Turner, C. L.; Taylor, R. E.; Kaner, R. B. *J. Phys. Chem. C* **2015**, *119* (24), 13807–13813.

(7) Komatsu, S.; Moriyoshi, Y. *J. Cryst. Growth* **1990**, *102* (4), 899–907.

(8) Wang, X.; Tian, J.; Yang, T.; Bao, L.; Hui, C.; Liu, F.; Shen, C.; Gu, C.; Xu, N.; Gao, H. *Adanced Mater.* **2009**, *19* (24), 4480–4485.

(9) Zhang, Y.; Ago, H.; Yumura, M.; Komatsu, T.; Ohshima, S.; Uchida, K.; Iijima, S. *Chem. Commun.* **2002**, *354* (23), 2806–2807.

(10) Wang, Z.; Shimizu, Y.; Sasaki, T.; Kawaguchi, K.; Kimura, K.; Koshizaki, N. *Chem. Phys. Lett.* **2003**, *368* (5-6), 663–667.

(11) Bai, H.; Dai, D.; Yu, J. H.; Nishimura, K.; Sasaoka, S.; Jiang, N. *Appl. Surf. Sci.* **2014**, *292*, 790–794.

(12) Bellott, B. J.; Noh, W.; Nuzzo, R. G.; Girolami, G. S. *Chem. Commun.* **2009**, No. 22, 3214–3215.

(13) Wu, Y.; Messer, B.; Yang, P. *Adv. Mater.* **2001**, *13* (19), 1487–1489.

(14) Meng, X. M.; Hu, J. Q.; Jiang, Y.; Lee, C. S.; Lee, S. T. *Chem. Phys. Lett.* **2003**, *370* (5-6), 825–828.

(15) Casey, J. D.; Haggerty, J. S. *J. Mater. Sci.* **1987**, *22* (2), 737–744.

(16) Pickering, A. L.; Mitterbauer, C.; Browning, N. D.; Kauzlarich, S. M.; Power, P. P. *Chem. Commun.* **2007**, No. 6, 580–582.

(17) Xu, T. T.; Zheng, J. G.; Wu, N.; Nicholls, A. W.; Roth, J. R.; Dikin, D. a.; Ruoff, R. S. *Nano Lett.* **2004**, *4*, 963–968.

(18) Thévenot, F. *J. Eur. Ceram. Soc.* **1990**, *6*, 205–225.

# Conclusion

The work presented throughout this manuscript displayed, as discussed in the introduction, a three-fold approach. Indeed, this study is first based on nanoparticles synthesis then on solid state chemistry, using high pressure and high temperature techniques.

The genesis of this work lies in the development of the synthesis in molten salts, described in Chapter II. Indeed this method yields nanostructured metal borides and allows tuning both size and stoichiometry of the metal borides. This synthetic route can be extended to numerous borides, though not to oxidation sensitive compounds, because of mandatory washing steps. The resulting boride nanoparticles have interesting intrinsic properties, as evidenced in recent works, notably for thermoelectricity or catalysis.[1] Yet, if SMS reaches nanostructured borides, they are obtained as part of a nanocomposite, as they are embedded in an amorphous boron-rich matrix. The new results obtained in the framework of this current PhD work show how complex this oxygen-sensitive amorphous matrix can be as, besides boron, it can also contain metal inclusions. Furthermore, we especially developed a new washing method to limit drastically the oxidation of the nanocomposite precursors that is of prime importance for further HPHT crystallisation treatments. Most recent developments of the synthesis in molten salts are metal-free syntheses: they consist in the thermal decomposition of borohydrides in molten salts. This synthetic pathway yields a unique nanostructured boron-rich (*ca.* 90 at% to 95 at%) material, which exhibits a reactivity unprecedented among elemental forms of boron. Previous works have established that a 5 at% content of alkaline elements cannot be avoided with the current synthetic and purification methods. During this work, it was established that the synthesised material also contains a few atomic percents of carbon, depending on the nature of the synthesis crucible. Two ways toward improvement of the materials' purity are currently investigated. On the one hand, preliminary works suggest the possibility to perform washing with argon-saturated deionised water, with very limited oxidation, which may help reduce the alkaline content thanks to the high solubility of alkali salts in water. On the other hand, the nature of the crucible can also be changed, by using for instance *h*-BN or metals such as boride-passivated molybdenum. Preliminary data concerning the first point have been presented in Chapter II.

Chapters III and IV aimed at demonstrating the possibility to crystallise this matrix while retaining (i) the composite nature of the material and (ii) the nanostructuration. To achieve this goal, not only state-of-the-art synthesis and HPHT experiments have been conducted, but they have also been coupled to extensive use of dedicated characterisation techniques, especially *in situ* X-ray diffraction on synchrotron beamlines, transmission electron microscopy and $^{11}$B solid state NMR.

Chapter III described the outcome of high pressure high temperature transformation conducted on $HfB_2$/B and $CaB_6$/B nanocomposites synthesised in conditions favouring oxidation of the amorphous matrix. As a result, this phase crystallised into borates ($HfB_2O_5$ and $CaB_2O_4$-IV), while preserving the initial boride inclusions. The resulting boride/borate nanocomposites materials showed an

impressive preservation of the nano-inclusions size, which only slightly increases up to 30 nm in size, despite a thermal treatment above 1000 °C. The synthesis of these unique nanocomposites demonstrated the possibility to crystallise the amorphous matrix while retaining the overall nanostructure, by taking advantage of the confinement effect of the matrix and of the reduced atomic diffusion lengths at high pressures.

The HPHT treatments of precursors handled specifically to avoid extended oxidation have been discussed in Chapter IV. Crystallisation of the matrix while conserving the borides' nature and structure was again demonstrated, even for temperatures exceeding 1500 °C. HRTEM has demonstrated that for both systems the matrix is crystallised into nanostructured β-B, with various particle sizes and morphologies. The materials thereby synthesised are the first occurrences of metal borides/crystalline boron nanocomposites. They also encompass one of the first example of β-B nanocrystals.[2–4] Further developments will focus on the investigation of the properties of such materials. Mechanical properties are particularly interesting, in the light of (i) the hardness of bulk boron allotropes, (ii) their chemical inertness, and (iii) the nanostructure-related Hall-Petch effect. The nanocomposite aspect also paves the way toward combination of the matrix and the boride particles properties. Among future developments, experiments above 10 GPa are envisaged, to probe the possibility to crystallise other boron allotropes in the matrix, for instance superhard γ-B.

The HPHT experiments conducted on nanostructured amorphous boron containing carbon impurities showed that this new precursor can be crystallised in various nanostructured phases. Among these, we reported the synthesis of a material close to ε-B (either pure or as a solid solution with the isostructural carbide $B_{13}C_2$). We also highlighted the first occurrence of nanoparticles for this phase. This is particularly interesting as ε-B is the known boron allotrope with the highest hardness, which might be enhanced by particle size reduction. We also report two new metastable phases, the structures of which are yet to be solved. The nanostructures of the synthesised materials also call for precise and local elemental analysis, to probe the location of remaining alkali elements for instance. Interestingly, nanostructured amorphous boron is crystallised in the same phases above 10 GPa, evidencing the strong influence of the boron precursor on crystallisation processes and on the phase diagram. It also underlines the fundamental difference between the borides/boron nanocomposites and nanostructured amorphous boron, which yield strictly different phases from the matrix of the composite systems.

All in all, this work allowed the development of an original synthetic methodology based on the preparation of specific nanostructured precursors, transformed with HPHT techniques. The unique nanostructured systems obtained were characterised with dedicated techniques, yet several remaining questions call for further experiments.

Further studies will focus on the isolation of pure occurrences of the new phases to facilitate structure resolution, which is already on the way for some solids. Larger volume HPHT treatments will enable in the future to probe the materials properties, especially hardness and thermoelectric properties. Furthermore, the explored systems should demonstrate further structural, nano- and micro-structural evolutions for long thermal treatments at high pressure, which can yield the first nanoparticles of known boron allotropes, or again new phases to be discovered.

## References


(1) Gouget, G. Approche moléculaire vers des nanomatériaux inorganiques composés de bore : nouvelles nanostructures fonctionnelles, **2016**.
(2) Komatsu, S.; Moriyoshi, Y. *J. Cryst. Growth* **1990**, *102* (4), 899–907.
(3) Wang, X.; Tian, J.; Yang, T.; Bao, L.; Hui, C.; Liu, F.; Shen, C.; Gu, C.; Xu, N.; Gao, H. *Adv. Mater.* **2009**, *19* (24), 4480–4485.
(4) Bai, H.; Dai, D.; Yu, J. H.; Nishimura, K.; Sasaoka, S.; Jiang, N. *Appl. Surf. Sci.* **2014**, *292*, 790–794.

# Appendices

## 1- Synthesis in molten salts

Before the experiments, all powders were handled into an argon filled glovebox. Anhydrous $HfCl_4$ (Alfa Aesar), anhydrous $CaCl_2$ (Alfa Aesar), LiI (Alfa Aesar), KI (Alfa Aesar) and sodium borohydride (Alfa Aesar) were used as received. Prior to synthesis, LiCl (Aldrich) and KCl (Aldrich) were previously mixed at the eutectic composition (LiCl:KCl = 45 : 55 wt%) and finely ground in a mortar. The resulting mixture was evacuated at 200 °C for 4 days and transferred into the glovebox. Before heating, anhydrous metal chlorides, sodium borohydride and the eutectic salt mixture (LiCl:KCl, 2.5 g or LiI/KI, 5 g) were finely ground together with a Retsch MM400 ballmiller (airtight vials of 50 mL, one steel ball of 62.3 g and a diameter of 23 mm) for 2 minutes at 20 Hz. The mixture was transferred into a glassy carbon or *h*-BN crucible, which was then placed in a quartz tube and heated under argon flow in a tube oven at 10 °C·min$^{-1}$. *h*-BN crucibles (AX05 grade) were provided by Ceraquest with the following dimensions: L = 200 mm, OD = 18 mm, ID = 12 mm. Glassy-carbon crucibles were provided by Sigradur with the following dimensions (two sizes were used): L = 200 mm, OD = 18 mm, ID = 12 mm and L = 200 mm, OD = 24 mm, ID = 18 mm.
The heating was performed in vertical tubular oven connected to temperature controllers from Eurotherm or Nabertherm. These ovens were calibrated every 50 °C between 500 and 950 °C and temperatures indicated throughout the manuscript correspond to the effective temperature in the crucible.

### 1-a- $HfB_2$/B nanocomposites

For $HfB_2$-based systems, the initial quantities of hafnium (IV) chloride and sodium borohydride are described in Table 1. The reaction medium was heated at 900 °C for 4 h. Syntheses in the LiCl/KCl were washed with water: after cooling, the frozen eutectic was dissolved in deionised water and sonicated for 5 min. The resulting black suspension was centrifuged (in 10 mL polycarbonate tubes at 26 krpm, 20 min) four times. Between each centrifugation steps, the supernatant was removed, the suspension re-dispersed in deionised water and sonicated for 5 min. It was then dried at 40 °C under vacuum for 15 h, in a vacuum oven.

Syntheses in LiI/KI were washed with methanol (VWR grade « normapur », $H_2O$ < 0,01 mol%): after cooling, the frozen eutectic was dissolved in methanol and sonicated for 1 min. The resulting black suspension was centrifuged (in 50 mL polycarbonate tubes at 16.5 krpm) four times. Between each centrifugation step, the supernatant was removed, the suspension re-dispersed in methanol and sonicated for 30 s. It was then dried at 40 °C under vacuum for 3 h, in a vacuum dryer, on a Schlenk line.

**Table 1. SMS of $HfB_2$/B nanocomposites.**

| Hf:B ratio | Solvent | Crucible (OD/ID | $HfCl_4$ (mmol) | $NaBH_4$ (mmol) |
|---|---|---|---|---|
| 1:4 | LiCl/KCl (2.5 g) | 18/12 | 1 | 2 |
| 1:8 | LiCl/KCl (2.5 g) | 18/12 | 1 | 2 |
| 1:12 | LiCl/KCl (2.5 g) | 18/12 | 1 | 2 |
| 1:4 | LiI/KI (5 g) | 18/12 | 1 | 2 |
| 1:4 | LiI/KI (20 g) | 24/18 | 4 | 8 |

1-b- $CaB_6$

For the calcium-based system, all previous steps were identical to those before-mentioned, but the medium was heated at 800 °C for 4 h. In the case of calcium, the reaction also starts as soon as the eutectic melts but it is more violent than for hafnium. Indeed, stirring is necessary to avoid the spilling of the liquid salt above the crucible's edge. Moreover, quick gas release within the highly viscous molten eutectic leads to the formation of a blockage as the reaction media is frozen in the upper parts of the crucible. As more salt deposited, the gas release may be blocked and further reaction results in the blockage ejection and loss of the reaction media. This also impedes reactions involving a low Ca:B ratio (1:10, 1/12 and lower), which consistently results in frozen salts in the bottom of the quartz tube that therefore breaks during cooling, as insertion of alkaline ions weakens quartz. For $CaB_6$, the initial quantities of calcium (II) chloride and sodium borohydride are described in Table 2.

Syntheses in LiI/KI were washed with methanol (VWR grade « Normapur », $H_2O$ < 0,01 mol%): after cooling, the frozen eutectic was dissolved in methanol and sonicated for 1 min. The resulting black suspension was centrifuged (in 50 mL polycarbonate tubes at 16.5 krpm for 20 min) four times. Between each centrifugation step, the supernatant was removed, the suspension re-dispersed in methanol and sonicated for 30 s. It was then dried at 40 °C under vacuum for 3 h, in a vacuum dryer, on a Schlenk line.

**Table 2. SMS of $CaB_6$/B nanocomposites.**

| Ca:B ratio | Solvent | Crucible (OD/ID) | $CaCl_2$ (mmol) | $NaBH_4$ |
|---|---|---|---|---|
| 1:8 | LiCl/KCl (2.5 g) | 18/12 | 1 | 6 |
| 1:8 | LiI/KI (5 g) | 18/2 | 1 | 6 |
| 1:8 | LiI/KI (20 g) | 24/18 | 2 | 24 |

1-c- Nano-$B_{am}$

For nano-$B_{am}$ synthesis, all previous steps were identical to those before-mentioned, but the medium was heated at 800 °C for 1 h. The initial quantity of sodium borohydride used is detailed in Table 3.

Reaction media were washed with methanol (VWR grade « normapur », $H_2O$ < 0,01 mol%): after cooling, the frozen eutectic was dissolved in deionised water and sonicated for 1 min. The resulting black suspension was centrifuged (in 50 mL polycarbonate tubes at 16.5 krpm) four times. Between each centrifugation step, the supernatant was removed, the suspension re-dispersed in methanol and sonicated for 30 s. It was then dried at 40 °C under vacuum for 3 h, in a vacuum dryer, on a Schlenk line.

**Table 3. SMS of nano-$B_{am}$.**

| Solvent | Crucible (OD/ID) | $NaBH_4$ (mmol) |
|---|---|---|
| LiI/KI (5 g) | g-C 18/12 | 6 |
| LiI/KI (5 g) | *h*-BN 18/2 | 6 |
| LiI/KI (20 g) | g-C 24/18 | 24 |

## 2- HPHT experiments

For chapter III, the high pressure assemblies were built in air. For all experiments in chapter IV and V, the assemblies were built in an argon-filled glovebox, sealed under argon. The assemblies were exposed to air for the minimum amount of time prior to compression: *ca.* 1-2 min for experiments in Paris-Edinburgh press and *ca.* 10 min for experiments in MAP.

2-a- Paris-Edinburgh press

The experiments at 5 GPa were performed in a two-columns VX3 Paris-Edinburgh press. Before building the high pressure assemblies, the powders (~ 30 mg) were compacted into 2 mm diameter pellets. The assemblies are described in Figure 1. The set-ups were loaded in 10 mm baked pyrophyllite gaskets prior to compression. The high-resistivity graphite inside the assembly was used as heater by injecting electrical current from the anvils through the assembly, with a SM3000 power supply from Delta Elektronika (15 V-200 A) for experiments up to 1550 °C (remote controlled), for superior temperatures a Genesys 5 kW power supply from TDK-Lambda was used (manual control). The temperature control was based on previous power supply output calibrations. The samples were compressed at 5 GPa within 3 h in a 2 columns VX3 Paris-Edinburgh press. Once at the desired pressure, the samples were heated for ramping and dwell times described in Chapter III, IV and V before quenching. After cooling, the samples were slowly decompressed over 6 h.

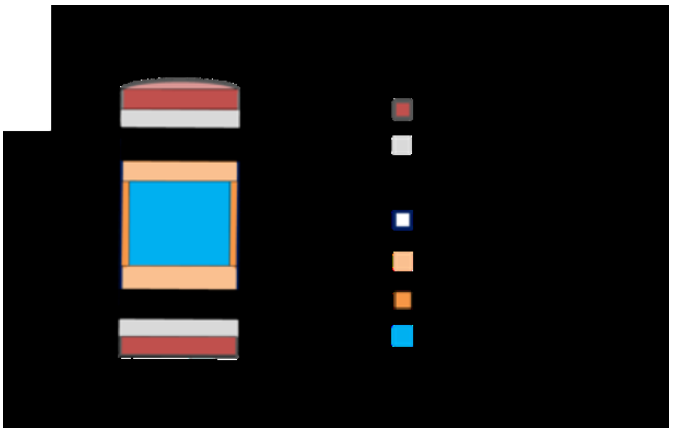

**Figure 1. 10 mm Paris-Edinburgh gasket and assembly. Total height is 6.5 mm. All parts have an OD of 3.5 mm. Other dimensions are the following: electrical contact is 0.6 mm thick, Mo foil is 0.25 mm thick, graphite heater caps are 0.65 mm thick, graphite heater is 3.5 mm long, ID is 3.0 mm, *h*-BN caps are 0.25 mm thick, capsule is 3.0 mm long, OD is 3.0 mm, ID is 2.2 mm**

2-b- Multi-anvil press

The experiments at 14 GPa (Chapter V) were conducted in the Laboratoire Magma et Volcans in Clermont-Ferrand with a 4-columns 1500 tons press from Voggenreiter, equipped with a Kawai-type 6-8 module. Heating is performed with a 140AMX power supply from Pacific. The temperature control was based on previous power supply output calibrations. For these experiments, 14/8 octahedra were used. The assembly is described in Figure 2. Note that the thermocouple was replaced with MgO in our case. The samples were compressed at 14 GPa within 4 h and slowly decompressed over 16 h after temperature quench.

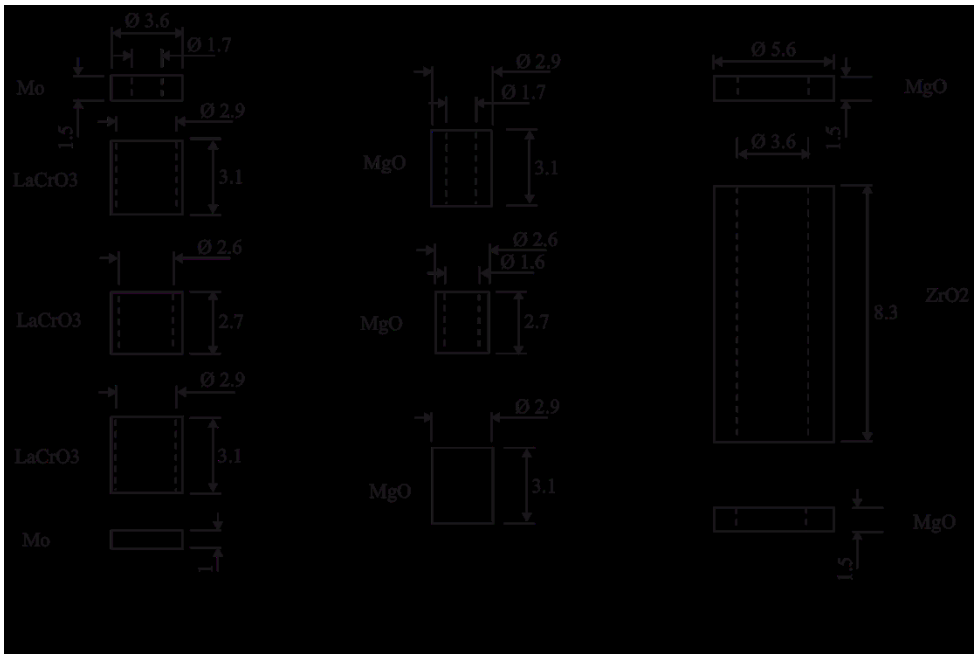


**Figure 2. 14/8 octahedron assembly.**

## 3- Characterisation techniques

### 3-a- X-Ray Diffraction

• Powder XRD of SMS-derived samples

The powders were characterised with a Bruker D8 X-ray diffractometer operating in the Bragg-Brentano reflection mode equipped with a nickel filter to select the Cu-$K_\alpha$ radiation. The data are collected in the $2\theta$ = 10-60 ° range with 0.05 ° steps, 2 s per step. For analysis in exclusion of air, a sample holder equipped with a protective dome designed to maintain an argon atmosphere from Bruker was used.

• XRD of HPHT-treated samples

After opening of the gasket, pieces of HPHT samples were introduced and sealed in a glass capillary in an argon filled glovebox. The samples were characterised in transmission mode with a MM07 HF diffractometer from Rigaku equipped with a Mo rotating anode ($\lambda$ = 0.709319 Å). The data are collected on a Raxis4++ detector equipped with a double image plate (300x300 mm, pixels dimensions are 200x200 µm). Measurements were done with a 500 µm collimator (*ca.* 80 µm beam size on sample) and the image plate exposed for 30 min. The sample to detector distance was calibrated with a $LaB_6$ reference and the image integration performed with the Fit2D software (ESRF).

### 3-b- TEM

Most TEM and HRTEM analyses were performed using a Tecnai spirit *G2* apparatus ($LaB_6$, operating at 120 kV). HRTEM analyses of the $CaB_6$/B nanocomposite (Chapter II and III) were performed by Patricia Beaunier on a JEOL JEM 2011 ($LaB_6$, operating at 200 kV) apparatus at the Microscopy Centre of Institut of Materials of Paris Centre, Sorbonne Universités-UPMC, Paris. The STEM-HAADF and STEM-DF observations were performed by Ovidiu Ersen and Simona Moldovan on a JEOL 2100 F operating at 200 kV and equipped with aberration correction on the electronic probe at the Institut de Physique et Chmie de la Matière de Strasbourg. STEM-EELS and STEM-EDS, not shown in this manuscript, were performed by Dario Taverna at the Institut de Minéralogie, de Physique des Matériaux et de Cosmochimie on a JEOL 2100F equipped with a Schottky field emission gun, a post-column GIF 2001 device from Gatan for EELS and a SiLi detector from Jeol for EDS analysis. SAED pictures are calibrated on a gold reference sample. Particle size distribution diagrams ($HfB_2$, nano-$B_{am}$) were based on measurements for 150 particles at least.

All samples were prepared by evaporating a drop of diluted suspension in ethanol on a carbon-coated copper grid.

### 3-c- ICP-OES

ICP-OES analyses were realised by Domitille Giaume at the Institut de Recherche de Chimie Paris on a iCAP 6000 apparatus from ThermoFisher. The powders were dissolved in nitric acid (2 to 5 $mol.L^{-1}$) prior to dilution in deionised water (10 fold). For all elements dosed, the error is *ca.* 1 %.

### 3-d- SEM-EDS

SEM-EDS analyses were realised on a SEM S-3400N from Hitachi, equipped with an EDS detector from Oxford. The acceleration voltage is set to 10 kV and the EDS signal calibrated for quantitative analysis on the K-line of titanium. The composition corresponds to mean values obtained on at least three different regions of the sample. The data were analysed with the INCA software from Oxford. Samples were deposited on a conductive carbon tape. For SMS-derived samples, the powders were recovered with a *ca.* 20 nm thick carbon layer prior to analysis, which was not the case for HPHT treated sample, to ensure sample recovery.

The detailed data for experiments 1 to 8 are presented in Table 4.

**Table 4. SEM-EDS analyses of experiment 1 to 8.**

| Experiment | B (at%) | K (at%) | Na (at%) | I (at%) |
|---|---|---|---|---|
| SMS-derived B | 94.2 | 4.8 | < 0.8 | < 0.5 |
| 1 | 96.6 | 3,4 | < 0.1 | < 0.1 |
| 2 | 96.3 | 3,7 | < 0.1 | < 0.1 |
| 3 | 97.4 | 2,6 | < 0.1 | < 0.1 |
| 4 | 95.9 | 4,1 | < 0.1 | < 0.1 |
| 5 | 97.1 | 2,9 | < 0.1 | < 0.1 |
| 6 | 97.3 | 2,7 | < 0.1 | < 0.1 |
| 7 | 97.7 | 2.3 | < 0.1 | < 0.1 |
| 8 | 95.7 | 4.3 | < 0.1 | < 0.1 |
| Post HPHT mean | 96.75 | 3.25 | < 0.1 | < 0.1 |

### 3-e- $^{11}$B NMR Spectroscopy

The $^{11}$B NMR spectra presented throughout the manuscript were realised by Cristina Coelho-Diogo on the IMPC platform. All spectra have been recorded on AV700 spectrometer from Bruker, equipped with a 16.3 T permanent magnet. The magic angle spinning experiments were conducted at 20 KHz in 2.5 mm rotors. For SMS-derived powders the rotors were filled with powder. For post-HPHT samples, a piece of the resulting pellet was placed between to Teflon pieces in the rotor. The rotors were loaded and unloaded inside an argon-filled glovebox to avoid contact with air. The $^{11}$B chemical shifts are reference *vs.* $BF_3(OEt)_2$ ($\delta$ = 0 ppm) and the spectra calibrated from boric acid (> 99.5 %, Sigma-Aldrich).

### 3-f- C-H-N elemental analysis

The CHN elemental analyses were performed by Marie-Françoise Bricot in the Institut des Substances Naturelles in Gif-Sur-Yvette on a CHN 2400 analyser from Perkinelmer, by combustion at 940 °C. Detection was done by thermal conductivity. The error is *ca.* 0.3 % for each element measured.

Résumé :

Dans cette thèse, nous nous intéressons à la synthèse de nouveaux matériaux nanostructurés sous conditions extrêmes de pression et de température (P > 5 GPa et T > 1000 °C). Les matériaux que nous étudions sont basés sur un élément en particulier : le bore. En effet, ces matériaux présentent des propriétés intéressantes. D'une part, les allotropes du bore présentent tous des duretés élevées et une grande inertie chimique. D'autre part, les alliages métal-bore (ou borures métalliques) présentent des propriétés variées, de la thermoélectricité ($HfB_2$) à la supraconductivité ($MgB_2$). Nous utilisons la synthèse en sels fondus afin d'obtenir des systèmes nanostructurés comprenant deux composants : des nanoparticules (environ 10 nm) cristallines de borure métallique ($HfB_2$ ou $CaB_6$) comprises dans une matrice de bore amorphe. Le traitement sous haute pression et température de ces systèmes permet de cristalliser l'amorphe, en conservant la nanostructure initiale. Nous synthétisons plusieurs nouveaux matériaux : des nanocomposites borure/borate ($HfB_2/HfB_2O_5$ ou $CaB_6/CaB_2O_4$) ou borure/bore ($HfB_2$/β-B ou $CaB_6$/β-B), premiers membres de nouvelles familles de nanomatériaux. Nous utilisons aussi un matériau nanostructuré de bore amorphe, synthétisé en sels fondus. Nous le cristallisons sous haute pression et haute température. En sus de la première occurrence de bore epsilon nanostructuré, nous obtenons deux nouvelles phases riches en bore, dont la structure est en cours de résolution. En somme, nous avons développé une méthode de synthèse à la frontière entre la chimie des nanomatériaux et le physique des hautes pressions et températures, à l'origine de nouveaux nanomatériaux et structures.

Abstract:

During this PhD, we were interested in the preparation of new nanostructured materials under extreme pressure and temperature conditions (P > 5 GPa et T > 1000 °C). We studied materials based on a specific element: boron. Indeed, these materials have interesting properties. On the one hand, boron allotropes exhibit high hardness and chemical inertness. On the other hand, metal-boron alloys (metal borides) span a wide range of properties, from thermoelectricity ($HfB_2$) to supraconductivity ($TiB_2$). We used the synthesis in molten salts to reach nanostructured systems with two components: crystalline boride nanoparticles (*ca.* 10 nm) embedded in an amorphous boron matrix.High pressure high temperature treatments on these systems allow crystallisation of the amorphous component. Several new nanomaterials were synthesised: boride/borate ($HfB_2/HfB_2O_5$ or $CaB_6/CaB_2O_4$) or boride/boron ($HfB_2$/β-B or $CaB_6$/β-B) nanocomposites, representing the first members of new nanomaterials families.We also used nanostructured amorphous boron, synthesised in molten salts. It is cristallised under high pressure and temperature. In addition to the first nanostructured occurrence of epsilon-boron, we report two new boron-rich phases, which structure is under resolution.

All in all, we developed a synthetic route at the frontier of nanomaterials chemistry and high pressure and temperature physics, reaching new nanomaterials and structures.

Keywords : [----------]